

**SUPERFLUID HELIUM DROPLETS: FROM  
SPECTROSCOPY TO MAGNETIC NANOPARTICLES**

**Thesis submitted for the degree of**

**Doctor of Philosophy**

**at the University of Leicester**

**by**

**Cheng Feng MSc**

**Department of Chemistry**

**University of Leicester**

**2015**

# Superfluid Helium Droplets: from Spectroscopy to Magnetic Nanoparticle Formation

Cheng Feng

## Abstract

This project applies superfluid helium droplets in two big areas: spectroscopy and nanoparticles formation. Helium droplets, consisted of more than  $10^3$  helium atoms, provide a non-friction and very cold ( $\sim 0.37$  K) environment for clusters/nanoparticles growth, which offers unique advantages as a medium in applications of both spectroscopy and nanostructures formation. By sequentially adding NaCl and water molecules, the dissolution process of NaCl in water can be experimentally studied for the first time. This is achieved by recording the infra-red spectra of  $\text{NaCl}(\text{H}_2\text{O})_n$  ( $1 \leq n \leq 7$ ) complexes in O-H stretching region in combination with *ab initio* calculations. In particular, two bands have been assigned to dissolution of NaCl in water.

The existence of quantum vortices in helium droplets has been firmly evident from spherical Ag nanoparticles formed in a chain. Quantum vortices provide a new route for the formation of one-dimensional nanostructures, which has been exploited in the fabrication of novel nanowires. Finally the pioneering work on the fabrication of both antiferromagnetic and ferromagnetic nanomaterials is reported for the first time, taking Cr and Ni as examples respectively. It is found that we can force ferromagnetic ordering in magnetic materials in superfluid helium. In particular, antiferromagnetic chromium has been discovered to convert to ferromagnetic, and the magnetism of ferromagnetic materials can have hugely enhanced magnetic moments that are close to the theoretical limit. This will have potential for applications in biomedical science, data storage and energy efficient technologies in the longer term.

# Acknowledgement

Upon accomplishing my PhD study, I must take this chance to thank my supervisor, Dr. Shengfu Yang, who has guided me in the study of nanoscience and have given me numerous valuable suggestions in my project and writing up this thesis. I have achieved incredible self-improvement during the 4 years learning from him, in the aspects of not only the knowledge, but also his integrity and industrious spirit. I also want to express my appreciation to Prof. Andrew Ellis for his constructive advice in discussions and his patient demonstration in science, in particular, spectroscopy science. In addition, I want to acknowledge Prof. Chris Binns and Dr. Corey Evans for their help with magnetic theory and computational chemistry, respectively.

Every other member in the NanoChemistry group at University of Leicester is also appreciated. In such a united and friendly group, I gained not only many help but also enjoyed the life. In particular, I want to thank Dr. Adrian Boatwright who helped to a reliable helium droplet system and generously shared his lab skills. Dr. Daniel Spence joined in the group in the same year as me, who had explored the adventure, gained knowledge and developed the techniques together with me. It has been an extremely memorable experience to work with Dan. Drs. Elspeth Latimer, Jon Tandy and Gautam Sarma have also provided their help to my project, for which I sincerely appreciate. I also wish to thank all the friends I met in Leicester who have delivered me a good memory.

This project has received constructive support from international collaborators, in particular, Dr. Davide Peddis in Italy and Dr. Liying Zhang in China. I also want to thank the technicians from Chemistry Workshop who helped the manufacturing some decent components for the project.

I want to thank my girlfriend Liping. Although most of the time she was far away from me by nearly 6000 miles, her love and comfort are irreplaceable mental support. Finally I want to deliver my special thanks to my parents to whom I want to dedicate this thesis. Without their encouragement and support, it is impossible for me to finish my PhD project.

# Table of Contents

<b>CHAPTER 1: INTRODUCTION.....</b>	<b>13</b>
1.1 BULK SUPERFLUID HELIUM.....	13
1.2 HELIUM DROPLETS TECHNIQUE.....	15
1.2.1 HeDs Formation – Supersonic Expansion.....	15
1.2.2 Superfluidity of HeDs.....	18
1.2.3 Size of HeDs.....	19
1.2.4 Pickup Process.....	21
1.2.5 Electron Ionization in HeDs.....	23
1.2.6 Quantum Vortices.....	24
1.3 SPECTROSCOPY IN HEDS.....	25
1.3.1 Depletion Spectroscopy.....	27
1.3.2 Infrared and Electronic Spectroscopy in HeDs.....	28
1.4 NANOPARTICLES FORMED IN HEDS.....	29
1.5 MAGNETIC NANOPARTICLES.....	32
1.5.1 Free Atom Magnetization.....	32
1.5.2 Magnetism Measured in Many-atom System.....	36
1.5.3 Types of Magnetic Materials.....	38
1.5.4 Magnetic Material at Nanoscale.....	42
<b>CHAPTER 2: EXPERIMENTAL APPARATUS AND CHARACTERIZATION.....</b>	<b>45</b>
2.1 OVERVIEW OF THE HELIUM DROPLET SOURCE.....	45
2.2 DETECTION EQUIPMENT.....	50
2.2.1 Quadrupole Mass Spectrometer.....	50
2.2.2 Laser System for Spectroscopy.....	52
2.2.3 TEM Imaging.....	54
2.2.4 Mass Measurement of Deposited Nanoparticles.....	56
2.2.5 XPS Analysis.....	59
2.2.6 Magnetic Property Measurement.....	60
2.3 CLUSTERS AND NANOPARTICLES FORMED IN HEDS.....	63
2.3.1 The Dependence of Helium Droplet Sizes on the Source Conditions.....	63
2.3.2 The formation of Small Clusters in HeDs.....	65
2.3.3 The Growth of Nanoparticles in HeDs.....	69
2.3.4 Core-shell Structural Nanoparticles Formation.....	72
<b>CHAPTER 3: INFRA-RED SPECTROSCOPY OF NA<sub>2</sub>CO<sub>3</sub>/(H<sub>2</sub>O)<sub>N</sub> COMPLEX IN HELIUM DROPLETS.....</b>	<b>75</b>
3.1 INTRODUCTION.....	75
3.2 METHOD.....	79
3.3 RESULTS AND DISCUSSION.....	81

3.3.1	<i>Mass Spectra of <math>(\text{NaCl})_m(\text{H}_2\text{O})_n^+</math> Clusters in HeDs</i> .....	81
3.3.2	<i>Infra-red Spectroscopy of Pure Water Clusters</i> .....	82
3.3.3	<i>Calculation Results of <math>\text{NaCl}(\text{H}_2\text{O})_n^+</math> Complex (<math>n = 1 - 6</math>)</i> .....	83
3.3.4	<i>Infra-red Spectroscopy of <math>\text{NaCl}(\text{H}_2\text{O})_n^+</math> Complex (<math>n = 1 - 3</math>)</i> .....	92
3.3.5	<i>Infra-red Spectroscopy of <math>\text{NaCl}(\text{H}_2\text{O})_n^+</math> Complex (<math>n = 4 - 7</math>)</i> .....	95
3.3.6	<i>Infra-red Spectroscopy <math>m/z = 23</math></i> .....	97
3.4	CONCLUSION.....	100
<b>CHAPTER 4: QUANTUM VORTICES IN HELIUM DROPLETS AND NANOWIRES GROWTH</b>		<b>101</b>
.....		
4.1	INTRODUCTION.....	101
4.2	FIRM EVIDENCE FOR QUANTUM VORTICES IN HELIUM DROPLETS .....	103
4.2.1	<i>Silver Aggregation in HeDs</i> .....	103
4.2.2	<i>Silver/Silicon Binary Nanowires in HeDs</i> .....	106
4.2.3	<i>Nanostructures Growth along the Vortex Line</i> .....	107
4.3	ONE-DIMENSIONAL NANOSTRUCTURES FORMATION IN HELIUM DROPLETS .....	110
4.3.1	<i>Au Nanostructures</i> .....	111
4.3.2	<i>Ni, Cr and Si Nanowires Formed in Helium Droplets</i> .....	114
4.3.3	<i>Advantage of Helium Droplets Technique in Forming One-dimensional Nanostructures</i> .....	116
4.4	MULTIPLY QUANTIZED VORTICES IN HELIUM DROPLETS.....	116
4.5	CONCLUSION.....	120
<b>CHAPTER 5: MAGNETIC NANOMATERIALS FORMED IN HELIUM DROPLETS</b> .....		<b>122</b>
5.1	INTRODUCTION .....	122
5.1.1	<i>Overview of Magnetism of 3d Materials</i> .....	122
5.1.2	<i>Antiferromagnetic Materials at the Nanoscale</i> .....	124
5.1.3	<i>Ferromagnetic Materials at the Nanoscale</i> .....	127
5.2	EXPERIMENTAL .....	133
5.3	FERROMAGNETIC CR NANOMATERIALS.....	135
5.3.1	<i>Cr Mass Spectrum</i> .....	135
5.3.2	<i>TEM Images of Cr Nanoparticles and Nanowires</i> .....	136
5.3.3	<i>Magnetic Properties of Cr Nanoparticles</i> .....	138
5.3.4	<i>Magnetic Properties of Larger Cr Nanoparticles</i> .....	141
5.3.5	<i>Magnetic Properties of Cr Nanowires</i> .....	142
5.3.6	<i>Summary the Ferromagnetism of Cr Nanostructure</i> .....	147
5.4	ORIGIN OF FERROMAGNETISM IN CR NANO-OBJECTS .....	148
5.5	NI NANOPARTICLES WITH GIANT MAGNETISM.....	152
5.5.1	<i>Mass Spectrum of Ni and Ni/Au clusters</i> .....	152
5.5.2	<i>Pure Ni and Ni/Au Core-shell Nanoparticles</i> .....	153
5.5.3	<i>M-H Curve of Ni and Ni/Au Core-shell Nanoparticles</i> .....	154
5.5.4	<i>Ni/Ag Core-shell Nanoparticles</i> .....	156

5.5.5	<i>M-H Curve of Ni and Ni/Ag Core-shell Nanoparticles</i> .....	158
5.5.6	<i>Enhanced Magnetism of Ni</i> .....	159
5.6	CONCLUSION AND FUTURE WORK .....	160
	<b>THESIS SUMMARY</b> .....	<b>162</b>
	<b>BIBLIOGRAPHY</b> .....	<b>165</b>

## List of Tables

Table 1- 1 Comparison between experimental and theoretical value of atomic magnetization of selected <i>4f</i> metals and fulfilled <i>3d</i> ions.....	37
Table 1- 2 Comparison between experimental and theoretical value of atomic magnetization of ferromagnetic metals including the theoretical magnetization after orbital quenching.....	38
Table 2- 1 Comparison of deposition rate measured by deposition monitor and TEM images. Samples taken in account is Ag tested at different source temperature from 10 K to 6.25 K..	58
Table 2- 2 the sizes and fluxes of Ag nanoparticles measured in different oven temperature.....	71
Table 2- 3 Ag nanoparticles formed at different Source temperature with the oven temperature maintained at 980 K. ....	71
Table 3- 1 Optimized geometry for $\text{NaCl}(\text{H}_2\text{O})_n$ ( $1 \leq n \leq 6$ ) complexes, together with their relative energy to the global minimum structure, intensities and transition frequencies. ....	84
Table 5- 1 Saturation magnetization ( $M_s$ ) of Fe nanoparticles, using different synthetic methods with similar diameter of about 10 nm, measured at room temperature.....	129
Table 5- 2 Size dependence of the saturation magnetisation of Fe nanoparticles synthesized by wet chemical method. ....	130
Table 5- 3 Magnetic properties of Cr nanoparticle without a diameter of 2.4 nm, at different temperatures.....	139
Table 5- 4 Magnetic properties of Cr nanowires measured at various temperatures.	143
Table 5- 5 Comparison of saturation magnetization of our sample and the wet-chemical samples with different particle sizes.....	156
Table 5- 6 Summary of the magnetic properties of Ni and Ni/Ag nanoparticles. ....	159

## List of Figures

Figure 1- 1 Phase diagram of $^4\text{He}$ . The dash lines are the isentropic lines which helium follows in the process of droplets formation. The figure is a reprint from Ref. (10) where the isentropic data were measured at 20 bar stagnation pressure.....	14
Figure 1- 2 Schematic representation of the velocity distribution of supersonic expansion. Reprinted from Ref. (29). .....	16
Figure 1- 3 Schematic representation of the helium droplet formation by the supersonic expansion of helium gas.....	17
Figure 1- 4 Variation of the helium droplet size respect to the source temperature, reprinted from Ref. (10). The data represented by the squares and circles are measured via titration technique using collisional helium and argon gas respectively. The stars and triangles are the data measured by the deflection technique <sup>(40, 42)</sup> .....	20
Figure 1- 5 The probability of the number of dopant atoms/molecules (k) being picked up by helium droplets in response to the partial pressure. Graph is reprinted from Ref. (28).....	22
Figure 1- 6 Electron impact mode for a He atom. ....	23
Figure 1- 7 A typical depletion signal recorded by a quadrupole mass spectrometer. The width of the depletion peak is the fly time of the ion from the pickup region to the mass spectrometer. ....	28
Figure 1- 8 Schematic of atomic magnetic moment from spin-orbital coupling. ....	33
Figure 1- 9 (a) Illustration of the occupation of $J_z$ energy level by atomic magnetic moments when saturation, taking Mn as an example whose $J = 5/2$ . (b) The occupation at $J_z$ energy level of magnetic moments in the process of magnetizing. (c) A macroscopic view of the magnetizing process. Every blue arrow corresponds to a discrete energy level. $\theta$ is the ultimate angle of an atomic magnetic moment can rotate towards the magnetizing direction (z axis).....	35
Figure 1- 10 Bethe-Slater curve demonstrating the value of exchange constant in function of the inter-atom separation of different element. Figure is reprinted from Ref. (121).....	40
Figure 1- 11 Magnetic moments display with the existence of external magnetic field in (a) ferromagnetic materials; (b) anti-ferromagnetic materials; (c) ferrimagnetic materials. ....	42

Figure 1- 12 M-H curve expression of the transition from ferromagnetic material in bulk phase to superparamagnetic material at nanoscale. ....	43
Figure 2- 1 Block diagram showing the overall chamber configuration of the helium droplets system. (a) helium source; (b) skimmer; (c) pick- up cells; (d) deposition monitor and shutter; (e) deposition station; (f) load-lock chamber; (g) quadrupole mass spectrometer; (h) He/Ne laser for alignment of the chamber .....	45
Figure 2- 2 Schematic of the UHV helium droplets for the synthesis of nanoparticles. ....	46
Figure 2- 3 Left: The configuration and dimensions of the ceramic oven used. Right: Oven at working in the vacuum chamber. ....	48
Figure 2- 4 The UHV helium droplet source for the synthesis of nanoparticles. ....	50
Figure 2- 5 Mass spectrum of pure helium droplets ( $6 < m/z < 100$ ), recorded at $T_0 = 12$ K, $P_0 = 15$ bar, $IE = 70$ eV. ....	51
Figure 2- 6 Optics configuration and working principle of OPO/OPA laser.....	53
Figure 2- 7 The description of how the software “Image J” works in determining the size of the nanoparticles from TEM image. ....	55
Figure 2- 8 The deposition rate measurement using the thin film deposition monitor. Upper panel: the original frequency change. Lower panel: Accumulated Mass calculated from the frequency change according to Equation 2-2. The gradient is the deposition rate in unit of $\mu\text{g}/\text{min}$ . ....	57
Figure 2- 9 Typical M-H curves of (a): diamagnetic material; (b): paramagnetic material; (c): ferromagnetic material. Hysteresis loop of multi domain ferromagnetic material (dash line) is narrower than the single domain one (solid line); (d): superparamagnetic material. Picture is abstracted from Ref. (140). ....	61
Figure 2- 10 $\text{He}_4^+/\text{He}_2^+$ ratio variation in the source temperature range of 15 K to 5.5 K, recorded by the quadrupole mass spectrometer at stagnation pressure of 15 bar, $IE = 65$ eV. ....	63
Figure 2- 11 The dependence of $\text{He}_4^+/\text{He}_2^+$ ratios on the source temperatures. Different stagnation pressures have been applied, <i>i.e.</i> , at 10 bar, 15 bar, 20 bar, 25 bar and 30 bar, respectively.....	65
Figure 2- 12 Mass spectra of Ni clusters recorded at different source temperatures... ..	67
Figure 2- 13 Mass spectra of Ni clusters at different oven temperatures. ....	68

Figure 2- 14 TEM images of Ag nanoparticles at various oven temperatures: (a) 876 K, (b) 882 K, (c) 888 K, (d) 902 K and (e) 980 K. In all these experiments the source condition is kept at $T_0 = 9.5$ K and $P_0 = 15$ bar, and the deposition time $t_{\text{deposition}} = 5$ min. ....	70
Figure 2- 15 Evidence for the formation of Ni/Au core-shell structures. (a) TEM image of Ni/Au nanoparticles. (b) Comparison of XPS on the Au 4f edge between pure Au and Ni/Au nanoparticles. ....	73
Figure 2- 16 TEM images of Ag/Si core shell nanoparticles. ....	74
Figure 3- 1 Schematic illustration of four Eigen-Tamm states of the dissociated solution. Reprinted from Ref (154).....	76
Figure 3- 2 Experimental set-up for the depletion spectroscopy on $\text{NaCl}(\text{H}_2\text{O})_n$ clusters doped in helium droplets.....	79
Figure 3- 3 Mass spectrum of helium droplets doped with NaCl and $\text{H}_2\text{O}$ molecules. ...	81
Figure 3- 4 Pure water IR spectrum recorded at helium dimer channel ( $m/z = 8$ ). ....	82
Figure 3- 5 Infrared depletion spectra recorded for (a) $m/z$ 41, (b) $m/z$ 59 and (c) $m/z$ 77. Also shown are the predicted global minimum energy structures. The blue stick beneath the IR spectra is the calculation results, which mark the corresponding frequencies predicted by the global minima structures. Note that doublers are observed in the depletion spectra because of Fermi resonance. ....	93
Figure 3- 6 Depletion spectra recorded at (a) $m/z$ 95, (b) $m/z$ 113, (c) $m/z$ 131 and (d) $m/z$ 149. ....	96
Figure 3- 7 Depletion spectra on $m/z$ 23 with the SSIP structure of $\text{NaCl}(\text{H}_2\text{O})_6$ . The black curve was recorded when both water and NaCl doped in; the red one was obtained when salt oven was switched off; the blue sticks shows the predicted bands from the SSIP structure complex. The main bands of the water clusters are also assigned, including Free OH, D (water dimer), T (water trimer), Q (water tetramer) and P (water pentamer).....	98
Figure 4- 1 TEM images of Ag aggregations in helium droplets with different source temperatures of (a) 9.5 K; (b) 8.5 K; (c) 7.5 K; (d) 6.5 K; (e) 6 K; (f) 5.5 K; (g) 5 K; (h) 4.5 K. The scale bars for (a) – (c) are 20 nm, (f) – (h) are 100 nm. Image (i) shows the expanded views of images (g) and (h). ....	105
Figure 4- 2 TEM images of Ag-Si nanowires formed in helium droplets at temperature of (a) 6.5 K and (b) 4.5 K. ....	107

Figure 4- 3 TEM images of Au nanostructures formed in helium droplets of different initial diameters of: (a) 25 nm; (b) 55 nm; (c) 75 nm; (d) 135 nm; (e) 250 nm; (f) 790 nm. (g) 1.7 $\mu\text{m}$ . The scale bars for (a) – (c) are 20 nm and for (d) – (g) are 50 nm. The Au oven is fixed at 1300 K. ....	112
Figure 4- 4 Dependence of the diameter (blue triangle) and the length (red triangle) of Au nanowires on the oven temperature for helium droplets with a mean initial diameter of 1.7 $\mu\text{m}$ . ....	114
Figure 4- 5 (a) Ni nanorods formed in 790 nm helium droplets; (b) Ni nanowires formed in 1.7 $\mu\text{m}$ helium droplets; (c) Cr nanowires formed in 790 nm helium droplets; (d) Si nanowires formed in 1.7 $\mu\text{m}$ helium droplets. ....	115
Figure 4- 6 The variation of partial pressure $P_3$ in the quadrupole chamber and $\text{He}_2^+$ signal at different nozzle positions. ....	117
Figure 4- 7 TEM images of Ag nanoparticle grown in the droplets at the centre of the helium beam. The scale bar is 200 nm. The expanded image in the blue frame shows the details of nanoparticle display. ....	118
Figure 5- 1 Illustration of spin-canting induced magnetization for AFM nanoparticles. ....	127
Figure 5- 2 Illustration of the evolution of the magnetism of ferromagnetic material ( $M$ ) with the material size ( $N$ ) in different dimension scales. ....	131
Figure 5- 3 Data processing of the M-H curves of Cr nanoparticles. (a) M-H curve of the raw data, which contains contributions from sample, PEEK substrate and the glass rod. (b) M-H curve after subtraction of the substrate contribution. The blue solid lines show the gradient of the M-H curve. (c) M-H curve after subtraction of the linear contribution from the glass rod. ....	134
Figure 5- 4 Mass spectrum of $\text{Cr}_n^+$ ( $n = 1 - 19$ ) detected at $T_0 = 12$ K and $T_{\text{Cr}} = 1275$ K. ....	136
Figure 5- 5 (a) TEM image of Cr nanoparticles deposited at $T_0 = 9.5$ K. (b) Size distribution of Cr nanoparticles deposited at $T_0 = 9.5$ K. (c) TEM image of Cr nanoparticles deposited at $T_0 = 8$ K. (d) Size distribution of Cr nanoparticles deposited at $T_0 = 8$ K. (e) High resolution TEM image of Cr nanoparticles deposited at $T_0 = 9.5$ K. (f) TEM image of Cr nanowires deposited at $T_0 = 6$ K. All of the TEM samples were deposited for 5 minutes. ....	137

Figure 5- 6 M-H curves of Cr nanoparticles with mean diameters of 2.4 nm measured at 300 K and 5 K, respectively. The insert shows the expanded view of the hysteresis loop near the origin. ....	139
Figure 5- 7 Ratio of the remanent magnetization to the saturation magnetization of Cr nanoparticles at different temperatures. The inset shows the gradient of the saturation and remanence with respect to temperature.....	140
Figure 5- 8 Comparison of saturation magnetization of the two different sized Cr nanoparticles at different temperatures. The solid lines are fitted curves. ....	142
Figure 5- 9 M-H curves of Cr nanowires at 300 K and 5 K. The insert shows the expanded hysteresis loops near the origin.....	143
Figure 5- 10 Variation of remanent magnetization to saturation ratio of Cr nanowires at different temperatures. The inset shows the gradient of the saturation and remanence with respect to temperature. ....	145
Figure 5- 11 Variation of magnetization of Cr nanowires at different temperatures after ZFC including the rotation of magnetic moments orientation. The insert shows the gradient and the phase transition.....	146
Figure 5- 12 (a) Schematic illustration of the Ta wire coil generating a weak magnetic field. The black arrows present the electric current flow and the blue curved arrows present the magnetic induction line. (b) Magnetic moments of pre-aligned Cr atoms before being picked up by helium droplet. (c) Cr atoms bonded together in helium droplets with a longer inter-atom separation $d_1$ than the lattice constant, which results from the pre-aligned magnetic moments. ....	150
Figure 5- 13 Mass spectra of $Ni_n^+$ clusters (upper panel) and $Ni_nAu_m^+$ clusters (bottom panel), recorded at $T_0 = 12.5$ K. ....	153
Figure 5- 14 (a) TEM images of bare Ni nanoparticles formed at $T_0 = 9.5$ K and an oven temperature of 1580 K. The scale bar is 50 nm. (b) Size distribution of bare Ni nanoparticles. (c) TEM images of Ni/Au core-shell nanoparticles formed at $T_0 = 9.5$ K, with oven temperatures at 1580 K for Ni and 1350 K for Au. The scale bar is 20 nm. (d) Size distribution of Ni/Au core-shell nanoparticles.....	154
Figure 5- 15 M-H curve of Ni and Ni/Au core-shell nanoparticles measured at 300 K.	155
Figure 5- 16 (a) TEM images of bare Ni nanoparticles formed a source temperature of 8 K and an oven temperature of 1460 K for Ni. (b) Size distribution of bare Ni nanoparticles. (c) TEM images of Ni/Ag core-shell nanoparticles with $T_0 = 8$ K, $T_{Ni} =$	

1460 K,  $T_{Ag} = 1250$  K. (d) Size distribution of Ni/Ag core-shell nanoparticles. The scale bars are 50 nm in the TEM images. .... 157

Figure 5- 17 M-H curves of Ni and Ni/Ag core-shell nanoparticles at 300 K. .... 158

# Chapter 1

## Introduction

### 1.1 Bulk Superfluid Helium

Helium, with two isotopes of  ${}^4\text{He}$  and  ${}^3\text{He}$ , is the only element in nature that cannot be solidified at atmospheric pressure even at absolute zero temperature. This is attributed to the small atomic mass of helium together with the very weak attractive force between helium atoms due to their closed electron shell. It is calculated that the zero point vibrational energy of helium, which is inversely proportional to the atomic mass in the function :  $E = \frac{p^2}{2m}$  ( $p$  is the atomic momentum and  $m$  is the atomic mass), is about 7.15 K for  ${}^4\text{He}$  <sup>(1)</sup> which is comparable with their inter-atomic potential energy ( $\sim 7.2$  K) <sup>(2-4)</sup>. Therefore a helium atom can still maintain its mobility even at 0 K, without being confined within the lattice.

As seen in the phase diagram of  ${}^4\text{He}$  (Figure 1- 1),  ${}^4\text{He}$  does not have a triple point like other elements. Below 25 bar stagnation pressure, as the temperature decreases helium transits from a normal liquid phase (He I) to a superfluid phase (He II). The transition temperature for He I to He II, which is also the boundary point of gas phase helium, He I and He II, is around 2.17 K. Generally this transition point is also called Lambda point –  $T_\lambda$  for the similarity of the shape of the boundary line with the Greek letter  $\lambda$ . To solidify  ${}^4\text{He}$ , both low temperature and high pressure ( $> 25$  bar) are required.

The superfluidity of  ${}^4\text{He}$  was first discovered in 1938 by a series of extraordinary observations of liquid helium: (i) non-friction flow through the narrow capillaries, (ii) the fountain effect and (iii) the exponentially high thermal conductivity (30 times higher than copper) below  $T_\lambda$  <sup>(5,6)</sup>, *i.e.* in the He II phase. The earliest mode of He II was proposed by Tisza <sup>(7)</sup> and Landau <sup>(8)</sup>, in which the He II phase helium is composed of a mixture of the normal fluid He and superfluid He with separated velocity vectors, so the liquid can undergo separate motions at the same time. This mode was first

experimentally proved by Andronikashvili <sup>(9)</sup> by solvating a stack of compact disk torsional oscillators in He II. Instead of observing the increase of the moment of inertia of the disks with the temperature reduction, which is expected in the normal liquid with certain viscosity, he observed the moment of inertia quickly decays after the temperature was cooled down to  $T_\lambda$ . This experiment provided convincing support to the existence of a superfluid in He II and proved below 2.17 K, helium is superfluid.

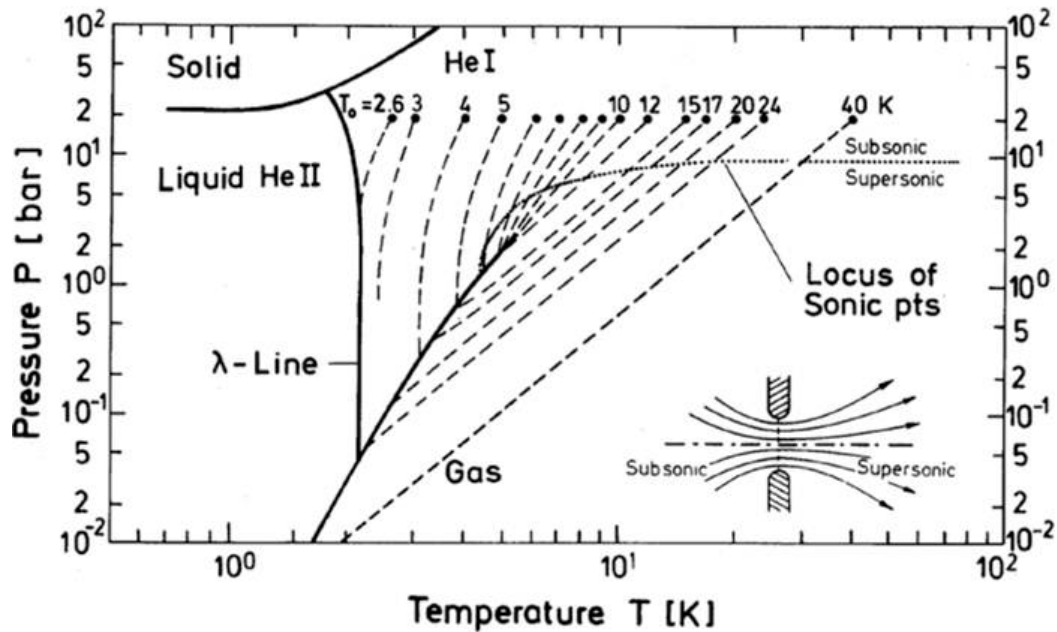


Figure 1- 1 Phase diagram of <sup>4</sup>He. The dash lines are the isentropic lines which helium follows in the process of droplets formation. The figure is a reprint from Ref. (10) where the isentropic data were measured at 20 bar stagnation pressure.

Fundamentally the superfluidity of helium can be explained by Bose-Einstein Condensation (BEC), first proposed by London in 1938 <sup>(11)</sup>. As a boson with no net spin, <sup>4</sup>He transfers into a BEC state at sufficiently low temperature (He II), *i.e.* all the He atoms can occupy the same quantum state – ground state, dismissing their individual particle identities. Therefore the entire ultra-cold helium atoms can be described by a single macroscopic wave function. Since all the atoms are indiscriminately trapped in their ground states, none of the atoms can be excited to higher energy levels when one atom moves close to other atoms; therefore its energy and momentum can be maintained during the movement. In the macroscopic scale, it behaves as if it is experiencing no friction, thus superfluidity.

It is worth mentioning that  $^3\text{He}$  is also a superfluid with a transition temperature of 0.003 K, at which two  $^3\text{He}$  atoms pair up, giving rise to a net integer spin. Since the technique used throughout this thesis takes advantages of superfluid  $^4\text{He}$ , all the helium mentioned in the following sections refer to  $^4\text{He}$ .

## 1.2 Helium Droplets Technique

Although the intriguing superfluidity of helium was discovered in the 1930s, it has not presented much potential benefit to either scientific research or human's real life for a long time. Most of the early research focused on investigations of the properties of superfluid helium. For example: the stable mass spectra of pure helium clusters had been recorded using molecular beam technique<sup>(12)</sup>; the appearance energy of  $\text{He}_2^+$  at around 20 eV, which is lower than the fully ionization energy of 24.6 eV due to Penning ionization had been discovered<sup>(13, 14)</sup>; the magic number of  $\text{He}_4^+$  in the mass spectra had attracted great interests<sup>(14-16)</sup>; and the ionization cross section of  $\text{He}^+$  had been systematically studied with the impact energy varying from 24.6 eV to 4000 eV<sup>(17-22)</sup>.

However, almost all the early attempts of seeding foreign species into liquid helium failed because the high mobility of helium prevented the dopants being isolated, but made them precipitate out or aggregate on the surface<sup>(23-25)</sup>, which significantly limited the applications of the superfluid helium. It was not until the 1990s when J. P. Toennies' group in Gottingen first successfully captured and isolated foreign species<sup>(26, 27)</sup> in helium nanodroplet. Since then helium droplet techniques have been quickly developed in mass spectrometry and spectroscopy investigations of molecules and molecular clusters, and recently in the synthesis of nano structural materials.

### 1.2.1 HeDs Formation – Supersonic Expansion

Helium droplets are helium clusters consisting of more than  $10^3$  atoms<sup>(23, 28)</sup>. Although there were some attempts of forming helium droplets via liquid helium expansion in the early days, the most common way currently to form helium droplets is using

molecular beam techniques, where droplets are formed by the supersonic expansion of pre-cooled helium gas in high vacuum <sup>(23)</sup>. Supersonic expansion occurs when the gas ejects from a high backing pressure into a high vacuum environment via a small pinhole. Apart from effusive expansion which happens at low backing pressure conditions, supersonic expansion is favourable to aggregate into high density clusters with the velocity higher than sound and concentrating in a narrow region <sup>(29)</sup>, as shown in Figure 1- 2.

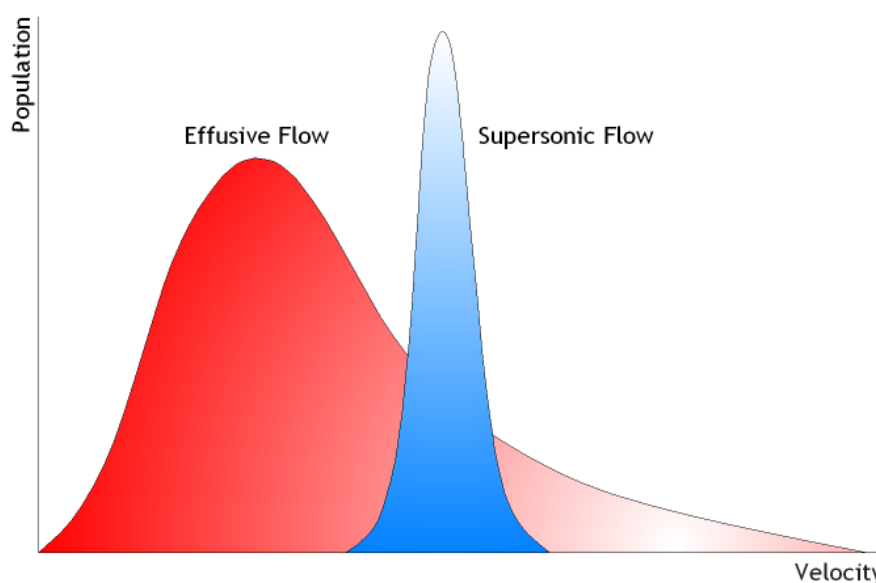


**Figure 1- 2 Schematic representation of the velocity distribution of supersonic expansion. Reprinted from Ref. (29).**

The molecular beam technique was first proposed in 1951 <sup>(30)</sup> and was experimentally realized shortly after <sup>(31)</sup>. The first attempt of applying molecular beam technique to helium droplets synthesis was reported by Becker *et al.* in 1961 <sup>(32)</sup>. The advantage of using a molecular beam to generate helium droplets is that it is feasible to precisely control the droplet size; so the applications of helium droplets have been widely stretched <sup>(33)</sup>. Additionally it is economically cheaper than directly pouring liquid helium.

The process to form helium droplets by supersonic expansion can be described as follows: compressed helium gas with stagnation pressure of 5 – 200 bar is pre-cooled below 30 K before ejecting from an orifice of 5 – 20  $\mu\text{m}$  into vacuum. Helium gas then

expands into high vacuum, condensing into liquid when the temperature is below the critical point. A typical nozzle configuration for helium droplets formation is sketched in Figure 1- 3, where a 0.5 mm diameter skimmer is placed 15 mm downstream from the source to collimate the droplets into a beam propagating forward.

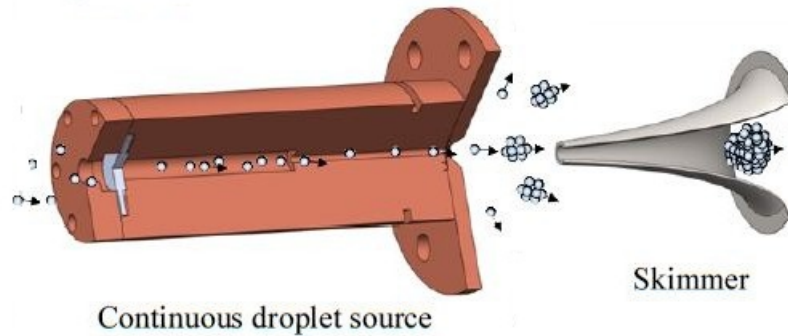


**Figure 1- 3 Schematic representation of the helium droplet formation by the supersonic expansion of helium gas.**

Supersonic expansion is an adiabatic process during which the system entropy maintains constant. The isentropic lines which helium should follow during supersonic expansion with respect to different pre-cooled temperatures  $T_0$  from 40 K to 2.6 K are plotted in the dash lines in Figure 1- 1. The boundary line between the gas phase and He I phase almost overlaps with the isentropic line at 11 K. Above 11K, helium crosses the gas – liquid boundary line into the superfluid phase from the gas phase side, which means helium droplets are formed by the aggregation of the helium atoms. The regime of  $T_0 > 11$  K is referred to as the “sub-critical regime”. On the contrary, when  $T_0 < 11$ K, helium crosses the boundary line from the liquid side, indicating the droplets formation is due to the fragmentation of the large droplets ejecting from the pinhole. This regime is defined as “super-critical regime”.

Figure 1- 1 also includes the separation line (the dotted line) of the helium velocity varying from sub-sonic to supersonic. Above 6 K, helium crosses the velocity separation line prior to the phase boundary line. That means after ejecting from the nozzle, helium clusters are accelerated from sub-sonic to supersonic while expanding

and cooling. However when  $T_0$  below 6 K, helium directly crosses the phase boundary bypassing the velocity separation line, representing a new regime of helium droplet in which helium is ejected from the nozzle as a liquid<sup>(23, 28)</sup>.

The regime division according to the source temperature ( $T_0$ ) determines the droplets size and the flux (see details in section 1.2.3), which in turn determines the different applications of the helium droplets technique (as discussed in Chapter 2). However, no matter in which regime, helium droplets would keep cooling themselves during the expansion by evaporating the excess He atoms, each removing  $5 \text{ cm}^{-1}$  internal energy from the droplet<sup>(34)</sup>. This process continues until the droplet reaches its equilibrium temperature of  $0.37 \text{ K}$ <sup>(35-37)</sup>, at this temperature the internal energy is not sufficient to remove any He atoms from the droplet.

### **1.2.2 Superfluidity of HeDs**

The superfluidity of helium droplets was proved by Toennies' group<sup>(36)</sup>, who had doped  $^4\text{He}$  droplets with the OCS molecule and had then recorded the infra-red rotational spectrum. Well-resolved lines corresponding to the rotational transitions from  $J$  to  $J - 1$  and  $J$  to  $J + 1$  ( $J = 0, 1, 2$ ), where  $J$  is the rotational quantum number, were observed in the wavenumber range  $2061 \text{ cm}^{-1}$  to  $2063 \text{ cm}^{-1}$ . The line width is about  $0.02 \text{ cm}^{-1}$ . The generation of the distinct transition lines and their line width are close to the spectrum recorded in gas phase. That means molecules trapped in  $^4\text{He}$  droplets can rotate freely in a way similar to that in the gas phase, which indicates that  $^4\text{He}$  droplets are superfluid. In comparison, the OCS rotational spectrum was also recorded in  $^3\text{He}$  droplets whose equilibrium temperature is  $0.15 \text{ K}$ . At this temperature  $^3\text{He}$  behaves as normal liquid whose transition temperature to superfluidity is  $0.003 \text{ K}$ . Only one broad peak was observed at the corresponding wavenumber position in the spectrum. These experiments therefore proved the superfluidity of  $^4\text{He}$  droplets.

Another remarkable feature observed in the rotational spectrum of OCS in  $^4\text{He}$  droplets is the spacing between rotational lines is much smaller than in the gas phase. This suggests a significantly increased moment of inertia<sup>(23)</sup>, because the energy

spacing between two neighbouring rotational transitions for a linear molecular in the P and R branches is equal to:

$$P(J) = 2B(J + 1) \quad (1-1)$$

Where  $B$  is the rotational constant, equals to  $h^2/8\pi^2I$ ,  $h$  is Plank constant,  $I$  is the moment of inertia of the molecule and  $J$  is the rotational quantum number.

The increased moment of inertia derives from the attachment of helium atoms to the dopant. By sequentially adding helium atoms into the OCS molecule, Toennies *et al.* found superfluidity can only be observed when at least two layers of helium shells are wrapping the dopant molecule which corresponds to 60 helium atoms. Fewer than 60 atoms, helium clusters would still behave as the normal fluid with viscosity hence induce extra moment of inertia of the OCS molecule <sup>(38)</sup>. The experimental result agreed very well with theoretical predication that the superfluidity occurs when a droplet containing more than 64 He atoms <sup>(39)</sup>.

In the same paper, the equilibrium temperature of the <sup>4</sup>He droplet, which is 0.37 K, was also experimentally determined by fitting the rotational line intensities to the Boltzmann distribution. This also agrees with the theoretical results <sup>(35, 37)</sup>.

### **1.2.3 Size of HeDs**

The size of helium droplets is highly dependent on the pre-cooled source temperature if other conditions, such as stagnation pressure and nozzle size, are fixed. During the expansion process, the droplets are cooled from the source temperature to the equilibrium temperature of 0.37 K by evaporating excess helium atoms. In the sub-critical regime, the droplets size follows a log-normal distribution at each specific source temperature <sup>(40)</sup>. Whereas in the super-critical regime, the droplets size have an exponential function distribution <sup>(41)</sup>.

The average size of the droplets and their distributions at different source temperatures are important for the applications of helium droplets. The average

droplet size can be estimated by the average number of helium atoms  $\langle N_{He} \rangle$  contained in one droplet according to the relation <sup>(10)</sup>:

$$R \approx 0.22 \cdot (N_{He})^{1/3} \quad (1-2)$$

where R is the radius of the droplet.

The average number of He atoms in the droplet beam can be measured either by the deflection technique <sup>(42)</sup> or the titration technique <sup>(10)</sup>. The former has been achieved by doping a  $SF_6^+$  ion into each He droplet and then electrically deflecting the beam into a mass spectrometer, the angular distribution of the ion signal intensity, which depends on the electron impact probability, can then be converted to the size distribution. The latter estimates the number of atoms in a droplet by measuring the He atom loss after colliding with the titrated gas.

The average size of helium droplets at various source temperatures has been measured by Vilesov's group at 20 bar stagnation pressure, as shown in Figure 1- 4. Helium droplet size gradually increases as the source temperature drops in the sub-critical regime and sharply rises up in the super-critical regime.

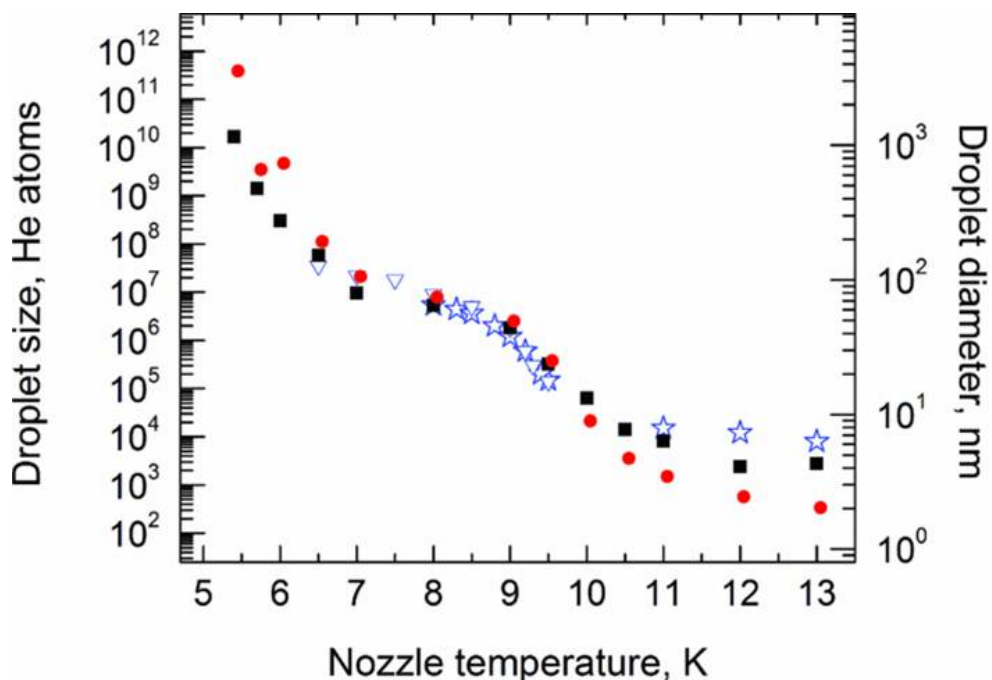


Figure 1- 4 Variation of the helium droplet size respect to the source temperature, reprinted from Ref. (10). The data represented by the squares and circles are measured via titration technique using collisional helium and argon gas respectively. The stars and triangles are the data measured by the deflection technique <sup>(40, 42)</sup>.

It is worth mentioning that (see discussed in Section 2.3.1) our helium droplet system is consistent with Vilesov's system. Therefore the droplet size presented in Figure 1- 4 will be used as the reference to determine the droplets size in our experiments demonstrated in the following chapters.

#### **1.2.4 Pickup Process**

It has been widely accepted that helium droplets are capable of capturing almost any foreign species when they collide <sup>(23, 26, 27, 33)</sup>. Most of the atoms and molecules prefer to be solvated in the droplets, however, alkali metals and alkaline earths materials tend to reside on the centre of the droplet surface <sup>(43, 44)</sup> due to relatively weaker He–M interaction (M represents for alkali and alkaline earth material) <sup>(43, 45)</sup>. This was experimentally observed by the rotational spectroscopy of the HCN-Na complex in helium droplets <sup>(46)</sup>. The rotational constant of HCN-Na complex is 55 times smaller than that of HCN-Mg, which is, however, supposed to be similar in gas phase. Therefore the explanation must be that the Na atom resides on the droplet surface so that the rotational motion of the HCN-Na complex is greatly hindered by the droplets.

Due to the ultra-cold environment and ultra-high thermal conductivity of helium droplets, the dopants would largely stay at their ground states in helium droplets after releasing their kinetic energy and potential energy into the droplets through evaporative loss of helium atoms. Since the average potential energy per He atom in the droplets is  $5 \text{ cm}^{-1}$  <sup>(2-4)</sup>, every electron volt excess energy will lead to the evaporation of about 1600 He atoms from the droplets. Therefore there will be a size limit of the dopants that can be added to each helium droplet.

The dopants can move freely inside of the superfluid helium droplets, therefore when more than one atom/molecule is picked up by one droplet, they will bond into clusters. To reach the optimum pickup conditions for a certain cluster size, the partial pressure and the average size of droplets should be balanced, as will be discussed in detail in Chapter 2. If we ignore the droplet size distribution during the pickup process, the

pickup probability of a specific number of the dopants can be represented by a Poisson distribution:

$$P_k = \frac{(\rho\sigma l)^k}{k!} \exp(-\rho\sigma l) \quad (1-3)$$

where  $k$  is the number of dopant atoms/molecules being picked up,  $\rho$  is the number density of the dopant,  $\sigma$  is the pickup cross section of the helium droplets beam and  $l$  is the length of the pickup region <sup>(28, 47)</sup>. The pickup probability can be schematically presented as in Figure 1- 5.

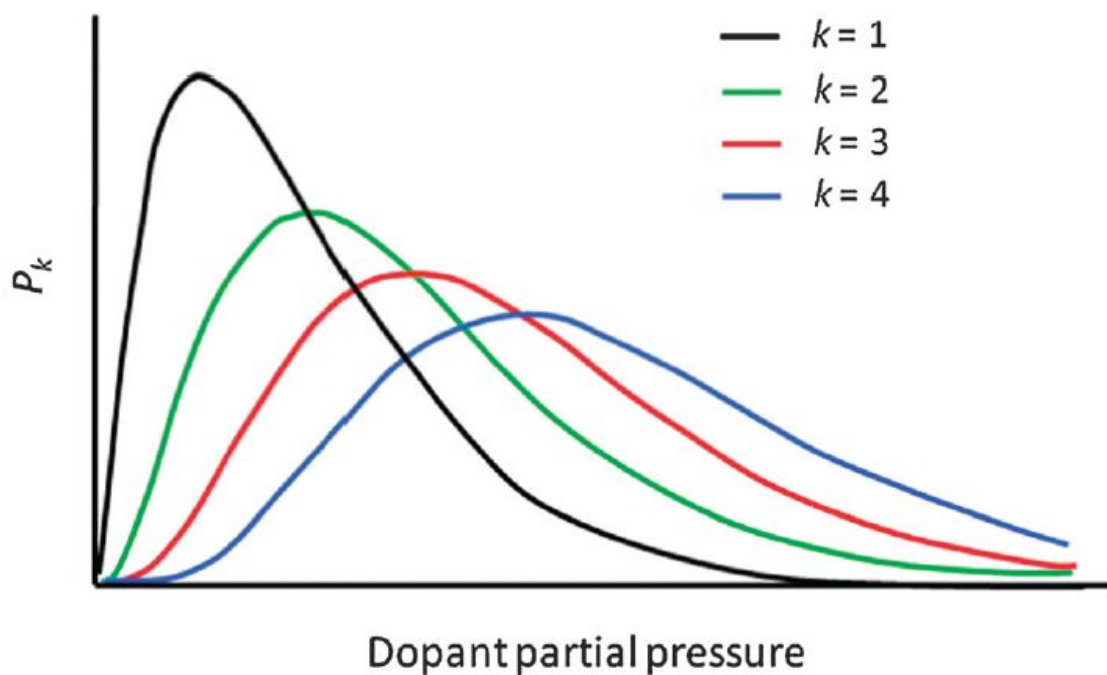


**Figure 1- 5 The probability of the number of dopant atoms/molecules ( $k$ ) being picked up by helium droplets in response to the partial pressure. Graph is reprinted from Ref. (28).**

Helium droplets will pick up any dopants or impurities on their pathways. Therefore when helium droplets sequentially pass through more than one pickup region where different types of dopants are present, binary clusters, such as HCN-H<sub>2</sub> <sup>(48, 49)</sup>, HCN-C<sub>2</sub>H<sub>2</sub> <sup>(50)</sup> and HF-Ar<sub>*n*</sub> <sup>(51)</sup> *etc.*, and core-shell structural clusters including H<sub>2</sub>O/O<sub>2</sub> and H<sub>2</sub>O/N<sub>2</sub> *etc.* <sup>(52)</sup>, can be experimentally formed and investigated. Particularly the formation of core-shell clusters stimulates ambitions in forming core-shell nanoparticles in helium droplets.

### 1.2.5 Electron Ionization in HeDs

Electron impact ionization is the most widely used technique for detecting the dopants trapped in helium droplets and thus plays a key role in mass spectroscopy<sup>(53-58)</sup>, optical spectroscopy<sup>(59-64)</sup> and configuration determination of the nanoparticle<sup>(33, 65-67)</sup> in helium droplets. Besides the obvious dependency of the droplet flux and the geometric cross section of the droplet, the cross section of the electron impact also relies on the impact energy (IE) of the incident electron. The electron impact cross section proportionally increases with IE, increasing from 24.6 eV (ionization threshold of He) to 100 eV<sup>(17-22)</sup>.

Basically, the electron impact collision of a helium atom can be explained by the elastic collision mechanism<sup>(68)</sup>, in which, particularly for a He atom, the incident electron equally delivers half of its excess energy to the two projectile electrons after fully ionizing the He atom. The two projectile electrons fly back-to-back in most of the cases, as illustrated in Figure 1- 6.

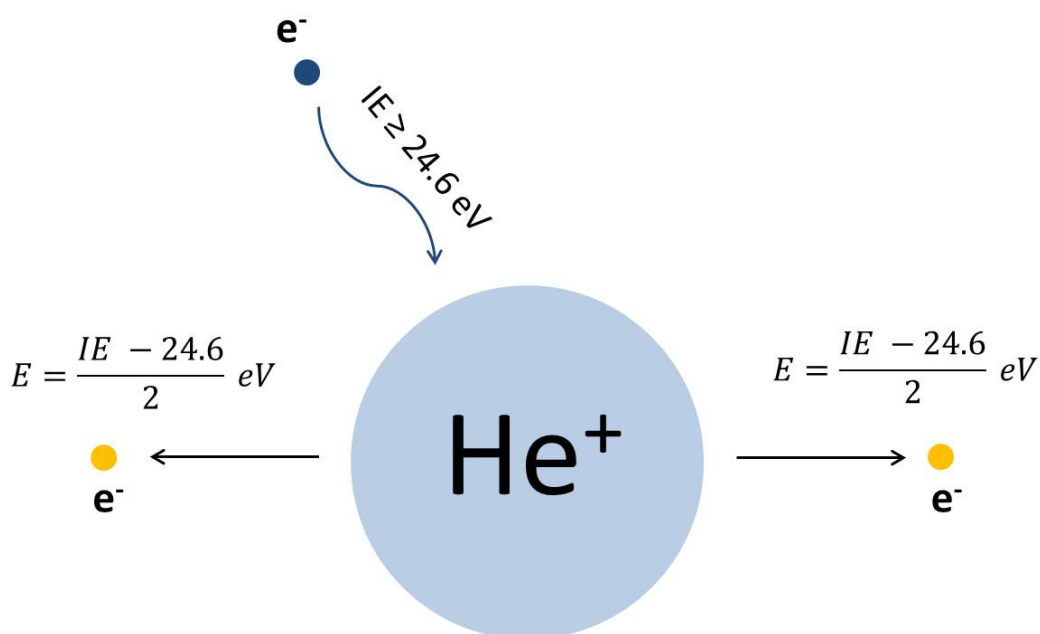


Figure 1- 6 Electron impact mode for a He atom.

The helium droplet has a dense core with He atoms loosely bound in the outer shell. There is a surface barrier, which is the energy that has to be consumed from an incident electron before colliding and ionizing one He atom on the droplet surface. The surface barrier of helium droplets is about 0.6 eV to 1.2 eV<sup>(69)</sup>. There is an exponential decay of the collision probability between an incident electron and the helium atoms from surface to the interior (due to the geometric cross sections)<sup>(70)</sup>; therefore the electrons are likely to collide with helium atoms near the surface of the droplets and ionize He atoms before penetrating deeper into the droplets.

After being ionized, the charge near the surface will migrate to two possible terminals via resonant hopping: (i) to the dopant which is normally trapped in the centre of the droplet or on the surface<sup>(28)</sup>; (ii) towards the droplet centre where attracting one He atom to form a He<sub>2</sub><sup>+</sup> core<sup>(71)</sup>. This charge hopping process occurs within in 60 – 80 fs<sup>(71-73)</sup> and the charge can hop in the droplets for an average distance of 34 Å<sup>(70)</sup>. The generation of He<sub>2</sub><sup>+</sup> and dopant ions releases huge amounts of energy into the droplet, causing massive fragmentation so that further charge hopping is prevented and the dopants ions without He clusters attached can be dominantly detected<sup>(71, 74, 75)</sup>. In other words, both processes terminate the charge transfer, leading to ions that are ejected from the droplets.

### 1.2.6 Quantum Vortices

One of the unique features of superfluid helium is the existence of quantum vortices, which is the circulation of the superfluid around a hole. The hole is a must because in superfluid helium each atom needs to be identical; hence under rotation each atom possesses the same angular momentum. Consequently at the vortex core no helium atom can stay in order to avoid zero-angular momentum. Quantum vortex was first predicted by Onsager<sup>(76)</sup>, in whose theory the circulation can be quantized defined as:

$$\kappa = \frac{h}{M} \quad (1-4)$$

$\kappa = \oint v_s \cdot dl$ ,  $v_s$  is the circulation velocity,  $l$  is a closed path representing the vortex ring,  $h$  is Plank constant and  $M$  is the mass of the superfluid. Calculations further

suggest vortices can exist within helium droplets consisted by only a few hundred He atoms<sup>(77, 78)</sup> and foreign particles can pin to the vortex line in the droplets<sup>(79, 80)</sup>.

Experimental evidence of quantum vortices in bulk helium was first obtained by Rayfield *et al.*<sup>(81)</sup>, by measuring the inverse proportional relationship between the velocity of the ions doped in the liquid He and their energy, proving that ions circulate with the vortex ring. Visual evidence was first seen in 2006 by bubbling the mixture gas of hydrogen and helium through liquid helium<sup>(82)</sup>. In the superfluid phase ( $T < 2.17$  K) arrays of the condensed hydrogen particles were observed showing that the particles are pinned to the vortex line and the vortex core is about an angstrom in diameter.

The existence of quantum vortices in helium droplets had not been proved until recently. Vilesov's group first noticed the head-to-tail aligned Ag nano rods formed in large helium droplets consisting of  $10^7 - 10^{12}$  helium atoms. They attributed this pattern as an indication of vortices existing in helium droplets<sup>(83)</sup>. Later Spence *et al.* provided solid evidence for the vortices existence with the similar experiments by obtaining chains of spherical nanoparticles. Further addition of Si following Ag proved that the alignment into a chain is intrinsic in the droplets<sup>(65)</sup>. So other possible driving forces of forming the chain structure such as the anisotropy of the nano rods and the breaking up effect of the nanowire after impact to the substrate can be ruled out. Direct imaging of quantized vortices in superfluid helium droplets has also been achieved recently. Gomez *et al.* have imaged helium droplets embedded by Xe atoms using X-ray diffraction technique<sup>(84)</sup>. Until now all the evidence for quantum vortices is observed in large helium droplets, *i.e.* in super-critical regime of helium droplets, there is still no clue if they exist in sub-critical regime, despite the suggestion by theorists that vortices should universally exist in all size of helium droplets<sup>(77, 78)</sup>.

### 1.3 Spectroscopy in HeDs

The low-temperature environment is crucial in spectroscopy since the lower the temperature, the more possibility that atoms/molecules can be constrained in low quantum states, which makes the spectral peaks distinct and easy to assign.

Additionally some chemical reactions can only happen at low temperature and hence can only be investigated in a low temperature environment <sup>(28)</sup>. Currently two techniques are widely applied to provide cold environment for spectroscopy study: molecular beam technique and matrix isolation technique.

In the molecular beam technique, the target atoms/molecules are seeded in the carrier gas such as Ar or He, and then the mixed gas is expanded under pressure into a vacuum chamber and undergoing a supersonic expansion. The temperature is cooled by two-body collisions during the expansion and the internal energy of the seeded molecules is largely converted into translational energy. However, the quickly reduced gas density in the vacuum eliminates the occurrence of multi-collisions so that the cooling may not be completed and some of the “hot band” may confuse the output spectra <sup>(85)</sup>. Another challenge existing in conventional molecular beam techniques is the difficulty to produce the binary clusters which contain more than one species <sup>(23)</sup>. The reactions between the desired dopants are hard to control due to lack of isolation.

Matrix isolation, however, can freeze the target atoms/molecules in a cold environment, such as Ar or H<sub>2</sub>, and the temperature can reach as low as sub-Kelvin range <sup>(86)</sup>. Since this technique normally involves co-deposition of the matrix and target atoms/molecules into a solid matrix, any probing laser can be easily aligned to the target. The biggest problem for this technique is the solid matrix provides a crystal field<sup>i</sup> to the target atoms/molecules. The strong interaction between the targeted species and the surrounding matrix significantly broadens the spectral line. Moreover since being constrained in the solid crystal, the species cannot be mobile anymore which makes it difficult to investigate the reactions between two or more types of atoms/molecules.

---

<sup>i</sup> Crystal field is induced by the surrounding electrons, such as the non-bonding electrons from ligands, and effect on the transition metals trapped. The interaction between the surrounding electrons and the metals breaks the degeneracies of the electron orbitals, usually *d* or *f* orbitals. In particular, sub-orbitals with magnetic quantum numbers (*m<sub>l</sub>*) in *d* or *f* orbitals are split, causing the energy gaps in between. Therefore electrons in the metal atom are re-coordinated in these sub-orbitals. And the product in crystal field can be classified as high-spin or low-spin complex. Crystal field theory can successfully explain some magnetic properties, colours, hydration enthalpies and spinel structures of transition metal complex. <sup>4</sup>He, due to its closed electron shell structure and highly constrained distribution of the electrons around nuclei (small radius), eliminates the crystal field to the dopants trapped in.

Helium droplet technique, as a combination of the conventional molecular beam technique and the matrix isolation technique have the advantages over these two. Firstly, due to its low equilibrium temperature of 0.37 K and ultra-high thermal conductivity, dopants being picked up will be instantly cooled down to the ambient temperature of helium droplets. Secondly, since superfluid helium remains liquid at equilibrium temperature without any viscosity, dopants trapped in the helium droplets can move freely and bind to form clusters; so each droplet provides ideal isolation for the dopants. Thirdly, there is no crystal field in liquid helium matrix<sup>(87)</sup>. This is highly important property for helium droplets, which not only greatly improves the spectral quality but also dramatically benefits the cluster and nanoparticle formation which will be discussed in detail in Chapter 4 and 5. In addition, helium droplets are transparent to electromagnetic waves from the far IR to UV range<sup>(23, 28)</sup>, making it suitable for most of the spectroscopy required. Finally by carefully adjusting the source temperature and the partial pressure of the dopants, precise control of the pickup conditions and thus optimal pickup of the desired clusters can be achieved. Helium droplets can acquire more than one type of materials so binary clusters and even core-shell structural clusters can be formed in helium droplets.

### **1.3.1 Depletion Spectroscopy**

The most widely used technique in recording the spectra using HeDs is the depletion technique. Once the dopants in helium droplets are excited, the specific absorption energy in most cases converts to heat. The heat is then dissipated by the droplets and causes the droplet size to shrink; about 1600 He atoms will be evaporated by every eV thermal energy.

Depletion spectroscopy was initially observed using a bolometer detector, which is sensitive to the total energy of the incoming helium droplets<sup>(62)</sup>. Alternatively taking advantage of electron ionization by an equipped mass spectrometer, ions can be detected. The droplet size shrinkage reduces the electron ionization cross section thus reducing the probability of the ionization of the helium droplet and the dopants trapped in, which leads to the depletion of the number of ions detected by the mass

spectrum at the resonant laser frequency. As shown in Figure 1- 7, when laser is fired with the resonant frequency, around 15% of the total number of the ion counts is depleted comparing to the counterpart when laser pulse is absent. The width of the depletion is the fly time of the dopants travelling from the pickup cell to the ion detector.

When laser scans across a wavelength range, optical spectra will be obtained with the depletion peak appearing at the resonance wavelength.

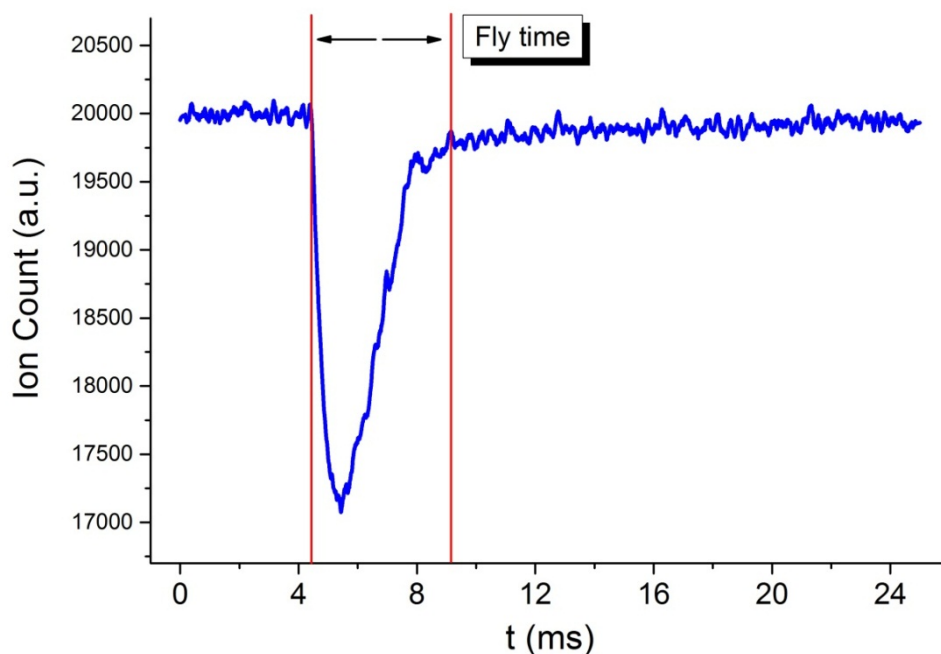


**Figure 1- 7** A typical depletion signal recorded by a quadrupole mass spectrometer. The width of the depletion peak is the fly time of the ion from the pickup region to the mass spectrometer.

### **1.3.2 Infrared and Electronic Spectroscopy in HeDs**

The first spectroscopy experiment in helium droplets was reported by Scoles *et al.* in 1992 <sup>(62)</sup>. Using a bolometer detector, they observed SF<sub>6</sub> vibrational spectra. The half-width of the absorption lines are approximately 0.25 cm<sup>-1</sup> which is much narrower than in other matrices. Since then vibrational spectroscopy on molecules, clusters and binary clusters isolated in helium droplets has attracted more attention. Special examples include two important works carried out by Miller's group, who used

infrared (IR) spectroscopy to discover the formation of a cyclic structure of  $(\text{H}_2\text{O})_6$ <sup>(60)</sup> and a chain structures formed by  $(\text{HCN})_n$  clusters<sup>(88)</sup> in helium droplets. Moreover the IR spectrum of binary clusters of  $(\text{HCl})_m(\text{H}_2\text{O})_n$  have been successfully studied in helium droplets which is impossible to obtain the resolved spectra using other techniques<sup>(89, 90)</sup>. This pioneering study opens up intriguing research in the science of the dissociation process of the molecules in water<sup>(90)</sup>.

All the previous IR spectroscopy work in helium droplets suggested that the shift of the vibrational transitions in helium droplet system is limited to less than  $10 \text{ cm}^{-1}$  compared to the gas phase spectra, although the bands are somehow broadened.

Depletion techniques can also be used to record the electronic spectra of the dopants inside helium droplets<sup>(59, 64, 91)</sup>. However, in contrast to the IR spectroscopy in which the excited vibrational energy is normally rapidly released into helium droplet, causing significant depletion spectrum, excess energy released from the electronic excited states are usually much slower which restricts the depletion technique being used in the investigation electronic spectroscopy of molecules embedded in helium droplet. In some occasions, energy in electronic excited states does not transform to heat but radiates in form of fluorescence. Therefore laser-induced fluorescence (LIF) technique<sup>(92)</sup> and resonance-enhanced multi-photon ionization (REMPI) technique<sup>(93, 94)</sup> are the alternative means for the investigation of electronic spectroscopy in helium droplets.

## 1.4 Nanoparticles Formed in HeDs

Compared to the fruitful research on the spectroscopy, it was not until 2011 when Vilesov *et al.* used helium droplets in the super-critical regime, with the average droplets composed of  $2.4 \times 10^6 - 4 \times 10^7$  He atoms, to achieve another important application for helium droplets technique – the formation of nanoparticles. The Ag particles they deposited is within the range of 300 to 6000 Ag atoms according to the TEM images<sup>(95)</sup>. A subsequent spectroscopy measurement on Ag nanoparticles suggested one important phenomenon for particle aggregation in helium droplets – multi-centre growth<sup>(96)</sup>, which occurs in large He droplets when the time between

successive doping events is shorter than the time required for atoms aggregating together, leading to the formation of a number of small particles in the droplets rather than one large compact particle inside a helium droplet. This phenomenon is further supported by our research which will be discussed in details in Chapter 2.

Core-shell structural nanoparticles were first synthesised in 2013 at Leicester by sequentially passing the helium beam through two evaporators containing Ni and Au respectively, where the core-shell structure was confirmed by the XPS analysis <sup>(67)</sup>. Since the discovery of quantized vortices, our group has exploited the growth of 1D nanostructures in superfluid helium droplets, taking advantage of quantum vortices existing in the ultra-large helium droplets. These include Au, Ag, Si, Ni and Cr <sup>(65, 66)</sup>. More recently core-shell structural Au/Ag nanowires were also synthesized in helium droplets <sup>(97)</sup> following the same idea. Until now in addition to the materials mentioned above, materials such as Mg <sup>(98)</sup>, Al <sup>(58)</sup>, have also been used in forming nanoparticles, core-shell nanoparticles and nanowires in helium droplets.

Helium droplets provide a unique environment for nanoparticle growth. The ultra-cold ambient temperature and ultra-high thermal conductivity cool all the atoms picked up down to 0.37 K. Therefore not only solid material, but also liquid and gas which normally cannot be used in forming nano materials in other techniques can be condensed in helium droplets, hence can be the ingredients of nano materials. Superfluidity allows atoms to freely move inside of droplets while maintaining their temperature at 0.37 K. When atoms aggregate into nanoparticles one by one, the process is out of thermal disturbance. Therefore nanoparticles formed in this way are supposed to have perfect crystalline structure, which has been proved by high resolution TEM images <sup>(67, 99)</sup>. In conventional ways of forming nanoparticles the annealing process is always included, which aims for improving the crystalline structure by rapid cooling. However, this cannot completely prevent defects emerging in the crystalline structure which inevitably causes negative effects on properties of the desired nano structures <sup>(100)</sup>. The ultra-high vacuum system eliminates the impurities involved in the particle growth process and the isolation induced by the inert helium further prevents the crystal field effect to the dopants, particularly for those highly active materials, therefore the purity can be protected.

As mentioned above, core-shell structural nano materials, which are normally a big challenge in other techniques, can be easily realized by using helium droplets and the inter-diffusion between the different layers can be minimized due to the ultra-cold environment. It has been noticed that the size of nanoparticles formed in helium droplets follows either log-normal or normal distribution <sup>(67, 99)</sup> with the majority of nanoparticles of uniform size. The particle size can be easily controlled by adjusting the droplets source temperature and dopants vapour pressure.

In summary, compared to the conventional methods of forming nanoparticles, such as wet chemistry, lithography or chemical vapour deposition methods, the helium droplets technique has its unique advantages:

- i. It is a highly versatile technique. There is nearly no limitation for materials selection. Materials of solid, liquid and gas can all be applied to this technique as long as they can be vaporized. Highly active materials can also be compatible with this technique where their elemental purities can be maintained.
- ii. Perfect crystalline structures can be realized.
- iii. Nano structures formed in this way are free of contaminations.
- iv. Core-shell structures with minimum inter-diffusion can be generated.
- v. Particles formed have a narrow and tuneable size distribution.
- vi. Nano rods and nanowires can also be formed without seriously changing the experimental set-up. Lowering the source temperature and regulating vapour pressure simply make the formation possible.

However, there are two major drawbacks of this technique in forming nanostructures at current stage:

- i. The particles struggle to grow larger due to the vortices existence and multi-centre growth in large helium droplets. The largest nanoparticles grown in helium droplets we observed until now is Ag nanoparticles, with a size of limitation about 8 nm in diameter. For other materials, particles more favourably aggregate into rods rather than spherical nanoparticles inside large helium droplets.

- ii. The production rate is relatively low, and it is much lower than wet-chemical methods. The typical production rate is a few nano-grams per minute for nanoparticle growth. Therefore in most cases the nanoscience in helium droplets is restricted to proof-of-concept and/or generates high-standard nanoparticles that need scaling up by other methods.

## 1.5 Magnetic Nanoparticles

Like other materials, magnetic materials at the nanoscale possess some extraordinary properties compared to their bulk phase, such as superparamagnetism, enhanced unit magnetization *etc.*, which have great potential in applications in biomedicine <sup>(101)</sup>, magnetic resonance imaging <sup>(102)</sup>, data storage <sup>(103)</sup>, optical filter <sup>(104)</sup> and energy efficiency technologies. Besides the conventional synthesis methods such as wet-chemical methods <sup>(105)</sup> and gas phase deposition <sup>(106)</sup>, helium droplets can also be applied to magnetic nanoparticles synthesis, which will be exploited in this work.

### 1.5.1 Free Atom Magnetization

Although the origin of the atomic magnetization is still not fully understood, it is widely accepted now that atomic magnetic moment originates from the magnetic moments of orbitals and spin <sup>(107)</sup>, which are generated as electrons travel around the nuclei in a closed loop. The orbital and spin moments can be expressed as:

$$\boldsymbol{\mu}_L = -\frac{e}{2m_e} \mathbf{L} \quad (1-5)$$

$$\boldsymbol{\mu}_S = -\frac{e}{m_e} \mathbf{S} \quad (1-6)$$

$\boldsymbol{\mu}_L$  and  $\boldsymbol{\mu}_S$  are the magnetic moments induced by the orbital and spin respectively;  $e$  and  $m_e$  are the charge and mass of the electron respectively;  $\mathbf{L}$  and  $\mathbf{S}$  are the orbital angular momentum and spin angular momentum respectively, their absolute values are:

$$|\mathbf{L}| = \sqrt{L(L+1)}\hbar \quad (1-7)$$

$$|\mathbf{S}| = \sqrt{S(S+1)}\hbar \quad (1-8)$$

where  $L$  is the total orbital angular momentum quantum number given by the sum of the magnetic quantum number  $m_l$ ;  $S$  is the total spin angular momentum quantum number. Only unpaired electrons can contribute to the magnetic moment, each has a spin quantum number of  $m_s = 1/2$ . The paired electrons occupying the same sub-orbital according to Pauli's exclusion principle should have anti-parallel spins, therefore giving rise to a spin quantum number  $S = 1/2 - 1/2 = 0$ .

The overall atomic magnetic moment has a contribution from both orbital and spin; therefore spin-orbital coupling would play an important role in determining the atomic magnetic moment. The spin-orbital coupling can be schematically illustrated in Figure 1- 8.  $\mathbf{J}$  is the total angular momentum which equals the vector sum of  $\mathbf{L} + \mathbf{S}$ , and its absolute value is:

$$|\mathbf{J}| = \sqrt{J(J+1)}\hbar \quad (1-9)$$

$$J = |L \pm S| \quad (1-10)$$

The +/- sign in Equation (1-9) is determined by Hund's rules<sup>ii</sup>.

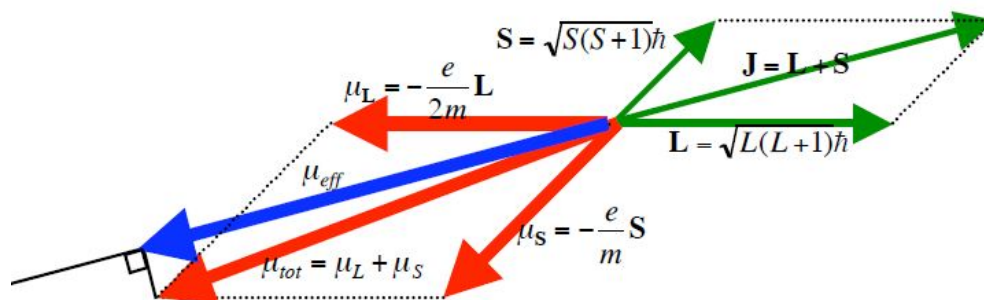


**Figure 1- 8 Schematic of atomic magnetic moment from spin-orbital coupling.**

<sup>ii</sup> Hund's rules were proposed by Friedrich Hund in 1927, which are the rules for electron configuration of the ground state of a multi-electron atom. The three rules are:

- 1) Electron configuration should maintain the largest possible multiplicity which equals  $2S+1$  to settle to its minimum energy,  $S$  is the total spin quantum number for all electrons. Therefore  $S$  should be as large as possible.
- 2) For a given multiplicity, the minimum energy criterion requires the total orbital quantum number  $L$  to be as large value as possible.
- 3) Having decided  $L$  and  $S$  values according to rules 1) and 2), the total quantum number  $J$  can be determined by the  $L$ - $S$  coupling scheme, which is  $J = L - S$  for electron shells that are less than half full and  $J = L + S$  for shells that are more than half full.

As the coefficients of  $L$  and  $S$  in  $\mu_L$  and  $\mu_S$  are not equal, the total magnetic moment is not parallel to the total angular momentum. Actually the total magnetic moment  $\mu_{tot} = \mu_L + \mu_S$  can be regarded as rotating around  $J$ , resulting in a permanent magnetic moment  $\mu_{eff}$  that can be calculated by combining Equation (1-4) to (1-8), given as:

$$\mu_{eff} = -g\left(\frac{e}{2m_e}\right)J \quad (1-11)$$

$g$  is called Landé  $g$ -factor, which equals:

$$g = \frac{3}{2} + \frac{S(S+1) - L(L+1)}{2J(J+1)} \quad (1-12)$$

From the discussions above, the direction that  $\mu_{eff}$  points is determined by the direction of  $J$ , which however, can point to any direction in the three dimensional space without an external magnetic field. When an external field  $B$  is applied, atomic magnetic moments will respond accordingly.

Assuming  $B$  is aligned to  $z$  axis, the component of  $J$  along  $z$  axis is defined by:

$$|J_z| = \hbar J \quad (1-13)$$

Therefore the theoretical limit of an atomic magnetic moment (along  $z$  axis) can be deduced as:

$$|\mu_z| = gJ\mu_B \quad (1-14)$$

$\mu_B$ , called Bohr magneton, equals to  $-e\hbar/2m_e \approx 9.27 \times 10^{-21}$  emu.

For a given  $J$ , there are  $2J+1$  discrete magnetic energy levels from  $-J_z$  to  $J_z$  with integer spacing. When all the atoms in a system simultaneously stabilize at the minimum magnetic energy level  $-J_z$ , the system possesses the maximized magnetization  $NgJ\mu_B$  ( $N$  is the number of atoms). This state is called magnetic saturation, as shown in Figure 1- 9 (a). At the ground state, the electron configuration strictly follows Hund's rules with the maximal  $J$  and the minimum  $-J_z$  energy level. Therefore the saturation can reach the globally maximizing magnetization. At higher temperature, thermally excited electrons break the Hund's rules. Consequently a lower  $J$  value notated  $J'$  is expected, whose  $z$  component can be notated as  $J'_z$ . Therefore the system can only potentially

reach a lower saturation of  $NgJ'\mu_B$  when all atoms are populated at the local minimum magnetic energy level  $-J_z'$ .

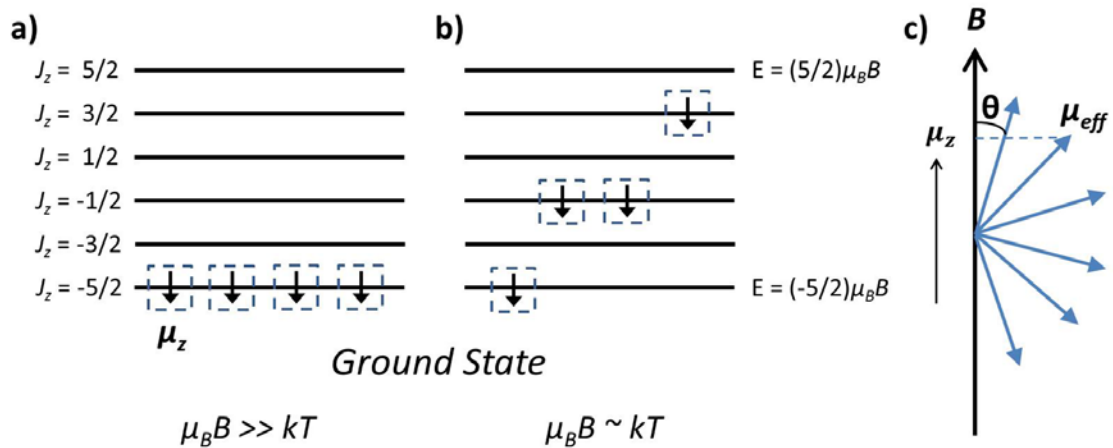


**Figure 1- 9 (a) Illustration of the occupation of  $J_z$  energy level by atomic magnetic moments when saturation, taking Mn as an example whose  $J = 5/2$ . (b) The occupation at  $J_z$  energy level of magnetic moments in the process of magnetizing. (c) A macroscopic view of the magnetizing process. Every blue arrow corresponds to a discrete energy level.  $\theta$  is the ultimate angle of an atomic magnetic moment can rotate towards the magnetizing direction (z axis).**

In order to reach the saturation state, the external magnetic field need be sufficiently strong, thus can override the thermal disturbance. When the strength of the external magnetic field is comparable with the thermal disturbance, *i.e.* the material is in the process of being magnetized, atomic magnetic moments will have some probability occupying higher  $J_z$  levels (Figure 1- 9 (b)). Therefore to reach saturation, stronger external magnetic field is needed to populate all the atoms to the minimum  $-J_z$  magnetic energy level. Taking a macroscopic view, the magnetizing process can be regarded as the atomic magnetic moment  $\mu_{eff}$  rotating towards z axis, driven by the external field  $B$ . The measured magnetization is the projection of the  $\mu_{eff}$  onto the z axis. The saturation state corresponds to the angle limitation that  $\mu_{eff}$  and z can reach, as shown in Figure 1- 9 (c).

In summary, the electron configuration of an atom and hence the value of  $J$  and  $\mu_{eff}$  depend on the temperature; while the angle ( $\theta$ ) between  $\mu_{eff}$  and z, hence the measured magnetization  $\mu_z$  for a fixed temperature are determined by the intensity of

external field  $B$ . The temperature and external field dependence of the atomic magnetic moment can be deduced according to Brillouin Function as <sup>(107)</sup>:

$$|\mu| = gJ\mu_B \left[ \frac{2J+1}{2J} \coth\left(\frac{2J+1}{2J}y\right) - \frac{1}{2J} \coth\left(\frac{y}{2J}\right) \right] \quad (1-15)$$

where  $y = \left(\frac{Jg\mu_B B}{kT}\right)$ .

### 1.5.2 Magnetism Measured in a Many-atom System

From the discussion above, it is known that magnetism originates from the unpaired electrons. Therefore magnetism is normally observed in  $3d$  and  $4f$  (rare earth) transition metals due to their high number of unpaired electrons. For  $4d$  and  $5d$  metals, which also contain large numbers of unpaired electrons, no obvious magnetism can be observed. The reason for this contradiction is still unclear, yet it is widely thought to be due to strong spin-orbital coupling or  $d-d$  hybridization <sup>(108, 109)</sup>. In this section, we start to illustrate the magnetism in the many-atom system, from clusters to the bulk phase, which is the magnetism that can be measured by a magnetometer and applied in reality. Currently, we will only concentrate on the  $3d$  and  $4f$  materials.

According to Equation (1-14), the theoretical limit of atomic magnetization at the ground state can be calculated. The outcome of this calculation matches pretty well with the experimental results measured at 0 K for  $4f$  (rare earth) metals and the fulfilled ions of  $3d$  materials such as Gd <sup>(110)</sup>, Dy <sup>(111)</sup>, Mn<sup>2+</sup>, Eu<sup>2+</sup> <sup>(112)</sup>, Cr<sup>3+</sup>, Fe<sup>3+</sup> and Gd<sup>3+</sup> <sup>(113)</sup>. Table 1- 1 shows the comparison between the theoretical and experimental atomic magnetization for selected materials. For unfilled ions of  $3d$  materials, such as V<sup>2+</sup>, Cr<sup>3+</sup>, Mn<sup>4+</sup>, Cr<sup>2+</sup>, Mn<sup>3+</sup>, Fe<sup>2+</sup>, Co<sup>2+</sup>, Ni<sup>2+</sup> and Cu<sup>2+</sup> etc., the measured magnetization is far below the theoretical value predicted by Equation (1-14) <sup>(107)</sup>. However, when considering only the spin contribution to the magnetization, the two values are much closer. That suggests the orbital contribution to the magnetization has been quenched for  $3d$  metals.

The orbital quenching is thought to be due to the crystal field.  $3d$  electrons have a higher probability of extending into the outer shell, so they are more likely to generate chemical bonds due to the strong interaction with the environment. Therefore only the spin should be responsible for the aroused magnetic moment. In contrast, since the  $4f$  electron density is more concentrated within the  $5s$ - $p$  orbitals, atoms of  $4f$  materials are more isolated. Therefore the magnetization of the rare earths is more free-atom-like.

**Table 1- 1 Comparison between experimental and theoretical value of atomic magnetization of selected  $4f$  metals and fulfilled  $3d$  ions.**

Element	Electron configuration	S	L	J	Theoretical limit ( $\mu_B$ /atom)	Measured M ( $\mu_B$ /atom)
Gd	$4f^7 5d^1 6s^2$	4	2	6	7	7.63
Dy	$4f^{10} 6s^2$	2	6	8	10	10.2
Eu <sup>2+</sup>	$4f^7$	7/2	0	7/2	7	6.8
Mn <sup>2+</sup>	$3d^5$	5/2	0	5/2	5.92*	5.9

\*This value is calculated *via* effective magneton number known as  $g\mu_B\sqrt{S(S+1)}$ , where only spin is counted.

For  $3d$  metals, particularly the ferromagnetic material of Fe, Co and Ni, the magnetic property becomes more complicated. It is observed that once the atoms start to cluster the magnetization of the system quickly decays from the atomic value, and can never return to the atomic value<sup>(114)</sup>. Even if taking off the orbital contribution, the measured magnetization is still much lower than the expected value<sup>(107)</sup>. This is because the high density  $3d$  electrons appearing in the outer space easily bond together, so that the discrete energy levels are broadened to energy bands. In these bands, electrons of both spin up and spin down co-exist, both with varying distribution of the density of states. When polarized by a magnetic field, some of the spins will reverse their orientation to align with the external field, resulting in the imbalance of the populations of the two spins. In this case not all the unpaired electrons in the free atom can contribute to the magnetism, the detected magnetization derives only from the net spins as:  $\mu = (n_1 - n_2)\mu_B$ ,  $n_1$  is the number of majority spins which orientate

to the same direction with the magnetic field,  $n_2$  is the number of spins orientating oppositely <sup>(107)</sup>. That means the magnetic contribution from spin is also partially quenched in 3d transition metals.

When the 3d atoms keep aggregating beyond the cluster scale to the bulk phase, magnetic domains start to form and the magnetism is reduced to a fixed value for each specific material, as listed in

Table 1- 2. Magnetic domains are very small regions inside which all the atomic moments point into one direction. Magnetic moments in different domains have different orientations in order to decrease the total magnetic energy, although at the domain boundary the misaligned moments cause the exchange interaction to increase. The domain size is determined by the minimum total energy as a compromise between the magnetic energy and exchange interaction. Consequently under an external field, the stimulated magnetic moments in a bulk phase metal cannot be fully aligned, resulting in the quenched magnetization.

The magnetization of bulk phase ferromagnetic metals, Fe <sup>(115)</sup>, Co <sup>(116)</sup> and Ni <sup>(117, 118)</sup> measured at 0 K in comparison with the theoretical values are shown in

Table 1- 2, it can be noticed that even ignoring the orbital contribution, the measured magnetizations in bulk phase still deviate significantly from the atomic theoretical limit.

**Table 1- 2 Comparison between experimental and theoretical value of atomic magnetization of ferromagnetic metals including the theoretical magnetization after orbital quenching.**

Element	Electron configuration	S	L	J	Theoretical limit ( $\mu_B$ /atom)	Calculated M at L=0 ( $\mu_B$ /atom)	Measured M ( $\mu_B$ /atom)
Fe	$3d^6 4s^2$	2	2	4	5	4	2.22
Co	$3d^7 4s^2$	3/2	3	9/2	6	3	1.72
Ni	$3d^8 4s^2$	1	3	4	3	2	0.61

### 1.5.3 Types of Magnetic Materials

Equation (1-15) suggests the atomic magnetic moment only arises under an external magnetic field. When  $\mathbf{B} = 0$ , the magnetic moment is extinct, this represents the case where there is no interaction between the magnetic moments of the neighbouring atoms, so that the atomic magnetic moments can randomly point in any direction with equal probability. Therefore the overall magnetic moment has been cancelled out. A material that behaves like this is known as paramagnetic material, for example Mg, Al and Na *etc.*.

For materials with fully filled electron shells, under the influence of an external magnetic field, there will be no net spin and the moving electrons will generate a weak magnetic moment antiparallel to the external field, according to Lenz's law. The internal resistant magnetic field will disappear when the external field is absent. These materials are classified as diamagnetic, such as N<sub>2</sub>, Au and Ag.

For transition metals with large number of unpaired 3d electrons, Equation (1-14) and (1-15) can no longer be used to predict the magnetization of the system containing more than one atom, because the electron cloud of 3d electrons has a large radius and the exchange interaction between the neighbouring magnetic moments cannot be neglected. Exchange interaction is a short-range interaction, only occurring between neighbours and is a purely quantum effect<sup>(107)</sup>.

Assuming two neighbouring atoms with the total spin momentum of  $\mathbf{S}_1$  and  $\mathbf{S}_2$  respectively, the exchange interaction can be expressed as:

$$E_{ex} = -2J\mathbf{S}_1 \cdot \mathbf{S}_2 \quad (1-16)$$

$J$  is called exchange constant, which can be either positive or negative corresponding to the parallel alignment favoured or the anti-parallel alignment favoured magnetic moments excited by the external magnetic field. Only spins are taken into account here because of the orbital quenching by the crystal field. The exchange interaction is in the magnitude of a few eV, significantly stronger than the magnetic dipolar interaction which is normally about  $2.5 \times 10^{-6}$  eV<sup>(119)</sup>.

The function presenting the relationship between the value of  $J$  and the inter-atom separation is known as Bethe - Slater curve<sup>(120)</sup>. As seen in the Figure 1- 10, clearly two

groups of materials can be classified according to the sign of the exchange constant among 3d transition metals (Cr, Mn, Fe, Co and Ni).  $r_{ab}$  is the equilibrium distance between atom a and b,  $r_d$  is the atom radius up to  $d$  orbital.

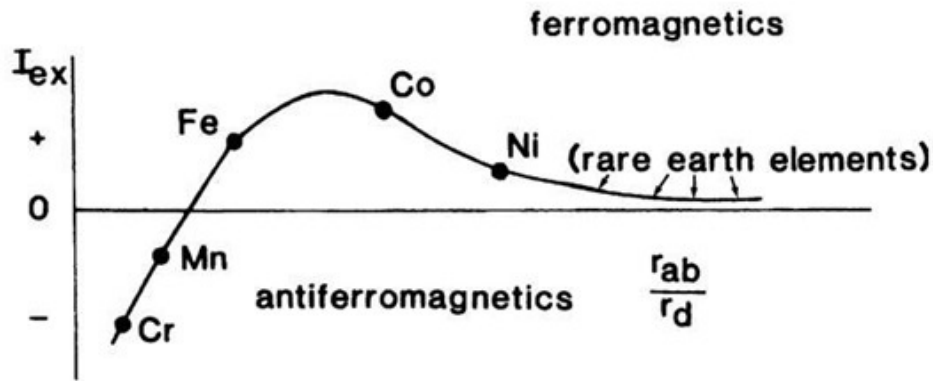


Figure 1- 10 Bethe-Slater curve demonstrating the value of exchange constant in function of the inter-atom separation of different element. Figure is reprinted from Ref. (121).

Elements with negative  $J$  and smaller inter-atom separation are classified as antiferromagnetic materials, such as Cr, Mn and NiO. For antiferromagnetic materials, each stimulated magnetic moment orientates anti-parallel to its closest neighbour to maintain the minimum total energy. Therefore a bulk antiferromagnetic material does not manifest any magnetism.

Whereas for ferromagnetic materials corresponding to positive exchange constant, such as Fe, Co and Ni, the magnetic moments tend to align in parallel to each other. Consequently the exchange interaction between the neighbouring atoms generates an internal magnetic field so that remanent magnetization can be detected after the external magnetic field is removed, which is a typical character of ferromagnetism<sup>(107)</sup>. Another typical feature for ferromagnetic material is the saturated magnetization can be achieved at a moderate magnetic field, *i.e.*, at a magnetic field, normally below 2 T, the stimulated magnetization can reach the maximum and cannot be further enhanced no matter how large the external magnetic field further increases. This saturation character is also a consequence of exchange interaction<sup>(107)</sup>. As suggested by the Brillouin Equation (1-15),  $y$  needs to approach infinite high to result in a saturated magnetic moment  $\mu$  for a free atom, *i.e.*,  $\mu_B B \gg kT$ . However, a simple calculation will

suggest that requires  $B \gg 447$  T at room temperature. This is inconsistent with the practical observations where ferromagnetic materials can be easily magnetized to saturation at room temperature. Fundamentally it is the ferromagnetic exchange interaction which assists to align the magnetic moments inside of the materials so that the saturation can be achieved under a moderate magnetic field. In contrast, the Brillouin Function is only valid for predicting the magnetism of a paramagnetic material in which the exchange interaction is absent. Therefore it is almost impossible to magnetize paramagnetic material to saturation.

One critical feature that can be read from the Bethe–Slater curve is that the exchange interaction, thus the magnetic ordering, both depends on the inter-atom separation. Ferromagnetic ordering forces the neighbouring atoms to be repulsive to each other, thus corresponds to the longer inter-atom distance. In contrast, antiferromagnetic ordering attracts the neighbouring atoms closer, resulting to a shorter inter-atom separation. For both anti-ferromagnetic and ferromagnetic material, longer inter-atom separation will result to a weaker exchange interaction. For antiferromagnetic material, larger inter-atom separation will weaken the antiferromagnetic ordering between atoms, or even reverse flip them to ferromagnetic ordering. For ferromagnetic material, when inter-atom separation further enlarges, the exchange interaction quickly decays, and atom involved in the system returns to the free-atom style, such as for rare earth material. All of these deductions can be obtained from Figure 1- 10.

Both antiferromagnetic and ferromagnetic properties are temperature dependent, which tend to be paramagnetic at high temperature. This is because high temperature thermally disrupts the order of the magnetic moments inside of the materials, so that the magnetic moments have equal probability of orientating to all the possible directions and no net magnetization can be detected when the external magnetic field is absent. The transition temperatures of paramagnetism to antiferromagnetism and ferromagnetism are known as Néel temperature ( $T_N$ ) and Curie temperature ( $T_C$ ), respectively.

Another member in the group of magnetic materials is called ferrimagnetic materials, which are similar to antiferromagnetic materials is that the magnetic moment stimulated by an external field will orientate opposite to its closet neighbour, but the moments amplitudes are not equal <sup>(122)</sup>. Therefore a spontaneous magnetization remains under external field. The most common examples of ferrimagnetic materials are ferrite, such as  $\text{Fe}_3\text{O}_4$ . A simple schematic illustration of the magnetic moments under the influence of an external magnetic field for ferromagnetic, anti-ferromagnetic and ferrimagnetic materials are shown in Figure 1- 11.

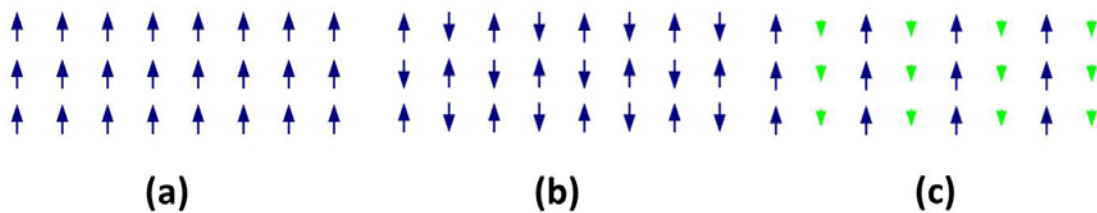


**Figure 1- 11 Magnetic moments display with the existence of external magnetic field in (a) ferromagnetic materials; (b) anti-ferromagnetic materials; (c) ferrimagnetic materials.**

#### **1.5.4 Magnetic Material at Nanoscale**

At nanoscale the magnetic properties of materials show dramatically different properties when compared to their bulk phase. For instance, a diamagnetic material such as Ag <sup>(123)</sup> and Au <sup>(124, 125)</sup> can have weak magnetism in small clusters, due to the contribution from the unpaired 5s and 6s electrons that can no longer be neglected at such scale. Antiferromagnetic nanomaterials can show certain magnetism in all temperature range due to the uncompensated spins locating on the surface <sup>(126)</sup>. Meanwhile ferromagnetic (FM) materials at nanoscale become superparamagnetic (SPM) below the Curie temperature <sup>(127)</sup>. SPM has recently attracted more and more attention in scientific research, since its great potential in applications of drug delivery, magnetic hyperthermia and being a contrast agent in magnetic resonance imaging (MRI) etc. <sup>(127)</sup>.

As shown in Figure 1- 12, M-H curve reflects the detected magnetization **M** of the sample in response to the external magnetic field **H**. For ferromagnetic materials in the

bulk phase, M-H curve presents as the hysteresis loop with the saturated magnetization at high H value, the remanence magnetization for H = 0, and the coercivity value  $H_c$  as the threshold external field that material can start to be demagnetized. While at the nanoscale, thermal influence becomes dominant relative to the internal magnetic field when the external field is removed. As a result the M-H curve will pass through the origin point, with no remanent magnetization when the external field is switched off. On the other hand, the magnetic susceptibility<sup>iii</sup> of the nanomaterial is still as high as its bulk value, so they can be easily magnetized to saturation. This kind of materials is known as the superparamagnetic materials.

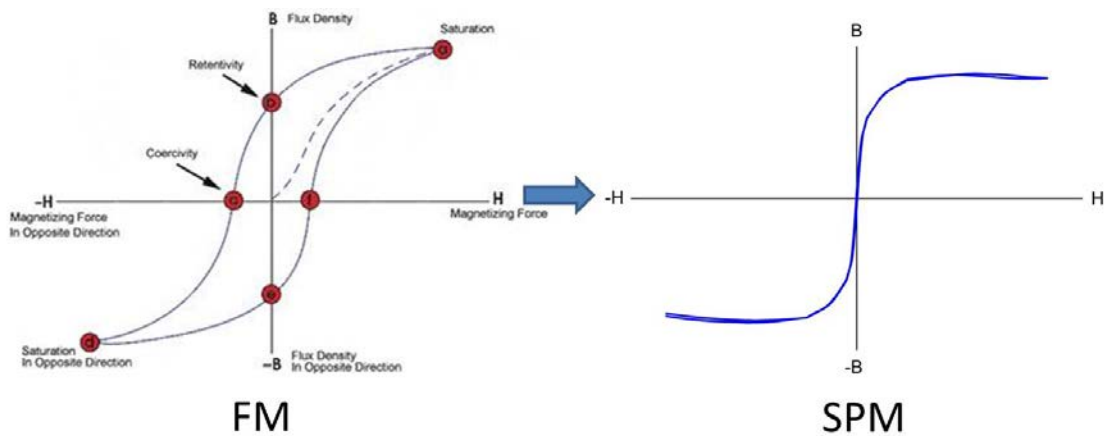


**Figure 1- 12 M-H curve expression of the transition from ferromagnetic material in bulk phase to superparamagnetic material at nanoscale.**

## 1.6 Aim and Structure of the Thesis

As a blooming experimental technique, at current stage helium droplet is mainly used within two areas of study, specifically in areas of spectroscopy study and nanostructure formation. Helium droplets can behave as an ultra-cold matrix with superfluidity to freezing molecules in the spectroscopy study, which has been proven to be an irreplaceable technique since 1990s. On the other hand, helium droplet has been developed as a versatile technique for nanostructures growth in the last few years, which provides a cold and disturbance free environment for nanostructures

<sup>iii</sup> Magnetic susceptibility reflects the ability of a material being magnetized, which can be mathematically expressed as:  $\chi = \frac{M}{H}$ .

aggregating atom by atom. By this means, this thesis focuses on a series of study which aim to penetrate deeper in the applications of the helium droplets technique, covering both of the mainstreams.

In Chapter 2, the apparatus of the helium droplets system equipped in the University of Leicester and all the characterization equipment involved in this project will be introduced in detail. Particularly we will systematically demonstrate our effort on how to synthesize nanoparticles and control its growth in helium droplets.

In Chapter 3, we will present our pioneer study on the dissolution process by sequentially doping NaCl and H<sub>2</sub>O molecules into helium droplets. The complex molecules are investigated by Infra-red spectroscopy within the O-H stretching region, from which the boundary structure of the dissolution occurrence can be determined.

In Chapter 4, the quantum vortex in helium droplets will be studied. Solid evidence of the existence of the quantum vortex will be given by observing the nanoparticles aggregation along the vortex line. Taking advantage of the quantum vortex, helium droplets can perform as a highly versatile nano-reactor to produce 1 dimensional nanostructure without material limitation, which will also be demonstrated in this Chapter. Additionally the trace of the high order quantized vortex in helium droplets will be discussed.

Finally in Chapter 5, we will present the first attempt in the world to produce the functional nanostructures in helium droplets, *i.e.*, to generate magnetic nanoparticles/nano wires. Both anti-ferromagnetic and ferromagnetic materials will be taken into concern, taking chromium (Cr) and nickel (Ni) as examples respectively. Both Cr and Ni samples synthesized perform much stronger magnetism than the counterparts formed by conventional methods, which indicates great potential for the applications in the future.

## Chapter 2

### Experimental Apparatus and Characterization

#### 2.1 Overview of the Helium Droplet Source

Figure 2- 1 shows the block diagram of the UHV helium droplet apparatus that has been used in this project. Metal-sealing using copper gaskets are employed instead of O-rings to achieve ultra-high vacuum, which is the essential for the synthesis of high-purity nanoparticles without the contamination of the water and other residuals in background. In addition, to fully avoid oil contamination, the vacuum system is evacuated by Maglev turbomolecular pumps and is backed up by scroll pumps.

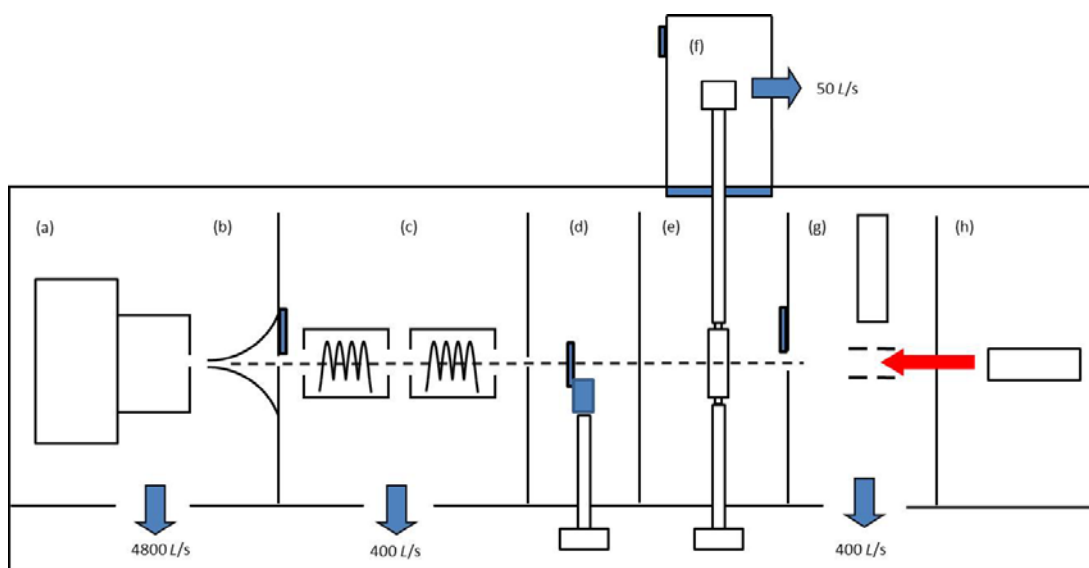


**Figure 2- 1** Block diagram showing the overall chamber configuration of the helium droplets system. (a) helium source; (b) skimmer; (c) pick- up cells; (d) deposition monitor and shutter; (e) deposition station; (f) load-lock chamber; (g) quadrupole mass spectrometer; (h) He/Ne laser for alignment of the chamber.

The apparatus can be divided into three sections: source chamber, middle chamber which includes the pick-up chamber and the deposition station and mass spectrometer, isolated by two gate valves. When both valves are closed, the mass spectrometer chamber can be vacuumed to  $10^{-10}$  mbar, and the middle chamber can

reach low  $10^{-9}$  mbar. For the source chamber, the pressure can be maintained at  $10^{-6}$  mbar at the room temperature with a stagnation pressure of 15 bar.

The key components assembled inside of the UHV helium droplets system is schematically shown in Figure 2- 2. A key apparatus in the helium droplet source is a close-cycle cryostat (Sumitomo RDK-415D) in the source chamber, which is used to pre-cool the helium gas expanded through a pinhole nozzle. The nozzle is a 5  $\mu\text{m}$  diameter disk (Pt/Ir (95/5) electron microscope aperture produced by Frey Precision) with a 5  $\mu\text{m}$  circular aperture and a thickness of 2 mm. This disk is sandwiched between a copper cylinder with a 1 mm diameter straight channel cut through its centre, and a copper face plate with a 0.5 mm diameter aperture and conical angle of  $90^\circ$  extending outwards in to the vacuum chamber. The sealing between the nozzle and the copper cylinder is achieved by using an indium sheet.

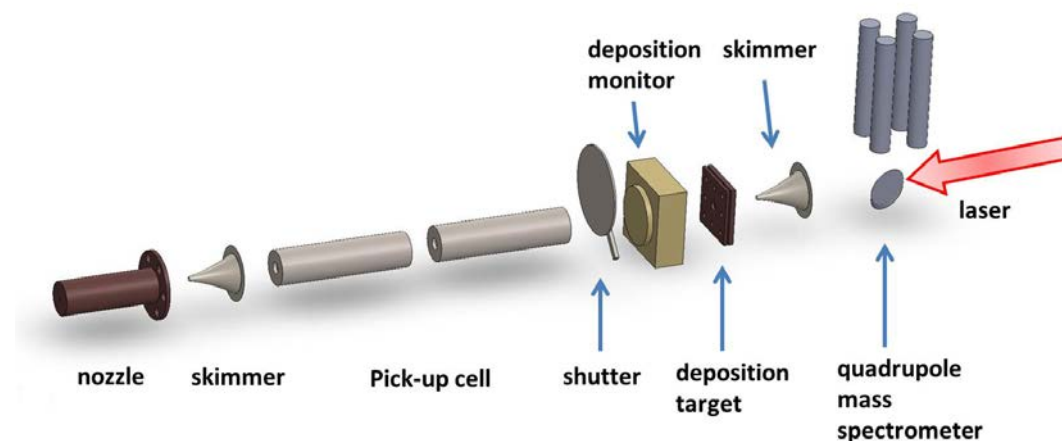


**Figure 2- 2 Schematic of the UHV helium droplets for the synthesis of nanoparticles.**

Within the cryostat, the high-purity helium gas (99.9999%) can be pre-cooled to as low as 2 K. To fully control the temperature in the range of 4 – 300 K a button heater is attached to the nozzle body, which can control the temperature of the nozzle through a balance of heating (by the heater) and cooling (by the cryostat). A temperature controller (LakeShore 336) is then used to stabilize the source temperature through a PID control, offering a minimum temperature variation of  $\pm 0.2$  K after optimizing the PID control of proportional, integral and derivative values. When expanded through the nozzle, helium gas experiences a supersonic expansion, which further reduces the

temperature of helium gas, leading to the formation of helium droplets (HeDs). Helium droplets are then collimated into a droplets beam by passing through a 0.5 mm diameter skimmer. In addition, an XYZ manipulator is mounted on the cryostat with a DN CF150 port, which allows the helium beam to be precisely aligned all through the apparatus at real time. The nozzle-skimmer distance is usually 15 – 20 mm.

When the helium droplet beam enters the pick-up chamber, the droplets can pick up atoms and molecules in the gas phase when they encounter, and sequential pickup of more than one material is possible when the droplets travel through different pickup regions. In this case binary molecule clusters and/or core-shell structural nanoparticles can be formed.

There are two types of pick-up cells used in our experiments. The first is the stainless steel cell that is used to add liquid and/or gas samples with/without additional heating. The stainless steel cell has a central axial hole with an inner diameter of 6 mm, allowing the helium beam to travel through and capture impurities. Solid samples with relatively high vapour pressures can be loaded directly inside the tube; while gaseous and liquid samples can be externally prepared and fed to the tube through Swagelok connections. In the latter case a needle valve is employed to adjust the partial pressures of liquid/gaseous samples in the pickup region in order to control the doping rate.

The other type of pick-up cells is high-temperature ceramic oven resistively heated by Ta wires. The oven is 70 mm long with 22 mm outer diameter and 14 mm inner diameter. The external surfaces have been carved with fine grooves where Ta wires can be fitted. On each end, a ceramic wafer is pasted to the oven to prevent the material flow, with a 6 mm hole in the centre to allow the helium beam travelling through. The details of the ceramic oven can be seen in Figure 2- 3. Tantalum wires are chosen rather than tungsten because they are more flexible, and can be easily wrapped around the grooves. High-temperature alumina glues are then pasted on the grooves in order to enhance thermal conduction between the wire and the alumina cell. The oven can reach a temperature up to 1950 K, which is capable of evaporating a wide range of materials. To reduce the heat load to the vacuum system, we have used

water cooling pipes surrounding the alumina cell. Finally, an alumina lid with 6 mm hole is mounted at each end of the oven to eliminate the free diffusion of the evaporated materials and also to concentrate the heat within the oven.

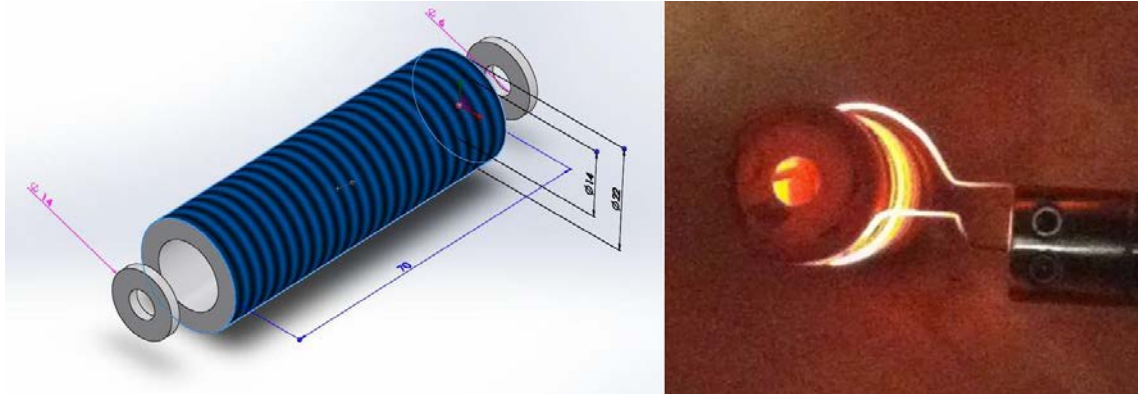


**Figure 2- 3 Left: The configuration and dimensions of the ceramic oven used. Right: Oven at working in the vacuum chamber.**

So far a maximum of 4 ovens have been placed in the pickup region and potentially a few more ovens can be inserted. Downstream to the pick-up region is a thin film deposition monitor with a shutter mounted on the front face. The shutter can be manually controlled to block the helium beam when necessary, in order to precisely control the deposition time of nanoparticles. The thin film deposition monitor can be manipulated by a one-dimensional translating arm, and can be translated across the helium droplet beam. The working principle of the thin film deposition monitor will be described in the next section.

As shown in Figure 2- 1 and Figure 2- 2, further downstream a deposition station is employed with which the deposition target can be loaded or unloaded without breaking the vacuum through a load-lock system, *i.e.*, a separate vacuum system that can be isolated from the UHV helium source by a gate valve. Sample substrates can be fixed to the baseplate attached to a magnetically coupled translation arm when the gate valve is shut and the load-lock chamber is opened to air. After uploading the deposition targets, the load-lock chamber can then be evacuated by a turbomolecular pump (50 L/s) before translating samples into the UHV chamber. At a pressure of  $10^{-6}$  mbar the gate valve between the load-lock chamber and the UHV helium source can be opened to allow the deposition targets being translated into the deposition region.

A XYZ manipulator mounted on the opposite side of the pick-up chamber can then receive the baseplate through a “click-lock” mechanism. The translational arm can then be withdrawn from the UHV chamber and the gate valve can be shut. A reverse procedure will be applied after the deposition, allowing the deposition targets being removed from the vacuum for investigations.

Two sets of sample holders have been used to clamp substrates in position: one is for TEM substrates (3mm diameter carbon thin film disk with meshed Cu grids) and the other is for clamping rectangle polyether ether ketone (PEEK) substrates used for large amount sample deposition. For TEM substrates, the sample holder has a 3 × 3 array for loading multiple substrates. At the centre of the sample holder is a through hole with slightly larger aperture, which allows helium droplets to pass through. Alignment of the helium droplet beam through the centre of this aperture can be achieved by monitoring helium gas signal in the mass spectrum. The hole position can then serve as the reference to precisely target all the TEM substrates during the deposition. For PEEK substrate, a hollow frame with a girder in the middle can hold two substrates to the substrate holder, one of which can be moved to the axis of helium droplet beam for deposition.

Beyond the deposition station, helium droplets will enter the quadrupole mass spectrometer (QMS) through a second skimmer (2 mm aperture). On the very end of the quadrupole chamber, a quartz observation window is mounted to a CF40 port. Therefore the He/Ne laser beam can be guided through to align the apertures in the UHV chambers, including 2 skimmers and ovens/pickup cells using as the reference. The picture of the UHV helium droplet system is shown in Figure 2- 4.

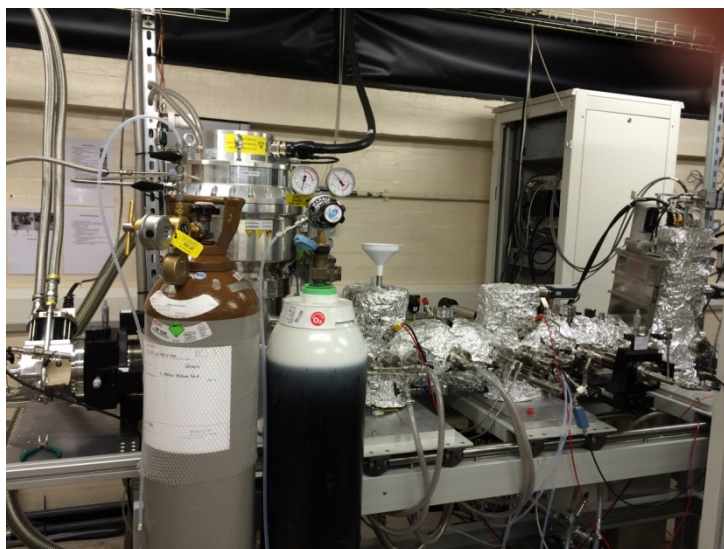


Figure 2- 4 The UHV helium droplet source for the synthesis of nanoparticles.

## 2.2 Detection Equipment

### 2.2.1 *Quadrupole Mass Spectrometer*

A quadrupole mass spectrometer (Extrel MAX-4000) has been used to characterization of helium droplet source and the pickup of molecules/atoms (see Figure 2- 1 and Figure 2- 2), which provides useful information for the pickup condition, in particular, in the formation of nanoparticles. The mass spectrometer is equipped with an electron impact ionization source, where continuously emitted electrons can ionize molecules/atoms and their clusters *via* a charge transfer mechanism when they impinge on the droplets<sup>(70)</sup>. The electron impact energy (IE) is normally set between the range of 60 eV to 90 eV depending on experiment conditions and dopants. The resolution of the impact energy is  $\pm 1$  eV.

After being ionized, the ejected cluster and molecular ions can be directed into the quadrupole region through a series of ion optics. In quadrupole region, the ions fly up through a DC ramp voltage and an RF voltage varying with time. At a specific RF voltage, ions of a particular mass to charge ratio ( $m/z$ ) are allowed to pass through, which are then detected by an ion counting device, the channeltron. As the RF voltage changes, ions of different  $m/z$  are detected and an overall mass spectrum covering a

certain  $m/z$  range can be obtained. The signal can be enhanced by an analogue or a digital preamplifier, and can be displayed in Merlin software.

The QMS is capable to detect the mass range up to 4000  $m/z$ . A typical mass spectrum recorded is shown in Figure 2- 5, which shows prominently the helium clusters. The spectrum shows a very weak water monomer peak at  $m/z = 18$ , and trace  $N_2$  and  $CO_2$  at  $m/z = 28$  and 44 respectively, which means the UHV system is free of contamination.

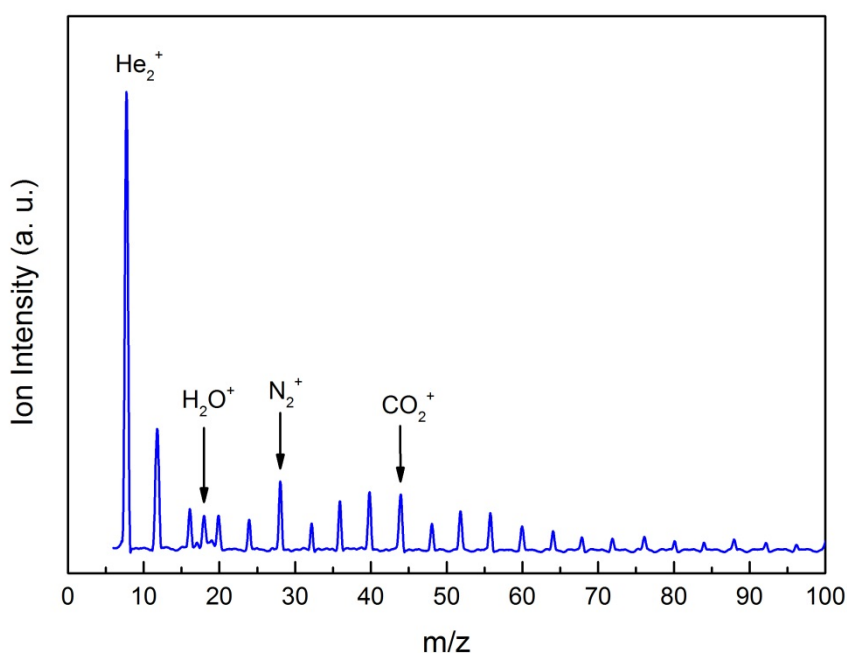


**Figure 2- 5 Mass spectrum of pure helium droplets ( $6 < m/z < 100$ ), recorded at  $T_0 = 12$  K,  $P_0 = 15$  bar,  $IE = 70$  eV.**

In spectroscopy measurement, the ion signal at a particular  $m/z$  can be monitored as a function of time using single ion mass (SIM) scan function, which allows the optical spectrum for a single mass channel being detected. The  $m/z$  width and accumulation time can be tuned in Merlin software.

SIM scan is a very useful tool for the alignment of helium droplet beam and optimization of the pickup conditions. For example, it can be used to monitor the real-time changes on the ion signal, which provides a good reference to align the helium beam, *i.e.*, by maximizing the helium signal (normally helium dimer signal) with respect to the different nozzle positions. On the other hand, it can be used to show the

variation of a particular ion channel at different pickup conditions, *e.g.* by varying the source temperature and the doping rate. Therefore the optimum combination of the experimental set-up can be determined. The influence of the free diffusion from the metal oven can also be inspected by comparing the gas phase mass spectra (when the gate valve close to the source chamber is shut) and the mass spectrum of doped helium droplets. It is suggest by the comparison that the free diffusion influence can be neglected in our project, and only the helium droplets picked up dopants can reach to the deposition target and the quadrupole mass spectrometer.

### **2.2.2 Laser System for Spectroscopy**

The optics configuration and working principle of OPO/OPA laser is schematically shown in Figure 2- 6. A Nd:YAG laser pumped OPO/OPA laser has been employed to excite molecules embedded in the droplets and the optical spectroscopy is detected using a depletion technique. The repetition rate of the Nd:YAG laser is 10 Hz, and the emission at 1064 nm is used as the pumping source with a horizontal polarization. The pump laser first passes through a beam splitter and split into two beams. One is frequency doubled to 532 nm and then oscillates in OPO stage consisted of a plain mirrors cavity with a KTP crystal in the middle. The KTP crystal converts the radiation into two beams with different frequencies. The higher frequency beam is known as *signal* beam with horizontal polarization and the lower frequency beam is termed as *idler* beam with vertical polarization. After radiated from OPO stage, the signal beam is dumped and the polarization of the idler beam is flipped when they pass through a variable half-wave plate (Wp). And then the horizontal polarized idler beam enters the OPA stage.

The other beam from the beam splitter is directed through a delay stage before combining with the idler output from the OPO stage. The combined beam then passes through an OPA stage containing four KTA crystals, producing two additional signal and idler beams *via* difference frequency mixing. As exiting from the OPA stage the mixed beam consisted by the residual 1064 nm pump, signal and idler beam co-propagate into a dichroic (Dc) where the residual 1064 nm beam is removed. A Brewster “stack of

plates” polarizer is positioned in the downstream to isolate either the vertically polarized idler beam in the mid-IR range or the horizontally polarized signal beam in the intermediate range.

The OPO/OPA laser is capable to generate laser of the near-IR range (710 nm – 845 nm), intermediate IR range (1.3  $\mu\text{m}$  – 2.1  $\mu\text{m}$ ) and mid-IR range (2.1  $\mu\text{m}$  – 5  $\mu\text{m}$ ) by adjusting the orientation of the 532 KTP crystal and four 1064 KTA crystals, with a resolution of 2  $\text{cm}^{-1}$ . The precise orientation control of the crystals is achieved by software-controlled motors.

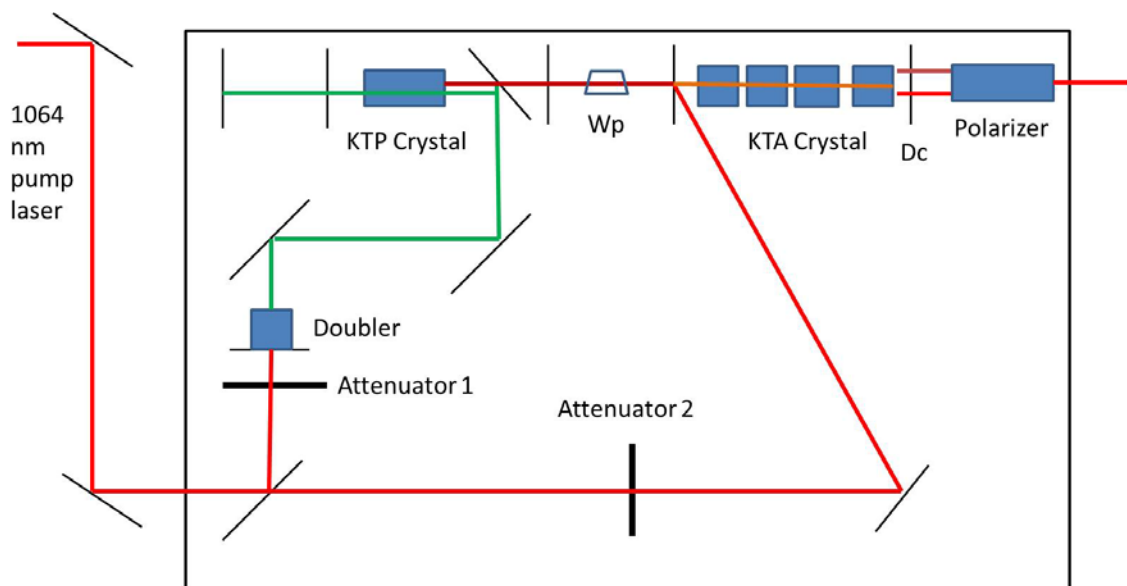


**Figure 2- 6 Optics configuration and working principle of OPO/OPA laser.**

Through several prisms and lenses the laser beam is steered into the UHV chamber, where it counter-propagates against the helium droplet beam. To achieve the maximal overlapping of the laser light to the helium droplet beam, a combination of concave and convex lenses have been used to focus the laser beam. The focus point is tuned right in front of the pick-up cell.

A two-channel photon counter (SR400) is used to process the signal from the channeltron and count the ions flux. Two gates with the different time delays are set to collect the respective ion counts in order to obtain the depletion signal. One gate is set when laser fires, and its duration is set equal to the flight time of the helium droplets from the pick-up cell to the quadrupole chamber. The other gate has the

same duration but it measures the ion count when the laser is absent. Generally 400 counts in each gate are accumulated in order to obtain decent signal/noise ratio. The vibrational intensity of the dopants can then be correlated to the ion counts difference between the two gating channels.

### **2.2.3 TEM Imaging**

Transmission electron microscopy (TEM) is a microscopy technique taking advantage of the much shorter wavelength of electron compared with light to overcome the Abbe diffraction limit<sup>iv</sup>. When a highly focused electron beam emitted from the electron gun transmits through an ultra-thin specimen, the image is obtained due to the interaction between electrons and the samples, for example, heavier atoms generally give rise to darker images because more electrons are scattered. The image is then magnified and focused onto imaging device, such as a fluorescent screen or a CCD camera. In theory TEM can have atomic resolution.

Compared to other microscopy techniques, such as AFM, SEM and STM, TEM has unique advantages which make it the best option for our research. For example, TEM can offer much higher resolution than SEM which is suitable for probing our small nanoparticles<sup>(128)</sup>. TEM can keep fidelity of the particle size better than STM and AFM. For STM it has been found that the scanned particle size is generally larger than the actual size<sup>(129, 130)</sup>; while for AFM, the particle size is normally lower evaluated than its real size<sup>(129)</sup>.

The most significant drawback of TEM is that under high resolution mode a high voltage electron gun is required, which means that samples may be damaged by the highly energetic electron beam, in particular, for relatively more chemically active materials. For instance, we have observed the Ni nanoparticles being “melt” in the

---

<sup>iv</sup> Abbe diffraction limit defines the theoretical angular resolution of an optical system due to the diffraction, which is mathematically expressed as:  $d = \frac{\lambda}{NA}$ , where  $d$  is the resolution limit,  $\lambda$  is the wavelength of the incident light,  $NA$  is a dimensionless number called numerical aperture depending on the material intrinsic property. In microscopy,  $NA = 2n \sin \vartheta$ ,  $n$  is the index of refraction of the medium,  $\vartheta$  is the half-angle of the maximum cone of light that can enter or exit the optics.

TEM when high-resolution mode is applied. It is therefore highly challenging to obtain high-resolution TEM images of small magnetic nanoparticles.

The TEM used in this work is a JEOL JEM-2100 LaB6 transmission electron microscope at the Advanced Microscopy Centre in the University of Leicester, which is equipped with a field emission electron gun (FEG). The stated-resolution of this instrument is 0.14 nm for lattice structure, which, however, is hard to achieve in practice. Samples can be tilted within the range between  $-42^{\circ}$  –  $42^{\circ}$ , and a Gatan  $2k \times 2k$  digital camera is installed to take pictures of samples.

Normally 3 nm ultra-thin carbon substrates on 300 mesh copper grids (*Ted Pella, Inc.*) are used as the substrate for sample deposition. Other types of substrates such as non-porous 5 nm thickness silicon grids (*SiMPore, Inc.*) can also be used if necessary.

Particles sizes can be statistically obtained from the TEM images using software called “Image J”, which can give the intersection areas of all the particles deposited. The software working panel is shown in Figure 2- 7. In order to obtain a promising size distribution, more than 1000 particles of each sample are normally taken into account.

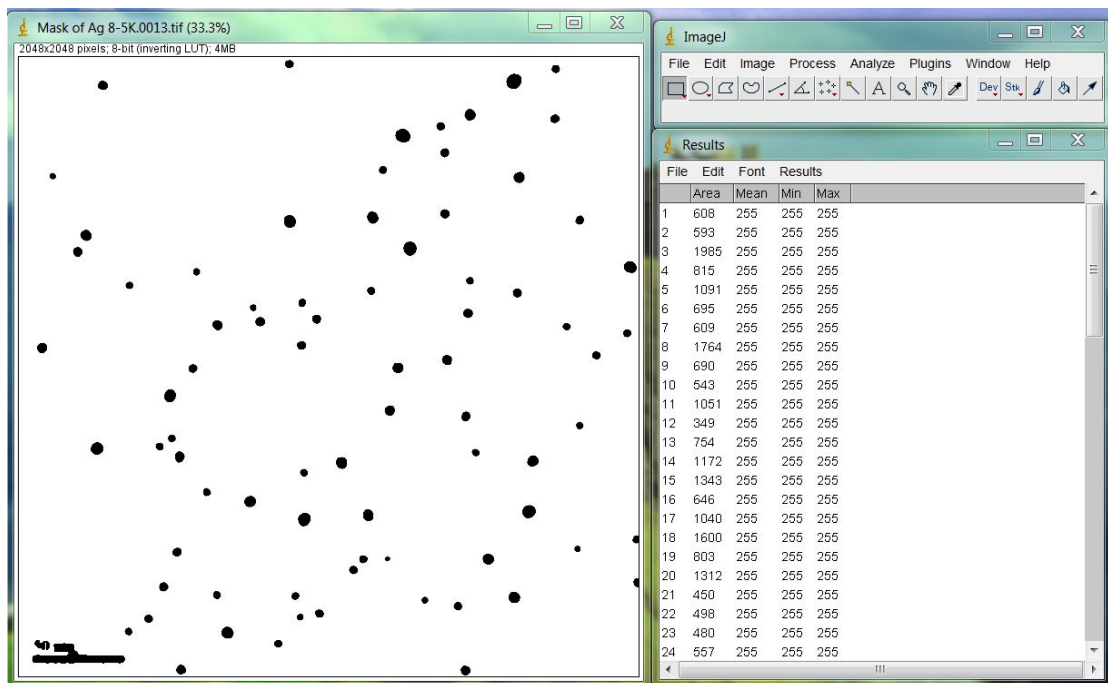


Figure 2- 7 The description of how the software “Image J” works in determining the size of the nanoparticles from TEM image.

#### 2.2.4 Mass Measurement of Deposited Nanoparticles

A SQM-160 deposition monitor manufactured by INFICON Inc. is placed downstream to the metal ovens in order to measure the mass deposition rate in real time. A deposition sensor is located in the vacuum chamber and can be controlled by a 2-D translational manipulator. A shutter is fixed in front of the sensor so that the deposition time can be precisely controlled.

The core component of the detective sensor is a 6 MHz type AT-cut quartz, which is of 0.55 inch diameter and gold-coated electrodes. The crystal is made by a piezoelectric material that can create an electronic vibration signal whose frequency is precisely proportional to the mass deposited with sensitive resolution. The resolution of the deposition monitor can reach atomic level, as high as 1 Å. To reduce the error caused by temperature rise (due to thermal radiation of the high-temperature ovens), a circulated water cooling system is introduced to keep the temperature stable at room temperature. This is essential to achieve the best performance for the quartz thin film.

The vibration frequency shift is measured and can be converted to mass changes *via* the control software provided by the manufacturer. According to the Sauerbrey Equation <sup>(131-133)</sup>, the mass deposited on the quartz surface can be calculated from the frequency change as:

$$\frac{M_a}{M_q} = \frac{\Delta F}{F_q} \quad (2-1)$$

Where  $M_a$  is the mass added to the crystal since the measurement starts;  $M_q$  is the mass of the uncoated quartz crystal;  $\Delta F = F_q - F_c$ , where  $F_q$  is the vibration frequency of the quartz before deposition,  $F_c$  is the frequency of the quartz after the addition of materials. After simple substitution, this equation can be transformed into:

$$M_a = \frac{N_{at}\rho_q S_q}{F_q^2} (F_q - F_c) \quad (2-2)$$

where  $N_{at} = 166100 \text{ Hz}\cdot\text{cm}$  is the frequency constant of the AT-cut quartz;  $\rho_q = 2.649 \text{ g/cm}^3$  is the density of the quartz;  $S_q = 1.53 \text{ cm}^2$  is the deposition area of the quartz.

Equation (2-2) is valid only when the frequency shift is no more than  $0.05F_q$ . Beyond this range, a more precise equation should be used which extends the valid frequency change range to  $0.4F_q$ <sup>(134)</sup>:

$$M_a = \left( \frac{N_{at}\rho_q S_q}{\pi F_c Z} \right) \arctan\left( Z \tan\left[ \frac{\pi(F_q - F_c)}{F_q} \right] \right) \quad (2-3)$$

Here  $Z$  is a material special constant called acoustic dependent ratio. In practice, the frequency shift for 30 min (the typical measurement time used in our experiments) is only a few Hz (compared with the quartz frequency of 6 MHz); therefore equation (2-2) can provide sufficient precision in our measurement.

Figure 2- 8 shows a typical deposition rate of Ni nanoparticles measured in 30 minutes. The red spots are the original vibration frequency change of the quartz during the measure period and the blue are the mass accumulation transformed from the frequency change according to Equation 2-2. It can be noticed that the mass deposition is steady in our experiments because of a constant dopants pick-up by helium droplets, resulting a linear relationship between the mass accumulation and the deposition time. The gradient of the linear line is the deposition rate, which can be transformed into the sample mass deposited by multiplying the total deposition time.

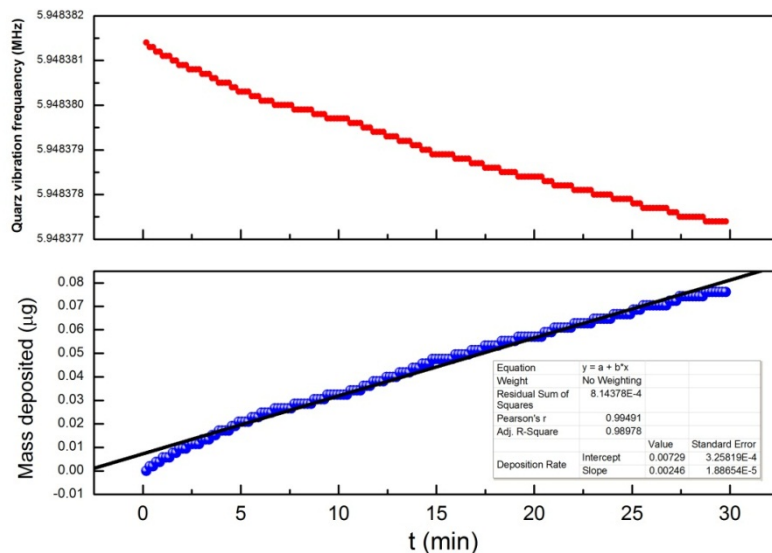


**Figure 2- 8** The deposition rate measurement using the thin film deposition monitor. Upper panel: the original frequency change. Lower panel: Accumulated Mass calculated from the frequency change according to Equation 2-2. The gradient is the deposition rate in units of  $\mu\text{g}/\text{min}$ .

In our experiments the deposition rate is measured both before and after the sample deposition, each for 30 minutes, to confirm its consistency. The final deposition rate used for the sample mass estimation in this work is obtained from the average of the two measurement results.

It is worth mentioning that the mass estimated by this way is the upper limit of the real mass deposited on the substrate. Because there is an implicit assumption underlying in this method that all the samples reaching to the deposition monitor will be deposited on the substrate. However in practice, some of the samples may drift out of the substrate in the downstream because the helium beam is slightly divergent; so the deposition substrates, such as TEM grid with 3 mm diameter, will not be able to cover the entire helium droplet beam.

Alternately the mass of the deposited sample can be determined according to the TEM images. We can calculate the mass density of the samples observed in the TEM image with respect to the area of the image and then convert it to the mass deposition rate. Based on our comparison using Ag as an example, mass estimated from TEM images has a good agreement with that estimated from the deposition monitor, as shown in Table 2- 1.

**Table 2- 1 Comparison of deposition rate measured by deposition monitor and TEM images. Samples taken in account is Ag tested at different source temperature from 10 K to 6.25 K.**

$T_0$ (K)	Deposition Rate by XTM (ng/min)	Deposition Rate by TEM (ng/min)	Error
10	10.65	9.27	12.9%
9	12.21	11.11	9.0%
8.5	14.23	11.02	22.6%
8	11.29	8.90	21.1%
7	8.08	6.52	19.3%
6.25	17.07	14.87	12.9%

**XTM = quartz crystal thin film deposition monitor.**

As expected, the deposition rate estimated by TEM images is slightly lower than that measured by deposition monitor. However, measurement using TEM images is more reliable than the thin film deposition monitor because this counts the exact number of particles deposited on the surface of the TEM substrates.

### 2.2.5 XPS Analysis

To detect the particle composition and the abundance of each element, X-ray photoelectron spectroscopy (XPS) can be employed to analyse the elements within nanoparticles. This is one of the key techniques applied in this work to confirm core-shell in Ni/Au nanoparticles.

The working principle of XPS can be generally described by photoelectron effect. An X-ray source is used to produce photons at a given frequency. When photons are incident to a sample surface, atoms will be ionized and projectile electrons will be generated. The excess energy is then transformed to the kinetic energy of the projectile electrons, which can be measured through the velocity of the electrons. Therefore the original binding energy between the electron and nuclei can be worked out following the equation:

$$E_{binding} = E_{photon} - (KE + \phi) \quad (2-4)$$

$E_{binding}$  is the electron binding energy,  $E_{photon}$  is the X-ray photon energy, KE is the kinetic energy detected from the ejected electrons and  $\phi$  is the work function of the spectrometer accounting for the kinetic energy absorbed by instrument detector.

According to the calculated binding energy, the quantum orbitals from which the electron originates can be determined; hence the element with its valence can be identified. This is laid out in form of individual peak in XPS spectra and the intensity of each peak reflects the abundance of the elements in the sample. Normally peaks of pure metals have a full width at half maximum (FWHM) in the range of 0.3 eV – 1.0 eV and for their metal oxides the peaks are significantly broader, with an FWHM often in the range of 0.9 eV – 1.7 eV<sup>(135-138)</sup>.

XPS spectra are charge-corrected in reference to the main C 1s peak at 285 eV. After

subtracting the baseline signal using the Shirley background subtraction method <sup>(139)</sup>, the peaks can be resolved into individual component peak in shapes of Gaussian curves.

It is desirable to have a substrate that contributes little to the spectrum in XPS measurement, so highly ordered pyrolytic graphite (HOPG) is chosen. The XPS measurements are carried out in collaboration with University of Nottingham, where a Kratos AXIS ULTRA with a monochromated Al  $K\alpha$  source (1486.6eV) operated at a 10 mA emission current and 10 kV anode potential is used. The ULTRA XPS is used in fixed analyzer transmission (FAT) mode with a pass energy of 80 eV for wide scans and 20 eV for high resolution scans. The take-off angle of the photoelectron analyzer is 90° and the acceptance angle is 30° (in magnetic lens mode). The X-ray can penetrate as deep as 10 nm down to the sample surface.

#### **2.2.6 Magnetic Property Measurement**

Magnetic measurements that have been employed in this project include the M-H curves and zero-field cooling and field cooling (ZFC/FC) measurements.

M-H curve shows stimulated magnetization of samples in response to the applied magnetic field, from which the classification of the sample magnetism, such as diamagnetic, paramagnetic, ferromagnetic or superparamagnetic, can be identified. For diamagnetic materials (DM), the stimulated magnetization of the material is inversely proportional to the external field. For paramagnetic material (PM), the M-H curve is normally a straight line or a smooth curve passing through the origin point. The magnetization weakly increases with the external field and cannot be saturated unless an exceptional high magnetic field (>10 T) is applied. While the M-H curve for ferromagnetic material (FM) presents a shape of hysteresis loop with interceptions on both the H axis (applied magnetic field), known as coercivity and the M axis (measured magnetization), known as remanent magnetization. The magnetization is often saturated at around 1 T external field. Superparamagnetism (SPM) is the magnetic property presented by the ferromagnetic material at nanoscale below Curie temperature. The M-H curve can be saturated under moderate external magnetic field

as ferromagnetic material meanwhile it also pass through the origin point as paramagnetic material, *i.e.*, at zero field both coercivity and remanent magnetization are zero <sup>(122, 140)</sup>. The typical M-H curves assigned to different types of magnetic materials are shown in Figure 2- 9.

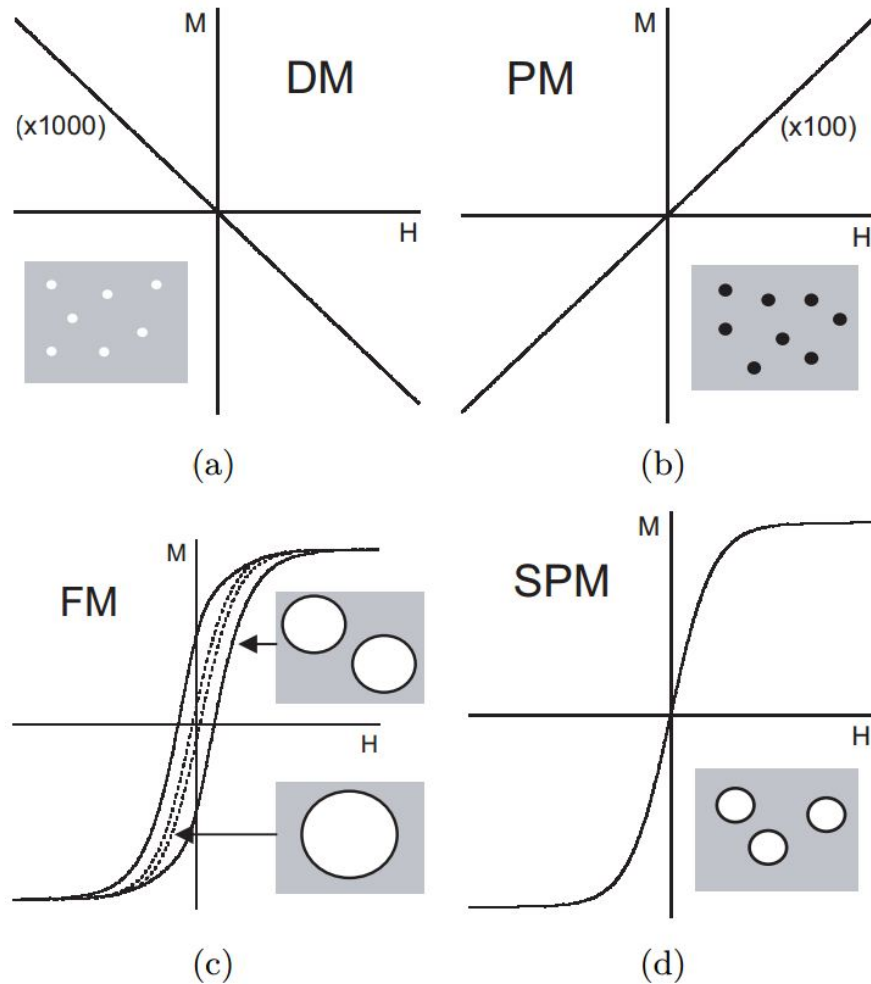


**Figure 2- 9 Typical M-H curves of (a): diamagnetic material; (b): paramagnetic material; (c): ferromagnetic material. Hysteresis loop of multi domain ferromagnetic material (dash line) is narrower than the single domain one (solid line); (d): superparamagnetic material. Picture is adapted from Ref. (140).**

ZFCFC measures the stimulated magnetization of magnetic materials in response to the environmental temperature. It contains two measurements over magnetization: zero field cooling (ZFC) and field cooling (FC). The process of measurement can be briefly described as: sample is first cooled down to a low targeted temperature, *e.g.* 5

K, without an external magnetic field, known as zero field cooling. Then an external magnetic field is applied and the sample is gradually warmed up, during which the magnetization of the sample is measured at each temperature step. This gives the relations between magnetization and temperature (M/T) under ZFC. To obtain the M/T curve under FC condition, the sample is cooled down to the target temperature again without removing the external field (field cooling process). And then the magnetization is measured at each temperature step as the sample is gradually warmed up. The features lying in ZFCFC curves, such as the appearance of peak and split between FC and ZFC curve, contain valuable information regarding to the magnetic properties of materials.

In this project the M-H curves at room temperature have been measured by use of a commercial vector vibrating sample magnetometer (VSM), (vVSM, ADE-Technologies, Model 10) equipped with two sets of pick-up coils and a rotating (from 0 to 36) electromagnet that can supply a maximum field of 2 T. The VSM has a detection limit of about 1  $\mu$ emu, and can detect the M-H curves in the temperature range of 100 - 780 K without the need to switch from a cryostat to a high-temperature module. Signals from the two sets of pick-up coils are combined and converted to give the components of the magnetization vector along four different directions, *i.e.* parallel and perpendicular to the sample (stationary reference system), parallel and perpendicular to the external magnetic field. The rotation and vector options allow angle-dependent measurements, magnetic anisotropy measurements and the determination of the intrinsic magnetic behaviour.

More precise measurement at lower temperatures can be achieved by employing a superconducting quantum interference device (SQUID) magnetometer, which can apply a high magnetic field up to 7 T and the temperature as low as 2 K.

The VSM and SQUID measurements were carried out in collaboration with the Institute of Structure of Matter, National Research Council (CNR) in Italy and Shanghai Jiaotong University in China.

## 2.3 Clusters and Nanoparticles Formed in HeDs

### 2.3.1 The Dependence of Helium Droplet Sizes on the Source Conditions

As discussed in Chapter 1, helium droplets, depending on the source temperature, can be formed in two regimes – subcritical regime and supercritical regime<sup>(13, 141)</sup>. Experimentally, the transition from subcritical to supercritical for a given helium nanodroplet system can be determined by recording the mass spectra of helium clusters with respect to the varying source temperature, and monitoring the ratio of  $\text{He}_4^+/\text{He}_2^+$  from the mass spectrometer. A typical example measured using our helium droplet apparatus is shown in Figure 2- 10.  $\text{He}_4^+$  and  $\text{He}_2^+$  signal are measured from 5.5 K to 15 K by the quadrupole mass spectrometer after the helium beam being aligned. The impact energy of the quadrupole is set to 65 eV, which gives maximum  $\text{He}_2^+$  signal intensity.

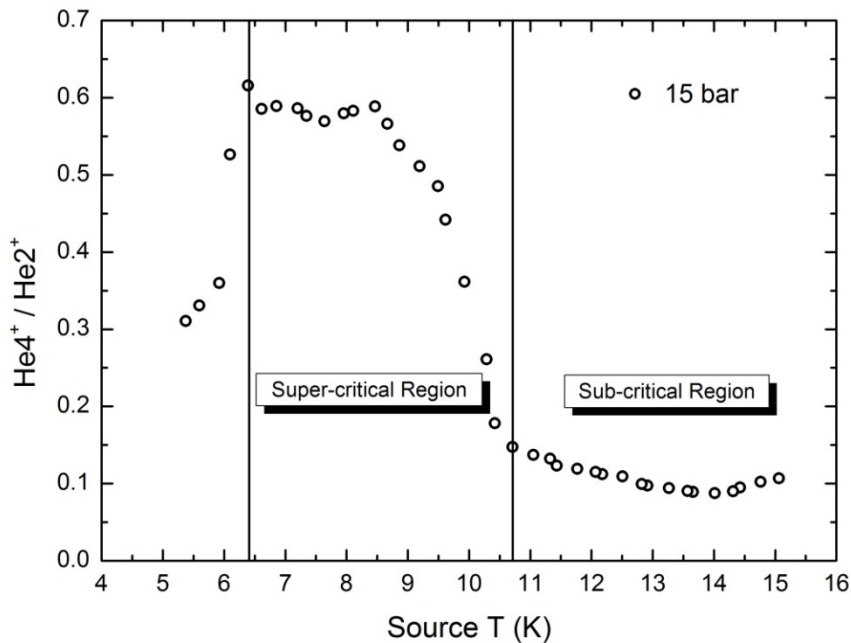


Figure 2- 10  $\text{He}_4^+/\text{He}_2^+$  ratio variation in the source temperature range of 15 K to 5.5 K, recorded by the quadrupole mass spectrometer at stagnation pressure of 15 bar, IE = 65 eV.

As the source temperature decreases, the  $\text{He}_4^+/\text{He}_2^+$  ratio experiences three stages:

- i) 15 K – 10.7 K: the ratio maintains roughly constant, which is not very sensitive to the temperature variation.
- ii) 10.7 K – 6.4 K: Starting from 10.7 K, the  $\text{He}_4^+/\text{He}_2^+$  ratio dramatically grows when the temperature drops and stabilizes at a plateau of about 60%. The turning point at 10.7 K is known as the boundary temperature between the sub-critical and supercritical regime of the helium droplets.
- iii) Below 6.4 K: The ratio sharply decays as the temperature drops further.

These three stages exactly fit the curve of the helium droplets size variation with respect to the temperature as discussed in Ref. (10), where helium droplets size experiences a gradual bloom from  $10^3$  to  $10^4$  He atoms, as the temperature cooled down in the subcritical region and then the size sharply increases up to  $10^{12}$  He atoms as the temperature further cooled down in supercritical region. Therefore three regions of helium droplets can be applied for different application purposes, as will be demonstrated in detail in later sections and following chapters. Here we first list the simple conclusion for each region:

- i) 15 K – 10.7 K: Small dopant clusters (less than 20 atoms/molecules) can be formed which is suitable for mass spectrum investigation and small clusters' spectroscopy study.
- ii) 10.7 K – 6.4 K: Nanoparticles (normally smaller than 10 nm in diameter) can be formed.
- iii) Below 6.4 K: Nanowires in wide range of length can be formed, taking advantages of quantum vortices which remarkably exist in helium droplets at this stage.

The boundary temperature depends on the helium stagnation pressure and the apparatus conditions including the cryostat, nozzle and vacuum conditions *etc.*

Figure 2- 11 plots the  $\text{He}_4^+/\text{He}_2^+$  ratio at different helium stagnation pressures. As the stagnation pressure increases, the boundary temperature rises correspondingly, *e.g.*, from 10.2 K at 10 bar to 12.2 K at 30 bar.

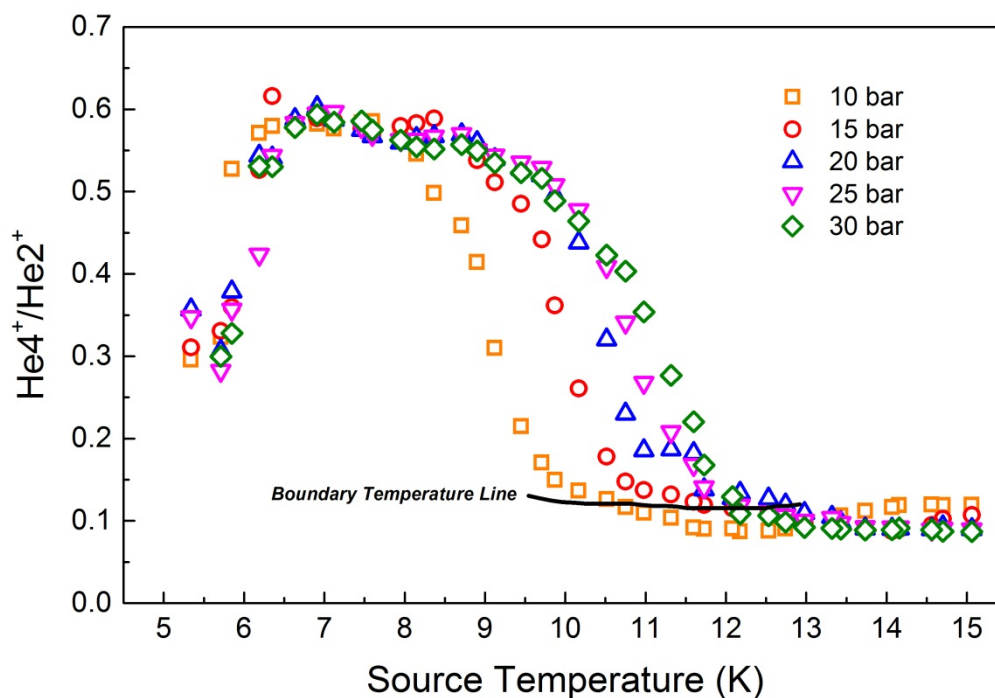


**Figure 2- 11 The dependence of  $\text{He}_4^+/\text{He}_2^+$  ratios on the source temperatures. Different stagnation pressures have been applied, *i.e.*, at 10 bar, 15 bar, 20 bar, 25 bar and 30 bar, respectively.**

In comparison with the Ref. (18), the boundary temperature at 15 bar of our apparatus is exactly the same as Vilesov's at 20 bar, which offers an easy way of calibration of the source temperature and the measurement of helium droplet size.

### **2.3.2 The formation of Small Clusters in HeDs**

The size distribution of helium droplets is temperature dependent, and it is known that the addition of molecules/atoms to the droplets follows a Poisson distribution for each droplet <sup>(28)</sup>. Consequently, at a specified source condition and a partial pressure of the sample in the pickup region, the overall distribution of the clusters embedded in the droplets is a convolution of the size distribution of helium droplets (lognormal or linear exponential) and the Poisson statistics. For clusters consisted of up to a few tens of atoms/molecules, the pick-up condition can be monitored by quadrupole mass spectrometry, which is critical for spectroscopy study and the formation of

nanoparticles. In this section, mass spectra of dopants embedded in helium nanodroplets will be discussed.

As mentioned in Chapter 1, when picking up dopants, helium droplets have to quench their kinetic energy and potential energy, which leads to the evaporation of helium atoms and the shrinkage of their geometric cross sections. Consequently to observe a promising mass spectrum in a helium nanodroplet, we need to balance two factors – the initial helium droplets size which determines the pick-up cross section, and dopant vapour pressure which controls the number density of the dopants in the pickup region.

First, the droplets size needs to be sufficiently large for picking up large clusters if we want to observe them in the mass spectrum. However, when the droplets become too large ( $>10^4$  helium atoms), the electron ionization probability of the dopant inside of the helium droplets becomes negligible<sup>(70)</sup>, therefore clusters cannot be detected by the mass spectrometer. That is because the electron impact cannot directly ionize the dopant locating at the centre of the helium droplets; instead, a helium atom near the surface of the droplets is first ionized, which then transfers the charge to the dopant through a resonant charge transfer process<sup>(142)</sup>. Theoretical calculation suggests,  $\text{He}^+$  can only freely hop by an average distance of 34 Å in helium droplets<sup>(70)</sup>. That means after picking up dopants and the size shrinkage, if the droplet is still over 13 nm in diameter (double of the average charge transfer distance in helium droplets), the probability of the charge transfer from  $\text{He}^+$  to the dopant can be neglected.

We take Ni as an example to examine the initial droplet size requirement to observe a promising mass spectrum. The dissociation energy for Ni cluster varies between 0.8 eV and 1.1 eV per atom<sup>(143)</sup>. Taking the upper limit for approximation, one added Ni atom bonded to an existed cluster in droplets would evaporate 1775 helium atoms, assuming one helium atom removal need  $6.2 \times 10^{-4}$  eV energy<sup>(23)</sup>. At 950 K, the kinetic energy of one Ni atom that needs to be quenched is  $E = \frac{3}{2}k_B T = 0.123$  eV, which removes 185 helium atoms. Therefore formation of a  $\text{Ni}_{10}$  cluster will result in the loss of *ca* 19,600 atoms. At  $T_0 = 10$  K and  $P_0 = 15$  bar, on average the helium droplets consist of about  $7 \times 10^4$  He atoms (15 nm). After picking up a  $\text{Ni}_{10}$  cluster, the droplet size will

shrink to 14 nm, which is still too large for the charge transfer to the dopant. Unsurprisingly at 10 K small  $Ni_n$  clusters ( $n = 1 - 10$ ) can hardly be observed in the mass spectrum. At even lower temperature, the droplet size will exponentially increase and there will be less chance to detect Ni clusters. However, Ni monomer ion can be observed, which is attributed to free diffusion of Ni atoms in the vacuum chamber<sup>(67)</sup>.

Figure 2- 12 shows a series of mass spectra of Ni clusters with varying source temperatures from 18 K to 10.5 K and fixed oven temperature at 950 K. It can be noticed as the source temperature drops from 18 K, more Ni clusters start to appear in the mass spectrum, but at 10.5 K source temperature, the clusters are less dominant again comparing to 11 K, which exactly justifies the initial droplet size effect to the mass spectrum observation discussed above.

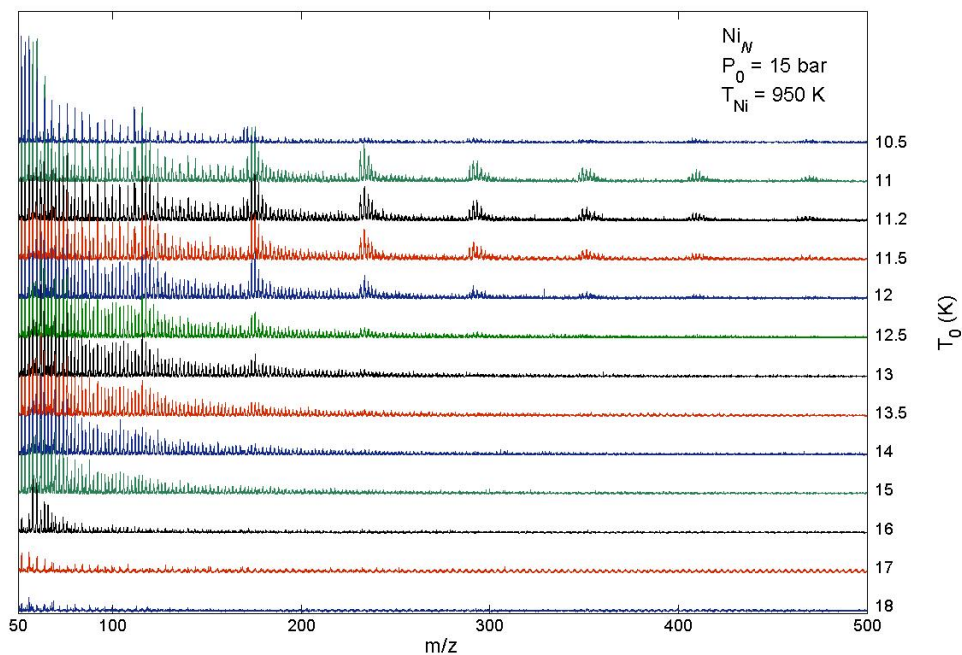


**Figure 2- 12 Mass spectra of Ni clusters recorded at different source temperatures.**

When the helium droplet size is sufficiently large but still below the charge transfer limit, the cluster ions observed from the mass spectrum should increase with the dopant vapour pressure, thus the doping rate. However, if the vapour pressure is too high, the number of the impurities colliding with the helium droplets will be sufficient

to completely remove helium atoms in the droplets, leading to weaker ion signals in the mass spectrum.

The Ni mass spectra observed at a fixed source temperature but varied oven temperature (835 K – 966 K) are displayed in Figure 2- 13. In this range the increase of oven temperature leads to the increase of metal vapour pressure<sup>v</sup>. The cluster ions start to appear in the mass spectrum at 835 K. The best pickup is found at 932 K, beyond which the ion signal starts to decay until they almost vanish at 966 K. Combined with the Figure 2- 12, the optimum pickup condition of Ni is at 11 K source temperature and 932 K Ni oven temperature.

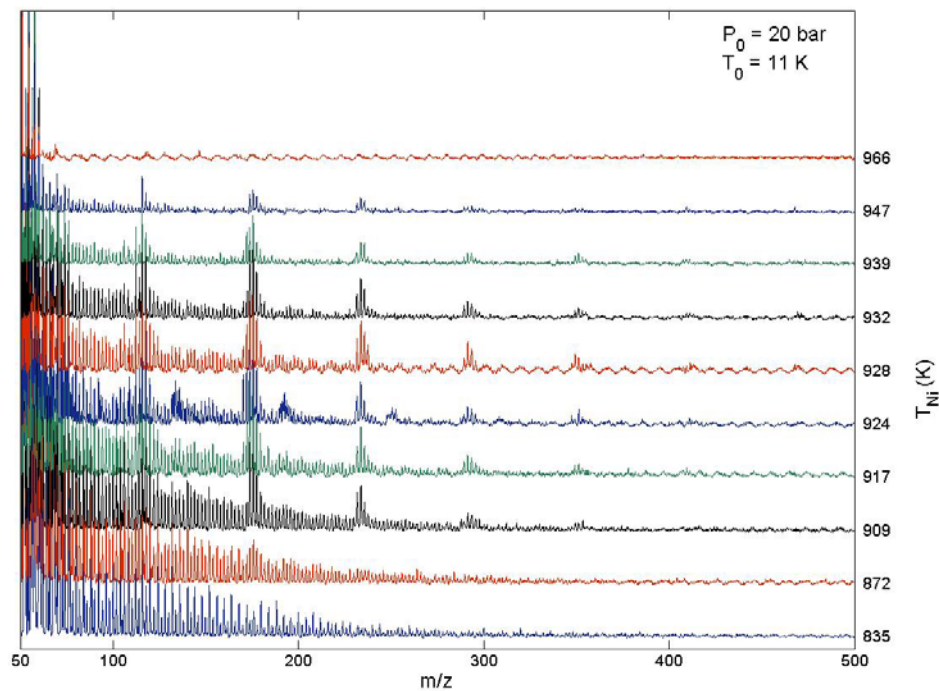


**Figure 2- 13 Mass spectra of Ni clusters at different oven temperatures.**

Liquid and gas dopants share the similar pickup condition: the observation of a high quality mass spectrum requires balance of the initial helium droplet size and dopant vapour pressure until the droplets being evaporated to a “just right” size when all the excess energy has been released. The bonding between gas/ liquid dopants is generally

<sup>v</sup> The vapour pressure corresponding to the oven temperature are acquired from the website: [http://www.iap.tuwien.ac.at/www/surface/vapor\\_pressure](http://www.iap.tuwien.ac.at/www/surface/vapor_pressure)

weaker than a metallic bond; hence higher source temperature (smaller initial droplet size) should be employed in order to observe decent cluster distribution in the mass spectrum (detailed in the spectroscopy measurement of salt-water complexes in Chapter 3).

### **2.3.3 The Growth of Nanoparticles in HeDs**

In super-critical expansion regime, the droplets size follows a linear exponential distribution, and very large helium droplets composed of  $>10^{10}$  atoms can be formed<sup>(10)</sup>, which are capable of capturing larger quantity of dopant atoms and molecules. When more and more dopants are added to the droplets, they can aggregate into very large clusters, with a dimension in nanometre scale. These are then termed as nanoparticles. In this section, growth of nanoparticle in helium droplet and the control over particle size will be addressed.

First, we focus on the nanoparticle growth at increasing vapour pressure using silver as the examples because they are easier to image using TEM.

A selection of TEM images of silver nanoparticles formed at a constant source temperature of 9.5 K with an approximate droplet size of  $10^6$  helium atoms, and the various oven temperatures (vapour pressure) has been shown in Figure 2- 14. The insets show the size statistics. We have tentatively used a Gaussian distribution<sup>vi</sup> to describe the size distribution of Ag nanoparticles, which fits very well with the particle sizes measured from the TEM substrates. With the vapour pressure gradually increasing, the average size increases accordingly.

---

<sup>vi</sup> Standard mathematical expression of Gaussian distribution is:  $f(x, \mu, \sigma) = \frac{1}{\sigma\sqrt{2\pi}} e^{-\frac{(x-\mu)^2}{2\sigma^2}}$ , where  $\mu$  is the expectation value of the distribution and  $\sigma$  is the standard deviation.

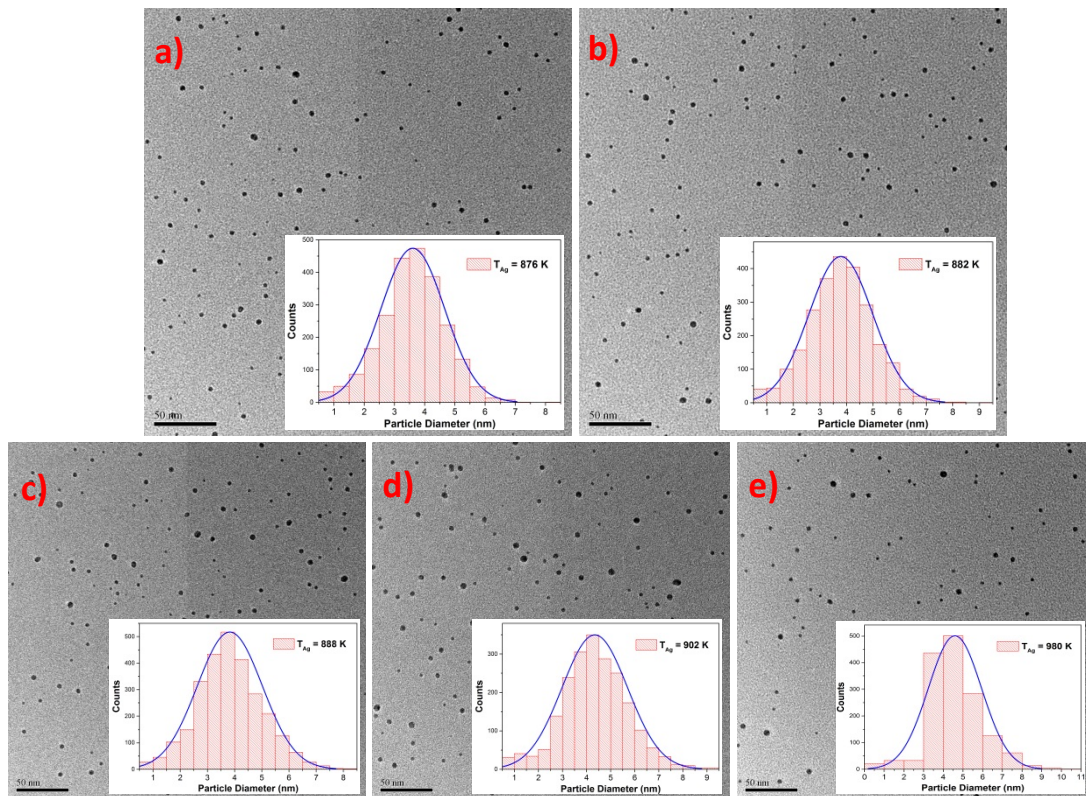


**Figure 2- 14 TEM images of Ag nanoparticles at various oven temperatures: (a) 876 K, (b) 882 K, (c) 888 K, (d) 902 K and (e) 980 K. In all these experiments the source condition is kept at  $T_0 = 9.5$  K and  $P_0 = 15$  bar, and the deposition time  $t_{\text{deposition}} = 5$  min.**

A full list of helium droplet sizes and fluxes at different oven temperature is given in Table 2- 2. The average particle size and counts per image ( $N/\text{image}$ ) are obtained by averaging more than 15 TEM images for each sample and over one thousand particles. The 15 TEM images were taken randomly from the different positions of the substrate. Besides the increase in the average size from 3.61 nm diameter to 4.41 nm with the oven temperature, a remarkable feature is that the number of nanoparticles on the TEM images significant decreases at higher oven temperature. This might be due to the full depletion of relatively small helium droplets when they pick up sufficient number of Ag atoms, each removing  $\sim 5000$  helium atoms. The consequence is that particles initially formed in those droplets are unable to reach the deposition target. This is also supported by the size distribution in Figure 2- 14 (e), where the count of nanoparticle in the smaller size range (on left wing of the Gaussian profile), is significantly lower than larger nanoparticles on the right wing of the profile.

**Table 2- 2 the sizes and fluxes of Ag nanoparticles measured in different oven temperature.**

No.	T <sub>Ag</sub> (K)	Particle Size (nm)	N/image	Vapour Pressure (mbar)	Vapour Gas Density (atoms/m <sup>3</sup> )
a	876	3.60±1.06	168	5.04×10 <sup>-8</sup>	4.16×10 <sup>14</sup>
b	882	3.79±1.20	167	6.55×10 <sup>-8</sup>	5.38×10 <sup>14</sup>
c	888	3.82±1.20	172	8.49×10 <sup>-8</sup>	6.92×10 <sup>14</sup>
d	902	4.34±1.36	152	1.53×10 <sup>-7</sup>	1.23×10 <sup>15</sup>
E	980	4.41±1.36	110	3.03×10 <sup>-6</sup>	2.24×10 <sup>16</sup>

Following the same protocol, Table 2- 3 outlines the sizes of Ag nanoparticles formed with a constant Ag oven temperature of 980 K, but various source temperatures from 10 K to 6.25 K, which correspond to the helium droplets composed of 10<sup>5</sup> to 5×10<sup>7</sup> He atoms. The deposition rates were measured by use of the thin film deposition monitor.

**Table 2- 3 Ag nanoparticles formed at different Source temperature with the oven temperature maintained at 980 K.**

T <sub>0</sub> (K)	Droplet Size (He atoms)	Particle Size (nm)	N/image	Deposition Rate (×10 <sup>-4</sup> μg/(cm <sup>2</sup> ·s))
10	1×10 <sup>5</sup>	4.11 ± 1.05	110	1.16
9	1.5×10 <sup>6</sup>	4.59 ± 1.16	101	1.33
8.5	3×10 <sup>6</sup>	4.98 ± 1.31	74	1.55
8	7×10 <sup>6</sup>	4.95 ± 1.27	59	1.23
7	1.8×10 <sup>7</sup>	6.36 ± 1.69	19	0.88
6.25	5×10 <sup>7</sup>	6.89 ± 2.3	31	1.86

Three features can be concluded from Table 2- 3 when the source temperature reduces: (i) The particle diameter continuously increases; (ii) The particle number density (N/image) generally decays; (iii) The deposition rate increases but experiences a dip at 8 K and 7 K. To explain these three features, the effect contributed by the balance of cross section and droplet flux should be proposed.

At 10 K, small droplets can be evaporated completely when sufficient numbers of Ag atoms have been added. As the source temperature continues to decrease, the droplet pick-up cross section (hence the effective doping rate) will be increased, more and more droplets can survive after picking up the dopants. Before the droplets become too large when multi-centre growth kicks in, the atoms picked up by the smaller and dispersing droplets are now able to aggregate into one single large nanoparticle in an integral droplet. That is why in this case the deposition rate and particle size increase with the temperature drop but the particle density decreases. When multicentre growth occurs, the atoms aggregates into small nanoparticles first before they reaches the centre of the droplets, *i.e.*, the aggregation time is longer than the time between successive pickup events<sup>(96)</sup>. As a result, smaller nanoparticles will be formed.

Another reason for the decrease of the number density is that the helium droplet velocity is inversely proportional to the droplet size, which can be decelerated from 239 m/s at 10 K to 200 m/s at 7 K<sup>(10, 144)</sup>. That means even without considering the influence of cross section change, the reduced flux will cause a reduction of 18% of the total number of particle deposited at 7 K compared to 10 K – that is about 20 particles fewer in 5 min deposition. This also partially explains why there is a decrease of the deposition rate at 8 K and 7 K in Table 2- 3.

#### **2.3.4 Core-shell Structural Nanoparticles Formation**

When sequentially passing through two pick up cells, helium droplets can serve as a matrix for core-shell structure growth<sup>(33, 52)</sup>, and Ni/Au core-shell nanoparticles have been first obtained which was confirmed by using XPS analysis<sup>(67)</sup>. Figure 2- 15 shows

the TEM image of nanoparticles formed in helium droplets by sequential addition of Ni and Au to the droplets, and XPS analysis on Au 4*f* edge. In principle, there are three possibilities when three different materials are added to helium droplets sequentially: (i) particle dimers; (ii) alloys; (iii) core-shell nanoparticles. The formation of particle dimers can be ruled out directly by TEM image (Figure 2- 15), where pairs of spherical nanoparticles in close vicinity is absent. The second case, alloy nanoparticles, is very unlikely according to the XPS analysis. The peaks in XPS are well correlated to the bonding energy of the electron from specific quantum state, which would be shifted by the surrounding atoms. So if Ni and Au atoms are mixed into alloy, Au 4*f* orbital will be hybridized, leading to a sizeable shift when compared with the corresponding peak of pure Au. However, as seen in Figure 2- 15 (b), the two Au 4*f* peaks in both spectrums, Au 4*f*<sub>7/2</sub> and Au 4*f*<sub>5/2</sub>, are both shifted by about 0.3 eV to the higher binding energy compared to the bulk value of Au due to the charge transfer<sup>(145)</sup>. When compared with the spectrum of Ni/Au nanoparticle, none of the Au 4*f* peaks are shifted relative to each other. Although we cannot completely rule out the possibility of alloy generation at the interface, this observation strongly suggests that core-shell Ni/Au nanoparticles have been formed in helium droplets.

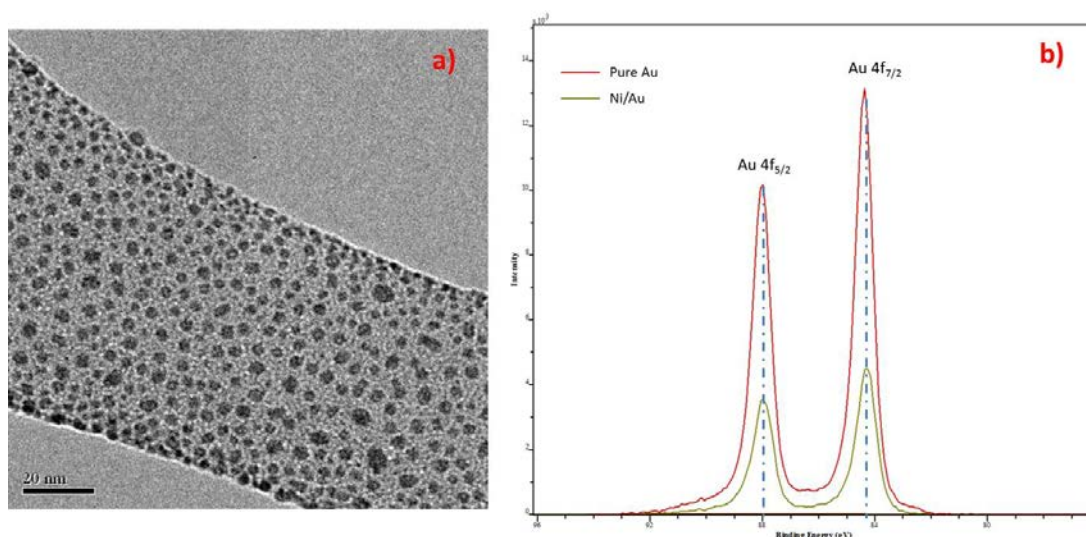


**Figure 2- 15 Evidence for the formation of Ni/Au core-shell structures. (a) TEM image of Ni/Au nanoparticles. (b) Comparison of XPS on the Au 4*f* edge between pure Au and Ni/Au nanoparticles.**

Direct visual evidence that core-shell nanoparticle is formed in the helium droplet is obtained afterwards from the TEM images of Ag/Si nanoparticle, where a high contrast has been obtained due to the remarkable difference in scattering cross sections for Ag and Si. On the TEM substrates Ag offers much higher contrast than Si, allowing core-shell structure to be identified if this does occur. As shown in Figure 2- 16 there is clearly a light Si shell surrounding the dense Ag core.

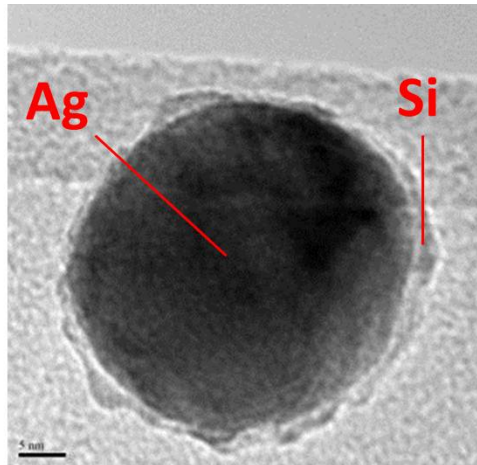


**Figure 2- 16 TEM images of Ag/Si core shell nanoparticles.**

## Chapter 3

# Infra-red Spectroscopy of NaCl/(H<sub>2</sub>O)<sub>n</sub> Complex in Helium Droplets

### 3.1 Introduction

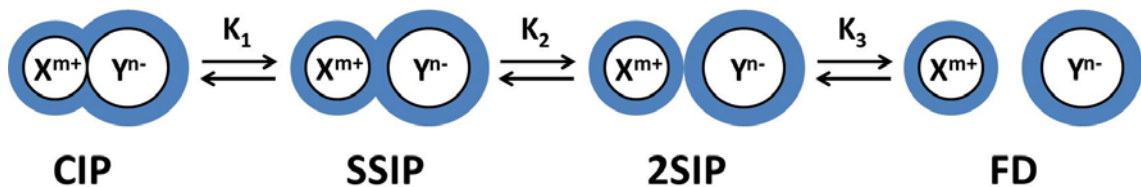
Dissolution of acids, bases and salts in the bulk phase, which leads to the proton transfer and solvation <sup>(146)</sup>, is a basic concept in chemistry. The corresponding generated ion pairs and the surrounded water, *i.e.* the electrolyte solution, play key roles in industrial products (*e.g.* battery industry), bio-chemistry <sup>(147, 148)</sup>, marine and atmosphere chemistry <sup>(149, 150)</sup>. Meanwhile Na<sup>+</sup> and K<sup>+</sup> in the electrolytic solutions in the human body are important in cell signalling mechanisms thus dissolution of salts is the foundation of biochemistry <sup>(147)</sup>. Understanding how and when the dissolution happens is of fundamental interests in chemistry.

The properties of electrolyte solutions, particularly at nanoscale, are challenging to investigate both theoretically and experimentally. From theoretical aspect, it is straightforward to simulate the case of infinitely diluted solution where only ion-solvent interactions need to be concerned as the model potentials <sup>(151)</sup> by computational approaches such as molecular dynamics and Monte Carlo simulations. However this cannot be applied to the concentrated electrolyte solutions which are commonly present in biological system and industrial process. In concentrated solution, ion-ion interaction is a predominant effect that cannot be neglected. Even in a finite concentrated solution, subtle balance between ion-solvent, solvent-solvent and ion-ion interactions should be systematically taken into account in a high quality modelling of aqueous electrolytes because there is a natural tendency for the cations and anions to associate.

A well-known theory describing the dissociation of salt into ion pair is the Eigen-Tamm model <sup>(152)</sup>, in which four states according to the energy minima are proposed.

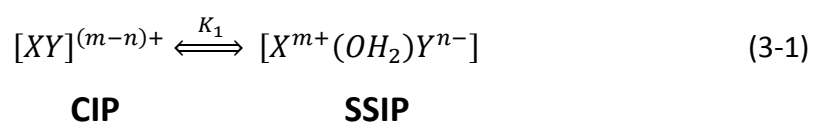
Molecular dynamics and Monte Carlo simulations show that these ion pairs correspond to distinct energy minima but the potential and the barriers separating one state from another depend strongly on the salt and the solvent <sup>(153)</sup>. Taking the simplest salt NaCl as an example, the energy minimum at closest distance of ions is called a contact ion pair (CIP). In this state NaCl remains intact, with a pair of ions surrounded by water molecules. However, the Na-Cl internuclear separation is longer than in the free NaCl molecule because of the effect of hydration. At a longer Na-Cl distance there is a second energy minimum, known as a solvent-separated ion-pair (SSIP), in which water has now inserted between the two ions. A third minimum can sometimes be identified which is known as a doubly-solvent-separated ions pair (2SIP) but this energy well is often very shallow and the difference between this and the fully separated ions may be insignificant for many electrolyte systems. Finally there is a fully dissociated (FD) state where ions are completely separated and surrounded by water.

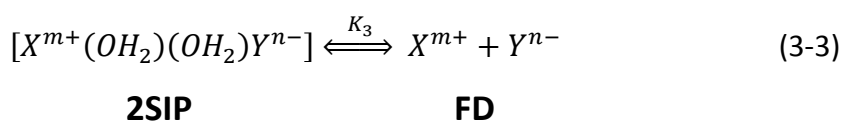
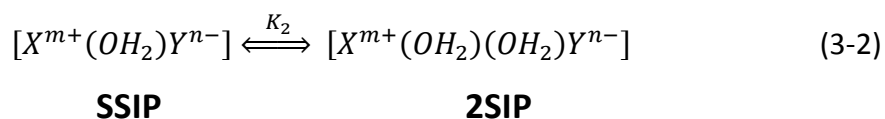
The importance of these four states depends on several factors such as the polarizabilities of the ions and the concentration of the solution. A vivid illustration of these four states is shown in Figure 3- 1, the blue rings surrounding ions of  $X^{m+}$  and  $Y^{n-}$  respectively are water.



**Figure 3- 1 Schematic illustration of four Eigen-Tamm states of the dissociated solution. Reprinted from Ref (154).**

Basically 2SIP means each ion is surrounded by an individual shell of solvent, SSIP means two ions have the shared solvent and CIP means two ions contact with each other without any solvent in between. The dissociation process under Eigen-Tamm mechanism, *i.e.* the process of CIP transferring to FD can be expressed step by step as <sup>(154)</sup>:





X and Y are two types of ions with +m and –n charges, respectively,  $K_1$ ,  $K_2$  and  $K_3$  are called association constants for each step. It is worth mentioning that the  $OH_2$  sandwiched in  $X^{m+}$  and  $Y^{n-}$  on the right side of Equation (3-1) does not mean that there is only one water molecule intervened in the two ions in SSIP state, and the same statement can be applied to the two  $OH_2$  in Equations (3-2) and (3-3).

An alternative means of extracting information relevant to CIPs and SSIPs is to form complexes involving one or more salt-molecules in contact with a small number of water molecules, and instigate the behaviour of small clusters at molecular level. Such systems provide a means for exploring some of the interactions at play in bulk solutions in a controlled environment and the complexes observed may approximate the CIPs and SSIPs occurring in real bulk aqueous solutions. In addition, small complexes are amenable to high quality quantum mechanical calculations.

Taking  $NaCl(H_2O)_n$  as an example, there have been several studies of these complexes using *ab initio* techniques<sup>(155-160)</sup>. These investigations have attempted to explore how the NaCl molecule is affected as water molecules are added, and predict the optimized geometry of the clusters. A particularly important aim has been to establish the number of water molecules required to form a SSIP-like complex, since this represents the onset of ionic dissociation of the solute at molecular level. Calculations have shown that for  $n \leq 5$  the CIP-like complexes are formed while at  $n = 6$ , where six water can form a closed cyclic structure and intervene between  $Na^+$  and  $Cl^-$ , a SSIP structural complex is obtained. CIP-like and SSIP-like complexes become nearly isoenergetic<sup>(157-159)</sup>. On this ground one might expect that heterolytic dissociation into  $Na^+$  and  $Cl^-$  can begin once six water molecules have been added to the complexes.

Although plenty of theoretical predictions on the ion-pair states have appealed, there is a notable lack of experimental information to test the theoretical predictions, in

particular, the direct proof of the individual Eigen-Tamm state <sup>(161)</sup>. The first spectroscopy study on the simplest complex, NaCl(H<sub>2</sub>O) cluster, was reported by Ault <sup>(162)</sup>, who co-deposited NaCl vapour and water molecules into an argon matrix and then recorded the infra-red spectrum. Two bands were observed in the O-H stretching region, which were assigned to the NaCl(H<sub>2</sub>O) complex and a structure was deduced in which the two O-H bonds were equivalent. However, this structure is inconsistent with more recent *ab initio* calculations <sup>(155-157, 159)</sup> which predict that the most stable structure has one O-H bond bound to the NaCl while the other is essentially a dangling (free) O-H bond. More recently, Endo *et al.* studied the microwave spectroscopy on NaCl(H<sub>2</sub>O)<sub>n</sub> clusters (*n* = 1, 2, 3) <sup>(163, 164)</sup>. In their study, NaCl was evaporated by laser ablation, and then mixed with water and argon gases in an adiabatic expansion. According to the increasing separation of Na-Cl bond with the addition of water molecules observed from rotational spectra, CIP state of the complex was assigned. For NaCl(H<sub>2</sub>O)<sub>3</sub> the Na-Cl bond length was found to be no more than 2.8 Å, which is the predicted inter-nuclear distance of CIP structures in an aqueous solution by molecular dynamics simulations. However, to obtain a full picture of the dissociation behaviour of NaCl, *e.g.* to form aSSIP state, three water molecules are insufficient to act as an intervened medium to separate Na<sup>+</sup> and Cl<sup>-</sup>.

The challenge in the experimental study of the dissociation behaviour of NaCl lies in finding a technique that can be applied to dope water molecules one by one and generalize sufficient large NaCl(H<sub>2</sub>O)<sub>n</sub> clusters so that various types of ion-pair complex identified above can be covered, and then the spectra can be recorded. Ideally, this technique should also be able to remove the strong spectroscopic contribution from the pure water clusters.

In this chapter we will tackle this problem by recording the infra-red (IR) spectra of the NaCl(H<sub>2</sub>O)<sub>n</sub> complex in the O-H stretching region. The complexes were formed in the superfluid helium droplets, which can resolve the difficulties mentioned above, and IR spectra with to *n* = 7 have been obtained. To make comparison with the experimental results, we have also performed *ab initio* calculations on NaCl(H<sub>2</sub>O)<sub>n</sub> clusters.

### 3.2 Method

The experimental set-up is sketched in Figure 3- 2. Helium gas of stagnation pressure of 30 bar is pre-cooled to 16 K and then expanded into the ultra-high vacuum, leading to the formation of droplets composed of  $\sim 5000$  helium atoms on average. After passing through the skimmer, the droplets beam sequentially passes through two cells. The first is an oven cell containing NaCl and the second is water pick-up cell. The oven is resistively heated to a temperature of 445 °C, producing molecular NaCl. Water has been de-gased before use. The partial pressure in the pickup cell is around  $10^{-6}$  mbar which can be controlled by a needle valve. By this means  $(\text{NaCl})_m(\text{H}_2\text{O})_n$  complexes can be formed in helium droplets and the abundance of specific cluster ion can be optimized by the partial pressures.

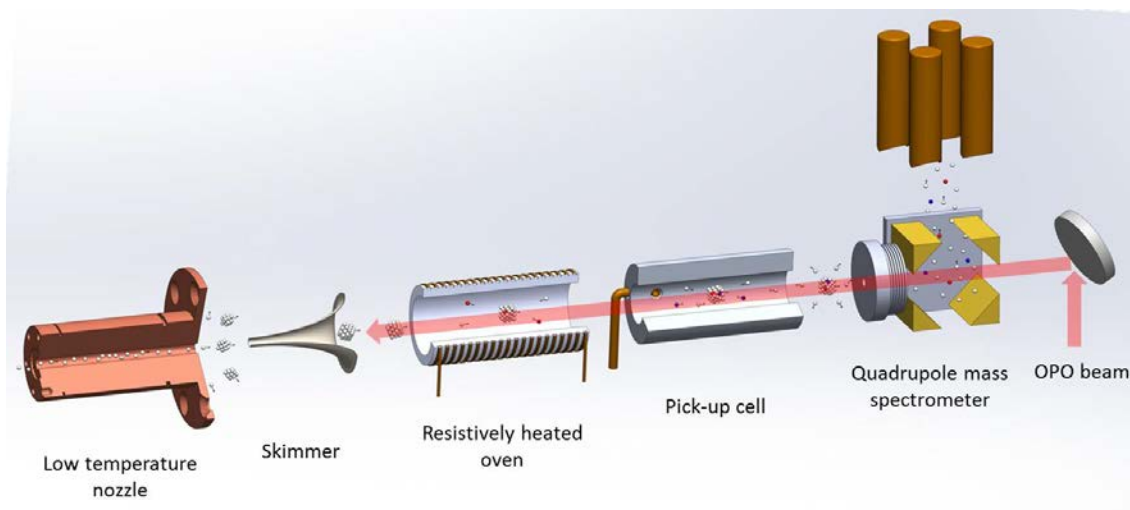


**Figure 3- 2 Experimental set-up for the depletion spectroscopy on  $\text{NaCl}(\text{H}_2\text{O})_n$  clusters doped in helium droplets.**

Infrared (IR) spectra of the  $\text{NaCl}(\text{H}_2\text{O})_n$  complex were recorded in the O-H stretching region, and we measure the depletion spectrometry focusing on  $\text{Na}^+$ -containing ion channels. By this means we can avoid the strong and broad absorption bands expected from the pure water clusters. This is an important advantage compared with the previous studies on  $\text{HCl}(\text{H}_2\text{O})_n$  clusters in helium droplets<sup>(90)</sup>, which produces  $\text{H}^+(\text{H}_2\text{O})_n$ . Therefore mass selection cannot eliminate the contribution from pure water clusters.

To measure IR spectra an OPO/OPA laser system with a tuneable wavelength that can cover the full range of the O-H stretching vibration modes has been employed. The laser beam was aligned anti-parallel to the helium beam and was focused just in front of the water pick-up cell to maximize the overlapping with the helium droplet beam. The complexes were then ionized through a charge transfer mechanism, *i.e.*, a  $\text{He}^+$  ion is first produced by electron impact, which then transfers its charge to the dopants if they can meet within some  $\sim 10$  hops. A specific ion channel is then selected and detected by the quadrupole mass spectrometer (QMS). The absorption of photons at vibrational frequencies of the complexes is then registered as the reduction of helium droplet size, thus the depletion spectra are obtained. Electron impact energy of the QMS is set to 90 eV to get optimized ion intensity.

To support the experimental work *ab initio* calculations were carried out on  $\text{NaCl}(\text{H}_2\text{O})_n$  complexes. The aim was to try and find as many energy minima as possible and to predict the resulting infrared spectra in each case. The calculations were performed at the MP2 level of theory and employed aug-cc-pVTZ basis sets. A scaling factor of 0.96 was applied to the O-H stretching harmonic vibrational frequencies, a value which accounts for the substantial anharmonicity of these modes<sup>(159)</sup>. The search for energy minima was carried out by performing geometry optimizations using a variety of initial structures. Once a minimum was found, vibrational frequencies were then calculated, as well as the intensities to establish it as a true minimum rather than a saddle point. The procedure used for finding possible minima is neither a systematic nor particularly sophisticated way of searching the potential energy landscape. Consequently, it is certainly possible that some minima were not found using this procedure, although we think that is unlikely for the smaller complexes ( $n \leq 3$ ) considered in this study. Due to computational limitations the calculations were restricted to complexes with  $n \leq 6$ . All the optimized calculation results are comparable with Ref. (158).

### 3.3 Results and Discussion

#### 3.3.1 Mass Spectra of $(\text{NaCl})_m(\text{H}_2\text{O})_n^+$ Clusters in HeDs

First we record mass spectra of the NaCl-H<sub>2</sub>O binary cluster to inspect the pick-up condition in helium droplets, as shown in Figure 3- 3. Two ion series are predominant in the mass spectrum, highlighted as  $\text{H}_3\text{O}^+(\text{H}_2\text{O})_n$  and  $\text{Na}^+(\text{H}_2\text{O})_n$ . Ion series containing more than one Na atom, *i.e.*  $\text{Na}_m^+(\text{H}_2\text{O})_n$  ( $m > 1$ ), are negligible in the mass spectrum because we have deliberately avoided the pickup of multiple NaCl molecules in the droplets. Other expected ion series, such as  $(\text{NaCl})_n^+$  and  $\text{NaCl}(\text{H}_2\text{O})_n^+$  are always less compared to the two highlighted series no matter how we regulate the doping rates of salt and water. It is known that the evaporation of NaCl at the current temperature in use produces almost exclusively intact NaCl molecules in the vapour phase, with negligible production of sodium atoms vapour<sup>(165)</sup>. Therefore the  $\text{Na}^+(\text{H}_2\text{O})_n$  ions are fragments from the ionization of  $\text{NaCl}(\text{H}_2\text{O})_m$  complexes in helium droplets, where  $m \geq n$ . In order to get a promising spectral quality, specific ion signal can be regulated by controlling the water doping rate.

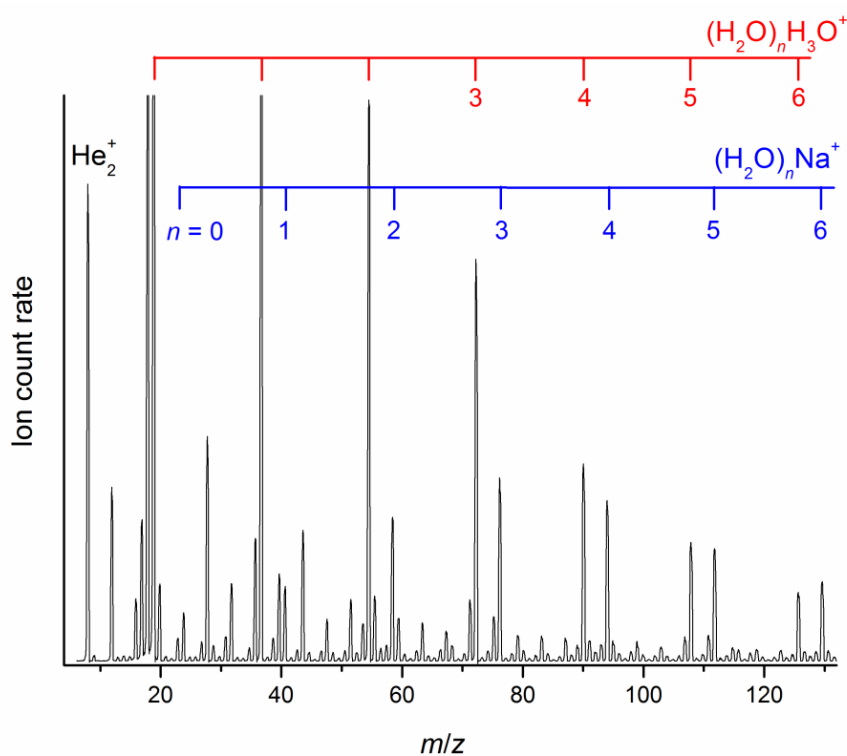


Figure 3- 3 Mass spectrum of helium droplets doped with NaCl and H<sub>2</sub>O molecules.

### 3.3.2 Infra-red Spectroscopy of Pure Water Clusters

Since our aim is to investigate the influence of water to NaCl, we first recorded the pure water IR spectrum in O-H stretching region as a reference when the salt oven was switched off and the water pick-up was tuned at maximal hexamer signal so that a reasonable water clusters distribution can be observed in the mass spectrum. Figure 3-4 shows all the O-H stretching bands from clusters  $(\text{H}_2\text{O})_n$  ( $n = 1 - 6$ ). This spectrum was recorded at  $\text{He}_2^+$  channel, which has contribution from all the water clusters picked up by helium droplets.

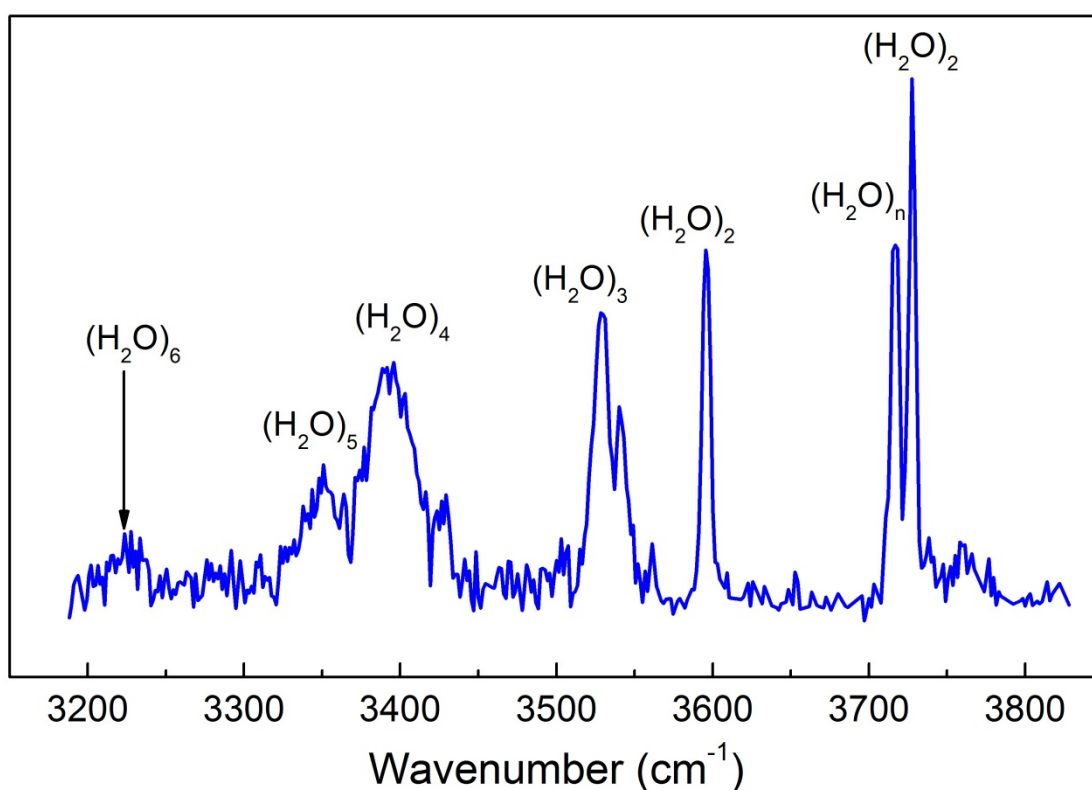


Figure 3- 4 Pure water IR spectrum recorded at helium dimer channel ( $m/z = 8$ ).

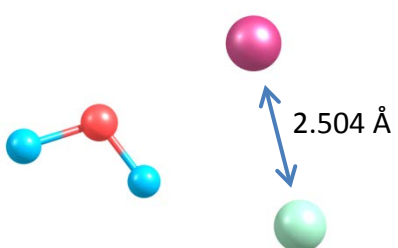
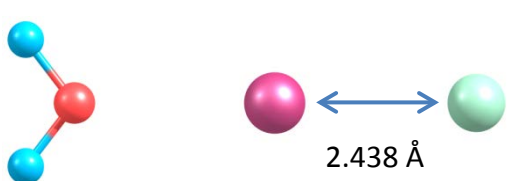
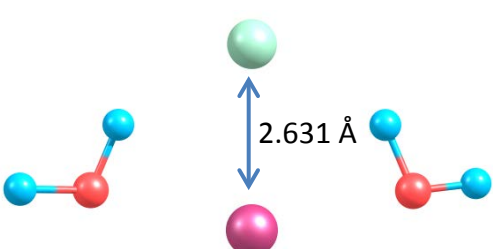
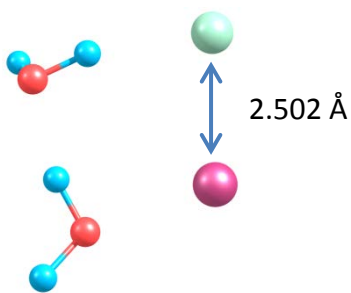
As seen in Figure 3- 3, the protonated ions are prominent, and each protonated ion is produced from larger clusters, for example,  $(\text{H}_3\text{O})^+$  ( $m/z = 19$ ) has to be generated from water dimer or larger clusters and  $(\text{H}_3\text{O})^+(\text{H}_2\text{O})$  ( $m/z = 37$ ) is from water trimer or larger clusters. Therefore we can assign these peaks via a “mass selection” protocol, *i.e.* by successively scanning the IR spectrum on the protonated ion channel like  $m/z = 19, 37$ ,

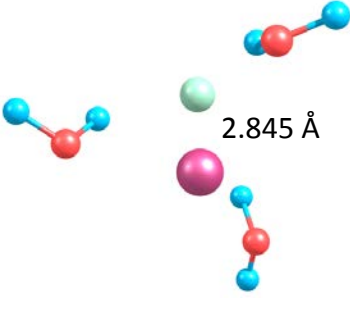
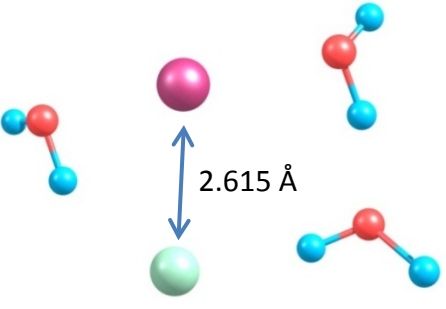
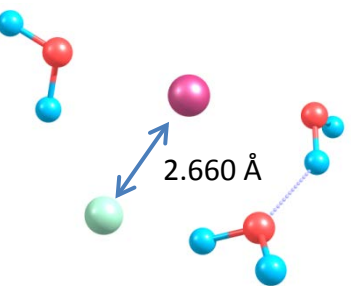
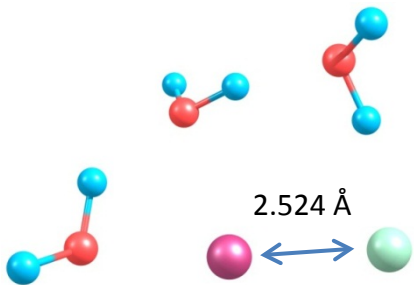
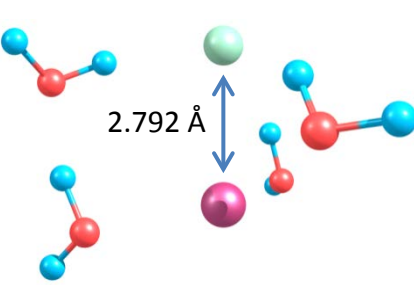
55 etc.. The peaks that disappear at higher mass channels must be attributed to the smaller water clusters. By this protocol we can assign the peaks in the spectra one by one if high-quality spectra can be obtained at higher mass ion channels. The peak assignment was also compared with the previous study on water clusters doped in helium droplets <sup>(60, 166)</sup>, and as marked in the Figure 3- 4, as well as *ab initio* calculations. The peaks located at 3792 cm<sup>-1</sup> and 3717 cm<sup>-1</sup> in the spectrum are known to arise from the free O-H stretch from (H<sub>2</sub>O)<sub>2</sub> and (H<sub>2</sub>O)<sub>n</sub> clusters respectively. The band assignments of (H<sub>2</sub>O)<sub>2</sub> to (H<sub>2</sub>O)<sub>6</sub> in the wavenumber range of 3260 – 3190 cm<sup>-1</sup> derive from the bonded O-H stretch of the clusters. The assignment shown in Figure 3- 4 provides a good reference to the IR spectrum when NaCl is added. Surprisingly we could not see any contribution from water monomer, which is possibly due to the very lower abundance of the water monomer in helium droplets.

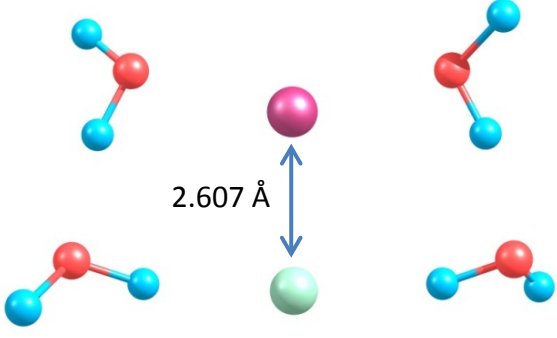
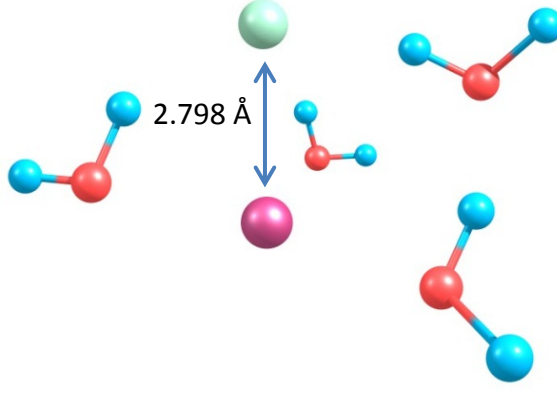
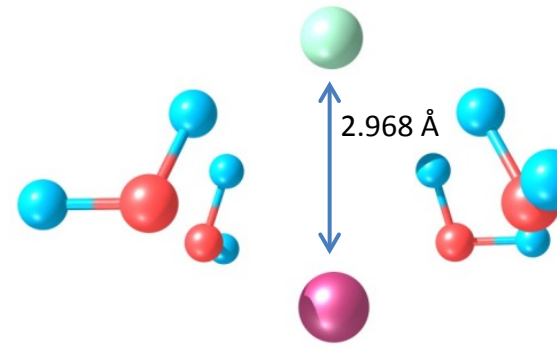
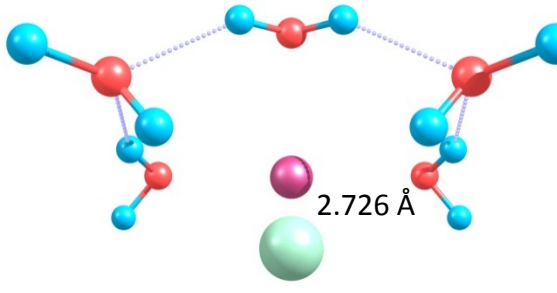
### **3.3.3 Calculation Results of NaCl(H<sub>2</sub>O)<sub>n</sub><sup>+</sup> Complex (n = 1 – 6)**

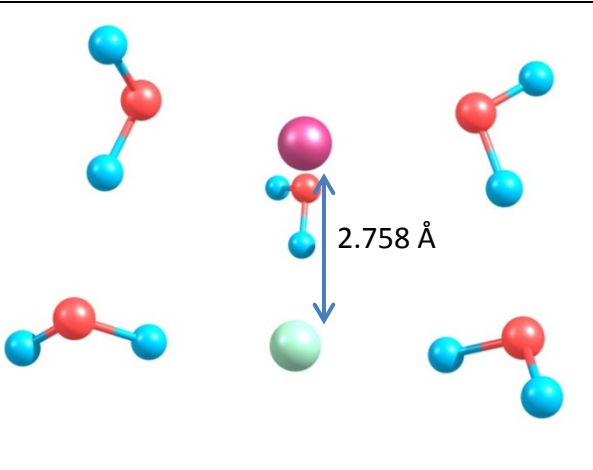
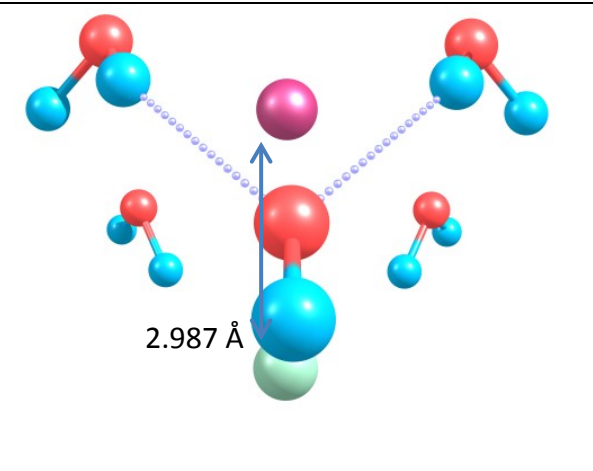
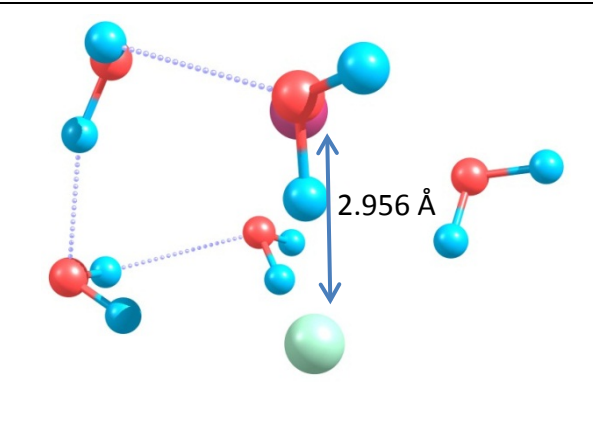
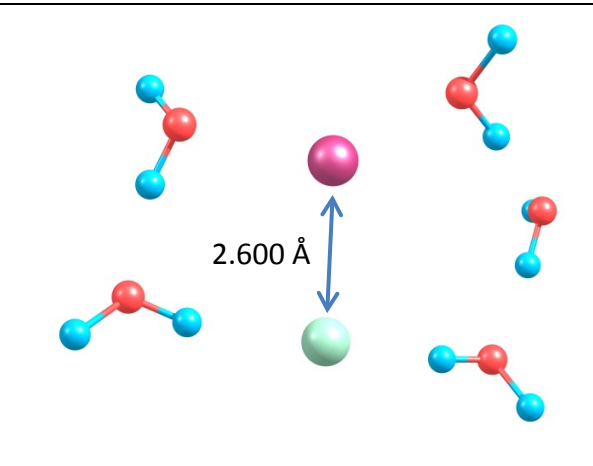
We start with presenting the global and local potential energy minima calculation we found for NaCl(H<sub>2</sub>O)<sub>n</sub> for n = 1 – 6. As expected there are some strong similarities of our findings with those from earlier calculations <sup>(155-159, 162)</sup>. The structures obtained including the Na – Cl separations, their relative energies and the frequencies contained are summarized in Table 3- 1. The number in the bracket in the last column is the intensity and the number highlighted in bold are those that have been assigned to the observed bands in the spectra. For small clusters (n ≤ 3), we are confident of finding all the possible structures existing in helium droplets since all the bands in the corresponding IR spectra can be well assigned to our calculated isomers, as will be discussed in details later. For large clusters (3 < n ≤ 6), too many potential structures can exist in helium droplets simultaneously since the significant broad bands observed in spectra, as will be shown in the later section. It is almost an impossible task to identify all the discrete bands in those broad features and certainly our limited calculation results cannot cover all the local minimum structures.

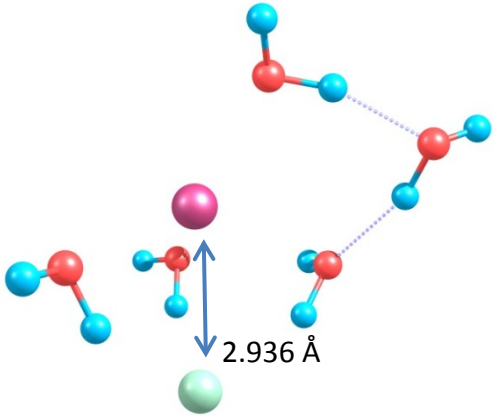
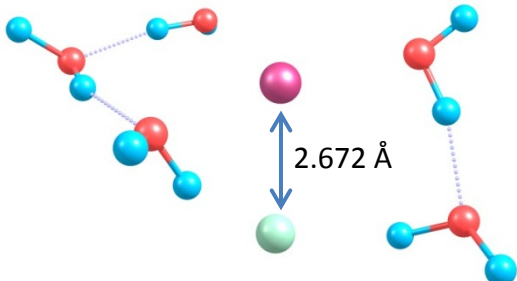
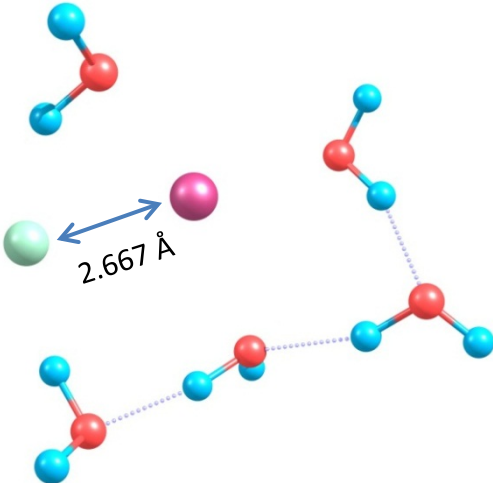
**Table 3- 1 Optimized geometry for NaCl(H<sub>2</sub>O)<sub>n</sub> (1 ≤ n ≤ 6) complexes including their Na – Cl separations, together with their relative energy to the global minimum structure, intensities and transition frequencies.**

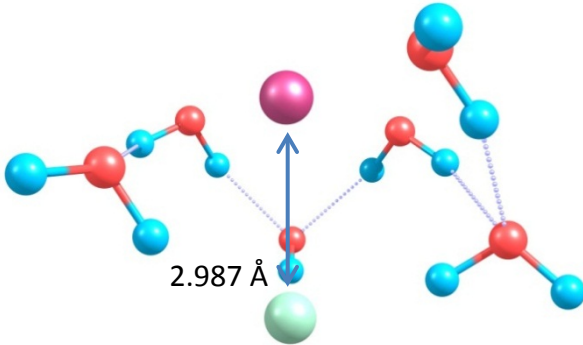
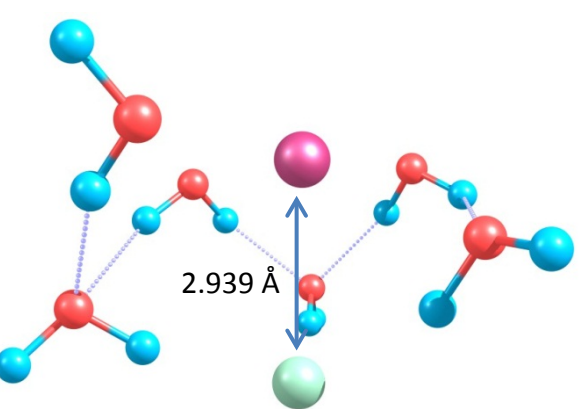
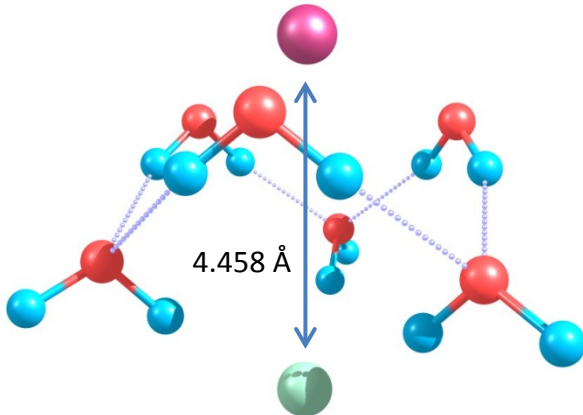
Molecule	Optimised Structure (Na pink, Cl green)	Relative Energy / eV	Frequencies / cm <sup>-1</sup> (Intensity)
NaCl(H <sub>2</sub> O)		0.00	<b>3266 (787)</b> 3758 (92)
		0.24	3720 (177) 3764 (131)
NaCl(H <sub>2</sub> O) <sub>2</sub>		0.00	<b>3307 (914)</b> <b>3335 (566)</b> 3760 (148) 3761 (37)
		0.05	<b>3132 (1122)</b> <b>3229 (979)</b> 3731 (88) 3764 (77)

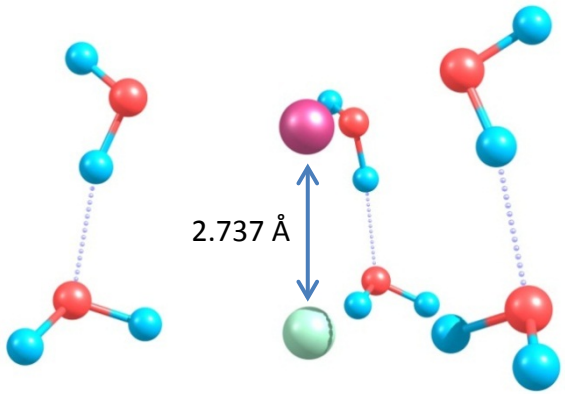
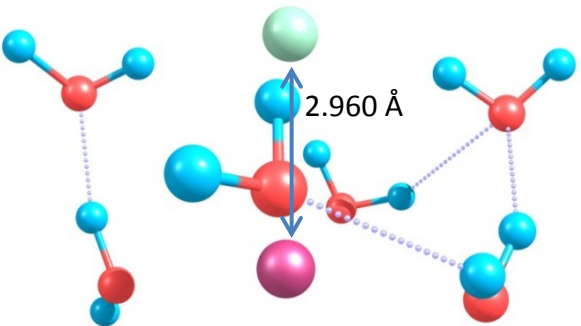
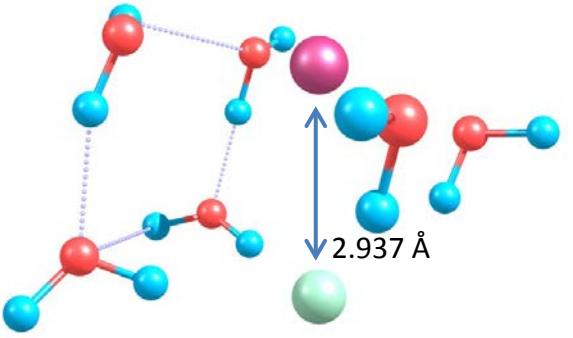
NaCl(H <sub>2</sub> O) <sub>3</sub>		0.00	<b>3330 (655)</b> <b>3330 (655)</b> <b>3367 (768)</b> 3751 (119) 3751 (119) 3753 (26)
		0.05	<b>3183 (992)</b> <b>3284 (1094)</b> <b>3374 (529)</b> 3730 (97) 3759 (88) 3762 (72)
		0.08	<b>3184 (1132)</b> <b>3341 (679)</b> <b>3488 (393)</b> 3739 (95) 3758 (96) 3759 (86)
		0.19	<b>3043 (1324)</b> <b>3165 (1130)</b> 3547 (301) 3731 (87) 3735 (75) 3764 (101)
NaCl(H <sub>2</sub> O) <sub>4</sub>		0.00	<b>3231 (869)</b> <b>3325 (1018)</b> <b>3381 (561)</b> <b>3405 (544)</b> 3730 (101) 3753 (105) 3753 (64) 3761 (70)

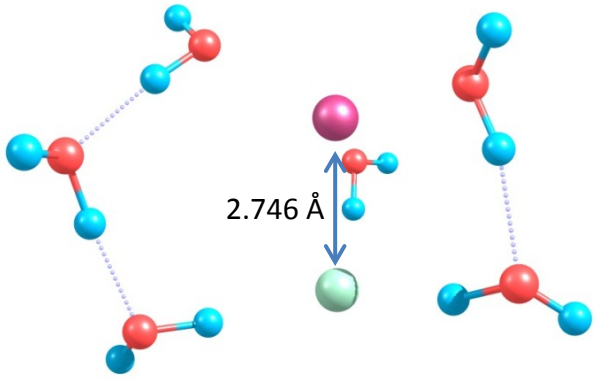
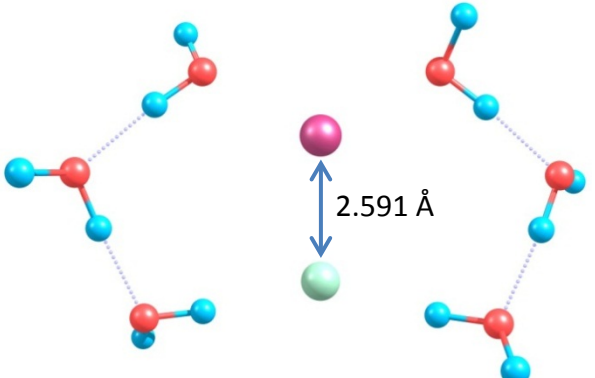
		0.01	<b>3212 (303)</b> <b>3230 (1749)</b> <b>3314 (1499)</b> <b>3339 (114)</b> 3730 (148) 3732 (47) 3760 (74) 3762 (63)
		0.02	<b>3250 (965)</b> <b>3345 (695)</b> <b>3396 (598)</b> <b>3436 (465)</b> 3718 (88) 3732 (106) 3755 (82) 3757 (76)
		0.05	<b>3405 (4)</b> <b>3408 (630)</b> <b>3408 (631)</b> <b>3450 (699)</b> 3733 (145) 3733 (139) 3733 (7) 3734 (64)
NaCl(H <sub>2</sub> O) <sub>5</sub>		0.00	<b>3146 (1284)</b> <b>3193 (774)</b> <b>3437 (26)</b> <b>3437 (934)</b> 3557 (118) 3635 (390) 3729 (105) 3729 (85) 3749 (132) 3749 (13)

		0.01	<b>3264 (319)</b> <b>3280 (1447)</b> <b>3347 (936)</b> <b>3366 (663)</b> <b>3438 (441)</b> 3733 (138) 3734 (65) 3755 (77) 3755 (58) 3756 (84)
		0.01	<b>3249 (952)</b> <b>3314 (693)</b> <b>3348 (644)</b> <b>3523 (209)</b> <b>3543 (315)</b> 3700 (115) 3703 (226) 3729 (98) 3741 (52) 3742 (93)
		0.10	<b>3361 (512)</b> <b>3374 (240)</b> <b>3383 (629)</b> <b>3419 (793)</b> <b>3518 (279)</b> 3683 (194) 3687 (68) 3730 (95) 3739 (75) 3749 (97)
		0.12	<b>3168 (1069)</b> <b>3234 (1378)</b> <b>3252 (1015)</b> <b>3320 (1178)</b> <b>3343 (231)</b> 3731 (125) 3733 (79) 3737 (76) 3760 (105) 3760 (30)

		0.13	<b>3268 (646)</b> <b>3308 (1008)</b> <b>3356 (685)</b> <b>3372 (731)</b> <b>3445 (488)</b> 3693 (94) 3739 (79) 3749 (117) 3754 (80) 3758 (78)
		0.15	<b>3136 (1311)</b> <b>3237 (1010)</b> <b>3315 (746)</b> <b>3343 (755)</b> <b>3434 (498)</b> 3727 (65) 3734 (100) 3747 (111) 3751 (79) 3760 (66)
		0.24	<b>3083 (1329)</b> <b>3214 (1150)</b> <b>3370 (515)</b> <b>3398 (601)</b> <b>3450 (534)</b> 3718 (66) 3734 (86) 3749 (116) 3754 (87) 3760 (83)

NaCl(H <sub>2</sub> O) <sub>6</sub>		0.00	<b>3234 (1037)</b> <b>3283 (782)</b> <b>3366 (536)</b> <b>3453 (477)</b> <b>3533 (199)</b> <b>3556 (184)</b> <b>3636 (371)</b> <b>3683 (227)</b> 3730 (111) 3731 (98) 3742 (66) 3752 (76)
		0.01	<b>3228 (1089)</b> <b>3283 (766)</b> <b>3386 (513)</b> <b>3446 (486)</b> <b>3533 (205)</b> <b>3557 (187)</b> <b>3641 (359)</b> <b>3687 (214)</b> 3728 (106) 3730 (98) 3740 (71) 3753 (74)
		0.02	<b>3147 (938)</b> <b>3147 (938)</b> <b>3223 (996)</b> <b>3482 (110)</b> <b>3482 (110)</b> <b>3500 (440)</b> <b>3530 (0)</b> <b>3562 (785)</b> <b>3562 (785)</b> 3722 (133) 3722 (133) 3724 (2)

	 <p>2.737 Å</p>	0.06	<b>3289 (185)</b> <b>3296 (522)</b> <b>3316 (1955)</b> <b>3375 (804)</b> <b>3377 (1066)</b> <b>3402 (38)</b> 3733 (178) 3733 (47) 3735 (83) 3754 (86) 3755 (48) 3761 (63)
	 <p>2.960 Å</p>	0.08	<b>3321 (744)</b> <b>3354 (665)</b> <b>3378 (1046)</b> <b>3407 (227)</b> <b>3518 (292)</b> <b>3581 (137)</b> <b>3663 (95)</b> <b>3671 (296)</b> 3732 (140) 3738 (60) 3740 (108) 3748 (72)
	 <p>2.937 Å</p>	0.09	<b>3243 (722)</b> <b>3316 (731)</b> <b>3446 (491)</b> <b>3473 (524)</b> <b>3489 (457)</b> <b>3492 (222)</b> <b>3648 (158)</b> <b>3696 (159)</b> 3729 (114) 3738 (77) 3740 (64) 3744 (92)

		0.15	<b>3217 (957)</b> <b>3285 (1107)</b> <b>3295 (925)</b> <b>3355 (852)</b> <b>3370 (649)</b> <b>3447 (405)</b> 3734 (159) 3735 (48) 3740 (83) 3753 (102) 3754 (49) 3756 (66)
		0.24	<b>3175 (98)</b> <b>3189 (2394)</b> <b>3259 (2159)</b> <b>3267 (203)</b> <b>3326 (861)</b> <b>3351 (321)</b> 3733 (122) 3736 (90) 3737 (89) 3738 (61) 3758 (77) 3758 (56)

For the simplest complex,  $\text{NaCl}(\text{H}_2\text{O})$ , two structures were identified. The global minimum has the O atom interacting with the Na atom, and one of the H atoms forms an ionic hydrogen bond (IHB) with Cl. The other structure is a  $C_{2v}$  structure which no longer has the IHB link and this isomer has considerably higher energy (by 0.24 eV) than the global minimum.

With two or more water molecules hydrogen bonds can be formed between water molecules. However, for both  $\text{NaCl}(\text{H}_2\text{O})_2$  and  $\text{NaCl}(\text{H}_2\text{O})_3$  the global minima are essentially the extended structures from  $\text{NaCl}(\text{H}_2\text{O})$ , but with two and three IHB linkages, respectively. In these structures, which have  $C_2$  and  $C_3$  point group symmetries, there is no hydrogen bonding between water molecules. As noted in previous studies<sup>(155-159)</sup>, the Na-Cl bond length progressively increases from 2.504 Å for

$n = 1$  to  $2.845 \text{ \AA}$  for  $n = 3$ . The expectation from molecular dynamics simulations is that the CIP complex in a bulk aqueous solution has a Na-Cl bond length of  $\sim 2.8 \text{ \AA}$  <sup>(160, 167, 168)</sup>. Thus on this ground the  $\text{NaCl}(\text{H}_2\text{O})_3$  complex resembles a CIP complex. For  $\text{NaCl}(\text{H}_2\text{O})_2$  there is an isomer with  $0.05 \text{ eV}$  energy above the global minimum which has a hydrogen bond between the water molecules. For  $\text{NaCl}(\text{H}_2\text{O})_3$  we have found three such local minima with different degrees of inter-water hydrogen bonding.

As more water molecules are added the potential energy landscape becomes more complex. For  $n \geq 4$  some degree of hydrogen bonding between water molecules is unavoidable. We are particularly interested in finding SSIP structures of  $\text{NaCl}(\text{H}_2\text{O})_n$  complexes where the  $\text{Na}^+$  and  $\text{Cl}^-$  have essentially separated. We have been unable to find such minima for  $n = 4$  and  $n = 5$  but an SSIP isomer was found for  $n = 6$ , whose structure agrees with previous theoretical studies of  $\text{NaCl}(\text{H}_2\text{O})_n$  complexes <sup>(157-159)</sup>. The SSIP complex calculated in this work consists of  $\text{Na}^+$  and  $\text{Cl}^-$  ions on opposite faces of a cyclic water hexamer with an ion-ion separation of  $4.458 \text{ \AA}$ . The total energy of this isomer is marginally above (by  $0.02 \text{ eV}$ ) the global potential energy minimum, which is a CIP-like complex. In addition we have found another CIP-like complex only  $0.01 \text{ eV}$  above the global minimum and a total of five CIP-like minima within  $0.1 \text{ eV}$  of the global minimum, as seen in the table.

### **3.3.4 Infra-red Spectroscopy of $\text{NaCl}(\text{H}_2\text{O})_n^+$ Complex ( $n = 1 - 3$ )**

To experimentally investigate NaCl dissolution in water, we first consider the IR spectra of the  $n = 1 - 3$  of the  $\text{Na}(\text{H}_2\text{O})_n^+$  complexes, with mass/charge ratios of 41, 59 and 77, respectively, in the mass spectrum. The spectra obtained in the O-H stretching region are shown in Figure 3- 5, together with the global minimum structure for each complex. The predicted bands of the global minimum structures are also displayed beneath the spectra. It is important to note that IR spectra of  $n = 1 - 3$  complexes are distinct from each other. If some water loss occurred on ionization then one could expect some contribution from the  $\text{NaCl}(\text{H}_2\text{O})_{n+1}$  complex to the depletion signal recorded in the  $\text{Na}^+(\text{H}_2\text{O})_n$  channel. However, the fact that such signals are not seen suggest that at least for small complex, the loss of the Cl atom is able to prevent

further fragmentation by loss of one or more water molecules. For this reason we attribute the IR spectra recorded by detecting the  $\text{Na}^+(\text{H}_2\text{O})$ ,  $\text{Na}^+(\text{H}_2\text{O})_2$  and  $\text{Na}^+(\text{H}_2\text{O})_3$  ions to the neutral complexes  $\text{NaCl}(\text{H}_2\text{O})$ ,  $\text{NaCl}(\text{H}_2\text{O})_2$  and  $\text{NaCl}(\text{H}_2\text{O})_3$ , respectively. These assignments are further supported by more detailed analysis and the predictions from *ab initio* calculations, as will be detailed below.

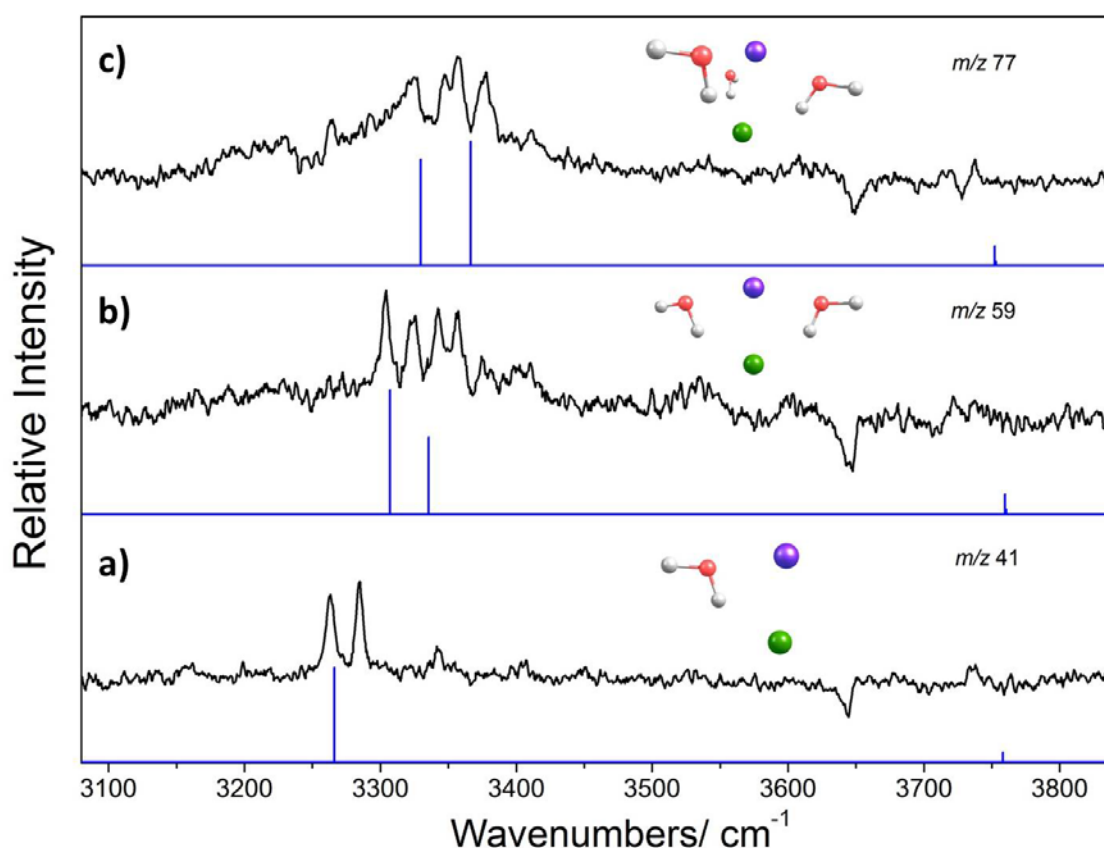


**Figure 3- 5** Infrared depletion spectra recorded for (a)  $m/z$  41, (b)  $m/z$  59 and (c)  $m/z$  77. Also shown are the predicted global minimum energy structures. The blue stick beneath the IR spectra is the calculation results, which mark the corresponding frequencies predicted by the global minima structures. Note that doublers are observed in the depletion spectra because of Fermi resonance.

For two predicted  $\text{NaCl}(\text{H}_2\text{O})$  structures shown in Table 3- 1, the  $C_{2v}$  structure isomer, which is 0.24 eV above the global minimum, can be ruled out according to the spectrum. In this structure neither O-H group undergoes hydrogen bonding, which would deliver two free O-H bands near  $3700\text{ cm}^{-1}$ . This is dramatically different from the observed IR spectrum. In addition due to its relative high energy compared to the

global minimum structure, this  $C_{2v}$  structure isomer is unlikely to be formed in the helium droplets.

For the global minimum isomer there are two distinct O-H bonds, with one dangling O-H bond and the other forming an ionic hydrogen bond (IHB) with the chloride ion. It can be seen that the NaCl(H<sub>2</sub>O) spectrum is featured by a doublet between 3250 and 3300 cm<sup>-1</sup> with almost equal intensities. These peaks are strongly red-shifted from the O-H stretching frequencies of the free water molecule, indicating that they arise from the O-H bond involved in the formation of an ionic hydrogen bond. As illustrated in the shown in Table 3- 1, it is the formation of an IHB link to the chloride ion that is responsible. This agrees with previous observation on anionic complexes between water and halide ions in the absence of the Na<sup>+</sup> counterion <sup>(169-171)</sup>, where the IHB interactions between a halide and the O-H bond result in intense red-shift. In contrast, the other O-H stretching vibration, *i.e.* the free O-H stretch, is similar to its value in free water molecules, which can be assigned to the peak appearing at around 3742 cm<sup>-1</sup>.

The observed IHB stretching bands in small water clusters are in excellent agreement with the *ab initio* prediction, as shown in Figure 3- 5 (a). The fact that we see two bands rather than one was explained elsewhere and is attributed to a Fermi resonance between the bending overtone mode ( $2\nu_2$ ) of H<sub>2</sub>O and the IHB stretching fundamental <sup>(169)</sup>. The predicted bending mode appears at 1641 cm<sup>-1</sup> thus  $2\nu_2 = 3282$  cm<sup>-1</sup>. Therefore the observed two peaks are in decent agreement with the Fermi resonance criteria in term of:  $\nu^+ - \nu^- = \nu_0^+ - \nu_0^-$ , where  $\nu^+$  and  $\nu^-$  are the frequencies of two perturbed (experimental observed) peaks as a consequence of Fermi resonance, equals 3300 cm<sup>-1</sup> and 3250 cm<sup>-1</sup>, and  $\nu_0^+$  and  $\nu_0^-$  are two original unperturbed (calculation predicted) bands, locating at 3282 cm<sup>-1</sup> and 3266 cm<sup>-1</sup>, respectively. The  $2\nu_2$  and  $\nu_{\text{IHB}}$  vibrations are heavily mixed since the two strong peaks have almost equal intensities.

We can readily extend this interpretation to the IR spectra of NaCl(H<sub>2</sub>O)<sub>2</sub> and NaCl(H<sub>2</sub>O)<sub>3</sub>. For NaCl(H<sub>2</sub>O)<sub>2</sub> the spectrum is featured by a series of four peaks, all with similar intensities. The calculated lowest energy structure has  $C_2$  point group symmetry with the two water molecules on essentially opposite sides of the NaCl. Symmetric and

antisymmetric combinations of the two  $\text{OH}_{\text{IHB}}$  stretches are expected in  $\text{NaCl}(\text{H}_2\text{O})_2$  and MP2 calculations predict a splitting of *ca.*  $35 \text{ cm}^{-1}$  between these two vibration modes, see Figure 3- 5 (b). Experimentally we see four rather than two bands in the  $\text{OH}_{\text{IHB}}$  region, suggesting that Fermi resonance with the water bending overtone mode occurs as in the case of  $\text{NaCl}(\text{H}_2\text{O})$ . Theory predicts that the  $\text{OH}_{\text{IHB}}$  bands are moderately blue-shifted as more water is added to the  $\text{NaCl}(\text{H}_2\text{O})_n$  clusters, a finding confirmed by experiment. The free O-H stretch of this complex is predicted to be very weak for the global minimum structure.

The spectrum shown in Figure 3- 5 (c) from  $\text{NaCl}(\text{H}_2\text{O})_3$  is further blue-shifted and consists of four bands. The series of spectra shown in Figure 3- 5 derive from CIP-like structures where the NaCl remains intact and there is limited interaction between the water molecules. This is in agreement with the structures for the  $n = 1 - 3$  complexes previously identified from microwave spectroscopy<sup>(163, 164)</sup>. In addition to the relatively sharp and prominent  $\text{OH}_{\text{IHB}}$  bands there are also some weaker, broader features in the spectra for  $n = 2$  and 3. These additional bands may indicate contributions from higher energy isomers containing hydrogen bonds between water molecules, leading to broader spectral features.

Also in Figure 3- 5, a sharp negative-going peak at  $3650 \text{ cm}^{-1}$  can also be observed in spectrum at each mass channel, which means these ions get their abundance enhanced at that specific frequency. This can be explained as part of the small complex ( $n \leq 3$ ) are from the fragmentation of  $\text{NaCl}(\text{H}_2\text{O})_4$  ions when this O-H band is excited, the experimental proof is shown in Figure 3- 6 (a) in the next section.

### **3.3.5 Infra-red Spectroscopy of $\text{NaCl}(\text{H}_2\text{O})_n^+$ Complex ( $n = 4 - 7$ )**

The IR spectra of the larger ( $n = 4 - 7$ ) complexes corresponding to the mass to charge ratio of 95, 113, 131 and 149, respectively, are distinctly different from the smaller ( $n = 1 - 3$ ) complexes, as can be seen in Figure 3- 6. Whereas the smaller complexes contained discrete and relatively narrow bands, in particular, for  $n = 1$  and 2, broad features dominate these larger complexes. There is also a blue shift in the band structure as more water molecules are added. One of the obvious features from Figure

3- 6 (a) is the band at  $3650\text{ cm}^{-1}$  turns into depletion peak for  $\text{NaCl}(\text{H}_2\text{O})_4$  ions (as shown in the blue circle); whereas for  $\text{NaCl}(\text{H}_2\text{O})_n^+$  ( $n = 1 - 3$ ) this band presents as the enhancement peak. This suggests this stretching mode is originally from  $\text{NaCl}(\text{H}_2\text{O})_4^+$ , which is fragmented by the electron impact and generate more abundant small clusters. The possibility is that an isomer of  $\text{NaCl}(\text{H}_2\text{O})_4$  can lose water and Cl during the charge transfer ionization when excited by photons at  $3650\text{ cm}^{-1}$ .

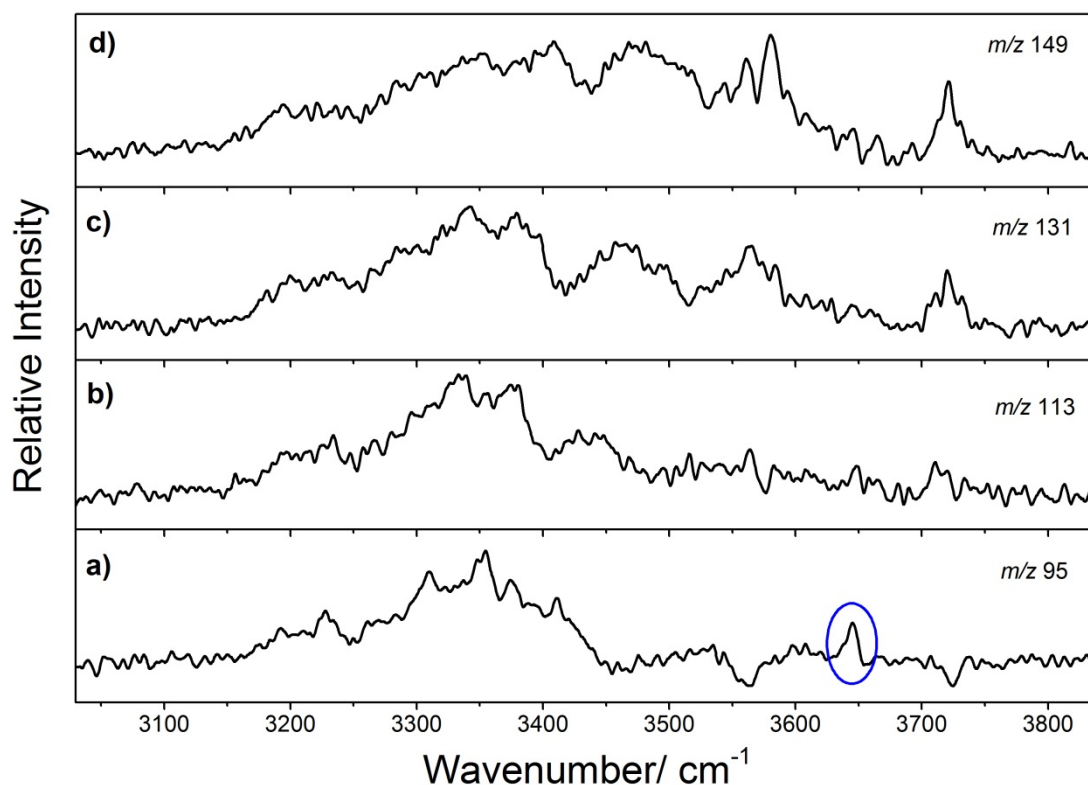


**Figure 3- 6** Depletion spectra recorded at (a)  $m/z$  95, (b)  $m/z$  113, (c)  $m/z$  131 and (d)  $m/z$  149.

*Ab initio* calculations of the larger complexes provide relatively limited assistance in interpreting the spectra. No single isomer has a simulated spectrum that matches the observed spectra. This may indicate that several different isomers co-exist which contribute to the experimental spectra. On the other hand, anharmonic behaviours, including combination bands, overtones and Fermi resonance, are known to invoke additional bands for the small complex spectra. Therefore it is a fair speculation that anharmonic may significantly influence the larger complexes and further complicate the spectra. For these reasons we opt for a more qualitative interpretation of the

spectra based on the types of OH bonds likely to be present in the complexes. These bonds can be classified into four types based on their expected stretching frequencies: (i) free OH stretches near to  $3700\text{ cm}^{-1}$ , (ii) double donor (DD) stretches ( $3500 - 3650\text{ cm}^{-1}$ ) arising when both hydrogen atoms in a water molecule participate in hydrogen bonding, (iii) single donor (SD) stretches ( $3300 - 3400\text{ cm}^{-1}$ ) arising when only one O-H bond in a water molecule is involved in hydrogen bonding and (iv) ionic hydrogen bonds, as discussed earlier, which can fall within a fairly wide range from  $3000 - 3400\text{ cm}^{-1}$ .

### **3.3.6 Infra-red Spectroscopy $m/z = 23$**

Calculation predicts aSSIP isomer of in complex of  $\text{NaCl}(\text{H}_2\text{O})_6$  with two bands at around  $3150$  and  $3220\text{ cm}^{-1}$ , respectively; we have therefore tried to find the trace of this structure in IR spectra. The band at  $3220\text{ cm}^{-1}$  could be assigned to one of the sub-structure in the broad band in Figure 3- 6 (c) of the  $\text{NaCl}(\text{H}_2\text{O})_6$  spectrum. However the  $3150\text{ cm}^{-1}$  band does not appear in any spectrum we concern so far. Considering the cyclic structure consisted by 6 water molecules intervened between  $\text{Na}^+$  and  $\text{Cl}^-$ , the formation of  $\text{Na}^+$  during the charge transfer ionization can be expected, which is significantly apart from water and  $\text{Cl}^-$  according to calculations. Hence we recorded the IR spectrum at  $m/z$  23.

It can be noticed in Figure 3- 7, the spectrum recorded at the  $m/z$  23 channel has distinct narrow features, suggesting that it is derived from a specific and simple isomer. In the spectra we have also seen several transitions in the O-H region arising from small water clusters, which are essentially from  $\text{He-H}_3\text{O}^+$  (as marked in "Free OH", "D", "T", "Q" and "P" in Figure 3- 7). This was confirmed by turning off the oven to eliminate any NaCl vapour and then recording the spectrum at  $m/z$  23 again. As seen in the red curve in Figure 3- 7, the bands with transition frequencies  $> 3300\text{ cm}^{-1}$  from the two spectra are almost identical.

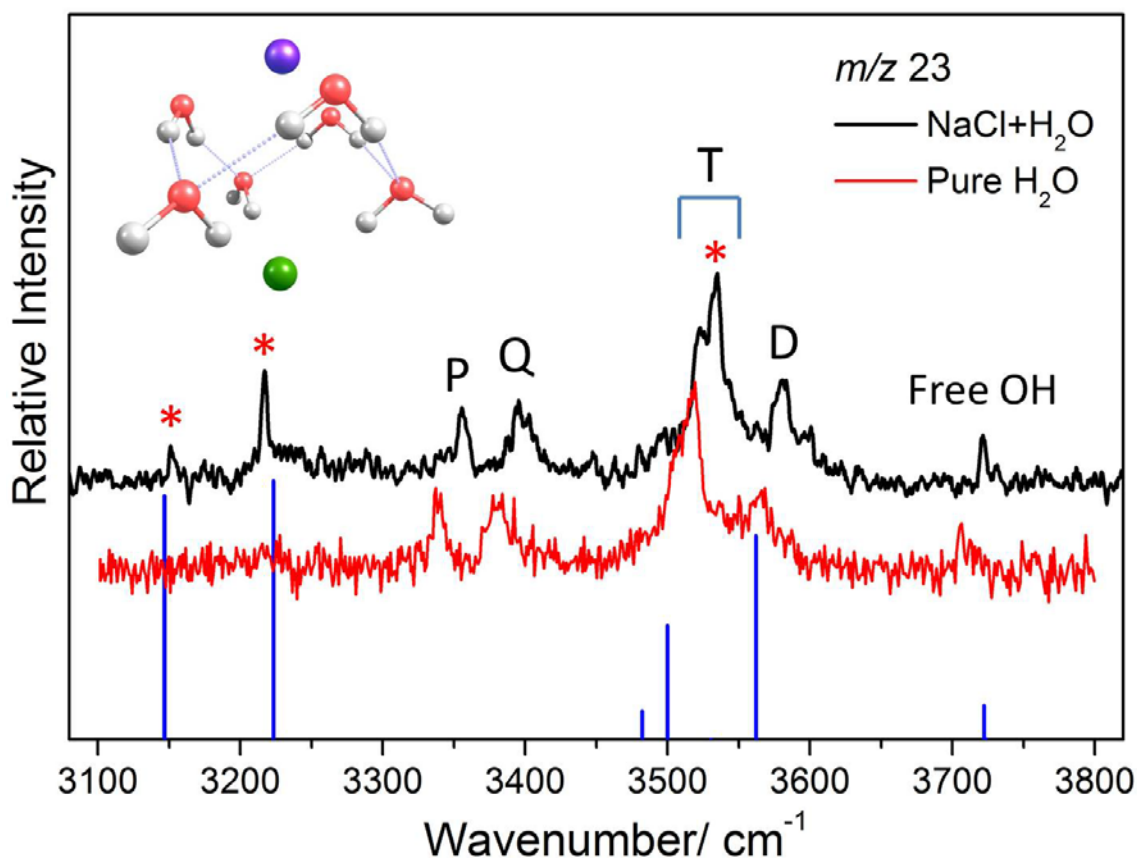


Figure 3- 7 Depletion spectra on  $m/z$  23 with the SSIP structure of  $\text{NaCl}(\text{H}_2\text{O})_6$ . The black curve was recorded when both water and NaCl doped in; the red one was obtained when salt oven was switched off; the blue sticks shows the predicted bands from the SSIP structure complex. The main bands of the water clusters are also assigned, including Free OH, D (water dimer), T (water trimer), Q (water tetramer) and P (water pentamer).

In Figure 3- 7 there are several peaks that disappear when NaCl vapour is absent (marked by \* in the spectrum), most notably two peaks at  $3151$  and  $3217 \text{ cm}^{-1}$ . There are only two plausible carriers of these remaining bands: (i)  $\text{Na}(\text{H}_2\text{O})_n$  or (ii)  $\text{NaCl}(\text{H}_2\text{O})_n$  complexes. In both cases it is necessary to assume that ionization leads to  $\text{Na}^+$  production. We can eliminate  $\text{Na}(\text{H}_2\text{O})_n$  for several reasons. First and foremost, as mentioned earlier, evaporation of solid NaCl at the low temperatures used in the current study will produce a negligible quantity of Na atoms. Second the spectral features are relatively simple and therefore cannot derive from  $\text{Na}(\text{H}_2\text{O})_n$  for a range of  $n$ .

This leaves one or more  $\text{NaCl}(\text{H}_2\text{O})_n$  complexes as the source of the unassigned bands in Figure 3- 7 and, given the simplicity of the spectral features, it seems likely to be

only a single complex. According to our MP2 calculations only two complexes can simultaneously produce the two low frequency peaks at around 3151 and 3217  $\text{cm}^{-1}$ . One possibility is an isomer of  $\text{NaCl}(\text{H}_2\text{O})_2$  lying 0.05 eV above the global minimum, with the predicted frequencies at 3132 and 3229  $\text{cm}^{-1}$ . The second possibility is the SSIP complex of  $\text{NaCl}(\text{H}_2\text{O})_6$ , where the low frequency vibrations at 3147 and 3223  $\text{cm}^{-1}$  come from weakened O-H bonds in direct contact with  $\text{Cl}^-$  *i.e.*, free from any immediate proximity to  $\text{Na}^+$ . The two low frequency bands are clearly narrower than those from water clusters, indicating that the O-H stretching vibrations in the spectral carrier are significantly decoupled from the other O-H stretching modes.

We have tried to use the dependence of the signal level on the quantity of added water to distinguish the two possible spectral carriers. Unfortunately, this is complicated by the strong underlying contribution from water clusters in the  $m/z$  23 channel. Nevertheless, the maximum signal for those two low frequency O-H stretching bands of the unknown carrier requires a quantity of water well above the optimum for making small  $\text{NaCl}(\text{H}_2\text{O})_n$  complexes ( $n \leq 3$ ), but requires water level to obtain an optimum spectrum for  $m/z$  131, *i.e.* the  $\text{NaCl}(\text{H}_2\text{O})_6$  complex. Moreover, there is evidence of additional bands from the unknown  $\text{NaCl}(\text{H}_2\text{O})_n$  complex in Figure 3- 7. For the two peaks at 3523 and 3535  $\text{cm}^{-1}$ , which would normally be assigned to the water trimer, the second of these peaks (marked with \*) has a hugely enhanced intensity compared to known spectra of  $(\text{H}_2\text{O})_3$  in helium nanodroplets shown in Figure 3- 4. On the other hand, the SSIP complex of  $\text{NaCl}(\text{H}_2\text{O})_6$  is predicted to have a strong band in this region (see simulation in Figure 3- 7) whereas the excited isomer of  $\text{NaCl}(\text{H}_2\text{O})_2$  is not (referred to Table 3- 1). For these reasons we tentatively assign the spectral carrier of the new peaks in Figure 3- 7 to the SSIP complex of  $\text{NaCl}(\text{H}_2\text{O})_6$ .

Finally we discuss why the SSIP structure of  $\text{NaCl}(\text{H}_2\text{O})_6$  can be determined by detecting  $\text{Na}^+$  ions. The calculated structure of the SSIP shown in Figure 3- 7 consists of a cyclic water hexamer sandwiched between  $\text{Na}^+$  and  $\text{Cl}^-$  ions, where the  $\text{Na}^+$ - $\text{Cl}^-$  distance is 4.458 Å. The production of bare  $\text{Na}^+$  might be a consequence of the large separation of the two ions in the SSIP isomer. In particular the location of the  $\text{Na}^+$  on the surface of the water cluster may assist its escape with no attached water molecules up on ionization, in contrast to  $\text{Na}^+$  ions embedded more deeply within a

water network. Detection of  $\text{Na}^+$  therefore yields an IR spectrum of  $\text{NaCl}(\text{H}_2\text{O})_6$  selective only to the SSIP isomer. On the other hand, the IR spectrum recorded by detecting  $\text{Na}^+(\text{H}_2\text{O})_6$  shows no significant contribution from the SSIP isomer, presumably because this isomer does not deliver hydrated  $\text{Na}^+$  ions on electron ionization. Thus the spectrum in Figure 3- 7 represents a superposition of signals from non-ionized CIP-like isomers.

### 3.4 Conclusion

In this chapter we have reported the first systematic investigation of  $\text{NaCl}(\text{H}_2\text{O})_n$  complex for a range of  $n$  from 1 to 7 by co-doping NaCl and water in helium droplets. The O-H stretching vibrations of the complex molecules at their ground states were investigated using infra-red spectroscopy. Compared with *ab initio* calculations, CIP-like complexes ( $n \leq 5$ ) are identified, particular for the small complex with  $n \leq 3$ . In all the spectra, the ionic hydrogen bond induced stretching is significant and is dominant in the small clusters, since the  $\text{Cl}^-$  ion deeply involved. Fermi resonances are clearly present in the spectra for all the clusters in the form of doublets. Finally, a possible SSIP complex at  $n = 6$  is observed for the first time in experiment, which contains a water hexamer ring sandwiched between the  $\text{Na}^+$  and  $\text{Cl}^-$ . The distinct vibrational bands observed were consistent with the calculation results as well as the earlier theoretical work. The assigned complex structure indicates that the dissolution of NaCl molecule starts to occur.

## Chapter 4

# Quantum Vortices in Helium Droplets and Nanowires Growth

### 4.1 Introduction

Quantized vortex is one of most dramatic hallmarks of a superfluid, which describes the rotational behaviour of superfluid, *i.e.*, only a certain angular moment would be allowed. Below 2.17 K helium is in the phase II, the superfluid phase, at which helium is essentially a Bose-Einstein condensate (BEC). This means that each atom in the system would have the same wavefunction (as in quantum mechanics) and they cannot be distinguished from each other. Therefore, when superfluid helium is under rotation, quantum vortices with a hollow core will be produced in order to avoid zero-angular moment helium atoms to occur<sup>(76)</sup>. In the helium droplet, helium atoms rotate around the vortex line which resides through the centre of the droplet and provides attractive force to the dopants nearby. The mathematical expression of a quantum vortex is:

$$\kappa = \frac{nh}{M} \quad (4-1)$$

where  $\kappa$  is the integration of circulation velocity along the vortex loop in the form of  $\kappa = \oint v_s \cdot dl$ ,  $v_s$  is the circulation velocity,  $l$  is a closed path representing for vortex ring,  $n$  is the quanta of quantized vortices,  $h$  is the Plank constant and  $M$  is the mass of helium. Experimental evidence of a quantum vortex in bulk liquid helium was first proposed in 1964 by Rayfield *et al.*, who measured the inverse proportional relationship between the velocity of the ions doped in liquid helium and their energy, which then suggested ions were circulating around the vortex line<sup>(81)</sup>. It was not until 2006 that a visual evidence was obtained by observing micro-sized hydrogen particles condensing along the vortices lines in the liquid helium<sup>(82)</sup>. The experiment was performed by bubbling highly diluted H<sub>2</sub> in helium through superfluid helium under

rotation. It is in the same experiment that the vortex diameter was estimated as in the order of an Ångstrom. In the meantime whether a quantum vortex exists in the nanoscale helium remains a puzzle since the early discovery of superfluidity of helium droplets.

The first implication of quantum vortices in helium droplets was discovered by Gomez *et al.* <sup>(83)</sup>. By doping Ag atoms in very large helium droplets composed of  $10^7 - 10^{12}$  helium atoms, they observed elongated Ag deposits aligned head-to-tail according to the transmission electron microscopy (TEM) investigation. The authors attributed these aligned nanorods to the effect of the quantum vortices in the helium droplets which may provide an attractive force to allow the Ag atoms pinning to the vortices lines and aggregating into nanorods. However this is not fully convincing because there exists other alternative interpretations, for example, the head-to-tail alignment may be driven by the transient dipole interactions due to the anisotropy of Ag nanorods. In this case the elongated nanoparticles naturally interpose shape anisotropy which might guide the atoms growing along one direction. In addition, it is also unclear whether the fragments are intrinsic or they were produced by fracture upon impact on the deposition targets. As the authors have stated in the paper, the possibility that the observation was caused by the breakup of the synthesized Ag nanowires in helium droplets after hitting on the deposition target cannot be ruled out.

On the other hand, all the traces of quantum vortices in liquid helium taken into concern until now is believed to be the singly quantized vortices, *i.e.*  $n = 1$  in Equation (4-1), because it is thought to be energetically more favourable to have lower quanta vortices. That is why the mathematical formula of quantum vortices in Chapter 1 has been described as  $\kappa = \frac{h}{M}$ . The possibility for multiply quantized vortices in bulk phase liquid helium had long been considered impossible since the energy of multiplied quantum vortices energy, which is proportional to  $n^2$ , is much higher than the multiple singly quantized vortices <sup>(172)</sup>. Hence any circulation of liquid helium stronger than  $h/M$  will be rapidly quenched to multiple single quanta vortices <sup>(173)</sup>, as proved by Vienn in 1961. The uniform arrays of condensed hydrogen particles observed by Bewley *et al.* <sup>(82)</sup> are also believed to be singly quantized vortices. So far it remains an open question

whether multiple quantum vortices exist in helium droplets since there is no experimental proof.

Although enlightened experimental results were shown in Ref. (83), more evidence is required to firmly prove the existence of quantum vortex in helium droplets. In this chapter, we present the convincing experimental proof of the quantum vortex's existence in helium droplets and then develop it as a new technique to produce various one dimensional nanostructures. Finally we will discuss new experimental evidence indicating the presence of multiply quantized vortices in superfluid helium droplets with experimental support.

## **4.2 Firm Evidence for Quantum Vortices in Helium Droplets**

### **4.2.1 Silver Aggregation in HeDs**

Since Gomez *et al.* claimed that the observation of chains of Ag nanosegments formed in large helium droplets was possibly a trace of the quantum vortices existence<sup>(83)</sup>, in order to explore the existence of quantum vortices, it is crucial to get a full picture of how silver nanostructures evolve in large helium droplets with the droplets size variation.

Here we carried a series of experiments on the addition of Ag to helium droplets, in which the Ag oven was maintained at about 1230 K. This temperature was chosen because we have found at this temperature the majority of Ag nanoparticles are spherical. The stagnation pressure of helium source was kept at 15 bar and the deposition time for all the samples were 2.5 min. The helium source temperature was tuned from 9.5 K to 4.5 K and at each temperature, the helium beam was aligned to maximize both the partial pressure in the quadrupole mass spectrometer chamber (the highest flux of overall helium) and  $\text{He}_2^+$  signal detected (the highest flux of helium droplets). The Ag doped helium droplets were then allowed to deposit to a TEM substrate, which can then be removed from vacuum investigated by high resolution

transmission electron microscopy (TEM) at the Advanced Microscopy Centre at University of Leicester.

We started with a helium source temperature initially set at 9.5 K, corresponding to a mean droplets diameter of 25 nm. As shown in Figure 4- 1 (a), small particles with diameters of 1 – 2 nm were formed. As temperatures gradually decreases to 8.5 K, 7.5 K, 6.5 K to 6 K (producing helium droplets with average diameters of 40 nm, 90 nm, 120 nm and 200 nm, respectively), the particle counts gradually decreases but the average particle size increases. Meanwhile the particles, which randomly distribute on the substrates at higher temperatures, tend to line up gradually as the droplets become larger, as shown in image (b) – (e). At a source temperature of 5.5 K (with droplet diameter of 790 nm), uniform spherical Ag nanoparticles aligned in a chain can be observed from the TEM image (see Figure 4- 1 (f)). The particles are about 6 nm in diameter with an inter-particle separation of 22 nm.

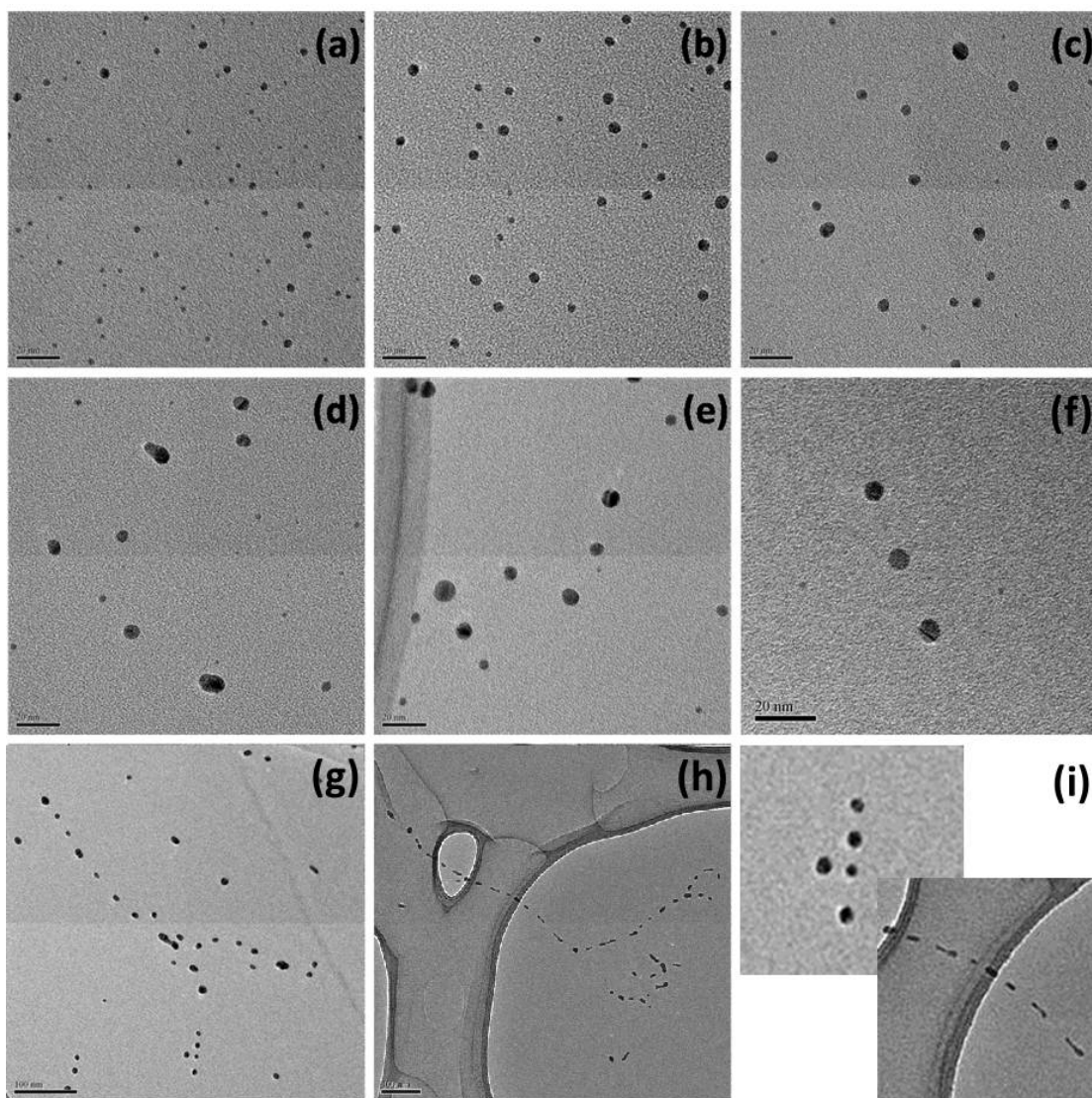


**Figure 4- 1** TEM images of Ag aggregations in helium droplets with different source temperatures of (a) 9.5 K; (b) 8.5 K; (c) 7.5 K; (d) 6.5 K; (e) 6 K; (f) 5.5 K; (g) 5 K; (h) 4.5 K. The scale bars for (a) – (f) are 20 nm, (g) – (h) are 100 nm. Image (i) shows the expanded views of images (g) and (h).

At lower temperature, the particle chain gets longer and the individual spherical particle gets larger. At 5 K (with the droplet diameter of about 1.7  $\mu\text{m}$ ) the average particle diameter grows to about 10 nm (see Figure 4- 1 (g)). At even lower temperature the chain continues to grow in length, and elongated nanorods are observed rather than spherical nanoparticles. At 4.5 K when helium droplets have an average diameter of 3  $\mu\text{m}$ , very long chain of nanorods are observed, each segment of rod has an average length of 21 nm and diameter of 8 nm. Figure 4- 1 (i) shows the expanded views of image (g) and (h), providing more details of the evolvement from

spherical nanoparticle to nanorods. It is worth mentioning that the centre-to-centre separations between neighbouring nano-objects in all images (f) – (h) are pretty similar, of 28 nm, 26 nm and 29 nm respectively.

#### **4.2.2 Silver/Silicon Binary Nanowires in HeDs**

Vilesov *et al.* have suggested that fragments of Ag in TEM images are possibly caused by the fractures of the nanowires after being deposited on a solid target<sup>(83)</sup>. In order to investigate whether the structures displayed in Figure 4- 1 (f – h) are the intrinsic features in helium droplets, we sequentially added Ag and Si into helium droplets. The motivation is: if the segmented structures were resulted from the fracture, core-shell structural segmented structures should be observed; on the other hand, if the segments were intrinsically generated in helium droplets before hitting on the target, Si should be able to fill in the gaps between the Ag segments and no fracture should be observed.

In this experiment, Si was heated to 1400 K and Ag oven was maintained at 1230 K. Two source temperatures were selected at 6.5 K and 4.5 K in order to compare, corresponding to an average droplets diameter of 250 nm and 3  $\mu\text{m}$  respectively. The helium beam was again aligned to maximize both partial pressure in the quadrupole chamber and the  $\text{He}_2^+$  signal. All the samples were deposited for 2.5 minutes and the TEM images of the two samples are shown in Figure 4- 2.

In relatively smaller helium droplets, with a diameter of 250 nm, Ag aggregates into spherical nanoparticles instead of nanorods or nanowires (darker images marked in Figure 4- 2 (a)). Si was then added to the droplets which produced a Si coating on the surface of Ag nanoparticles, resulting to a clear core-shell structure (lighter image marked in Figure 4- 2 (a)). Figure 4-2(a) also indicates that Si tends to grow into nanowires rather than spherical nanoparticles, as a tail can be observed. In large helium droplets of 3  $\mu\text{m}$  diameter (Figure 4- 2 (b)), Ag aggregates into a chain of nanorods, similar to the images shown in Figure 4- 1 (h), while Si was found to fill in the gaps between the Ag segments. This image clearly proves the segmented nanostructures of Ag are intrinsic in helium droplets before hitting on the target, which

completely rules out the possibility that the Ag segments were resulted from the breaking of the nanowires suggested by Gomez et al. (83).

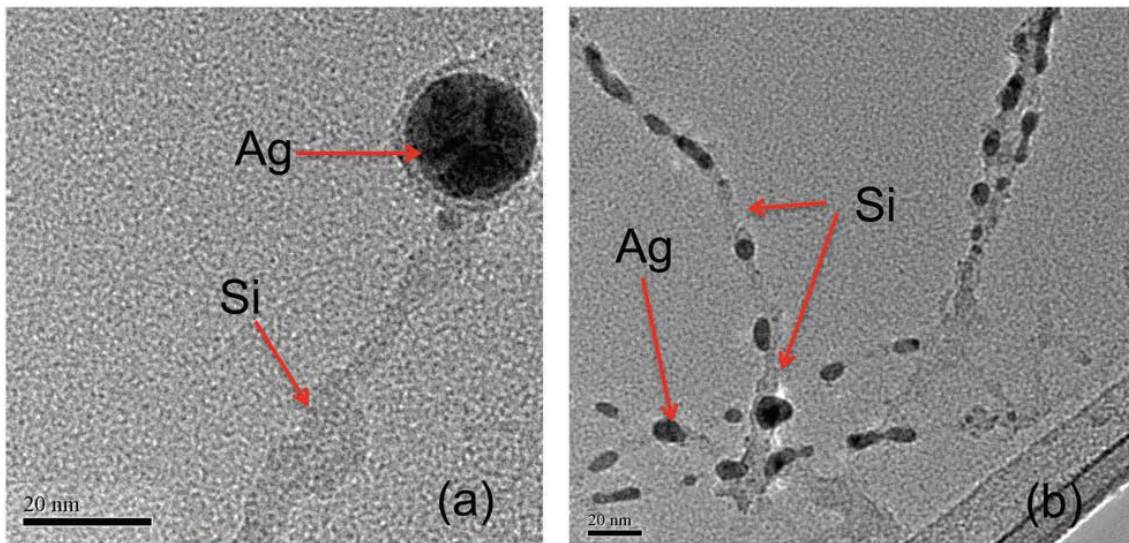


**Figure 4- 2** TEM images of Ag-Si nanowires formed in helium droplets at temperature of (a) 6.5 K and (b) 4.5 K.

The spherical Ag nanoparticles chains shown in Figure 4- 1 (f) – (g) rule out the shape anisotropy as a potential source of the guiding force for nanoparticles aggregation in one direction, since the spherical nanoparticles do not have any anisotropy. The binary Ag-Si nanowires formed with Si filling in the gaps between the Ag nanorods eliminates the possibility of the segment chains are induced by the fragmentation of the nanowires on the hard target. In superfluid helium there are no other guiding forces that can cause the one-dimensional growth; the only factor that can interpret the observation is therefore the quantized vortex. Hence our experiment provides solid evidence for quantized vortices in superfluid helium droplets.

#### **4.2.3 Nanostructures Growth along the Vortex Line**

The aligning force provided by the quantum vortex for nanoparticles pinning originates from the increased density gradient near the vortex core to the atoms and molecules compared to other part of the superfluid, which leads to a binding energy of about 3 – 10 K ( $2 - 7 \text{ cm}^{-1}$ ) for an atom <sup>(174)</sup>. This is a very short-ranged, but sufficiently strong attractive force, for the atoms being trapped in helium droplets, considering the

surrounding temperature is only 0.37 K. Therefore the aggregation in helium droplets tends to occur along the vortex line.

The reason that Ag forms segmented nanoparticles or nanorods instead of continuous nanowires as for Si shown in Figure 4- 2 is still unclear so far. As helium droplets are superfluid and they provide negligible viscosity that can hinder the migration of Ag atoms and Ag particles, there must be a repulsive force along the vortex line which prevents the pinned nanoparticles from combining together. It was suggested that the addition of Ag might distort the vortex core and the curved vortex could generate high energy boundary between the two energy minimal <sup>(175)</sup>. Therefore nanoparticles can only aggregated at the energy minimal position of the vortex line and repulsive from the neighbouring particles. The roughly equal inter-particle spacing between the centres of the two neighbouring particles indicates the equilibrium distance comprised by the long-range inter-particle attraction and the repulsive force caused by the vortex distortion. Indeed this explanation is quite speculative and may not apply to the universal cases since Si clearly prefers to form nanowires along the vortex line. Therefore there also may be some unique properties of Ag that we did not understand at the moment.

Recently it has been experimentally proven that multiple quantum vortices can co-exist in the same helium droplet. By X-ray diffraction images, xenon atoms pinning to the vortex lines in helium droplets can be visually investigated <sup>(84)</sup>. The diffraction patterns showed multiple parallel vortices arranged in a lattice within the droplets in a manner similar to bulk superfluid helium, which is assigned to multiple quantum vortices.

Till now all the evidences of quantum vortices in helium droplets were discovered in large helium droplets, *i.e.* when source temperature below 6 K. In smaller droplets, vortices should still exist in theory; however it is a big challenge to trace them in experiments since the finite inter-atom spacing inside the helium droplets, atoms are more preferable to bound together, aggregate into larger particles and therefore overwhelm the vortices effect.

Figure 4- 1 displays a fully evolution picture of Ag from small nanoparticles through large aligned nanoparticles and then to long chain of nanorods when the mean droplets diameter increases from 25 nm to 3  $\mu\text{m}$ . Here we can summarize three extreme scenarios of nanoparticle growth in helium droplets according to the observation, which combines the effect of quantum vortices and multi-centre growth:

- i. In relatively small helium droplets, the successive added Ag atoms can quickly migrate to an existing  $\text{Ag}_n$  cluster in the droplet due to the low effective doping rate and reasonably strong long-range dispersion interaction. Therefore the inter-atom attraction can overcome the quantum vortices and a single spherical nanoparticle will result. In TEM images, spherical nanoparticles are randomly distributed and particles grow larger with the doping rate increases either by increasing the oven heating or by increasing the droplets size.
- ii. When droplets are enlarged to an intermediate scale, the new added atoms are too far away from any other atoms. It will be a semi-random way for atoms migrating to the existing nanoparticles which are possibly already pinned to the vortex line. When the new atoms encounter and attach to the existing particles, particles along the vortex line grow larger. As the atoms can approach to the vortex line from any direction, the particles can maintain quasi-spherical shape, forming the spherical nanoparticle chains shown in Figure 4- 1 (f). Scenarios (i) transforms to (ii) gradually as the droplets size increases.
- iii. When the droplets are extremely large so that Ag doping rate is so high that multi-centre growth happens <sup>(95, 176)</sup>. When the time between successive atom pickup events is shorter than the migration time to the centre of helium droplets, atoms can aggregate into small particles at multiple locations inside helium droplets, which then continue to migrate toward the vortex line. Eventually these nanoparticles will reach the vortex line and elongate the existing nanoparticles that have been already pinned. In this case chains of nanorods will be formed.

## 4.3 One-dimensional Nanostructures Formation in Helium Droplets

One dimensional nanostructures, including rods, wires and tubes have attracted more and more attentions in recent years for some unique properties they possess, such as quantum conductance <sup>(177)</sup>, ballistic conduction <sup>(178, 179)</sup>, extraordinary magnetic properties <sup>(180)</sup>, negative magneto-resistance <sup>(181)</sup> and low thermal conductivity <sup>(182)</sup>. Therefore ultra-thin nanowires have significant importance in applications of catalysis <sup>(183)</sup>, chemical and biosensors <sup>(184, 185)</sup> and miniature electronic circuits <sup>(186)</sup>.

Currently various methods have been applied to synthesis ultra-thin nanowires which normally involve an anisotropy force including substrates <sup>(187)</sup>, templates <sup>(188, 189)</sup>, ligand control <sup>(190)</sup> and oriented attachment <sup>(180)</sup> to allow atoms growing along one direction. Besides monometallic nanowires which are the focus of current research in this field, it is found that nanowires consisted by two types of metals present improved electronic, magnetic and catalytic properties compared to the monometallic ones <sup>(191-193)</sup>.

Although have been widely investigated, there is no universal synthetic technique that can apply to all the materials. Synthesis procedure is always system dependent and it is still big challenge to produce nanowires with diameter of less than 10 nm for most of the techniques, which are of great importance to research due to the sensitive size effect at nanoscale. Meanwhile for nanowires composed by two or more types of materials, precise control of the quantity of each component is still difficult in technique due to the different nucleation and growth rates of different components.

Using superfluid helium droplets the materials can be added when helium droplets pass through the pickup region and acquire impurities in the gas phase, and the intrinsic anisotropy, the quantized vortices, will allow the materials to aggregate along the vortex line. Hence helium droplets can potentially be used as a unique and universal tool for nanowire growth. In the following sections, we will exploit the potential to form nanorods and nanowires in helium droplets, taking advantage of quantum vortices, including both metallic and non-metallic materials.

### 4.3.1 Au Nanostructures

As discussed in previous sections, silver atoms can gradually evolve from nanoparticles to nanorods as the size of helium droplets gradually enlarges. The evolution is determined by the combined effect of quantum vortices and multi-centre growth. Figure 4- 3 shows the evolution of Au nanostructures formed in helium droplets with initial helium droplet diameter ranging from 25 nm to 1.7  $\mu\text{m}$ . Here the helium droplet beam was aligned to its maximal  $\text{He}_2^+$  signal and partial pressure of the quadrupole chamber. Au oven was fixed at about 1300 K through all the experiments and the sample deposition time was 2.5 minutes.

As seen in Figure 4- 3 (a), at 9.5 K (corresponding to an average helium droplets diameter of 25 nm), only spherical nanoparticles can be observed, with an average diameter smaller than 3 nm. When helium droplets are enlarged to 55 nm in diameter (Figure 4- 3 (b)), both spherical and elongated Au nanoparticles can be seen. Further increase of helium droplet size leads to more elongated Au nanorods, (see Figure 4- 3 (c – g)). When helium droplets are about 135 nm in diameter, nanorods have a length of  $20 \pm 7$  nm and a width of  $3.9 \pm 0.5$  nm on average. For helium droplets with a diameter of 790 nm, nanorods grow to a length of nearly 50 nm and a width of 4 – 5 nm. When helium gas is cooled down to 5 K, producing droplets with  $\sim 1.7 \mu\text{m}$  in diameter, continuous Au nanowires longer than 250 nm have been obtained (Figure 4- 3 (g)). The nanowire diameter is about 3.6 nm in average. This is a very different behaviour compared to Ag which tends to form chains of segmented nanorods.

The expanded view of a long Au nanowire formed in 1.7  $\mu\text{m}$  helium droplets, as shown in the inset of Figure 4- 3 (g), has a “peas-in-a-pod” structure, which indicates the formation of nanowires is a combined effect of quantum vortices and multicentre growth. Here each “pea” is a spherical nanoparticle formed at a random place in the droplets which eventually moves to the vortices lines, and attaches to the particles already pinned in the vortex core if they are in close vicinity. Compared with Ag, Au can migrate freely along the vortex line and form a continuous nanowire.

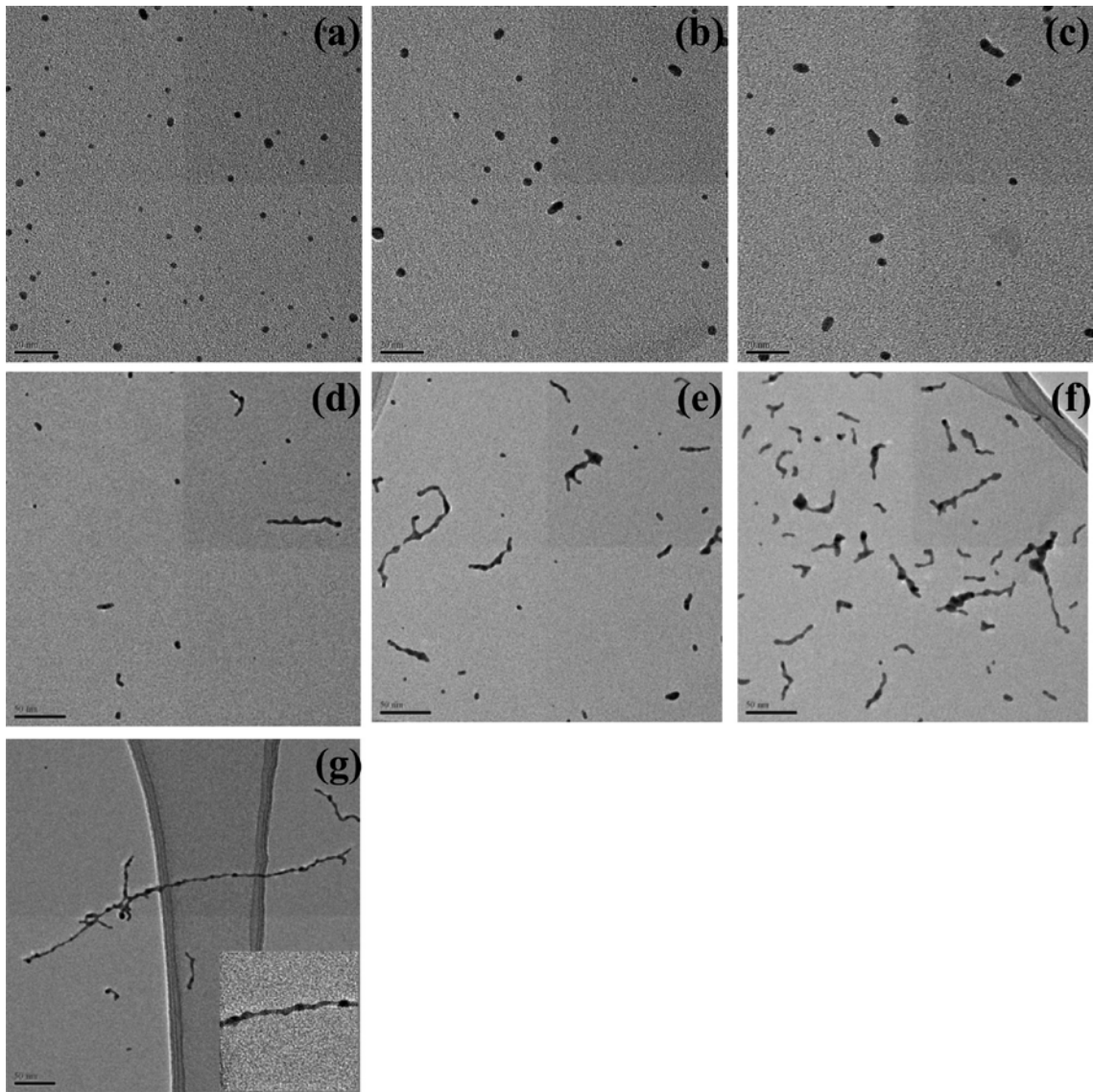


**Figure 4- 3** TEM images of Au nanostructures formed in helium droplets of different initial diameters of: (a) 25 nm; (b) 55 nm; (c) 75 nm; (d) 135 nm; (e) 250 nm; (f) 790 nm. (g) 1.7  $\mu\text{m}$ . The scale bars for (a) – (c) are 20 nm and for (d) – (g) are 50 nm. The Au oven is fixed at 1300 K.

Another remarkable feature is the branched nanowires are observed in all the images in Figure 4- 3. As we have deliberately deposited nanowires at relatively short duration in order to avoid overlapping on the TEM substrates, there is little probability that one wire was deposited on top of another. The branches must be intrinsic to the nanowires formation process in helium droplets. One possibility may derive from the multicentre growth mechanism. If the nanoparticles are formed at the locations remote from vortex line, they may not all be able to reach to either end of the vortex line by free

diffusion. Instead, they will encounter a continuous nanowire at a middle position where they can attach and form localized anisotropy. The continuous addition of Au to the droplets can then start to grow near these locations and form branches. This process is similar to the diffusion-limited aggregation occurring in wet chemistry synthesis of nanostructures, where nanostructures are transported and bounded together by diffusion <sup>(194, 195)</sup>. Another possibility is that the branched nanowires may come from the multiple vortices array existing in the same helium droplet, leading to the separate strands of the nanowires formed fusing together when deposited onto a target.

Figure 4- 3 indicates the nanowires can be significantly elongated with the increase of helium droplet size. In another set of experiments the dependence of the diameter and length of Au nanowires on the oven temperature was measured, in order to examine whether the length and the diameter of the Au nanowires can be controlled. As shown in Figure 4- 4, the size of helium droplets was maintained at 1.7  $\mu\text{m}$  and the Au oven temperature was varied. The diameter of the nanowires significantly increases with the oven temperature when it is relatively low and then reaches to a nearly constant level of 5 nm. On the other hand, the length of nanowires monotonically increases with the oven temperature. This set of experiments shows that by careful control over the doping rate and the size of helium droplets, the length of the nanorods/nanowires can be controlled while the diameter can be maintained at a very narrow level. Further increase of nanowire diameter can be expected when the nanowire reaches the maximal length in the helium droplets, which is close to the diameter of the droplets.

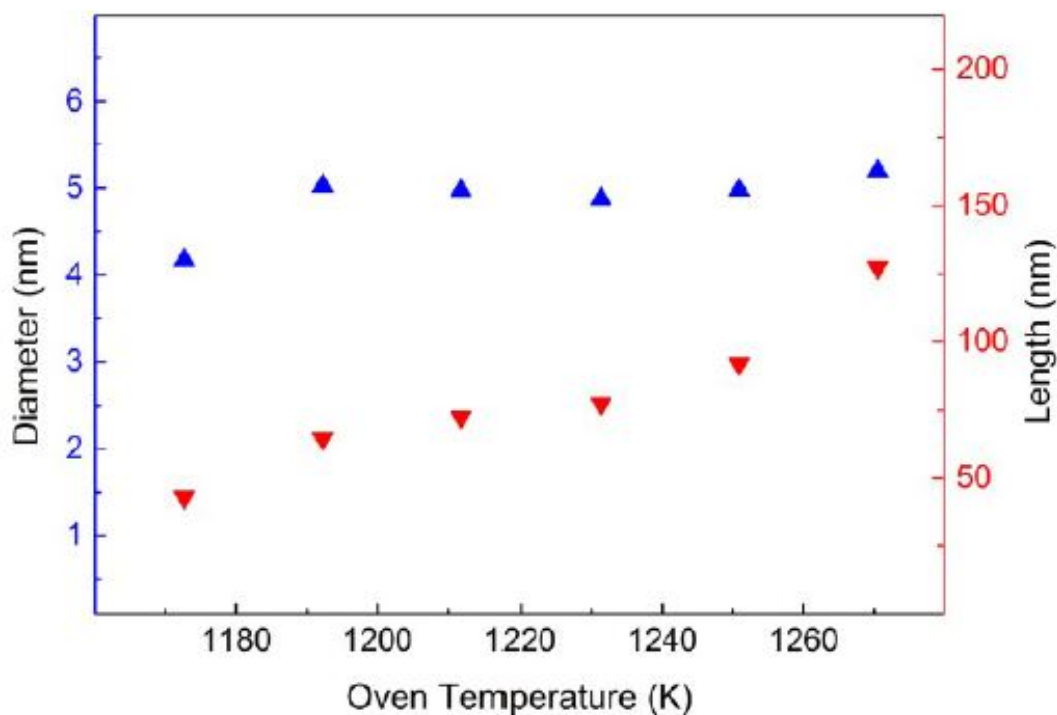


Figure 4- 4 Dependence of the diameter (blue triangle) and the length (red triangle) of Au nanowires on the oven temperature for helium droplets with a mean initial diameter of 1.7  $\mu\text{m}$ .

#### 4.3.2 Ni, Cr and Si Nanowires Formed in Helium Droplets

In this section we exploit the formation of nanowires using quantum vortices with different types of materials, including Ni, Cr and non-metallic Si. The experimental procedure is essentially the same as in the Ag and Au experiments. The TEM images of these materials are shown in Figure 4- 5.

The Ni oven was heated constantly up to 1700 K. Comparing Figure 4- 5 (a) with (b), Ni nanowires synthesized were significantly elongated with the droplet diameter increased from 790 nm to 1.7  $\mu\text{m}$ . Particularly at 1.7  $\mu\text{m}$  helium droplets, continuous nanowires as long as a 500 nm can be obtained, and the diameter of the nanowires is about 4 nm. At the lower right corner of the image Figure 4- 5 (b), there is a straight wire with a length of over 300 nm spanning the gap of across the lacey carbon film of the TEM substrate. In particular, on this wire branches can be clearly observed which provides evidence to support our speculation in the previous sections, *i.e.*, the branched structures are formed in the nanowire growth process inside helium droplets

as there is little possibility for the nanowires to get overlapped in the hollow region of the lacey carbon substrates.

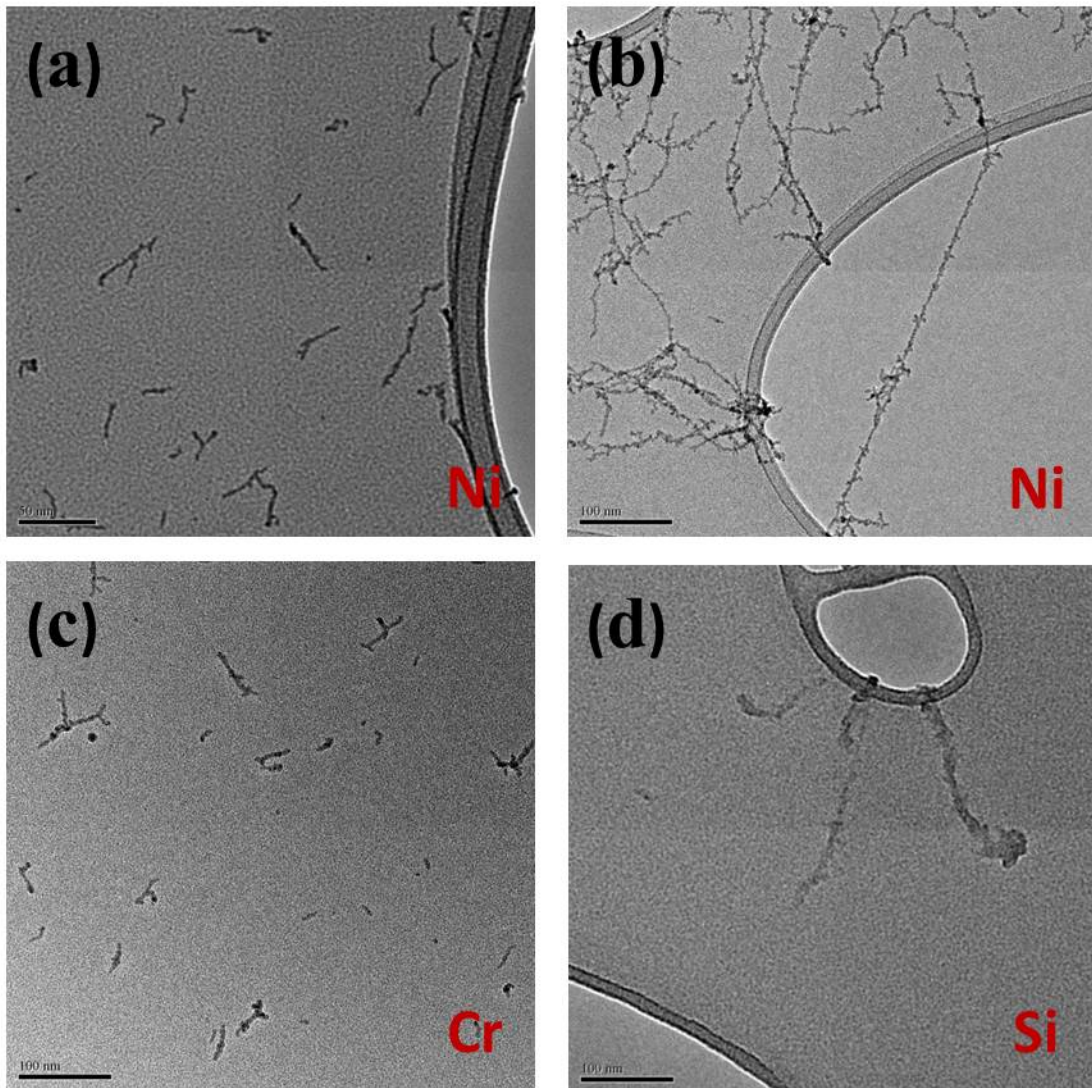


**Figure 4- 5 (a) Ni nanorods formed in 790 nm helium droplets; (b) Ni nanowires formed in 1.7  $\mu\text{m}$  helium droplets; (c) Cr nanowires formed in 790 nm helium droplets; (d) Si nanowires formed in 1.7  $\mu\text{m}$  helium droplets.**

Cr nanowires are also synthesized in large helium droplets. As seen in Figure 4- 5 (c). When Cr oven was heated to 1500 K with 790 nm diameter helium droplets, nanowires with average length of 69 nm and diameter of 3.3 nm can be observed.

For Si we heated the oven to 1400 K, Si nanowires longer than 100 nm have been synthesized in helium droplets with diameter of 1.7  $\mu\text{m}$ , as shown in Figure 4- 5 (d).

The contrast of the TEM image for Si is much lower than the other metals illustrated before because Si does not scatter electrons as readily as metals.

### **4.3.3 Advantage of Helium Droplets Technique in Forming One-dimensional Nanostructures**

There are several major advantages of helium droplets, particularly in combination of quantum vortices in helium droplets and multi-centre growth mechanism, for the formation of one-dimensional nanostructures:

- i. It is a universal technique for the fabrication of nanowires, which has no limitation on material selection. Any metallic and non-metallic materials, as long as they can be evaporated, can be added to helium droplets and pinned to the vortex line. In this process neither template nor substrate is needed; hence the synthesis process is straightforward and the products are expected to have high purity in an ultrahigh vacuum system.
- ii. The growth of one-dimensional nanostructures can be controlled, and ultrathin nanowires with diameter < 10 nm can be easily formed.
- iii. Core-shell structured one-dimensional nanostructures can also be easily produced using this technique<sup>(97)</sup>, *i.e.*, by sequential addition of different types of materials to helium droplets when they pass through the pickup region.

## **4.4 Multiply Quantized Vortices in Helium Droplets**

In all the experiments described in the previous sections, we have aligned the helium droplets beam to the maximal helium droplet flux meanwhile the overall helium flux, which is, surprisingly, achieved by off-centre alignment of the helium droplets beam. When the helium droplets beam is centrally aligned, we have found that the  $\text{He}_2^+$  signal maintains the maximal but the pressure in the mass spectrometer chamber  $P_3$ , reaches a minimum (see Figure 4- 6). In this section we present the experimental results measured on the central axis of the chamber, corresponding to the maximum

of  $\text{He}_2^+$  and relatively low overall helium flux. To compare we have set the source temperature at 4.5 K, producing helium droplets with a diameter of 3  $\mu\text{m}$ .

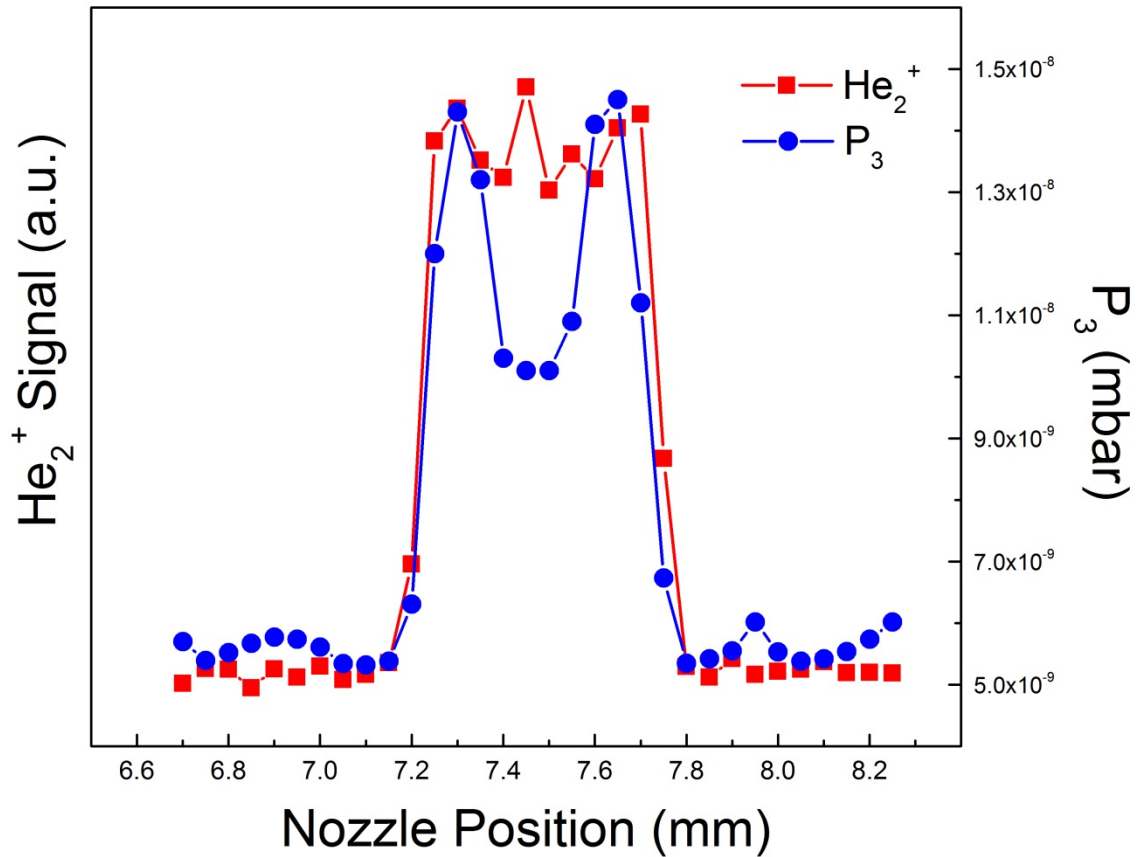


**Figure 4- 6** The variation of partial pressure  $P_3$  in the quadrupole chamber and  $\text{He}_2^+$  signal at different nozzle positions.

In Figure 4- 6, the x-axis marks the horizontal position of the manipulator mounted to the cold head.  $\text{He}_2^+$  signal maintains constant level in the middle range which means there are near constant number of helium droplets in the helium beam when the position of the source is slightly varied, since it is known each  $\text{He}_2^+$  ion is exclusively donated by one helium droplet <sup>(71, 74, 75)</sup>. On the contrary, a 0.25 mm wide dip appears in the middle of  $P_3$  variations, indicating although the droplets flux are constant, the droplets size in the beam centre is smaller at the centre of the droplet beam. It is because  $P_3$  is measured from the helium gases atoms after the droplets colliding with the wall of the detection chamber and breaking into gases atoms <sup>(10)</sup>. It can be estimated from Figure 4- 6 that a 40% reduction of the  $P_3$  value occurs in the centre of

the droplet beam, corresponding to an average 15% smaller in diameter of the droplets at the centre than at the edge.

We select Ag as the doping material and keep the Ag oven at 1230 K; so the experimental conditions including the droplet size and Ag doping rate can be controlled the same as the counterpart in Figure 4- 1, and the results from the two experiments can be directly compared.

Ag nanostructures synthesized in the beam centre when other experimental conditions are kept constant is shown in Figure 4- 7, in which some large nanoparticles still form in a chain but are surrounded by some smaller ones. The expanded view in the blue frame shows clear details of the particle distribution.

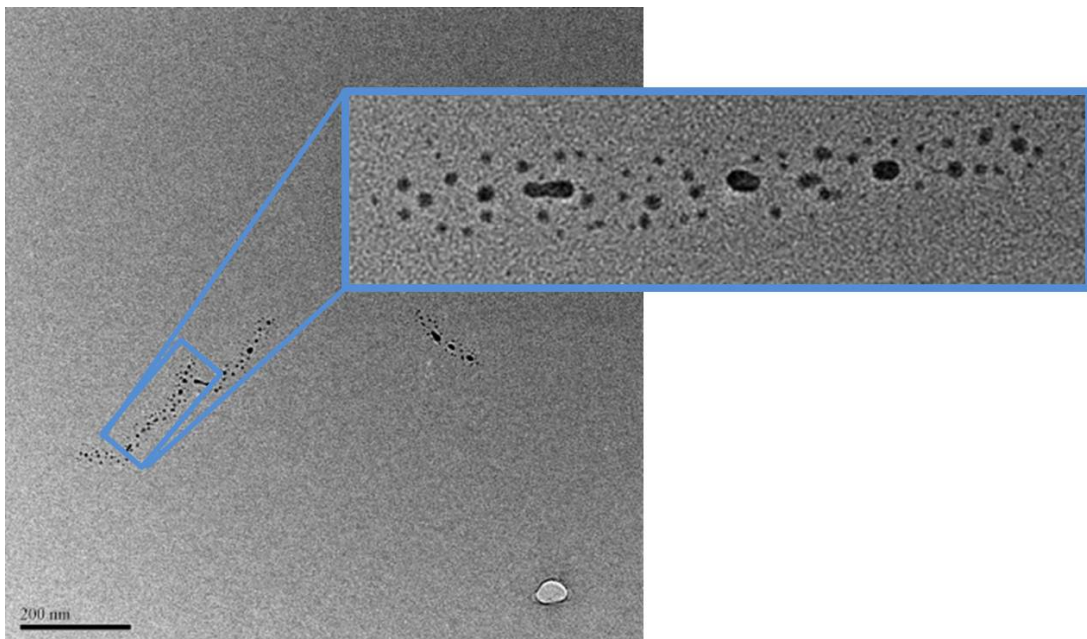


**Figure 4- 7 TEM images of Ag nanoparticle grown in the droplets at the centre of the helium beam. The scale bar is 200 nm. The expanded image in the blue frame shows the details of nanoparticle display.**

The different particle aggregation behaviour at different positions of helium beam suggests different factors that govern the particle aggregation. It is known the particle aligned in the chain is attributed to the singly quantum vortices in helium droplets; therefore the question aroused include: 1) what causes the small particles surrounding the large aligned ones? 2) Why do the surrounding nanoparticles neither align

themselves nor attach to the existing large aligned nanoparticles which are so close to them?

We first discuss the effect induced by the shape of the helium droplets, which are known to be statistical within a droplet beam <sup>(84)</sup>. The shape of the droplets can influence the migration time of the atoms towards the vortex line. The more ellipsoidal the droplet is, the longer time that some atoms might need to reach the vortex line. Hence if the migration time is longer than the flight time (from the Ag oven to the deposition target) smaller particles might not be able to reach the vortex, as a result they will locate at the vicinity of the existing particle chains. Nevertheless, according to TEM results we only see the images of Figure 4- 1 or Figure 4- 7 corresponding to the centred or off-centred helium beam, rather than a mixer. This therefore excludes the influence of the shape of the droplets to the TEM images.

Secondly we discuss whether the size of the helium droplets can lead to the different images. If the droplets produced at the central section of the expansion beam are much larger than the off-centre ones, it would take longer time for the Ag atoms to migrate towards the vortex line in the centre. As a result if some of the atoms cannot reach the vortex line within the flight time of the droplets from the oven to the deposition target (a few milliseconds), it is possible that they will eventually locate at the vicinity of the vortices. On the contrary, the pressure variation shown in Figure 4- 6 has suggested at the centre of the helium beam the droplets are about 15% smaller than the outer ones, which therefore eliminates the size effect contributing to the small particles located near the vortex lines.

These have left the only possible explanation to the best of our knowledge, which is attributed to the different rotational state of the helium droplets. If we assume that the “clean” chains of nanoparticles and nanorods are formed in singly quantized vortices, different rotational state means the central part of the helium droplets may form multiply quantized vortices. In this case all the helium atoms within the droplets will undergo a higher angular velocity, bearing a centrifugal force proportional to the square of the angular momentum. It is unclear whether the Ag atoms approaching the vortex line will circulate in the same manner as the helium atoms, or they are only little affected by the circulating helium atoms. In either case, multiply quantized

vortices will provide a stronger force against the migration of the Ag atoms toward the vortex line. Consequently, the droplets employed in Figure 4- 7 would have higher circulation velocity than Figure 4- 1, which means have a quanta  $> 1$ , although we are unsure what quanta the vortices have.

Finally we discuss the origin of quantized vortices generated in the expanded helium droplet beam and their lifetime. In bulk superfluid helium the rotating superfluid will have to interact with the container wall, which will drain the excess energy of helium, leading to reduced circulation velocity. Consequently multiply quantized vortices are intrinsically unstable from this aspect and will eventually evolve into multiple singly quantized vortices. For superfluid helium droplets they are isolated and free standing in the vacuum, therefore there is no channel to quench their rotational angular momentum. Consequently, multiply quantized vortices, once formed, could have very long lifetime. In this work the traveling distance between the expansion aperture and the Ag oven is  $\sim 40$  cm, and the distance between the Ag oven and the deposition target is  $\sim 60$  cm. Therefore the lifetime of the multiply quantized vortices is at least some milliseconds. In a previous work Gomez *et al.* have discussed the possibility to form vortices by the interaction of the fast-moving helium fluid with the walls of the nozzle in a similar way to normal fluid <sup>(83)</sup>. However, different rotational quanta at different region of the expanded helium droplet beam suggest that the shockwave generated in the free jet expansion might play an important role for the formation of multiply quantized vortices in superfluid helium droplets. Stronger interactions within the droplets at the edge of the silence zone are expected, which serves as a channel to release the rotational energy, leading to lower quanta of vortices in the off centred position of the helium droplets.

## 4.5 Conclusion

In this chapter, solid evidence of the quantized vortices existing in helium droplets have been experimentally given by chains of spherical nanoparticles formed in large helium droplets. The spherical nanoparticles lining up in a chain rules out the possible source of the aligning force induced by the shape anisotropy and the fact that the Si

nanowires filling between the Ag nano nanoparticles discriminates the assumption that the Ag nanoparticle chains are fractured by the impact on the substrate. Generally speaking, the particle aggregation in large helium droplets is a combined consequence of quantum vortices and multicentre growth, which leads to the formation of nanorods and nanowires.

As a result, helium droplets can perform as a highly adaptable technique that can be universally applied to fabricate one-dimensional nanostructures with easy preparation and no material limitation. The length of the nanostructure can be tuned by adjusting the material doping rate and the initial helium droplets size. To date, Au, Ni, Cr and Si nanowires and Ag/Au core shell nanowires have been synthesized in helium droplets, the length of the nanowires produced can reach up to  $\mu\text{m}$  scale.

We also generated evidence that suggests trace of multiply quantized vortices in helium droplets according to the TEM images of Ag nanoparticle aggregation where some small particles are seen at the vicinity of the chains of large particles. That the multiply quantized vortex can survive within the helium droplet is due to no energy quenching channel existing in the vacuum chamber and they can maintain stabilization for at least millisecond timescale.

# Chapter 5

## Magnetic Nanomaterials Formed in Helium

### Droplets

#### 5.1 Introduction

##### 5.1.1 Overview of Magnetism of 3d Materials

3d transition metals have great importance in magnetism due to the unpaired electrons in the 3d orbitals. The theoretical limit of the magnetism of individual atoms is known to depend on both electron spin and orbital moment, *i.e.*:

$$|\mu_z| = \left[ \frac{3}{2} + \frac{S(S+1) - L(L+1)}{2J(J+1)} \right] J \mu_B \quad (5-1)$$

where  $\mu_z$  gives the theoretical limit of the atomic magnetic moment,  $S$  is the total electron spin quantum number,  $L$  is the total orbital angular momentum quantum number, and  $J$  is the total angular momentum quantum number equal to  $|L \pm S|$  (+/- sign is determined by Hund's third rule).  $\mu_B$  is the Bohr magneton and is equal to  $-e\hbar/2m_e$  ( $m_e$  is the electron mass), which is a commonly used unit for magnetic moments.

In a many-atom system, because of the exchange interaction between neighbouring atoms, magnetic moments of 3d atoms align either in parallel or antiparallel under a magnetic field, in order to lower the overall energy. Materials with parallel alignment of atomic magnetic moments are known as ferromagnetic materials while antiparallel alignments correspond to antiferromagnetic materials. The exchange interaction is a purely quantum effect acting at very short range <sup>(107)</sup>, *i.e.*, between neighbouring electrons or atoms, and there is no analogue in classical physics. The exchange interaction between neighbouring electrons is the fundamental of Hund's rules while when exchange interaction functions to the neighbouring atoms; it determines the

classification of different types of materials, *i.e.*, anti-ferromagnetic or ferromagnetic materials, and their corresponding magnetic properties. The relationship between the strength of the exchange interaction and the inter-atom separation for different materials is reflected in Bethe-Slater curve <sup>(120)</sup>; see Figure 1- 10 in Chapter 1. Shortly speaking, both anti-ferromagnetic and ferromagnetic exchange interaction will be weakened by enlarging the inter-atom separation.

To give an example, chromium (Cr), with an electron configuration of  $3d^54s^1$ , has 6 unpaired electrons, which leads to an atomic magnetic moment of  $5 \mu_B$  as only  $3d$  electrons contribute to the magnetism. However, in the bulk phase, because the neighbouring atomic magnetic moments are aligned in opposite directions when being magnetized, no magnetism can be detected. Therefore Cr manifests antiferromagnetism in the bulk phase. In contrast, iron (Fe), with an electron configuration of  $3d^54s^2$  and an atomic magnetic moment of  $6 \mu_B$ , has aligned atomic magnetic moments when subjected to an external magnetic field due to the exchange interaction. It is also the exchange interaction that can lead to a spontaneous internal magnetic field. Hence remanent magnetization can be detected after the external field is removed. Materials including Fe, Co and Ni are known as ferromagnetic materials.

Even with aligned magnetic moments, magnetism in many-atom ferromagnetic systems cannot reach the atomic limit because both orbital and spin angular momentum can be quenched. With the high electron density in the outer space from the nuclei,  $3d$  electrons can interact with the crystal field which quenches the orbital contribution to the magnetism <sup>(107)</sup>. For spins, electrons of neighbouring atoms will interact and the discrete energy levels evolve into an energy band. The population of the bands for opposite spins are unbalanced, resulting in net unpaired electrons that contribute to the magnetism in many-atom systems. In the bulk phase, each band has a fixed population; hence bulk materials generally have a specific value of magnetisation. For example, the bulk phase of Fe has a magnetic moment of  $2.2 \mu_B/\text{atom}$  while for Ni it is only  $0.6 \mu_B/\text{atom}$ , which is much lower than the theoretical limit of  $3 \mu_B/\text{atom}$ . On the other hand, for rare earth materials, due to the distribution of electrons near the nuclei, magnetic moments of atoms in the crystal are decoupled. Consequently, the measured magnetism of rare earth metals is almost identical to

their theoretical limits, *e.g.* the ratio of measured magnetism and the maximum theoretical value for Gd is  $M_{\text{exp}}/M_{\text{theo}} = 7.63/7$ .

A systematic study on how magnetism evolves from atomic level to bulk as atoms gradually aggregate into clusters was reported by Billas *et al.* by measuring the magnetizations of ferromagnetic clusters,  $X_n$  (X for Fe, Co, and Ni,  $n = 25 - 700$ ), in a vacuum at 78 K <sup>(196)</sup>. It was shown that the magnetizations of all the three materials gradually decline from a high level down to the bulk phase value as the cluster size increases. Clusters composed of over a few hundred atoms have roughly the same magnetic moments as the bulk materials. Another study on evolution of the magnetism of antiferromagnetic materials showed that small clusters of Cr can possess strong ferromagnetism <sup>(197)</sup>. The magnetic moments of smaller clusters (fewer than 80 atoms) varies with the cluster size and possess a peak magnetisation of  $1.16 \mu_B/\text{atom}$  for  $\text{Cr}_{58}$  cluster. For clusters containing over 80 atoms, the magnetisation monotonously decays with the increase of cluster size till zero.

Magnetic nanomaterials, often containing at least a few hundred atoms, are essential to next generation nanoproducts. Therefore their magnetic properties are of increasing research interest. In the following sections we will first briefly review the progress in the study of nanomaterials of both Cr and Fe as examples of antiferromagnetic and ferromagnetic nanomaterials, respectively, with reference to our studies on these two nanomaterials.

### **5.1.2 Antiferromagnetic Materials at the Nanoscale**

Chromium, which has a Néel temperature of 312 K in the bulk, is one of the most important antiferromagnetic materials. One of the most interesting applications of Cr is as the intervening material sandwiched between ferromagnetic thin films (such as Fe) to form a (001)Fe/(001)Cr superlattice. When an electric current and a magnetic field are both added along the (110) direction in the plane of layer, the electric resistance decreases during the magnetization process and remains constant when the magnetization is saturated. The lower limit of the resistance that the superlattice can reach is highly dependent on the Cr film thickness. The thinner the Cr film is, the lower

resistance it can possess <sup>(198, 199)</sup>. This effect is known as Giant Magnetoresistance (GMR). The tuneable electrical resistance of such a superlattice results from the magnetization alignment of the adjacent ferromagnetic layers either in parallel or antiparallel, which can be controlled by the antiferromagnetic coupling induced by the Cr layer under an external magnetic field. GMR has been widely used, for example, in magnetic field sensors <sup>(200)</sup>, read heads in magnetic recording <sup>(201)</sup> and magnetoresistive random-access memory (MRAM) <sup>(202)</sup>. The 2007 Nobel Prize in Physics was awarded to Albert Fert and Peter Grünberg for the discovery of GMR.

Another extraordinary effect caused by antiferromagnetic materials is the exchange bias (EB), which was initially discovered in Co/CoO core-shell nanoparticles with a diameter of 20 nm <sup>(203)</sup>. EB effects occur at the interface of a ferromagnetic (FM) material and an antiferromagnetic (AFM) material. The mechanism of EB can be explained as follows. The magnetic moments of the AFM material at the interface will enhance the magnetization of the FM materials when the external magnetic field is parallel to the AFM magnetic moments pinned at the interface. On the other hand, magnetic moments of the AFM material at the interface will prevent the FM material being demagnetized when the external field reverses its direction. This is reflected in experimental measurements, where EB causes a horizontal shift in the magnetization hysteresis loop.

Currently most investigations of EB focus on thin films <sup>(204, 205)</sup> because a stronger interface effect between FM and AFM materials can be realized when compared with core-shell nanoparticles. EB effects in bi-layer thin films have been applied to the spin valves used in read heads <sup>(206)</sup>. EB effects of core-shell nanoparticles have also attracted increasing interest recently due to its importance not only in study of fundamental theories of nanomagnetism but also in potential applications such as the single nanoparticle storage by overcoming the superparamagnetic limit <sup>(207)</sup> and hyperthermia treatment of cancer <sup>(208)</sup>. As a good example of AFM materials, the EB effect of Cr has also attracted broad research interest <sup>(209, 210)</sup>.

The magnetism of AFM Cr has also attracted great interest <sup>(211-214)</sup> since it was predicted by Louis Néel that very small AFM materials with a reduction of Néel

temperature may have superparamagnetic or even weak ferromagnetic properties due to the uncompensated spin on the surface <sup>(215)</sup>. The uncompensated spins at the surface are basically the residual net spins on the surface after each pair of antiparallel aligned spins cancel each other out, giving rise to near zero magnetization. In the past few decades this model has been applied to explain the weak magnetic properties in diamagnetic materials such as CuO <sup>(216)</sup>, antiferromagnetic NiO <sup>(217, 218)</sup> and ferrimagnetic ferritin <sup>(219, 220)</sup>. However, the AFM NiO in Ref. (217, 218) does not show any superparamagnetic or ferromagnetic properties, although weak paramagnetic behaviour was observed. Since the uncompensated surface spin is a surface effect, it is expected to be more prominent when the surface to volume ratio increases. Thus the magnetization generated by this mechanism should be stronger as the particle size gets smaller <sup>(221)</sup>.

Another mechanism to explain the magnetization detected in AFM nanostructures is the canted spin model. Slightly different from the uncompensated spin theory, the canted spin model assumes that all the spins located at the particle surface can respond to an external magnetic field as a superparamagnetic material, and are thus canted towards the external magnetic field to some extent; therefore they can all partially contribute to the overall magnetization. This theory is designed to explain the stronger magnetization detected in an AFM system than that could be explained by the mechanism of uncompensated surface spin <sup>(222)</sup>. Canted spin effect is supposed to be more prominent at defect positions in nanostructures <sup>(223)</sup>, *i.e.*, position with larger curvature. An illustration of the canted spin model is shown in Figure 5- 1.

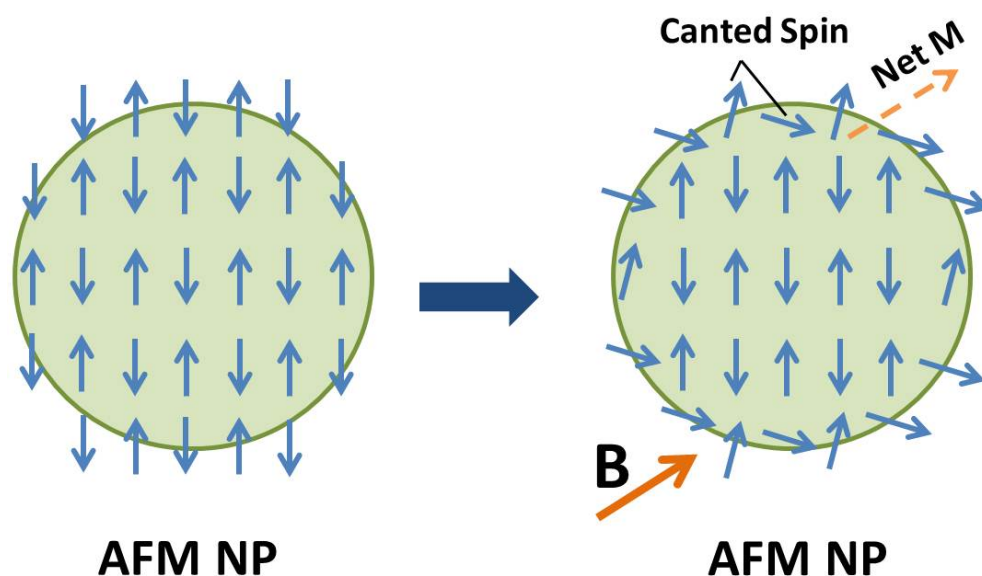


**Figure 5- 1** Illustration of spin-canting induced magnetization for AFM nanoparticles.

To date, the magnetic properties of pure Cr nanostructures has been only reported in two studies, to the best of our knowledge <sup>(126, 222)</sup>. In both attempts, very small magnetization, of less than  $0.02 \mu_B/\text{atom}$ , was detected from Cr nanoparticles at 5 K and the M-H curves in both cases were not saturated even at external fields as high as 5 T. Saturation magnetization at modest magnetic field is an indicator of ferromagnetism and superferromagnetism, which means in both cases Cr nanoparticles formed remain antiferromagnetic. In another experiment Cr was doped in ZnO nanoparticles at a low concentration of 7%, and saturated M-H curves were obtained <sup>(224)</sup>. When the Cr concentration was raised above 12%, the M-H curve could no longer be saturated. Therefore it is not entirely convincing that it is the Cr that independently delivers the ferromagnetism.

### **5.1.3 Ferromagnetic Materials at the Nanoscale**

Ferromagnetic nanomaterials can potentially be used in data storage, drug delivery, cell labelling, hyperthermia treatment and MR imaging <sup>(140, 225, 226)</sup>. One of the most important aims of research into ferromagnetic nanomaterials is to obtain stronger saturation magnetisation while maintaining small particle sizes. Higher magnetisation

is desirable for various applications, one of which is the potential in hyperthermia treatment of cancer. Hyperthermia treatment is achieved by tagging magnetic nanoparticles to the tumour through organic ligands, and then switching an external magnetic field on and off. During this process magnetic nanoparticles are magnetized and demagnetized, and the magnetic energy of nanoparticles is transferred into heat. If a critical local temperature can be reached, tumours will be destroyed. This method is potentially applicable to many types of cancer and results in nearly no harm to non-cancerous cells. However, at current stage, current nanoparticles do not possess sufficient magnetization to heat the tumour to a temperature sufficient to kill cells – about 45 °C <sup>(227)</sup>, since the ability to deliver magnetic energy is proportional to the magnetic moments of the nanoparticles. Currently most research on ferromagnetic nanomaterials focuses on Fe, which gives rise to the strongest ferromagnetism. Given the similarities of their electronic configurations, Ni and Co have similar magnetic properties. Therefore there is also broad interest in the nanomagnetism of Ni and Co.

Magnetic nanoparticles can be synthesized via various methods such as wet chemical methods, chemical vapour deposition and laser ablation. The magnetism of nanoparticles is highly dependent on the synthetic process.

Table 5- 1 lists the saturation magnetization of Fe nanoparticles measured at 300 K which were formed in different ways including chemical vapour deposition, plasma fragmentation and a wet chemical method. The average particle diameters in the table are all around 10 nm. It is seen that the saturation magnetisations are quite different in these examples, varying from 1.63  $\mu_B$ /atom to 0.08  $\mu_B$ /atom. Even using similar preparation protocols, the magnetism measured by different labs can also be quite different. As shown in the first two rows, Fe particles formed by chemical vapour condensation have been produced with the saturation magnetizations that differ by a factor of 8. The difference in magnetization is also noticed in wet chemical synthesis, which is the most widely used bottom-up technique for the fabrication of nanoparticles. For example, a batch of nanoparticles with an average diameter of 4.5 nm gave 1.34  $\mu_B$ /atom saturation magnetization at 300 K <sup>(228)</sup>, and in a different experiment another batch of Fe particles with an average diameter of 4 nm gave rise to a saturation magnetization of only 0.046  $\mu_B$ /atom <sup>(229)</sup>.

**Table 5- 1 Saturation magnetization ( $M_s$ ) of Fe nanoparticles, using different synthetic methods with similar diameter of about 10 nm, measured at room temperature.**

<b>Synthesis Method</b>	<b>Size (nm)</b>	<b><math>M_s</math> (<math>\mu_B</math>/atom)</b>
Chemical Vapour Deposition <sup>a</sup>	11	0.08 (300 K)
Chemical Vapour Deposition <sup>b</sup>	10	0.63 (300 K)
Plasma Fragmentation <sup>c</sup>	10	1.25 (300 K)
Wet Chemistry <sup>d</sup>	10	1.63 (300 K)

**Data are acquired from a: Ref. (230); b: Ref. (231); c: Ref. (232); d: Ref. (228).**

The magnetization response of Fe nanoparticles is also dependent on the internal structure and more specifically, the inter-atom separation. In order to generate a better crystalline structure, an annealing process is always involved. Experiments suggest that at higher annealing temperatures, the crystalline structure is improved, as well as the magnetisation <sup>(233, 234)</sup>.

Nanoparticle size is another factor that can affect the magnetism of the product. Table 5- 2 is taken from a series of studies by Kura *et al.* <sup>(228)</sup>. The authors used a wet chemistry method to produce Fe nanoparticles with different sizes and measured the magnetism of each batch of products at 5 K and 300 K. As the particle size decreases, the saturation magnetization at both temperatures monotonically decreases.

**Table 5- 2 Size dependence of the saturation magnetisation of Fe nanoparticles synthesized by wet chemical method.**

<b>Size (nm)</b>	<b>Ms (<math>\mu_B</math>/atom)</b>	
10	1.92 (5 K)	1.63 (300 K)
8	1.85 (5 K)	1.56 (300 K)
6.8	1.84 (5 K)	1.55 (300 K)
5.5	1.86 (5 K)	1.45 (300 K)
4.5	1.80 (5 K)	1.34 (300 K)
2.3	1.68 (5 K)	1.17 (300 K)

**Data are collected from Ref. (228).**

So far all the studies reported in the literature show lower magnetism possessed by ferromagnetic nanoparticles than their bulk value and the magnetization increases with the particle size. This is inconsistent with the magnetism at small cluster level. As mentioned earlier, magnetism of clusters (clusters size ranging from 25 to 700 atoms) which are aggregated in vacuum at 78 K is between the free atom value and the bulk phase value and decays as the cluster size increases<sup>(196)</sup>. Above all, the magnetization evolution with the material size according to measurement can be summarized as follows. The magnetism of material starts to decay from the theoretical atomic limit as the cluster size increases. Normally at the cluster size of a few hundreds atoms, the magnetism drops to the bulk value. When cluster size further enlarges to the

nanoscale (normally over 500 atoms), the magnetization will drop below the bulk value and then gradually increase with the particle size grows larger, until it approaches the bulk value when the material is over micro meter scale. A qualitative variation of the magnetism of ferromagnetic material ( $M$ ) with the material size ( $N$ ) is illustrated in Figure 5- 2.

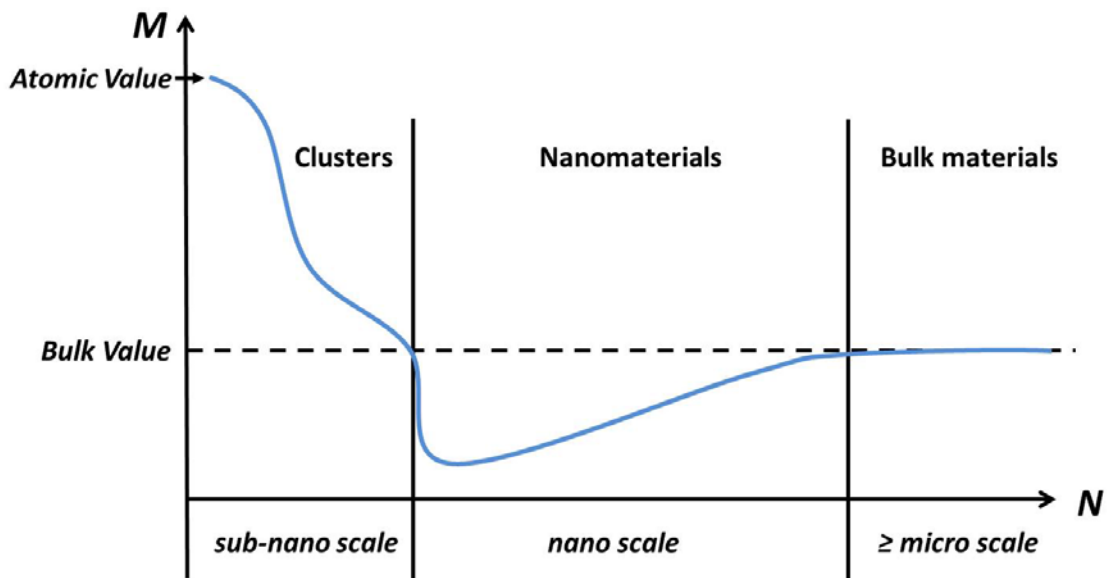


**Figure 5- 2** Illustration of the evolution of the magnetism of ferromagnetic material ( $M$ ) with the material size ( $N$ ) in different dimension scales.

A straightforward explanation of the positive correlation between the magnetism and the size of the nanoparticle is the oxidation at the nanoparticle surface, which can quench the magnetism. As the particle size decreases, the surface to volume ratio increases, the oxidation becomes more significant, and the magnetism decreases accordingly.

To avoid oxidation, noble metal such as Au or Ag can be used to coat ferromagnetic nanoparticles. Therefore fabrication of core-shell nanoparticles is another hot topic in nano magnetic research. Core-shell structures can offer added advantages, such as, reducing the toxicity of nanoparticles. Ferromagnetic materials such as Fe are toxic to human cells when they aggregate and this can lead to thrombosis. Adding a noble metal shell can improve the biocompatibility and chemical stability of the ferromagnetic nanoparticle <sup>(235)</sup>.

However, Au or Ag coated core-shell nanoparticles reported so far all manifest far lower magnetic moments when compared with the bulk metal value<sup>(236-238)</sup>, although they are higher than uncoated nanoparticles. This is thought to be due to the oxidation before the shell is coated in the synthesis process<sup>(239-241)</sup>, or it might be from coupling between the core and the shell atoms at the interface<sup>(238)</sup>. Theoretical calculations suggest Fe/Au core-shell clusters may possess higher magnetism than pure Fe clusters because the coupling at the interface can slightly magnetize the Au shell<sup>(235)</sup>. However the Fe core taken into account for simulation was consisted of fewer than 13 atoms and the Au shell was smaller than 42 atoms, and the magnetism enhancement was only marginal compared to pure Fe. Therefore this calculation result may not be able to apply to the nanoparticles which are consisted by at least a few hundreds atoms.

Another possibility for the low magnetization of magnetic nanoparticles may lie in an imperfect crystalline structure. As mentioned above, annealing is necessary to improve the crystalline structure and the higher the annealing temperature, the more crystalline will the structure be. When annealing to sufficiently high temperature (such as 800 °C), the magnetism of Fe nanoparticles can approach the bulk value of 2.22  $\mu_B$ /atom<sup>(233, 234)</sup>. If we assume the bulk value of magnetisation corresponds to the ideal crystalline structure, this means the synthesized nanoparticles have ineligible defects in their internal structure which need removing by annealing. It is unclear whether the annealing process enlarges or shortens the average inter-atom separation in the nanoparticles that responsible for the improvement of the magnetism. What is known is that the defects within the synthesized nanoparticles should have a negative correlation with the particle size – the smaller the particle is, the more defects in the crystalline structure and the lower magnetisation per atom it possesses when comparing with the bulk value.

To date, there is no report on the synthesis of magnetic nanoparticles under very cold conditions, as delivered by helium droplets. In this chapter, we will present our pioneering research in the synthesis of magnetic nanostructures in helium droplets and the characterization of their magnetic properties. Cr and Ni have been studied as representatives of antiferromagnetic and ferromagnetic materials, respectively. For the first time, antiferromagnetic element (Cr) converting to the ferromagnetic is

observed at nano scale, and the magnetism of ferromagnetic nanoparticle (Ni) is found to be able to approach the theoretical limit.

## 5.2 Experimental

We have synthesized magnetic nanomaterials including Cr nanoparticles and nanowires, bare Ni nanoparticles, core-shell Ni/Au and Ni/Ag core-shell nanoparticles. All of the samples were formed using the helium droplet apparatus described in detail in Chapter 2. Briefly, helium gas, with a stagnation pressure of 15 bar, is pre-cooled to a temperature from 9.5 K to 6 K which determines the initial size of helium droplets. A collimated helium droplet beam is then formed by passing the expanding droplet flow through a skimmer, and when the beam then enters metal evaporator zone. When more than one type of material is evaporated in different ovens, core-shell nanostructures will be formed. Each oven temperature was controlled in order to obtain desired the nanoparticle size. Downstream of the oven evaporators, a thin film deposition monitor can be moved into the pathway of the droplet beam, allowing the mass of the all the dopants carried in the helium beam to be detected. The mass of the samples can also be deduced from TEM images. Assuming spherical shapes for the nanoparticles and cylindrical shapes for the nanowires, once the dimension of each nanoparticle/nanowire is known, we can work out the total volume of the samples. At a constant doping rate the total mass of the deposited samples can then be calculated.

Beyond the thin film deposition monitor, helium droplets are allowed to hit a solid surface where helium atoms are evaporated, leaving nanoparticles or nanowires on the deposition targets. For TEM investigation, lacey carbon substrates are used while an organic thermoplastic polymer substrate (Polyether ether ketone (PEEK)) was employed for the measurement of magnetic properties. Further downstream, a quadrupole mass spectrometer (QMS) is used for simple characterization of the helium droplet beam, including checking any impurities from background gases and for aligning the beam. The QMS is also useful for optimizing the oven temperature by inspecting the formation of small metal clusters.

The magnetic properties of the samples were measured by vibrational sampling magnetometer (VSM) and superconducting quantum interference device (SQUID) magnetometers in collaboration with the National Research Council in Italy and Shanghai Jiaotong University in China.

In the measurement of magnetic properties the PEEK substrate needs to be wrapped on a diamagnetic glass rod. Consequentially the raw data of the measured magnetic properties will include a contribution from the diamagnetic rod and the diamagnetic PEEK substrate. It was found that the PEEK substrate has a non-linear response to the high external field ( $B > 3.5$  T) at low temperature ( $T < 10$  K) and a linear response in other circumstances, as seen in Figure 5- 3 (a). The substrate holder is absolute diamagnetic, which shows a negative linear response to the magnetic field across the full temperature range.

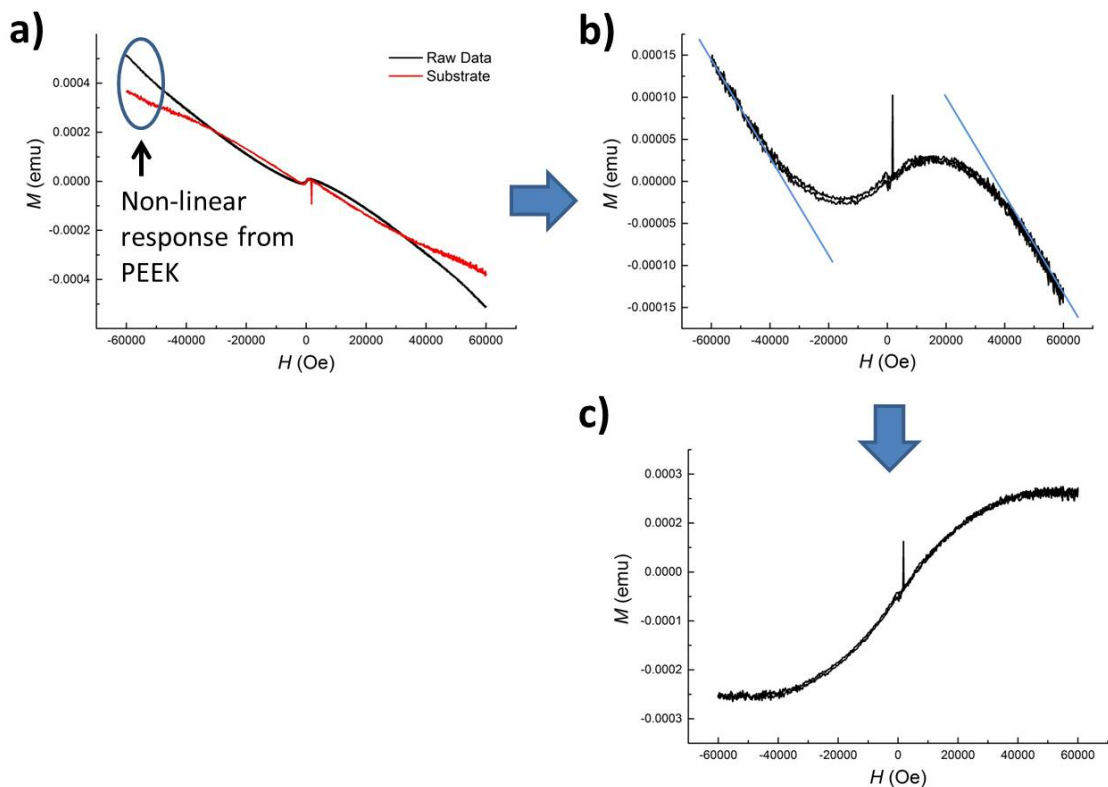


**Figure 5- 3 Data processing of the M-H curves of Cr nanoparticles. (a) M-H curve of the raw data, which contains contributions from sample, PEEK substrate and the glass rod. (b) M-H curve after subtraction of the substrate contribution. The blue solid lines show the gradient of the M-H curve. (c) M-H curve after subtraction of the linear contribution from the glass rod.**

In order to obtain the magnetic response of the sample, we have also measured the magnetization responses of a blank PEEK substrate of the same size. The M-H curve of the blank PEEK substrates was first subtracted from the Cr sample (Figure 5- 3 (a) – (b)). The linear diamagnetic component of the rest M-H curve was then removed by subtracting the product of the diamagnetic susceptibility multiplying the external magnetic field (Figure 5- 3 (b) – (c)). The diamagnetic susceptibility is the gradient of the M-H line when saturation is reached.

### **5.3 Ferromagnetic Cr Nanomaterials**

In this section the preliminary results on forming nanoparticles and nanowires of Cr – a well-known antiferromagnetic material are reported. The magnetic properties of these nano-objects will also be presented.

#### **5.3.1 Cr Mass Spectrum**

In order to gain some idea about a suitable operation temperature for Cr oven, we observed Cr cluster mass spectrum. A typical mass spectrum of the Cr cluster ions in the mass/charge range of 50 – 1000 is shown in Figure 5- 4, which was recorded at a source temperature of  $T_0 = 12$  K and a Cr oven temperature of  $T_{Cr} = 1275$  K. An even-odd alternation behaviour appearing in small clusters range can be clearly seen and which has been reported previously<sup>(242)</sup>. No other obvious peak besides  $Cr_n^+$  (except for  $He_n^+$  ions at low mass) can be observed in the mass spectrum, which means there are few impurities in our apparatus. Thus nanostructures formed in the droplets should be free of contamination.

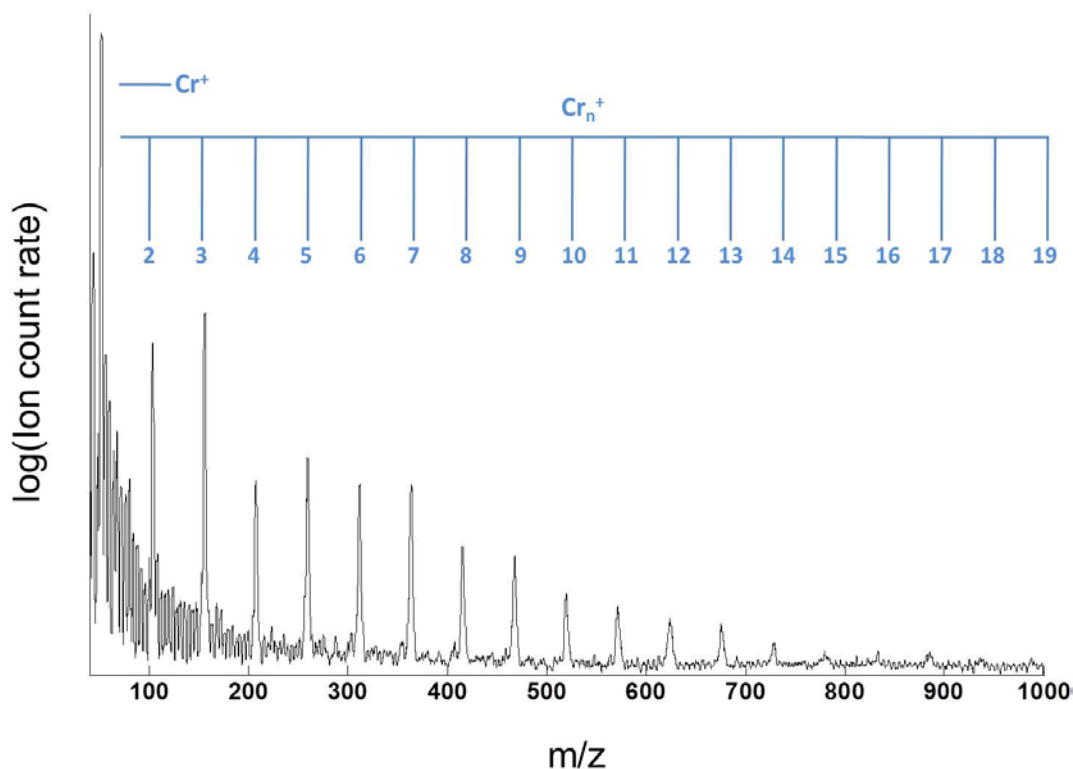
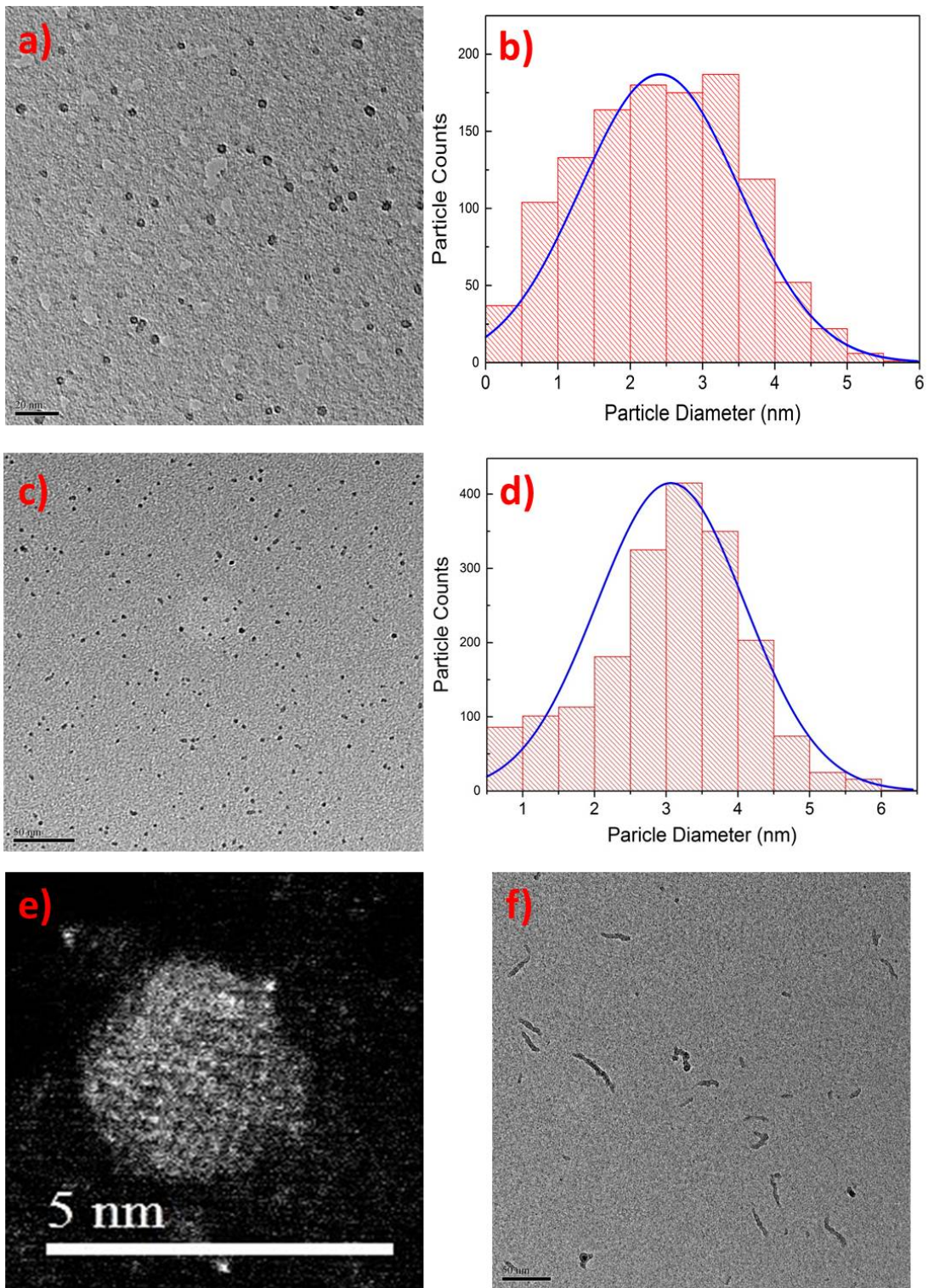


Figure 5- 4 Mass spectrum of  $\text{Cr}_n^+$  ( $n = 1 - 19$ ) detected at  $T_0 = 12$  K and  $T_{\text{Cr}} = 1275$  K.

### 5.3.2 TEM Images of Cr Nanoparticles and Nanowires

TEM images of Cr nanoparticles formed at two different source temperatures,  $T_0 = 9.5$  K and 8 K (corresponding to the initial helium droplets composed of  $1 \times 10^5$  and  $7 \times 10^6$  helium atoms, respectively) are shown in Figure 5- 5 (a – d). In both cases the Cr oven was heated to 1275 K. The size distribution was obtained based on over 1000 nanoparticles and follows a Gaussian distribution. The mean size of Cr nanoparticles formed were  $2.4 \pm 1.1$  nm and  $3.16 \pm 1.04$  nm, respectively, for  $T_0 = 9.5$  K and 8 K. A high resolution TEM image of a Cr nanoparticle is shown in Figure 5- 5 (e), which was taken by our collaborators in Glasgow using the SuperSTEM facility at Manchester.

Cr nanowires were formed at  $T_0 = 6$  K, corresponding to a droplet size of  $3 \times 10^8$  helium atoms (the Cr oven was maintained at 1275 K). A representative TEM image of the Cr nanowires is shown in Figure 5- 5 (f). The average diameter of the Cr nanowires is about  $3.57 \pm 0.48$  nm, while the length ranges from a few to a few of tens nanometres.



**Figure 5- 5 (a) TEM image of Cr nanoparticles deposited at  $T_0 = 9.5$  K. (b) Size distribution of Cr nanoparticles deposited at  $T_0 = 9.5$  K. (c) TEM image of Cr nanoparticles deposited at  $T_0 = 8$  K. (d) Size distribution of Cr nanoparticles deposited at  $T_0 = 8$  K. (e) High resolution TEM image of Cr nanoparticles deposited at  $T_0 = 9.5$  K. (f) TEM image of Cr nanowires deposited at  $T_0 = 6$  K. All of the TEM samples were deposited for 5 minutes.**

All the TEM samples were deposited for 5 minutes. The deposition rates were calculated according to the TEM images as 2.19 ng/min, 2.52 ng/min and 3.56 ng/min for nanoparticles formed at 9.5 K, nanoparticles formed at 8 K and nanowires respectively, resulting a total mass of 0.92  $\mu\text{g}$ , 1.06  $\mu\text{g}$  and 1.5  $\mu\text{g}$  for a 7-hour deposition, respectively.

### **5.3.3 Magnetic Properties of Cr Nanoparticles**

The magnetic properties of Cr nanoparticles and nanowires were characterized by hysteresis curves, which were measured using SQUIDs in the National Research Council, Italy and in Shanghai Jiaotong University, China. For the smaller Cr nanoparticles with a mean diameter of 2.4 nm, the M-H curves measured at 300 K and 5 K are shown in Figure 5- 6. Typical ferromagnetic features, including a saturated M-H curve, a non-zero coercivity and a non-zero remanent magnetization, can be observed at both temperatures, as shown in detail in the inset. The saturation magnetization at 300 K is  $\sim 0.45 \mu_{\text{B}}/\text{atom}$ , which is close to the bulk value of ferromagnetic Ni nanoparticles ( $\sim 0.6 \mu_{\text{B}}/\text{atom}$ )<sup>(117, 118)</sup>. At 5 K, the saturation magnetization increases to a value as high as  $\sim 1.29 \mu_{\text{B}}/\text{atom}$ , and the hysteresis loop becomes broader, as seen from the inset of the figure. An exchange bias (EB) effect, which shifts of hysteresis loop by as large as 84 Oe, can be observed at 5 K. The EB effect in Cr NPs at low temperature has been reported previously<sup>(126, 222)</sup>, and was attributed to surface oxidation, where the magnetized Cr nanoparticle core is supposed to play a weakly-ferromagnetic role while the surface oxidation acts as the antiferromagnetic shell<sup>(126, 222)</sup>.

The magnetic properties of 2.4 nm Cr nanoparticles are summarized in Table 5- 3. This table includes the saturated magnetization and the remanent magnetization (the magnetization when  $H = 0$ ) in units of Bohr magneton/atom, and the coercivity on both sides of H axis with the temperatures varying from 300 K to 5 K. The saturation magnetization increases at lower temperature with a minimum observed at 25 K. Both remanence and coercivity increase at lower temperature, with maxima at 10 K.

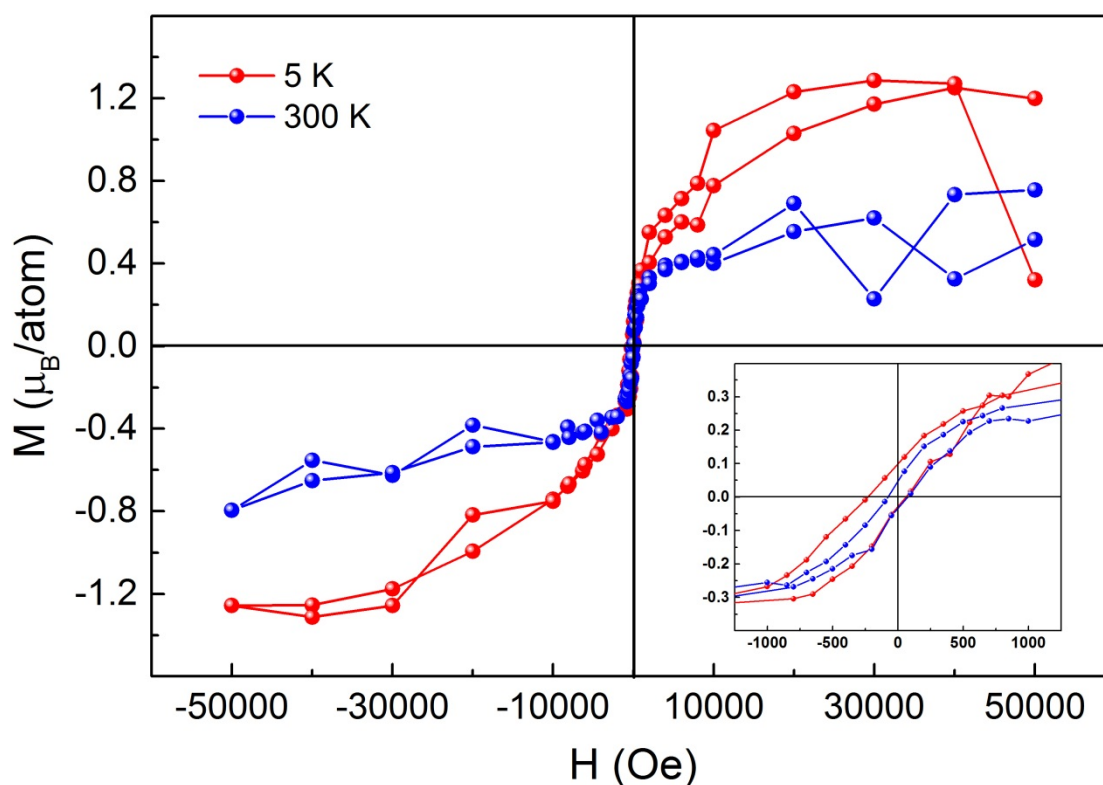
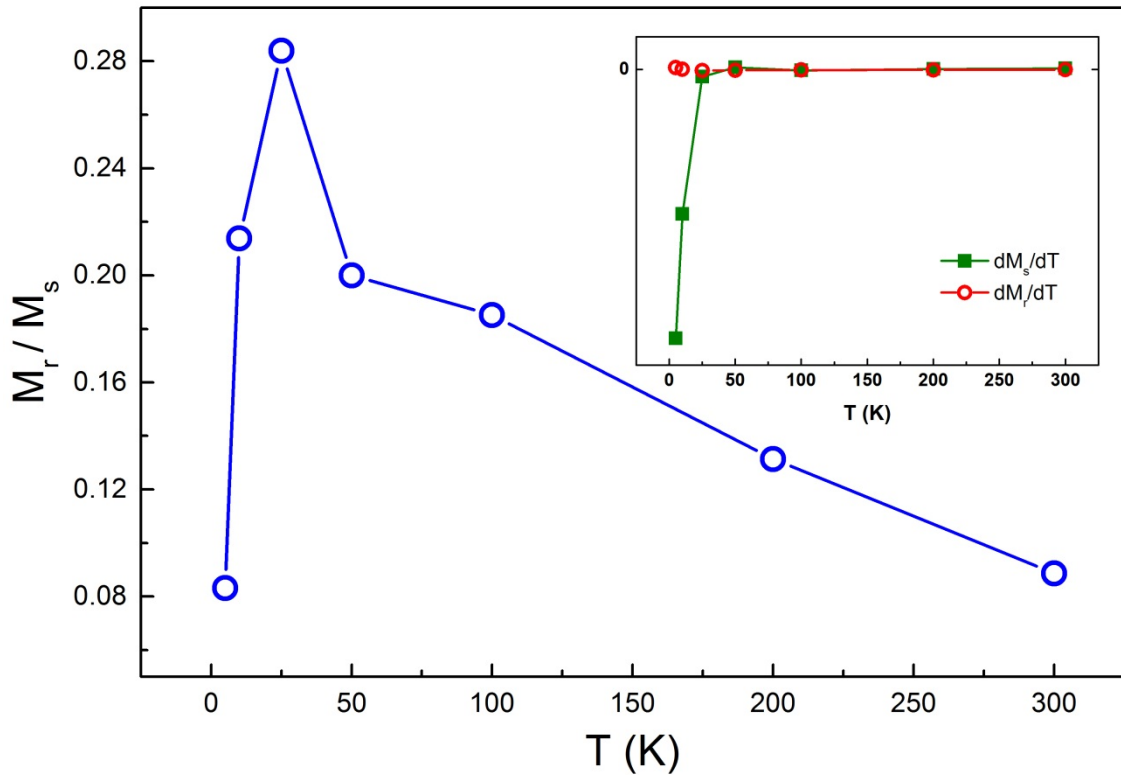


Figure 5- 6 M-H curves of Cr nanoparticles with mean diameters of 2.4 nm measured at 300 K and 5 K, respectively. The insert shows the expanded view of the hysteresis loop near the origin.

Table 5- 3 Magnetic properties of Cr nanoparticle without a diameter of 2.4 nm, at different temperatures.

Temperature (K)	Saturated Magnetization ( $\mu_B/\text{atom}$ )	Remanent Magnetization ( $\mu_B/\text{atom}$ )	Left Coercivity (Oe)	Right Coercivity (Oe)
5	1.29	0.11	-230	63
10	0.53	0.11	-272	246
25	0.36	0.10	-221	207
50	0.44	0.09	-170	169
100	0.4	0.07	-140	145
200	0.38	0.05	-90	89
300	0.45	0.04	-78	76

The variation of saturation and remanence with temperature are not monotonic and they both have minima at the same temperature (25 K). To understand this observation we investigate the dependence of the ratio of remanence and saturation ( $M_r/M_s$ ) on temperature, as shown in Figure 5- 7. The  $M_r/M_s$  values of the nanoparticles are generally low (< 50%) regardless of temperature, which is typical for 3d ferromagnetic nanoparticles<sup>(243, 244)</sup>. At room temperature  $M_r/M_s$  is only around 9%, and then sharply increases at lower temperature, with a peak value of 28% at 25 K. Below 25 K, the relative remanence decreases, *i.e.*, to only 8% at 5 K.



**Figure 5- 7 Ratio of the remanent magnetization to the saturation magnetization of Cr nanoparticles at different temperatures. The inset shows the gradient of the saturation and remanence with respect to temperature.**

The inset in Figure 5- 7 shows the gradient of both saturation and remanence. Remanence is an intrinsic feature of ferromagnetism, which is thought to be the consequence of the exchange interaction between the magnetic moments of the neighbouring atoms<sup>(245, 246)</sup>.  $dM_s/dT$  keeps a small constant at higher temperature while below 25 K it sharply decrease in the negative value region, indicating the

saturation enhancement is in a larger rate than in higher temperature as temperature decreases. On the other hand,  $dM_r/dT$  almost stabilizes at a small constant value in all of the temperature range. That suggests when  $T < 25$  K, the sharp increase of the atomic magnetization inside of Cr nanoparticles does not lead the exchange interaction between neighbouring atoms to increase synchronously. In other words, at least in low temperature range, exchange interaction between atoms is insignificant in this many-atom system. A longer inter-atom separation should be expected inside of our Cr nanoparticles since exchange interaction is a short-range effect and it will get weakened as larger inter-atom separation (see Bethe-Slater curve in Figure 1- 10, Chapter 1). Therefore atomic magnetic moment can increase independently in our nanoparticle, behaves atom-like.

#### **5.3.4 Magnetic Properties of Larger Cr Nanoparticles**

The effect of particle size on the magnetic properties of Cr nanoparticles has also been investigated. The M-H curves of larger nanoparticles, with average diameter of about 3.2 nm, were measured at Shanghai Jiaotong University. We have obtained results with all the key features similar to the smaller nanoparticles measured in Italy (see section 5.3.3). The M-H curve for this batch of nanoparticles was measured down to 3 K with a saturation of about  $1.83 \mu_B/\text{atom}$ , and the saturation magnetizations at different temperatures are shown in Figure 5- 8 together with the same quantities for smaller Cr nanoparticles (2.4 nm). The solid lines plotted are the fit curves by hyperbolic cotangent function, which are well fit to our measured data. The two fit curves are almost identical, indicating the measured magnetization for different size of Cr nanoparticles are consistent. The upper limit for the magnetization (at 0 K) of our samples can also be predicted according to the fit curves, of  $1.62 \mu_B/\text{atom}$  for 2.4 nm Cr nanoparticles and  $2.18 \mu_B/\text{atom}$  for 3.2 nm Cr nanoparticles.

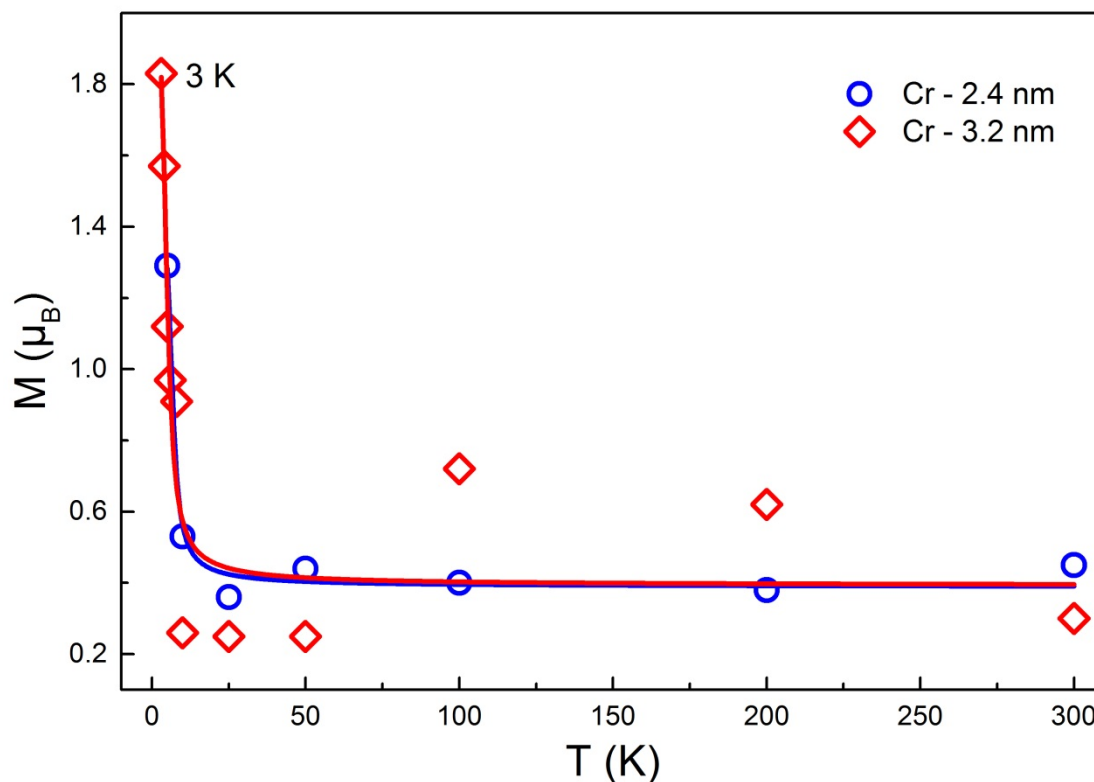


Figure 5- 8 Comparison of saturation magnetization of the two different sized Cr nanoparticles at different temperatures. The solid lines are fitted curves.

### 5.3.5 Magnetic Properties of Cr Nanowires

M-H curves of Cr nanowires at temperatures of 300 K and 5 K are shown in Figure 5- 9 and the key magnetic properties are summarized in Table 5- 4. Similar to the nanoparticles, ferromagnetic behaviour is obvious at all temperatures, with saturation magnetization and remanence at each temperature slightly lower than for the nanoparticles.

The coercivity of the nanowires has almost the same trend as the nanoparticles, *i.e.*, the coercivity grows as the temperature decreases. However, unlike nanoparticles, no exchange bias can be observed at any temperature, which is probably due to the smaller surface-to-volume ratio leading to insufficient oxidation in the outer layer or the relative weaker ferromagnetism of the inner core, so that the FM-AFM coupling at the interface is not as strong as in nanoparticles.

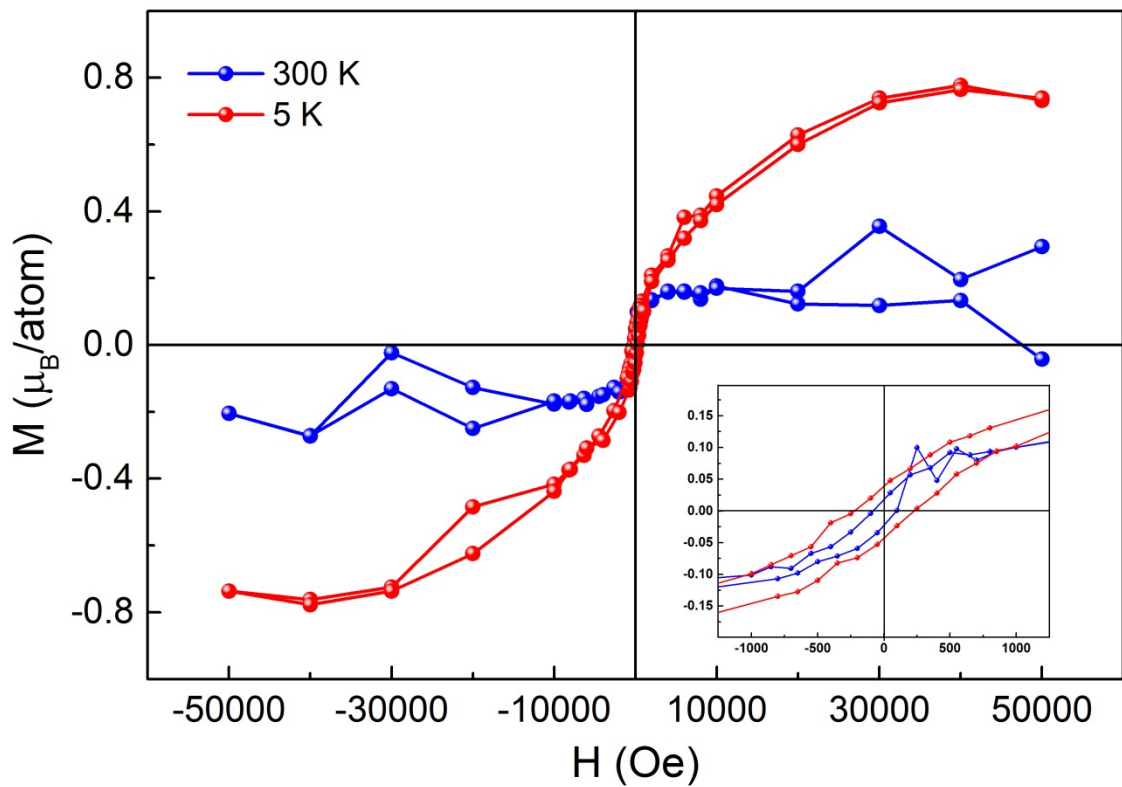
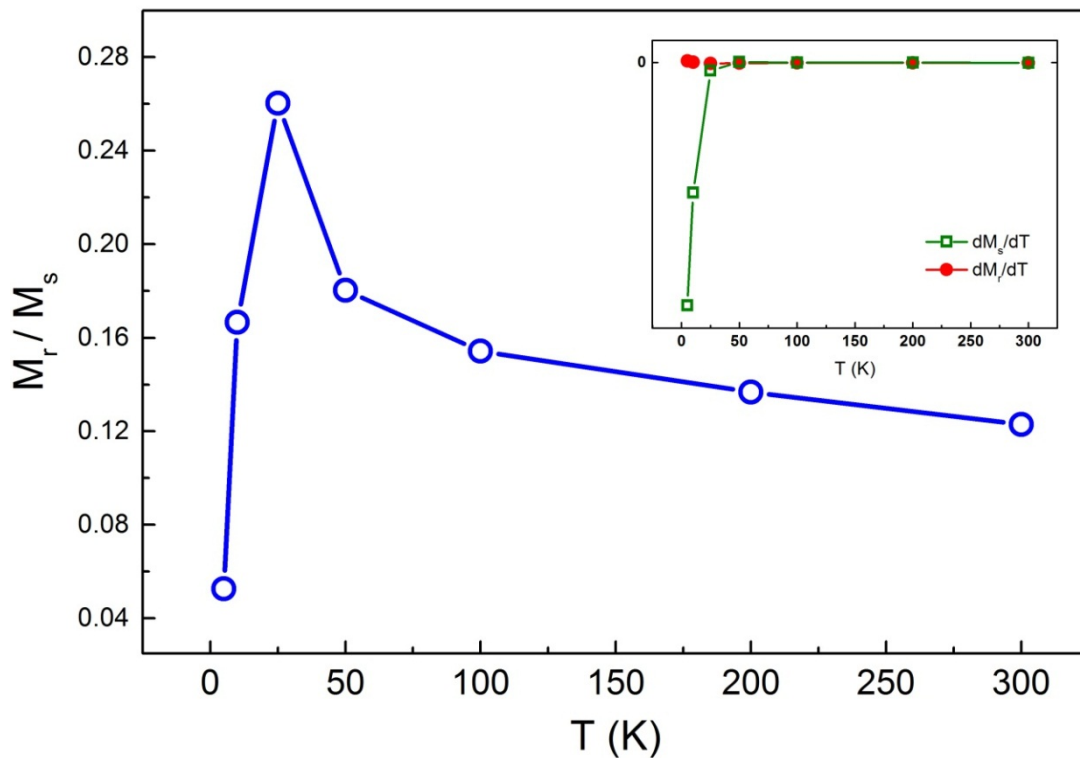


Figure 5- 9 M-H curves of Cr nanowires at 300 K and 5 K. The insert shows the expanded hysteresis loops near the origin.

Table 5- 4 Magnetic properties of Cr nanowires measured at various temperatures.

Measuring Temperature (K)	Saturated Magnetization ( $\mu_B/\text{atom}$ )	Remanent Magnetization ( $\mu_B/\text{atom}$ )	Left Coercivity (Oe)	Right Coercivity (Oe)
5	0.78	0.04	-223	228
10	0.27	0.05	-272	302
25	0.16	0.04	-232	225
50	0.17	0.03	-178	168
100	0.16	0.03	-130	139
200	0.18	0.02	-126	102
300	0.17	0.02	-82	96

The remanence to saturation ratio,  $M_r/M_s$ , of Cr nanowires follows the same general trend as for nanoparticles, including the respective changing rates ( $dM_r/dT$  and  $dM_s/dT$ ) with the temperature, shown in Figure 5- 10. A slight difference from the nanoparticles is that the  $dM_r/dT$  decays more slowly at higher temperatures. The higher thermal resistance may result from multiple magnetic domains existing in nanowires. Multi-domains lower the total energy of the system by partially misaligning the magnetic moment of each domain, and therefore nanowires can stabilize better at high temperature. The generation of multi-domains may relate to the synthesis process. As shown in Chapter 4, nanowires in helium droplets can be formed by the aggregation of individual nanoparticles formed at multiple locations in the droplets. In this case the nanoparticles/atoms pinned to the vortex lines might not possess the same orientation as the alignment of the magnetic moments delivered by the external magnetic field. As they approach the vortex lines, the circulation of helium around the vortex lines in the droplets might perturb the alignment of the magnetic moments, leading to mis-alignment of the magnetic moments. The pinning of distinct particles to the vortex lines therefore results in multiple magnetic domains, which reduces the magnetic moments of Cr nanowires when compared with their nanoparticle counterpart. This can also explain why the magneto-anisotropy of the nanoparticles and nanowires are almost identical, because nanowires are formed through the aggregation of chromium nanoparticles.



**Figure 5- 10** Variation of remanent magnetization to saturation ratio of Cr nanowires at different temperatures. The inset shows the gradient of the saturation and remanence with respect to temperature.

Table 5- 3 and Table 5- 4 show that the saturation magnetizations of nanoparticles and nanowires both experience a dip at 25 K. To get a comprehensive picture of the relation between magnetisation and temperature, a measurements of the magnetization with temperature from 2 K to 300 K (M-T curve) was carried out for Cr nanowires after a zero-field cooling (ZFC). The magnetization curve after eliminating the contribution from background is shown in Figure 5- 11. During the measurements, the applied magnetic field was maintained at 1 T in order to get a significant signal. At such a high magnetic field the nanowires were fully saturated above 10 K. We could not perform the same measurement for chromium nanoparticles because they could not show a reliable result under 1 T applied field for some reason.

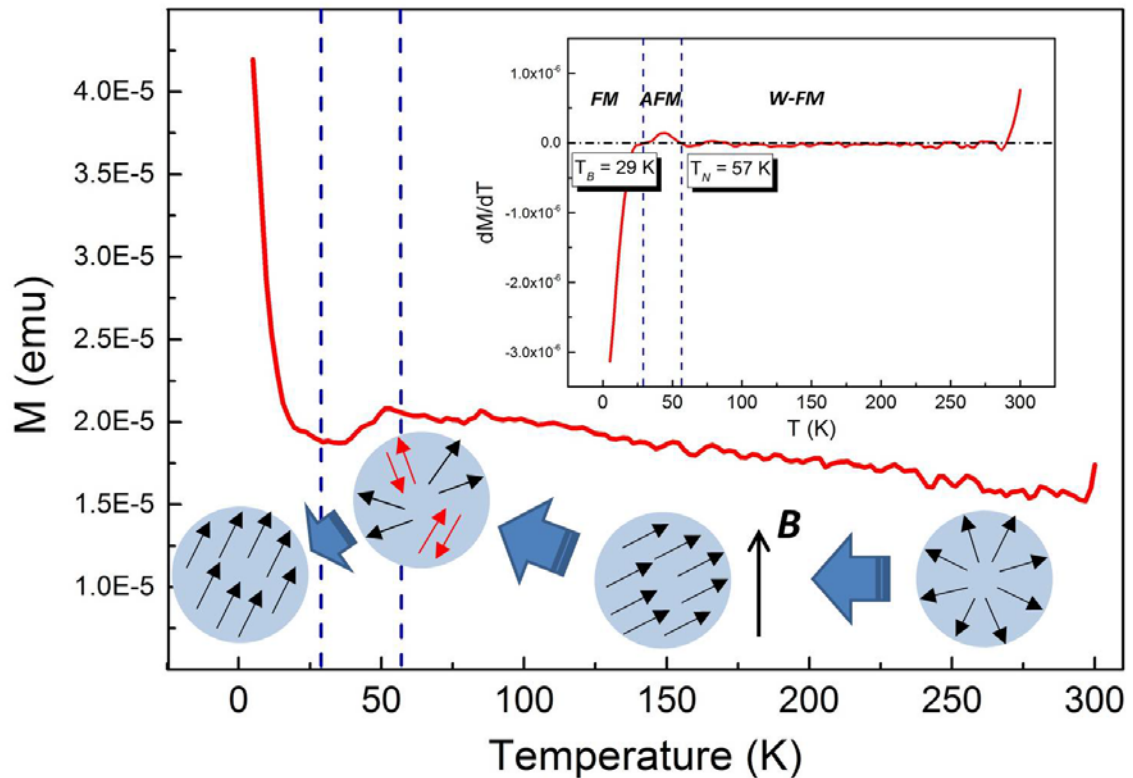


**Figure 5- 11** Variation of magnetization of Cr nanowires at different temperatures after ZFC including the rotation of magnetic moments orientation. The insert shows the gradient and the phase transition.

The M-T curve for nanowires clearly experiences three stages: (i). The magnetisation increases linearly as the temperature decreases. (ii). The magnetisation declines to a minimum. (iii). A sharp increase of magnetization at very low temperatures. The gradient, ( $dM/dT$ ), shows the boundaries between these three stages very clearly. As seen in the inset of Figure 5- 11, the constant  $dM/dT$  from 300 K to 57 K, suggests that the magnetic moments gradually align with the external field in this temperature region. After that a clear positive peak appears in the range of  $29\text{ K} < T < 57\text{ K}$ , indicating some reversal of magnetic moments back, *i.e.* antiparallel alignment, and thus the magnetization decreases with temperature. At 29 K, this antiparallel alignment reaches its maximum and therefore the magnetization reaches a local minimum. Below 29 K, the moments become parallel again and the magnetization sharply increases (in terms of  $dM/dT$  undergoes a sharp decline into the negative value).

Therefore in the temperature range of 29 K – 57 K the antiferromagnetism recovers a little as a minor magnetic order co-existing with ferromagnetic ordering. If we assign the region from 300 K to 57 K as the weak-ferromagnetic (W-FM) phase for Cr nanowires where the magnetism slowly increases as the temperature decreases, the region from 57 K to 29 K as the antiferromagnetic (AFM) phase (although AFM is only a minority in this region) and the region below 29 K as the ferromagnetic (FM) state, it can be noticed in the whole temperature range, Cr nanowires experience two state transitions, from W-FM to partially AFM and then to FM. The Néel temperature can be determined as 57 K. The blocking temperature for the ferromagnetic state is  $T_B = 29$  K, since below  $T_B$  ferromagnetism is unquestionably present in form of hugely enhanced magnetism and a broader hysteresis loop (including significantly enhanced coercivity and remanence) in the M-H curve.

### **5.3.6 Summary the Ferromagnetism of Cr Nanostructure**

The magnetic properties of the Cr nanostructures studied in this work have provided solid evidence that ferromagnetic Cr nanoparticles and nanowires have been synthesised. Key properties can be summarized as follows:

- 1) All the M-H curves, for both nanoparticles and nanowires, can be saturated at a moderate external field, even at room temperature. In comparison, the M-H curves for Cr nanoparticles reported in Ref. (222) are basically straight lines and are never saturated even at 5 K and subject to a 5 T external field. Materials with non-saturated M-H lines are normally attributed to paramagnetic materials since relation between M and H for a paramagnetic material can be interpreted by Curie's Law, which is a linear function of:  $M = \chi H$ ,  $\chi$  is called magnetic susceptibility and is a small constant specifically to each material. To achieve saturation magnetization, a huge external field, often  $\gg 10$  T should be applied. On the other hand, saturation is an indicator for ferromagnetism, which fundamentally means it is much easier for all the magnetic moments in ferromagnetic material to be fully aligned with the

external field than paramagnetic material. It is a consequence of the ferromagnetic exchange interaction.

- 2) The magnetization per atom obtained in our nanoparticle is around  $0.45 \mu_B/\text{atom}$  at 300 K, which is dramatic when compared with those counterparts reported previously, *e.g.*,  $0.005 \mu_B/\text{atom}$  at 300 K <sup>(126)</sup>. The saturation magnetisation of our Cr samples is comparable with other ferromagnetic nanoparticles, such as Ni of  $0.43 \mu_B/\text{atom}$  <sup>(247)</sup> and Fe of  $0.6 \mu_B/\text{atom}$  <sup>(231)</sup>.

## 5.4 Origin of Ferromagnetism in Cr Nano-objects

The observation of strong ferromagnetism in Cr nanostructures is unprecedented. It is therefore important to try and explain its origin. First, the influence of oxidation can be ruled out, although some degree of oxidation is inevitable at the surface of our Cr samples. Previous researchers have found that in  $\text{Cr}_2\text{O}_3$  nanoparticles <sup>(222)</sup> or naturally oxidized Cr nanoparticles <sup>(126)</sup>, no significant magnetization can be detected. In fact oxidized Cr is also antiferromagnetic in bulk phase and at nanoscale, with a saturation magnetization similar to pure Cr <sup>(126, 222)</sup>.

Another possibility is that the size of the Cr nano-objects produced in this work leads to the unusually high magnetic moments of the Cr particles. In our experiments we have produced particles which are about 10 times smaller in diameter than the particles in Ref. (222) and (126) (10 nm – 300 nm). As a result there might be a significant contribution from surface Cr atoms, as suggested by the “canted spin mechanism”. However a simple calculation shows that neither uncompensated surface spin nor canted spin can explain the strong magnetization of our Cr samples. Taking the 3.2 nm nanoparticle as an example: this will contain about 870 Cr atoms, assuming that the Cr nanoparticle maintains a bcc crystalline structure as in the bulk phase. The number of atoms contained in each atomic shell from outer to inner can be roughly deduced as: 195 – 163 – 135 – 109 – 85 – 66 – 47 – 33 – 21 – 11 – 6. The theoretical limit of the atomic magnetization of Cr is  $5 \mu_B/\text{atom}$  and hence even if all the surface atoms could be perfectly aligned to the external field and each contributed  $5 \mu_B/\text{atom}$

magnetization to the overall magnetization of the particle, the average magnetization shared by all the atoms in nanoparticle is only  $1.12 \mu_B/\text{atom}$ , which is significantly lower than the theoretical atomic magnetization at 0 K (calculated as  $2.18 \mu_B/\text{atom}$ ) in this work. Consequently, the ferromagnetism of Cr cannot result from canted spins.

The giant magnetic moment possessed by Cr has been reported at the cluster level by Payne *et al.* as they directly measured the strength of the magnetic moments of Cr clusters in vacuum at 78 K immediately after they were synthesized<sup>(197)</sup>. The authors reported a peak magnetism of  $1.16 \mu_B/\text{atom}$  for  $\text{Cr}_{58}$  and they attribute this magnetism to a geometry of the cluster in which the clusters are the least compact. However, the authors also found that when cluster size grows to more than 130 Cr atoms, the magnetization should decay to near the bulk value of 0.

In light of the above results, we propose a mechanism behind the ferromagnetism of chromium nano-objects formed in very cold superfluid helium droplets (see Figure 5-12). Helium droplets have a very low equilibrium temperature of 0.37 K, and they are capable of dissipating excess energies, including kinetic energy and the binding energy between chromium atoms when they aggregate, through bubble-free evaporative loss of surface helium atoms. Therefore, when a weak magnetic field, generated by the oven heating coil (Figure 5-12 (a)), is applied, the spins of the Cr atoms can align in the direction of the magnetic field before they aggregate. The perturbation-free superfluid helium then allows chromium atoms to aggregate with aligned magnetic moments in the droplets, leading to the formation of nanostructures that are stabilized in the very cold helium droplets with ferromagnetic ordering (Figure 5-12 (b)). Ferromagnetic ordering corresponds to a longer inter-atom distance (refer to Bethe-Slater curve in Figure 1-10, Chapter 1), and inevitably the antiferromagnetic exchange interaction will be replaced by the ferromagnetic exchange interaction. As more and more chromium atoms are added to the droplets, the ferromagnetic structure can collapse, leading to defects inside and on the surface of the nanoparticles, which is clearly seen in Figure 5-5 (e), where non-crystalline structure is shown in the high resolution TEM image instead of the perfect crystalline structure we observed before for Au nanoparticles shown in Ref. (67) and Chapter 2. In the non-crystalline structure, the inter-atom separation should still be larger than the naturally synthesized Cr crystal, due to the

pre-aligned magnetic moments (Figure 5- 12 (c)), therefore under external magnetic field, Cr nanoparticles still show ferromagnetism.

In large helium droplets, the circulation of helium around the vortex lines can perturb the magnetic moments of chromium nanoparticles, disturbing the pre-alignment of magnetic moments to the external magnetic field. As a result, lower magnetization is seen in chromium nanowires.

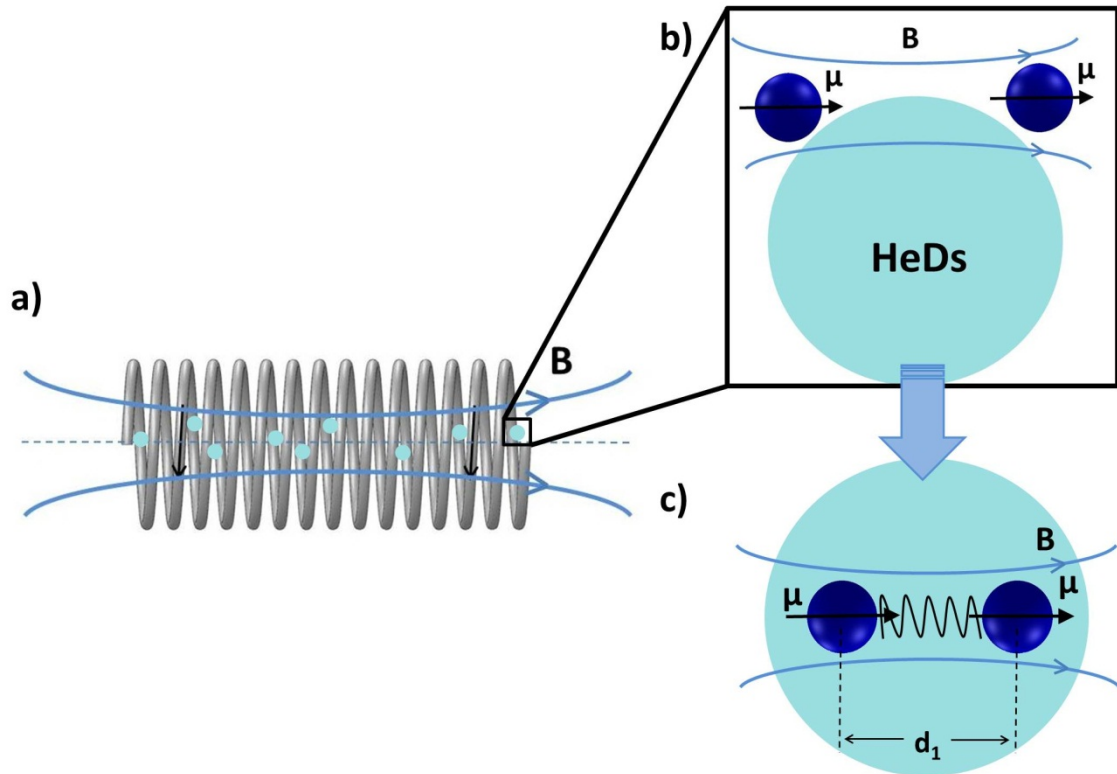


**Figure 5- 12 (a)** Schematic illustration of the Ta wire coil generating a weak magnetic field. The black arrows present the electric current flow and the blue curved arrows present the magnetic induction line. **(b)** Magnetic moments of pre-aligned Cr atoms before being picked up by helium droplet. **(c)** Cr atoms bonded together in helium droplets with a longer inter-atom separation  $d_1$  than the lattice constant, which results from the pre-aligned magnetic moments.

The magnetic field generated by the coil can be worked out via equations:

$$NI = HL = B\left(\frac{L}{\mu_0}\right) \quad (5-2)$$

Here  $N$  is the number of wire turns,  $I$  is the electric current,  $B$  is the magnetic field generated inside the coil,  $L$  is the length of the coil and  $\mu_0$  is the permeability of the

free space ( $4\pi \times 10^{-7} \text{ N} \cdot \text{A}^{-2}$ ). Since  $N = 33$ ,  $I = 10.8 \text{ A}$  and  $L = 0.04 \text{ m}$ ,  $B$  is calculated to be  $0.0112 \text{ T}$ .

$0.01 \text{ T}$  magnetic field is not significant; however, in a helium droplet with surrounding temperature of  $0.37 \text{ K}$ , it is sufficient to magnetize isolated Cr atoms thus leads the atomic magnetic moments aligned. The responded atomic magnetic moment can be calculated *via* Brillouin Function, which has been proven to be an accurate way to predict the magnetic moment of isolated free atoms<sup>(107)</sup>:

$$|\mu| = gJ\mu_B \left[ \frac{2J+1}{2J} \coth\left(\frac{2J+1}{2J}y\right) - \frac{1}{2J} \coth\left(\frac{y}{2J}\right) \right] \quad (5-3)$$

where  $y = \left(\frac{Jg\mu_B B}{kT}\right)$ .  $\mu$  is the atomic magnetic moment stimulated by the external magnetic field  $B$  under temperature  $T$ ;  $J$  is the total angular momentum quantum number;  $g$  is the Landé  $g$ -factor equals:  $\frac{3}{2} + \frac{S(S+1)-L(L+1)}{2J(J+1)}$ ;  $S$  is the total electron spin quantum number,  $L$  is the total orbital angular momentum quantum number;  $k$  is the Boltzmann constant.

For a Cr atom in helium droplet, since  $B = 0.01 \text{ T}$ ,  $T = 0.37 \text{ K}$ ,  $J = 5/2$ ,  $S = 5/2$ ,  $L = 0$ ,  $g = 2$ ,  $k = 8.62 \times 10^{-5} \text{ eV/K}$  and  $\mu_B = 5.79 \times 10^{-5} \text{ eV/T}$ , the atomic magnetic moment  $|\mu|$  can be calculated to be  $0.21 \mu_B$ . This is a notable magnetic moment considering the magnetism of most ferromagnetic Ni nanoparticles locate within the range of  $0.2 - 0.3 \mu_B/\text{atom}$ , as will be discussed later in Table 5- 5. Therefore significant ferromagnetic ordering should be expected among the Cr atoms in helium droplets in response to the  $0.01 \text{ T}$  magnetic field induced by the heating coil.

There is an experimental difficulty in finding out how much the inter-atom separation enlarges. However, even small enlargement may dramatically reduce the anti-ferromagnetic coupling since the exchange interaction is only valid over short distances<sup>(107)</sup>. Although the atoms are in ferromagnetic ordering, the ferromagnetic exchange interaction in our samples is also fairly weak as suggested in section 5.3.3 and 5.3.5, this is possibly because the elongated inter-atom separation resides near the boundary points between ferromagnetic ordering and anti-ferromagnetic ordering.

## 5.5 Ni Nanoparticles with Giant Magnetism

As seen from the discussion above, the magnetic field induced by the heating coil may increase the inter-atom separation in nanostructures, hence switching from antiferromagnetic Cr to ferromagnetic. In this section, we will apply this strategy to ferromagnetic materials and will demonstrate whether the pre-alignment of atomic magnetic moment can lead to enhanced magnetism in ferromagnetic nanoparticles.

### 5.5.1 Mass Spectrum of Ni and Ni/Au clusters

We start with the formation of Ni nanoparticles and Ni/Au core-shell nanoparticles. To determine the optimum pickup condition, the mass spectra of pure Ni cluster ions and Ni/Au complex ions were recorded. As seen in Figure 5- 13, both  $Ni_n^+$  and  $Ni_nAu_m^+$  spectra were recorded at a helium source temperature of  $T_0 = 12.5$  K, corresponding to an initial helium droplets of about 5000 helium atoms. The Ni oven was heated to 1580 K and the Au oven was heated to 1350 K. For pure Ni cluster ions consisting of up to 13 atoms can be observed. However, when Au was added the large Ni clusters almost disappeared; instead, binary Ni/Au ions were dominant in the mass spectrum. There are no impurity peaks besides the combination of Ni, Au and He, which suggests a contamination-free environment in the apparatus.

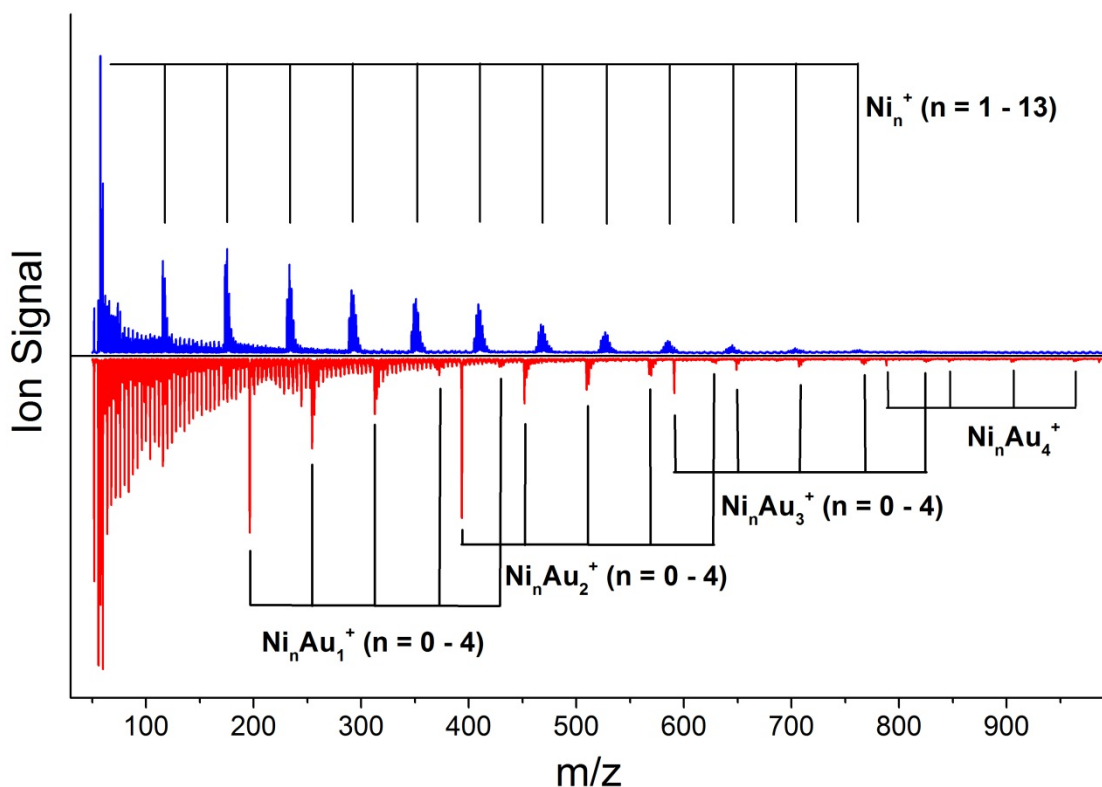
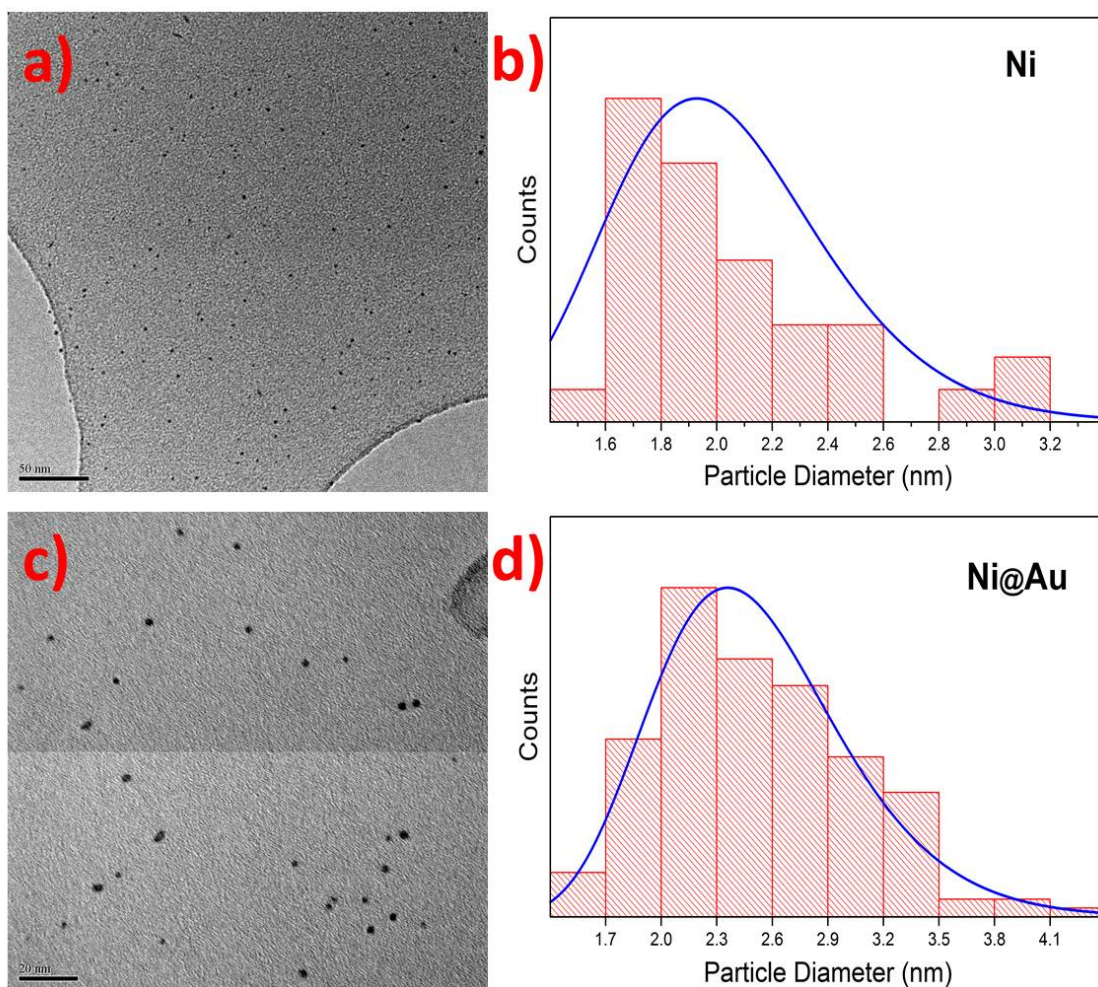


Figure 5- 13 Mass spectra of  $\text{Ni}_n^+$  clusters (upper panel) and  $\text{Ni}_n\text{Au}_m^+$  clusters (bottom panel), recorded at  $T_0 = 12.5$  K.

### 5.5.2 Pure Ni and Ni/Au Core-shell Nanoparticles

Nanoparticles were formed at a source temperature of  $T_0 = 9.5$  K, corresponding to helium droplet diameters of about 15 nm. First we synthesize bare Ni nanoparticles with the Au oven off and the Ni oven heated to 1580 K. The resulting bare Ni nanoparticles are shown in Figure 5- 14 (a). The contrast within the TEM image is poor due to the intrinsic low scattering of electrons by Ni. The size of bare Ni nanoparticles follows a roughly lognormal distribution with the average diameter of  $2 \pm 0.4$  nm, as seen in Figure 5- 14 (b). We then switched on the Au oven and heated it to 1350 K, so the Ni/Au core-shell nanoparticles were produced. As seen in Figure 5- 14 (c), the quality of the TEM image is significantly improved compared to the bare Ni particles when Au is added as a coating. The mean diameter of core-shell nanoparticles was  $2.5 \pm 0.5$  nm and also follows a log-normal distribution according to the TEM images. The thickness of the Au shell is therefore about 0.5 nm. As the lattice constant of Au is 0.41 nm, only a monolayer of Au is coated on the Ni surface.



**Figure 5- 14 (a) TEM images of bare Ni nanoparticles formed at  $T_0 = 9.5$  K and an oven temperature of 1580 K. The scale bar is 50 nm. (b) Size distribution of bare Ni nanoparticles. (c) TEM images of Ni/Au core-shell nanoparticles formed at  $T_0 = 9.5$  K, with oven temperatures at 1580 K for Ni and 1350 K for Au. The scale bar is 20 nm. (d) Size distribution of Ni/Au core-shell nanoparticles.**

### **5.5.3 M-H Curve of Ni and Ni/Au Core-shell Nanoparticles**

To acquire a sufficient quantity of nanoparticles for the measurement of magnetic properties, Ni and Ni/Au core-shell nanoparticle samples were deposited for 5 hours on a PEEK substrate. This gave rise to a total mass of deposited Ni of  $0.69 \mu\text{g}$ , as measured by use of a thin film deposition monitor.

The M-H curve of the synthesized Ni and Ni/Au core-shell nanoparticles were measured by VSM at 300 K in collaboration with the National Research Council, Italy.

When calculating the unit mass magnetization, we assume the magnetism is only attributed to Ni as Au and Ag are well known “magnetically-dead” materials. As shown in Figure 5- 15, the M-H curves for both bare Ni and Ni/Au core-shell nanoparticles are saturated below 5000 Oe and both pass through the origin point with nearly no remanence nor coercivity, which suggests superparamagnetism for both samples. The saturation magnetization of bare Ni nanoparticle is about  $0.25 \mu_B/\text{atom}$ , which is lower than the bulk phase value ( $0.6 \mu_B/\text{atom}$ ). However, when coated by a monolayer of gold, the magnetization is enhanced by 8 times to  $2.1 \mu_B/\text{atom}$ , which is far beyond the bulk phase magnetization.

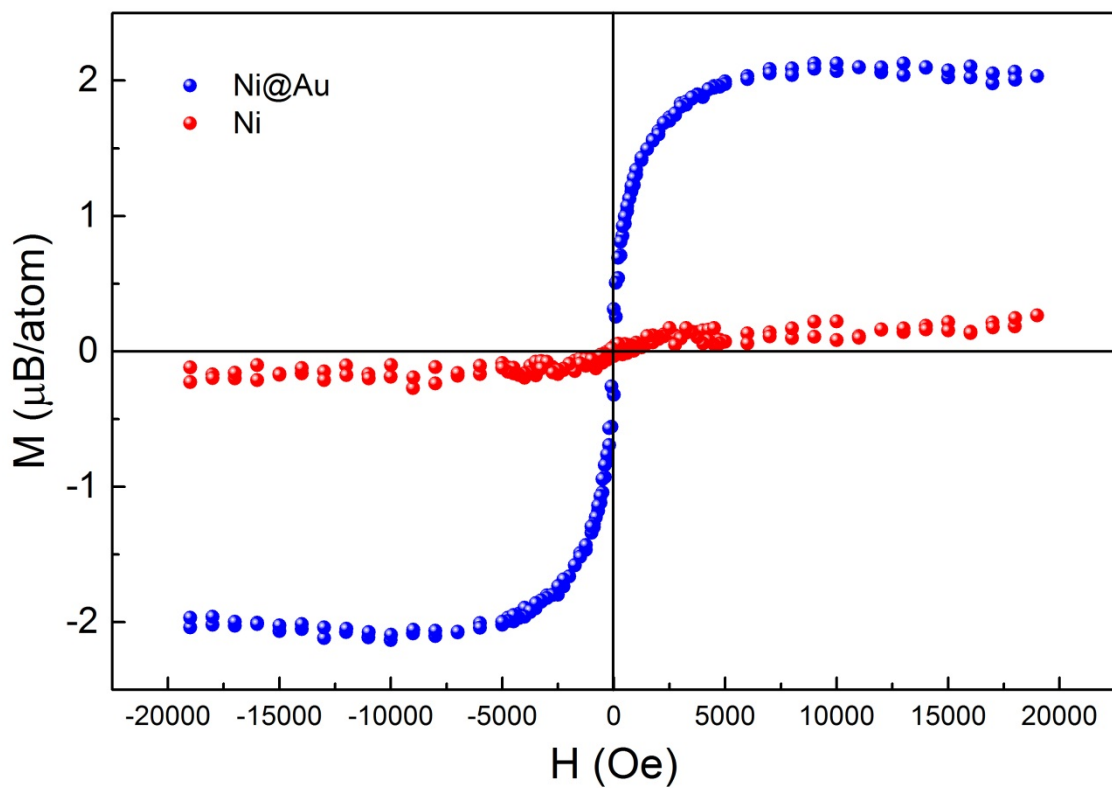


**Figure 5- 15 M-H curve of Ni and Ni/Au core-shell nanoparticles measured at 300 K.**

In Table 5- 5 the saturation magnetization of our nanoparticles are compared with nanoparticles reported by Tracy’s group <sup>(248)</sup>, which were formed by a wet chemical method and had diameters ranging from 8 to 24 nm. For each size of nanoparticles, the authors treated them in two different ways: one was naturally oxidized just like our nanoparticles; the other was manually oxidized to generate a thicker NiO shell. The size and saturation magnetization of the samples are listed in the Table 5- 5, in

comparison with our bare Ni and Ni/Au core-shell nanoparticles. The magnetisation of Ni nanoparticle declines with the particle size. Although our bare Ni nanoparticles are more than 3 times smaller than Ni 3 in reference, the saturation is only slightly lower. Our Au coated nanoparticles show much stronger magnetization than any Ni nanoparticles ever reported.

**Table 5- 5 Comparison of saturation magnetization of our sample and the wet-chemical samples with different particle sizes.**

<b>Reference Samples*</b>		
Sample	Diameter (nm)	$M_S$ ( $\mu_B$ /atom)
Ni 1	$23.8 \pm 2.6$	0.53
Ni 2	$8.2 \pm 0.8$	0.38
Ni 3	$7.6 \pm 0.5$	0.28
<b>Our Samples</b>		
Ni	$2.0 \pm 0.4$	0.25
Ni@Au	$2.5 \pm 0.5$	2.1

\*The reference data was obtained from Ref. (248).

For the batch of sample with a thicker oxidation shell, Tracy *et al.* found the magnetization is significantly reduced and the smaller the particle is, the smaller the magnetization due to the thicker oxidation shell. This shows that an oxidation shell can reduce the particle magnetism, as NiO is antiferromagnetic, and will have a negligible contribution to the magnetism of Ni nanoparticles.

#### **5.5.4 Ni/Ag Core-shell Nanoparticles**

In a second set of experiments we have produced core-shell nanoparticles using Ag as the coating material, in order to confirm how a noble metal coating will influence the magnetic moments of Ni nanoparticles. The helium source temperature was set to 8 K,

which allows the formation of slightly larger nanoparticles than the Ni/Au core shell nanoparticles synthesized. The Ni oven was maintained at 1460 K, giving rise to bare Ni nanoparticles with  $2.9 \pm 1.0$  nm in diameter (see Figure 5- 16 (a) and (b)). The Ag oven located downstream of the Ni oven was heated to 1250 K, giving core-shell nanoparticles with a diameter of  $3.6 \pm 1.3$  nm, as shown in Figure 5- 16 (c) and (d). In this case we obtain Ni/Ag nanoparticles with roughly a monolayer of Ag coated on the Ni surface.

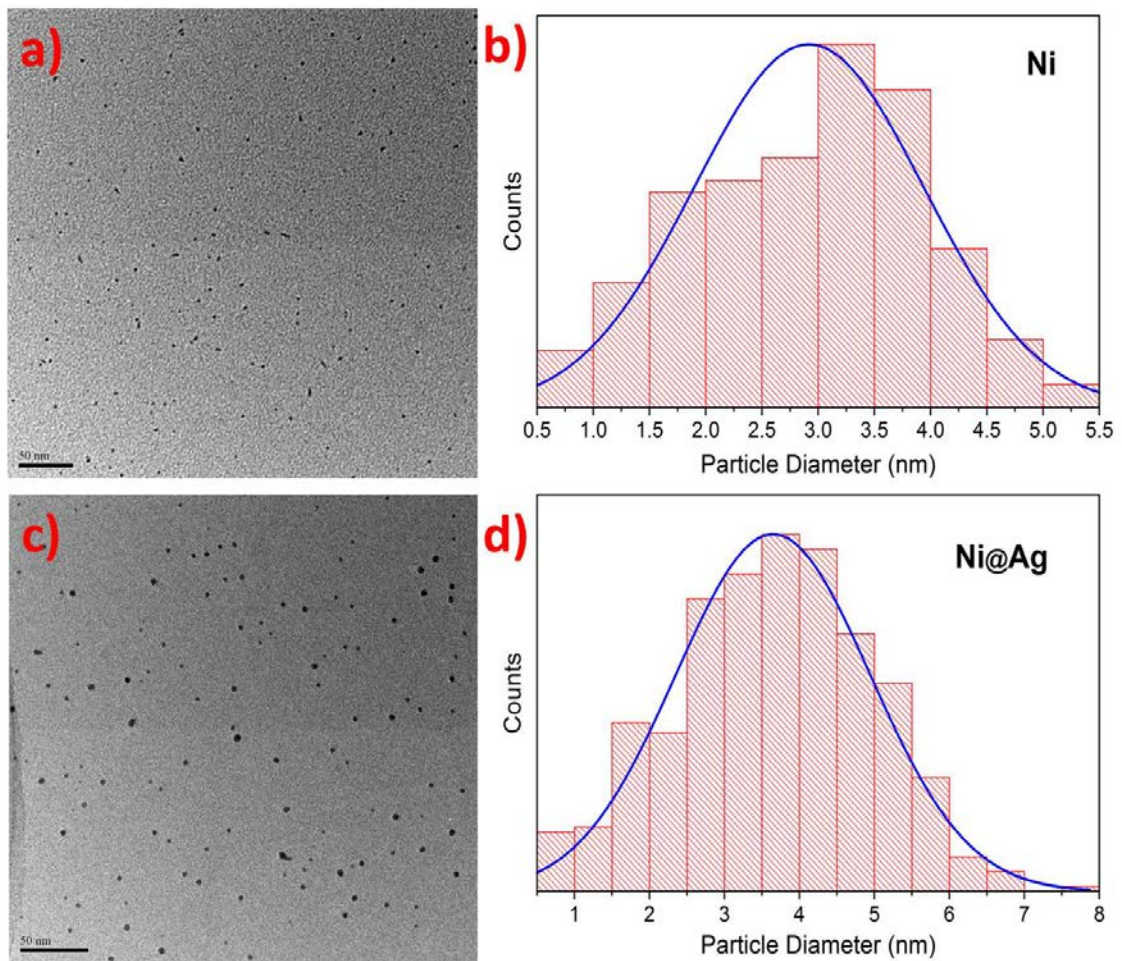


**Figure 5- 16 (a) TEM images of bare Ni nanoparticles formed a source temperature of 8 K and an oven temperature of 1460 K for Ni. (b) Size distribution of bare Ni nanoparticles. (c) TEM images of Ni/Ag core-shell nanoparticles with  $T_0 = 8$  K,  $T_{Ni} = 1460$  K,  $T_{Ag} = 1250$  K. (d) Size distribution of Ni/Ag core-shell nanoparticles. The scale bars are 50 nm in the TEM images.**

### 5.5.5 M-H Curve of Ni and Ni/Ag Core-shell Nanoparticles

The M-H curves for bare Ni and Ni/Ag core-shell nanoparticles were measured at 300 K in Shanghai Jiaotong University in China. As seen from Figure 5- 17, a 6-times enhancement of the saturation magnetization was observed after monolayer Ag was coated, which is about  $2.07 \mu_B/\text{atom}$  – similar to the Ni/Au particles. For bare Ni, the saturation reaches  $0.35 \mu_B/\text{atom}$ , which is slightly higher than the smaller nanoparticles with 2 nm diameter. For both samples in this batch, unlike the typical superparamagnetic features shown in Figure 5- 15, obvious hysteresis loops can be observed probably because monolayer Ag shell cannot protect as good as Au shell from oxidation, leading to the more significant exchange coupling between the ferromagnetic core (Ni) and the antiferromagnetic shell (NiO). The magnetic properties including coercivity ( $H_C$ ), remanent magnetization ( $M_r$ ) and saturation magnetization ( $M_s$ ) are summarized in Table 5- 6.

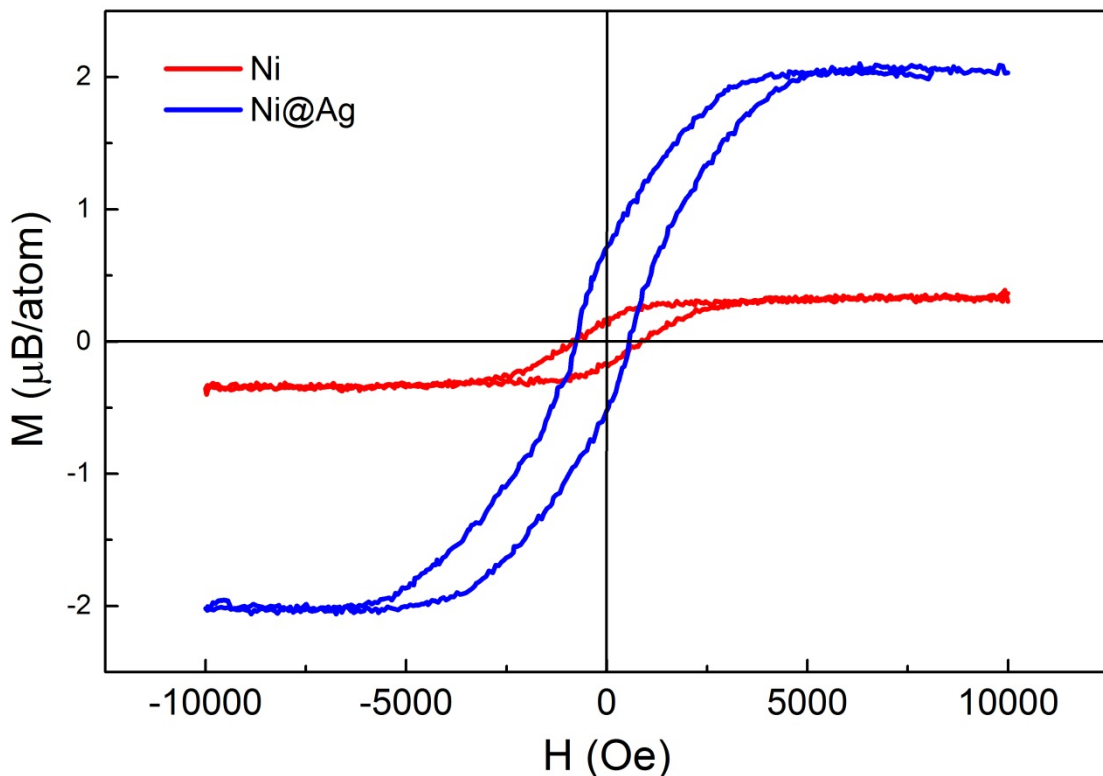


Figure 5- 17 M-H curves of Ni and Ni/Ag core-shell nanoparticles at 300 K.

**Table 5- 6 Summary of the magnetic properties of Ni and Ni/Ag nanoparticles.**

Sample	H <sub>C</sub> (Oe)	M <sub>r</sub> (μ <sub>B</sub> /atom)	M <sub>s</sub> (μ <sub>B</sub> /atom)
Ni	900	0.16	0.33
Ni@Ag	745	0.70	2.04

### 5.5.6 Enhanced Magnetism of Ni

The giant magnetism detected in the core-shell nanoparticles is unprecedented since the magnetization has exceeded the bulk phase value, approaching the atomic theoretical limit. This cannot be solely attributed to the lack of oxidation by the addition of an Au shell, because as suggested by others' work, although ferromagnetic nanoparticles will have their magnetism enhanced after having a coated shell, the magnetism should still be lower than the bulk phase value <sup>(236-238)</sup>. According to previous studies which measured the magnetism of free Ni<sub>n</sub> clusters (20 < n < 700) in vacuum at 78 K <sup>(196)</sup>, the magnetism decays from 1.05 μ<sub>B</sub>/atom of Ni<sub>20</sub> with the increase of Ni cluster size. For larger clusters with n > 350, the magnetism is about the same as the bulk phase. The reason for the higher magnetism of small clusters is that the inter-atom distance in small clusters is larger than that in large clusters; therefore atoms behave more like free atoms and can show higher magnetization. More elaborate experiments have discovered that in the small cluster region, the magnetism shows maxima at specific cluster sizes due to the different configuration of the clusters <sup>(249)</sup>. For our nanoparticles, even the smallest ones (2 nm Ni core with monolayer gold shell) still contain about 380 Ni atoms assuming an fcc crystalline structure. Thus the magnetization is not expected to exceed the bulk value.

The giant enhanced magnetism of Ni nanoparticles synthesized can also be explained by the pre-alignment of atomic magnetic moments in helium droplets prior to the aggregation, analogous to the ferromagnetism behaviour in Cr nanoparticles. The weak magnetic field applied by the Ta coil pre-aligns the Ni atoms, leading to an

increased inter-atomic separation when Ni atoms aggregate in helium droplets as the ferromagnetic exchange interaction repels neighbouring atoms<sup>(107)</sup>. The larger distance between neighbouring atoms makes the Ni atoms more isolated. The energy level of the electrons more likely maintain discrete rather than converging into energy bands, which discriminates the quench of the spin that usually occurs in crystals. Meanwhile there is no crystal field influence to the atoms in particle formation process due to the protection by the helium. After coating with Au and Ag shells, the crystal field effect induced by the environment, such as oxidation, can also be eliminated, therefore magnetism contributed by both spin and orbital as in the free atoms can be greatly maintained. That is why the magnetism of our Ni samples can approach its theoretical limit.

Giant magnetism in ferromagnetic materials has been reported before by Beckmann *et al.* in thin films<sup>(250)</sup>. The authors deposited 1% of a monolayer of Fe or Co, sandwiched between Cs thin films, each film containing a few atom layers. Measurement reveals the magnetism of such a system can even surpass the theoretical limit of Fe or Co. The authors attributed this giant magnetism to the fully localized *3d* atoms, so all the interactions of the neighbouring *3d* atoms and the effect from the crystal field will be fully quenched. In addition, the abundant host Cs atoms are thought to play a key role here, which isolates the *3d* metal atoms. This is a completely different case from our core-shell nanoparticles, where the giant magnetic moments are attributed to the pre-alignment of atomic magnetic moments prior to the aggregation.

## 5.6 Conclusion and Future Work

In this chapter, we report our preliminary attempts of synthesising magnetic nanomaterials in helium droplets. We have found that Cr, a well-known antiferromagnetic material, can be switched to ferromagnetic. We have obtained Cr nanomaterials with a magnetisation comparable with Ni and Fe nanostructures formed by other methods. For Ni, after being coated with a monolayer of Au or Ag, the magnetism is hugely enhanced, approaching to the atomic theoretical limit. The

discoveries for both elements are unprecedented. Using this technique, the strongest magnetic nanoparticles ever can be synthesized and may have great potential in biomedicine, high density storage and MR imaging applications.

These extraordinary magnetic properties observed in Cr and Ni can be attributed to the formation process. Here the Ta coil wrapping around the metal oven not only evaporates the magnetic materials, but also provides a weak magnetic field of  $\sim 0.01$  T that pre-aligns the atoms before they aggregate in the helium droplets. The pre-aligned atoms enlarge the average inter-atom separation by resisting the antiferromagnetic exchange interaction in Cr and by assisting ferromagnetic exchange interaction in Ni. Therefore the magnetism in our nanostructures is more atom-like and can therefore approach the theoretical limit.

This research provides a new strategy for producing nanomaterials with giant magnetism. At the moment, most of the attempts in seeking stronger magnetic materials focus on hybridizing  $3d$  orbitals by creating new alloys, such as FeCo<sup>(251)</sup> and FePt<sup>(252, 253)</sup>. However, our experiments suggest even higher magnetism can be achieved by aligning the atomic magnetic moments prior to aggregation thus controlling the internal structure of the nanomaterials.

More work is needed to fully understand the mechanism of magnetism enhancement. For example, with the limitation of droplet size and quantum vortices, we are struggling to add more than one layer of noble metal onto the Ni surface. Thus the shell effect is still an open question that needs to be solved in the future. In addition, a monolayer shell cannot completely guarantee elimination of oxidation. Therefore when coating thicker shell, even higher magnetism might be attainable. We also expect to obtain nanomaterials with even higher magnetic moments using high-spin transition metals such as Co and Fe, which might have strong impact for future technologies in energy efficiency, bio-medical treatment, drug delivery, magnetic data storage and MR imaging.

# Thesis Summary

The PhD project has focused on the two main-stream applications of superfluid helium droplet technique, including spectroscopy and the fabrication of novel nanomaterials, in particular, magnetic nanostructure formation. These take advantage of the unique properties of helium droplets, including superfluidity, very low temperature, exceptionally high thermal conductivity and transparency for the electromagnetic wave ranging from IR to UV. The atoms/molecules can be added to helium droplets, which are rapidly cooled to the ambient temperature of superfluid helium at 0.37 K. Helium droplets provide a disturbance free environment for cluster aggregation which results dramatic benefit in both spectroscopy and nanostructure formation.

For spectroscopy, helium droplets, as a superfluid matrix, are able to pick up a large size range of binary clusters and cool the majority of them to their ground states. In addition, spectra recorded in helium droplets have been found to have well-resolved band structures in a way similar to the gas phase. Therefore it is an ideal technique to study the dissolution process at molecule scale which is extremely challenging in other spectroscopy techniques.

Helium droplets have also proven to be a versatile technique for the fabrication of nanostructures, which has almost no limitation in material selection. Nanostructures formed inside of helium droplets can have perfect crystalline structures, minimized inter-diffusion, and the growth of nanoparticles can be precisely controlled. These make helium droplets a highly competitive technique in nanostructure fabrication compared with other techniques, such as wet chemistry method and chemical vapour deposition. The recent discovery of quantized vortices has also initiated the fabrication of novel nanowires in helium droplets, which has been first exploited in our group.

The key finding in this work can be summarized as:

In Chapter 2, we demonstrated multiple experimental techniques that can be incorporate to the helium droplets technique, including mass spectrometry, laser system, TEM images, XPS technique and magnetometer measurement. In addition, we

investigated the pick-up control of both small clusters in super-critical regime and nanoparticles in sub-critical regime, as a function of the initial helium droplets size and the doping rate of the dopants. These are important to establish the technology.

In Chapter 3, the dissolution behaviour of NaCl in water was systematically studied for the first time. By applying a counter propagating infra-red laser beam to the helium droplets, we have investigated salt water complexes in helium droplets, which were formed by sequential addition of NaCl and water to helium droplets. For a range of complexes of  $\text{NaCl}(\text{H}_2\text{O})_n$ , depletion spectra in O-H stretching region were recorded up to  $n = 7$ . *Ab initio* calculations have been performed to predict the structure, vibrational transitions and intensities, in order to interpret the experimental results. O-H stretching bands were assigned to the specific structures for the small complexes of  $n \leq 3$ . In particular, ionic hydrogen bonding was noticed to be dominant in the global minimum structures for small clusters. ASSIP structure for  $\text{NaCl}(\text{H}_2\text{O})_6$  complex was assigned by experiments for the first time, which agrees with *ab initio* calculations. The complex has  $\text{Na}^+$  and  $\text{Cl}^-$  sitting at the opposite side of a cyclic water hexamer, with the ion-ion separation of 4.458 Å.

In Chapter 4, we provided the solid evidence for the existence of quantum vortices in helium droplets by carefully doping Ag into large helium droplets and observing spherical Ag nanoparticles pinned in a chain from TEM images. Quantum vortices were then applied to form one-dimension nanostructures using Ag, Au, Si, Cr and Ni. In addition, traces of multiply quantized vortices were discovered, which is evident from small nanoparticles surrounding the chains of large nanoparticles.

In Chapter 5, we report novel magnetic nanomaterials, including Cr nanoparticles, Cr nanowires, Ni nanoparticles and Ni/Au, Ni/Ag core-shell nanoparticles, synthesized in helium droplets. Cr nanomaterials synthesized in this way were found to be ferromagnetic rather than antiferromagnetic, which is the first discovery of ferromagnetism in elemental chromium. The formation of ferromagnetic Cr was attributed to our synthesis process in which a weak magnetic field has pre-aligned the magnetic moments of Cr atoms and forced ferromagnetic ordering. The same experimental protocol was then applied to Ni, and it was found that after being coated

with an Au or Ag shell in order to prevent oxidation, the magnetism of Ni nanoparticles can be significantly enhanced, producing by far the highest magnetic moments for Ni, with a magnetic moment as high as  $2.1 \mu_B$  at room temperature, approaching its theoretical limit. These are major breakthroughs in nanomagnetism.

## Bibliography

1. Pekeris CL. The Zero-Point Energy of Helium. *Phys. Rev.* 1950;79(5):884-5.
2. Rama Krishna MV, Whaley KB. Wave functions of helium clusters. *J. Chem. Phys.* 1990;93(9):6738-51.
3. Chin SA, Krotscheck E. Systematics of pure and doped He<sub>4</sub> clusters. *Phys. Rev. B.* 1995;52(14):10405-28.
4. Lewerenz M. Structure and energetics of small helium clusters: Quantum simulations using a recent perturbational pair potential. *J. Chem. Phys.* 1997;106(11):4596-603.
5. Kapitza P. Viscosity of Liquid Helium below the  $\lambda$ -Point. *Nature.* 1938;141(3558):74-.
6. Allen JF, Misener AD. Flow of Liquid Helium II. *Nature.* 1938;141(3558):75-.
7. Tisza L. Transport Phenomena in Helium II. *Nature.* 1938;141(3577):913-.
8. Landau L. The theory of superfluidity of helium II. *J. Phys.* 1941;5(1):71-90.
9. Andronikashvili EL. Direct observation of two types of motion in helium II. *J. Phys. USSR.* 1946;10(201).
10. Gomez LF, Loginov E, Sliter R, Vilesov AF. Sizes of large He droplets. *J. Chem. Phys.* 2011;135(15):-.
11. London F. On the Bose-Einstein Condensation. *Phys. Rev.* 1938;54(11):947-54.
12. Brunt JNH, King GC, Read FH. A study of resonance structure in helium using metastable excitation by electron impact with high energy resolution. *J. Phys. B: Atomic and Molecular Physics.* 1977;10(3):433.
13. Buchenau H, Knuth EL, Northby J, Toennies JP, Winkler C. Mass spectra and time-of-flight distributions of helium cluster beams. *J. Chem. Phys.* 1990;92(11):6875-89.
14. Buchenau H, Toennies JP, Northby JA. Excitation and ionization of 4He clusters by electrons. *J. Chem. Phys.* 1991;95(11):8134-48.
15. Balasubramanian K. Comment on: Is n=4 a magic number for He+n? *J. Chem. Phys.* 1990;93(11):8403-4.
16. von Issendorff B, Haberland H, Fröchtenicht R, Toennies JP. Spectroscopic observation of a metastable electronically excited He<sub>4</sub><sup>+</sup>. *Chem. Phys. Lett.* 1995;233(1-2):23-7.
17. Montague RG, Harrison MFA, Smith ACH. A measurement of the cross section for ionisation of helium by electron impact using a fast crossed beam technique. *J. Phys. B: Atomic and Molecular Physics.* 1984;17(16):3295.
18. Rapp D, Englander-Golden P. Total Cross Sections for Ionization and Attachment in Gases by Electron Impact. I. Positive Ionization. *J. Chem. Phys.* 1965;43(5):1464-79.

19. Schram BL, Boerboom AJH, Kistemaker J. Partial ionization cross sections of noble gases for electrons with energy 0.5–16 keV.: I. Helium and neon. *Physica*. 1966;32(1):185-96.
20. Schram BL, Moustafa HR, Schutten J, de Heer FJ. Ionization cross sections for electrons (100–600 eV) in noble and diatomic gases. *Physica*. 1966;32(4):734-40.
21. Sorokin AA, Beigman IL, Bobashev SV, Richter M, Vainshtein LA. Total electron-impact ionization cross sections of helium. *J. Phys. B: Atomic, Molecular and Optical Physics*. 2004;37(15):3215.
22. Wetzel RC, Baiocchi FA, Hayes TR, Freund RS. Absolute cross sections for electron-impact ionization of the rare-gas atoms by the fast-neutral-beam method. *Phys. Rev. A*. 1987;35(2):559-77.
23. Toennies JP, Vilesov AF. Superfluid Helium Droplets: A Uniquely Cold Nanomatrix for Molecules and Molecular Complexes. *Angew. Chem. Int. Ed. Engl.* 2004;43(20):2622-48.
24. Silvera IF. Ultimate fate of a gas of atomic hydrogen in a liquid-helium chamber: Recombination and burial. *Phys. Rev. B*. 1984;29(7):3899-904.
25. Jortner J, Meyer L, Rice SA, Wilson EG. Energy Transfer Phenomena in Liquid Helium. *Phys. Rev. Lett.* 1964;12(15):415-6.
26. Scheidemann A, Schilling B, Toennies JP, Northby JA. Capture of foreign atoms by helium clusters. *Physica B: Condensed Matter*. 1990;165–166, Part 1(0):135-6.
27. Scheidemann A, Toennies JP, Northby JA. Capture of neon atoms by He<sub>4</sub> clusters. *Phys. Rev. Lett.* 1990;64(16):1899-902.
28. Yang S, Ellis AM. Helium droplets: a chemistry perspective. *Chem. Soc. Rev.* 2013;42(2):472-84.
29. Boatwright AL. Molecular behaviour in superfluid helium clusters: University of Nottingham; 2007.
30. Kantrowitz A, Grey J. A High Intensity Source for the Molecular Beam. Part I. Theoretical. *Rev. Sci. Instrum.* 1951;22(5):328-32.
31. Kistiakowsky GB, Slichter WP. A High Intensity Source for the Molecular Beam. Part II. Experimental. *Rev. Sci. Instrum.* 1951;22(5):333-7.
32. Becker EWK, R.; Lohse, P. Strahlen aus kondensiertem Helium im Hochvakuum. *Zeitschrift Naturforschung Teil A*. 1961;16:1259.
33. Yang S, Ellis AM, Spence D, Feng C, Boatwright A, Latimer E, et al. Growing metal nanoparticles in superfluid helium. *Nanoscale*. 2013;5(23):11545-53.
34. Stringari S, Treiner J. Systematics of liquid helium clusters. *J. Chem. Phys.* 1987;87(8):5021-7.
35. Brink DM, Stringari S. Density of states and evaporation rate of helium clusters. *Z. Phys. D - Atoms, Molecules and Clusters*. 1990;15(3):257-63.

36. Grebenev S, Toennies JP, Vilesov AF. Superfluidity Within a Small Helium-4 Cluster: The Microscopic Andronikashvili Experiment. *Science*. 1998;279(5359):2083-6.
37. Guirao A, Pi M, Barranco M. Finite size effects in the evaporation rate of  $^3\text{He}$  clusters. *Z. Phys. D - Atoms, Molecules and Clusters*. 1991;21(2):185-8.
38. Kwon Y, Ceperley DM, Whaley KB. Path integral Monte Carlo study of SF<sub>6</sub>-doped helium clusters. *J. Chem. Phys.* 1996;104(6):2341-8.
39. Sindzingre P, Klein ML, Ceperley DM. Path-integral Monte Carlo study of low-temperature He<sub>4</sub> clusters. *Phys. Rev. Lett.* 1989;63(15):1601-4.
40. Lewerenz M, Schilling B, Toennies JP. A new scattering deflection method for determining and selecting the sizes of large liquid clusters of  $^4\text{He}$ . *Chem. Phys. Lett.* 1993;206(1-4):381-7.
41. Knuth EL, Henne U. Average size and size distribution of large droplets produced in a free-jet expansion of a liquid. *J. Chem. Phys.* 1999;110(5):2664-8.
42. Henne U, Toennies JP. Electron capture by large helium droplets. *J. Chem. Phys.* 1998;108(22):9327-38.
43. Reho JH, Higgins J, Nooijen M, Lehmann KK, Scoles G, Gutowski M. Photoinduced nonadiabatic dynamics in quartet Na<sub>3</sub> and K<sub>3</sub> formed using helium nanodroplet isolation. *J. Chem. Phys.* 2001;115(22):10265-74.
44. Ancilotto F, Lerner P, Cole M. Physics of solvation. *J. Low. Temp. Phys.* 1995;101(5-6):1123-46.
45. Higgins J, Callegari C, Reho J, Stienkemeier F, Ernst WE, Gutowski M, et al. Helium Cluster Isolation Spectroscopy of Alkali Dimers in the Triplet Manifold. *J. Phys. Chem. A*. 1998;102(26):4952-65.
46. Tiggesbaumker J, Stienkemeier F. Formation and properties of metal clusters isolated in helium droplets. *Phys. Chem. Chem. Phys.* 2007;9(34):4748-70.
47. Toennies JP, Vilesov AF. SPECTROSCOPY OF ATOMS AND MOLECULES IN LIQUID HELIUM. *Annu. Rev. Phys. Chem.* 1998;49(1):1-41.
48. Moore DT, Ishiguro M, Miller RE. Binary complexes of HCN with H<sub>2</sub>, HD, and D<sub>2</sub> formed in helium nanodroplets. *J. Chem. Phys.* 2001;115(11):5144-54.
49. Moore DT, Ishiguro M, Oudejans L, Miller RE. High resolution infrared spectroscopy and ab initio calculations of HCN-H<sub>2</sub>/D<sub>2</sub> binary complexes. *J. Chem. Phys.* 2001;115(11):5137-43.
50. Nauta K, Miller RE. The formation of linear and T-shaped isomers of acetylene-hydrogen cyanide complexes in helium nanodroplets. *Chem. Phys. Lett.* 2001;346(1-2):129-34.
51. Nauta K, Miller RE. Vibrational relaxation of Ne, Ar, Kr-HF ( $\nu=1$ ) binary complexes in helium nanodroplets. *J. Chem. Phys.* 2001;115(10):4508-14.

52. Liu J, Shepperson B, Ellis AM, Yang S. Core-shell effects in the ionization of doped helium nanodroplets. *Phys. Chem. Chem. Phys.* 2011;13(31):13920-5.
53. Denifl S, Zappa F, Mähr I, Mauracher A, Probst M, Urban J, et al. Ionization of doped helium nanodroplets: Complexes of C60 with water clusters. *J. Chem. Phys.* 2010;132(23):-.
54. Shepperson B, Liu J, Ellis AM, Yang S. Communication: The formation of helium cluster cations following the ionization of helium nanodroplets: Influence of droplet size and dopant. *J. Chem. Phys.* 2011;135(4):-.
55. Shepperson B, Liu J, Ellis AM, Yang S. Ionization of Doped Helium Nanodroplets: Residual Helium Attached to Diatomic Cations and Their Clusters. *J. Phys. Chem. A.* 2011;115(25):7010-6.
56. Yang S, Brereton SM, Nandhra S, Ellis AM, Shang B, Yuan L-F, et al. Electron impact ionization of water-doped superfluid helium nanodroplets: Observation of He(H<sub>2</sub>O)<sub>n</sub><sup>+</sup> clusters. *J. Chem. Phys.* 2007;127(13):-.
57. Yang S, Brereton SM, Wheeler MD, Ellis AM. Electron Impact Ionization of Haloalkanes in Helium Nanodroplets. *J. Phys. Chem. A.* 2006;110(5):1791-7.
58. Spence D, Latimer E, York W, Boatwright A, Feng C, Yang S, et al. Formation of aluminium clusters in helium nanodroplets. *Int. J. Mass Spectrom.* 2014;365–366(0):86-8.
59. Shepperson B, Tandy J, Boatwright A, Feng C, Spence D, Shirley A, et al. Electronic Spectroscopy of Toluene in Helium Nanodroplets: Evidence for a Long-Lived Excited State. *J. Phys. Chem. A.* 2013;117(50):13591-5.
60. Nauta K, Miller RE. Formation of Cyclic Water Hexamer in Liquid Helium: The Smallest Piece of Ice. *Science.* 2000;287(5451):293-5.
61. Goyal S, Schutt DL, Scoles G, Robinson GN. The infrared spectrum of sulphur hexafluoride solvated in large molecular hydrogen clusters. *Chem. Phys. Lett.* 1992;196(1–2):123-7.
62. Goyal S, Schutt DL, Scoles G. Vibrational spectroscopy of sulfur hexafluoride attached to helium clusters. *Phys. Rev. Lett.* 1992;69(6):933-6.
63. Fröchtenicht R, Kaloudis M, Koch M, Huisken F. Vibrational spectroscopy of small water complexes embedded in large liquid helium clusters. *J. Chem. Phys.* 1996;105(15):6128-40.
64. Boatwright A, Besley NA, Curtis S, Wright RR, Stace AJ. A systematic shift in the electronic spectra of substituted benzene molecules trapped in helium nanodroplets. *J. Chem. Phys.* 2005;123(2):-.
65. Spence D, Latimer E, Feng C, Boatwright A, Ellis AM, Yang S. Vortex-induced aggregation in superfluid helium droplets. *Phys. Chem. Chem. Phys.* 2014;16(15):6903-6.
66. Latimer E, Spence D, Feng C, Boatwright A, Ellis AM, Yang S. Preparation of Ultrathin Nanowires Using Superfluid Helium Droplets. *Nano Lett.* 2014;14(5):2902-6.

67. Boatwright A, Feng C, Spence D, Latimer E, Binns C, Ellis AM, et al. Helium droplets: a new route to nanoparticles. *Faraday Discuss.* 2013;162(0):113-24.
68. Al-Hagan O, Kaiser C, Madison D, Murray AJ. Atomic and molecular signatures for charged-particle ionization. *Nat. Phys.* 2009;5(1):59-63.
69. Martini K, Toennies JP, Winkler C. Electron scattering from 4He and Ne clusters: determination of the cluster density from the electronic surface barrier potential. *Chem. Phys. Lett.* 1991;178(4):429-34.
70. Ellis AM, Yang S. Model for the charge-transfer probability in helium nanodroplets following electron-impact ionization. *Phys. Rev. A.* 2007;76(3):032714.
71. Halberstadt N, Janda KC. The resonant charge hopping rate in positively charged helium clusters. *Chem. Phys. Lett.* 1998;282(5-6):409-12.
72. Scheidemann A, Schilling B, Toennies JP. Anomalies in the reactions of helium(1+) with sulfur hexafluoride embedded in large helium-4 clusters. *J. Phys. Chem.* 1993;97(10):2128-38.
73. Seong J, Janda KC, Halberstadt N, Spiegelmann F. Short-time charge motion in Hen+ clusters. *J. Chem. Phys.* 1998;109(24):10873-84.
74. Fröchtenicht R, Henne U, Toennies JP, Ding A, Fieber-Erdmann M, Drewello T. The photoionization of large pure and doped helium droplets. *J. Chem. Phys.* 1996;104(7):2548-56.
75. Kim JH, Peterka DS, Wang CC, Neumark DM. Photoionization of helium nanodroplets doped with rare gas atoms. *J. Chem. Phys.* 2006;124(21):-.
76. Onsager L. Statistical hydrodynamics. *Nuovo Cim.* 1949;6(2):279-87.
77. Bauer G, Donnelly R, Vinen WF. Vortex configurations in a freely rotating superfluid drop. *J. Low Temp. Phys.* 1995;98(1-2):47-65.
78. Lehmann KK, Schmied R. Energetics and possible formation and decay mechanisms of vortices in helium nanodroplets. *Phys. Rev. B.* 2003;68(22):224520.
79. Barranco M, Guardiola R, Hernández S, Mayol R, Navarro J, Pi M. Helium Nanodroplets: An Overview. *J. Low Temp. Phys.* 2006;142(1-2):1-81.
80. Dalfovo F, Mayol R, Pi M, Barranco M. Pinning of Quantized Vortices in Helium Drops by Dopant Atoms and Molecules. *Phys. Rev. Lett.* 2000;85(5):1028-31.
81. Rayfield GW, Reif F. Quantized vortex rings in superfluid helium. *Phys. Rev.* 1964;136(5A):A1194.
82. Bewley GP, Lathrop DP, Sreenivasan KR. SUPERFLUID HELIUM: Visualization of quantized vortices. *Nature.* 2006;441(7093):588-.
83. Gomez LF, Loginov E, Vilesov AF. Traces of Vortices in Superfluid Helium Droplets. *Phys. Rev. Lett.* 2012;108(15):155302.
84. Gomez LF, Ferguson KR, Cryan JP, Bacellar C, Tanyag RMP, Jones C, et al. Shapes and vorticities of superfluid helium nanodroplets. *Science.* 2014;345(6199):906-9.

85. Ben-Horin N, Even U, Jortner J, Leutwyler S. Spectroscopy and nuclear dynamics of tetracene–rare-gas heteroclusters. *J. Chem. Phys.* 1992;97(8):5296-315.
86. Andrews L, Moskovits M. Chemistry and physics of matrix-isolated species: North-Holland; 1989.
87. Ulzega S. Theoretical and Experimental Study of the Stark Effect in the Ground State of Alkali Atoms in Helium Crystals 2006.
88. Nauta K, Miller RE. Nonequilibrium Self-Assembly of Long Chains of Polar Molecules in Superfluid Helium. *Science.* 1999;283(5409):1895-7.
89. Flynn SD, Skvortsov D, Morrison AM, Liang T, Choi MY, Douberly GE, et al. Infrared Spectra of HCl–H<sub>2</sub>O Clusters in Helium Nanodroplets. *J. Phys. Chem. Lett.* 2010;1(15):2233-8.
90. Gutberlet A, Schwaab G, Birer Ö, Masia M, Kaczmarek A, Forbert H, et al. Aggregation-Induced Dissociation of HCl(H<sub>2</sub>O)<sub>4</sub> Below 1 K: The Smallest Droplet of Acid. *Science.* 2009;324(5934):1545-8.
91. Hartmann M, Mielke F, Toennies J, Vilesov A, Benedek G. Direct Spectroscopic Observation of Elementary Excitations in Superfluid He Droplets. *Phys. Rev. Lett.* 1996;76(24):4560-3.
92. Hartmann M, Lindinger A, Toennies JP, Vilesov AF. Laser-induced fluorescence spectroscopy of van der Waals complexes of tetracene–Ar<sub>N</sub> (N ≤ 5) and pentacene–Ar within ultracold liquid He droplets. *Chem. Phys.* 1998;239(1–3):139-49.
93. Curtis S, Boatwright A, Wright RR, Stace AJ. Evidence of a shift between one- and two-photon processes associated with benzene trapped in helium nanodroplets. *Chem. Phys. Lett.* 2005;401(1–3):254-8.
94. Federmann F, Hoffmann K, Quaas N, Toennies JP. Spectroscopy of extremely cold silver clusters in helium droplets. *Eur. Phys. J. D.* 1999;9(1):11-4.
95. Loginov E, Gomez LF, Vilesov AF. Surface Deposition and Imaging of Large Ag Clusters Formed in He Droplets. *J. Phys. Chem. A.* 2011;115(25):7199-204.
96. Loginov E, Gomez L, Chiang N, Halder A, Guggemos N, Kresin V, et al. Photoabsorption of Ag<sub>N</sub> (N ~ 6–6000) Nanoclusters Formed in Helium Droplets: Transition from Compact to Multicenter Aggregation. *Phys. Rev. Lett.* 2011;106(23):233401.
97. Thaler P, Volk A, Lackner F, Steurer J, Knez D, Grogger W, et al. Formation of bimetallic core-shell nanowires along vortices in superfluid He nanodroplets. *Phys. Rev. B.* 2014;90(15):155442.
98. Emery SB, Rider KB, Little BK, Schrand AM, Lindsay CM. Magnesium cluster film synthesis by helium nanodroplets. *J. Chem. Phys.* 2013;139(5):-.
99. Volk A, Thaler P, Koch M, Fisslthaler E, Grogger W, Ernst WE. High resolution electron microscopy of Ag-clusters in crystalline and non-crystalline morphologies grown inside superfluid helium nanodroplets. *J. Chem. Phys.* 2013;138(21):-.

100. Papkov D, Goponenko A, Compton OC, An Z, Moravsky A, Li XZ, et al. Improved Graphitic Structure of Continuous Carbon Nanofibers via Graphene Oxide Templating. *Adv. Funct. Mater.* 2013;23(46):5763-70.
101. Gupta AK, Gupta M. Synthesis and surface engineering of iron oxide nanoparticles for biomedical applications. *Biomaterials.* 2005;26(18):3995-4021.
102. Mornet S, Vasseur S, Grasset F, Veverka P, Goglio G, Demourgues A, et al. Magnetic nanoparticle design for medical applications. *Prog. Solid State Ch.* 2006;34(2-4):237-47.
103. Hyeon T. Chemical synthesis of magnetic nanoparticles. *Chem. Commun.* 2003(8):927-34.
104. John P, Jaykumar T, Kalyanasundaram P, Baldev R. A tunable optical filter. *Meas. Sci. Technol.* 2003;14(8):1289.
105. Tilley RD, Jefferson DA. The preparation of chromium, nickel and chromium-nickel alloy nanoparticles on supports. *J. Mater. Chem.* 2002;12(12):3809-13.
106. Binns C, Trohidou KN, Bansmann J, Baker SH, Blackman JA, Bucher JP, et al. The behaviour of nanostructured magnetic materials produced by depositing gas-phase nanoparticles. *J. Phys. D: Applied Physics.* 2005;38(22):R357.
107. Buschow KHJ, de Boer FR. *Physics of Magnetism and Magnetic Materials*: Springer; 2003.
108. Stepanyuk VS, Hergert W, Wildberger K, Zeller R, Dederichs PH. Magnetism of 3d, 4d and 5d transition-metal impurities on Pd(001) and Pt(001) surfaces. *Phys. Rev. B.* 1996;53(4):2121-5.
109. Wang X-Y, Avendano C, Dunbar KR. Molecular magnetic materials based on 4d and 5d transition metals. *Chem. Soc. Rev.* 2011;40(6):3213-38.
110. Van Zee RJ, Li S, Weltner W. Gd<sub>2</sub>: The highest spin diatomic molecule? *J. Chem. Phys.* 1994;100(5):4010-2.
111. Pokrant S. Evidence for adiabatic magnetization of cold DyN Clusters. *Phys. Rev. A.* 2000;62(5):051201.
112. Mauger A, Godart C. The magnetic, optical, and transport properties of representatives of a class of magnetic semiconductors: The europium chalcogenides. *Phys. Rep.* 1986;141(2-3):51-176.
113. Henry W. Spin Paramagnetism of Cr<sup>+++</sup>, Fe<sup>+++</sup>, and Gd<sup>+++</sup> at Liquid Helium Temperatures and in Strong Magnetic Fields. *Phys. Rev.* 1952;88(3):559-62.
114. Gambardella P, Dhesi S, Gardonio S, Grazioli C, Ohresser P, Carbone C. Localized magnetic states of Fe, Co, and Ni impurities on alkali metal films. *Phys. Rev. Lett.* 2002;88(4):047202.
115. Tiago M, Zhou Y, Alemany M, Saad Y, Chelikowsky J. Evolution of Magnetism in Iron from the Atom to the Bulk. *Phys. Rev. Lett.* 2006;97(14):147201.

116. Yun WS, Hong SC, Lee JI, Hwang CY. Magnetism of Co layers grown on a W (001) surface: a density functional study. *J. Korean. Phys. Soc.* 2010; 56(5): 1472.
117. Kittel C, McEuen P. Introduction to solid state physics: Wiley New York; 1976.
118. Piskunov S, Zvejnieks G, Zhukovskii YF, Bellucci S. Atomic and electronic structure of both perfect and nanostructured Ni(111) surfaces: First-principles calculations. *Thin Solid Films.* 2011;519(11):3745-51.
119. Chen C, Wiesendanger R. Perturbation theory of exchange interaction. *Phys. Rev. B.* 2006;74(11):113102.
120. Jiles DC. Introduction to magnetism and magnetic materials: CRC Press; 1998.
121. Hummel R. Quantum Mechanical Considerations. *Electronic Properties of Materials:* Springer Berlin Heidelberg; 1985. p. 238-47.
122. Spaldin NA. *Magnetic materials: fundamentals and applications:* Cambridge University Press; 2010.
123. Pereiro M, Baldomir D, Arias J. Unexpected magnetism of small silver clusters. *Phys. Rev. A.* 2007;75(6):063204.
124. Selenska-Pobel S, Reitz T, Schöneman R, Herrmansdörfer T, Merroun M, Geißler A, et al. Magnetic Au nanoparticles on archaeal S-Layer ghosts as templates. *Nanomaterials and Nanotechnology.* 2011;1(2):8-16.
125. Li C-Y, Wu C-M, Karna S, Wang C-W, Hsu D, Wang C-J, et al. Intrinsic magnetic moments of gold nanoparticles. *Phys. Rev. B.* 2011;83(17):174446.
126. Zhang W, Brück E, Zhang Z, Tegus O, Li W, Si P, et al. Structure and magnetic properties of Cr nanoparticles and Cr<sub>2</sub>O<sub>3</sub> nanoparticles. *Physica B: Condensed Matter.* 2005;358(1):332-8.
127. Koksharov YA. *Magnetism of Nanoparticles: Effects of Size, Shape, and Interactions.* Magnetic Nanoparticles: Wiley-VCH Verlag GmbH & Co. KGaA; 2009. p. 197-254.
128. Warren JB, Panessa-Warren BJ. A Comparison of Nanometrology Using SEM and TEM. *Microsc. Microanal.* 2005;11(SupplementS02):1932-3.
129. Hornyak GL, Peschel S, Sawitowski T, Schmid G. TEM, STM and AFM as tools to study clusters and colloids. *Micron.* 1998;29(2-3):183-90.
130. van de Leemput LEC, Gerritsen JW, Rongen PHH, Smokers RTM, Wierenga HA, van Kempen H, et al. Scanning tunneling microscopy observations of metallic clusters Pd<sub>561</sub> and Au<sub>55</sub> and the implications of their use as a well defined tip. *J. Vac. Sci. Technol. B: Microelectronics and Nanometer Structures.* 1991;9(2):814-9.
131. Sauerbrey G. Wagung Dunner Schichten mit Schwingquarzen. *Phys. Verhandl.* 1957;8:S.193.
132. Lostis P. Etude, realisation et controle de lames minces introduisant une difference de marche d'Herminee entre deux vibrations rectangulaires. *Rev. Opt.* 1959;38 S.1-28.

133. Sauerbrey G. Verwendung von Schwingquarzen zur Wägung dünner Schichten und zur Mikrowägung. *Z. Physik.* 1959;155(2):206-22.
134. Lu CS, Lewis O. Investigation of film-thickness determination by oscillating quartz resonators with large mass load. *J. Appl. Phys.* 1972;43(11):4385-90.
135. Fuggle JC, Alvarado SF. Core-level lifetimes as determined by x-ray photoelectron spectroscopy measurements. *Phys. Rev. A.* 1980;22(4):1615-24.
136. Pessa VM. Data for graphical resolution of two overlapping X-ray emission lines. Natural widths of  $K\alpha_{1,2}$  of the elements  $Z = 10$  to 92. *X-Ray Spectrometry.* 1973;2(4):169-72.
137. Salem SI, Lee PL. Experimental widths of K and L x-ray lines. Atomic Data and Nuclear Data Tables. 1976;18(3):233-41.
138. Krause MO, Oliver JH. Natural widths of atomic K and L levels,  $K\alpha$  X-ray lines and several KLL Auger lines. *J. Phys. Chem. Ref. Data.* 1979;8(2):329-38.
139. Castle JE, Salvi AM. Interpretation of the Shirley background in x-ray photoelectron spectroscopy analysis. *J. Vac. Sci. Technol. A.* 2001;19(4):1170-5.
140. Pankhurst QA, Connolly J, Jones SK, Dobson J. Applications of magnetic nanoparticles in biomedicine. *J. Phys. D: Applied Physics.* 2003;36(13):R167.
141. Knuth EL, Schünemann F, Toennies JP. Supercooling of H<sub>2</sub> clusters produced in free-jet expansions from supercritical states. *J. Chem. Phys.* 1995;102(15):6258-71.
142. Lewis WK, Lindsay CM, Bemish RJ, Miller RE. Probing Charge-Transfer Processes in Helium Nanodroplets by Optically Selected Mass Spectrometry (OSMS): Charge Steering by Long-Range Interactions. *J. Am. Chem. Soc.* 2005;127(19):7235-42.
143. Massobrio C. Comment on 'structure and diffusion of clusters on Ni surfaces by C.-L. Liu and J.B. Adams'. *Surf. Sci. Lett.* 1993;289(3):L638-L40.
144. Schilling B. Max-Planck Institute for Dynamics and Self-Organization, Göttingen; 1993.
145. Zafeiratos S, Kennou S. Photoelectron spectroscopy study of surface alloying in the Au/Ni (s)  $5(0\ 0\ 1) \times (1\ 1\ 1)$  system. *Appl. Surf. Sci.* 2001;173(1-2):69-75.
146. Marx D. Proton Transfer 200 Years after von Grothhuss: Insights from Ab Initio Simulations. *Chem. Phys. Chem.* 2007;8(2):209-10.
147. Payandeh J, Scheuer T, Zheng N, Catterall WA. The crystal structure of a voltage-gated sodium channel. *Nature.* 2011;475(7356):353-8.
148. Zhou Y, Morais-Cabral JH, Kaufman A, MacKinnon R. Chemistry of ion coordination and hydration revealed by a K<sup>+</sup> channel-Fab complex at 2.0[thinsp][angst] resolution. *Nature.* 2001;414(6859):43-8.
149. Finlayson-Pitts B. The tropospheric chemistry of sea salt: A molecular-level view of the chemistry of NaCl and NaBr. *Chem. Rev.* 2003;103(12):4801-22.

150. Knipping EM, Lakin MJ, Foster KL, Jungwirth P, Tobias DJ, Gerber RB, et al. Experiments and Simulations of Ion-Enhanced Interfacial Chemistry on Aqueous NaCl Aerosols. *Science*. 2000;288(5464):301-6.
151. Zhang C, Raugei S, Eisenberg B, Carloni P. Molecular Dynamics in Physiological Solutions: Force Fields, Alkali Metal Ions, and Ionic Strength. *J. Chem. Theory Comput.* 2010;6(7):2167-75.
152. Eigen M, Tamm UK. Schallabsorption in Elektrolytlösungen als Folge chemischer Relaxation II. Meßergebnisse und Relaxationsmechanismen für 2—2-wertige Elektrolyte. *Zeitschrift für Elektrochemie, Berichte der Bunsengesellschaft für physikalische Chemie*. 1962;66(2):107-21.
153. Wiedemair MJ, Weiss AK, Rode BM. Ab initio quantum mechanical simulations confirm the formation of all postulated species in ionic dissociation. *Phys. Chem. Chem. Phys.* 2014;16(16):7368-76.
154. Buchner R, Hefter G. Interactions and dynamics in electrolyte solutions by dielectric spectroscopy. *Phys. Chem. Chem. Phys.* 2009;11(40):8984-99.
155. Woon DE, Dunning TH, Jr. The Pronounced Effect of Microsolvation on Diatomic Alkali Halides: Ab Initio Modeling of  $\text{MX}(\text{H}_2\text{O})_n$  ( $\text{M} = \text{Li}, \text{Na}; \text{X} = \text{F}, \text{Cl}; n = 1-3$ ). *J. Am. Chem. Soc.* 1995;117(3):1090-7.
156. Petersen CP, Gordon MS. Solvation of Sodium Chloride: An Effective Fragment Study of  $\text{NaCl}(\text{H}_2\text{O})_n$ . *J. Phys. Chem. A*. 1999;103(21):4162-6.
157. Jungwirth P. How Many Waters Are Necessary To Dissolve a Rock Salt Molecule? *J. Phys. Chem. A*. 1999;104(1):145-8.
158. Olleta AC, Lee HM, Kim KS. Ab initio study of hydrated sodium halides  $\text{NaX}(\text{H}_2\text{O})_{1-6}$  ( $\text{X}=\text{F}, \text{Cl}, \text{Br}, \text{and I}$ ). *J. Chem. Phys.* 2006;124(2):-.
159. Siu C-K, Fox-Beyer BS, Beyer MK, Bondybey VE. Ab Initio Molecular Dynamics Studies of Ionic Dissolution and Precipitation of Sodium Chloride and Silver Chloride in Water Clusters,  $\text{NaCl}(\text{H}_2\text{O})_n$  and  $\text{AgCl}(\text{H}_2\text{O})_n$ ,  $n = 6, 10, \text{and } 14$ . *Chemistry – A European Journal*. 2006;12(24):6382-92.
160. Ghosh MK, Re S, Feig M, Sugita Y, Choi CH. Interionic Hydration Structures of NaCl in Aqueous Solution: A Combined Study of Quantum Mechanical Cluster Calculations and QM/EFP-MD Simulations. *J. Phys. Chem. B*. 2012;117(1):289-95.
161. Marcus Y, Hefter G. Ion Pairing. *Chem. Rev.* 2006;106(11):4585-621.
162. Ault BS. Infrared spectra of argon matrix-isolated alkali halide salt/water complexes. *J. Am. Chem. Soc.* 1978;100(8):2426-33.
163. Mizoguchi A, Ohshima Y, Endo Y. Microscopic Hydration of the Sodium Chloride Ion Pair. *J. Am. Chem. Soc.* 2003;125(7):1716-7.
164. Mizoguchi A, Ohshima Y, Endo Y. The study for the incipient solvation process of NaCl in water: The observation of the  $\text{NaCl}-(\text{H}_2\text{O})_n$  ( $n = 1, 2, \text{and } 3$ ) complexes using Fourier-transform microwave spectroscopy. *J. Chem. Phys.* 2011;135(6):-.

165. Miller RC, Kusch P. Molecular Composition of Alkali Halide Vapors. *J. Chem. Phys.* 1956;25(5):860-76.
166. Kuyanov-Prozument K, Choi MY, Vilesov AF. Spectrum and infrared intensities of OH-stretching bands of water dimers. *J. Chem. Phys.* 2010;132(1):014304.
167. Dang L, Chang T-M. Computational Studies of Liquid Water Interfaces. In: Buch V, Devlin JP, editors. *Water in Confining Geometries*. Springer Series in Cluster Physics: Springer Berlin Heidelberg; 2003. p. 227-47.
168. Timko J, Bucher D, Kuyucak S. Dissociation of NaCl in water from ab initio molecular dynamics simulations. *J. Chem. Phys.* 2010;132(11):114510.
169. Ayotte P, Weddle GH, Kim J, Johnson MA. Vibrational Spectroscopy of the Ionic Hydrogen Bond: Fermi Resonances and Ion-Molecule Stretching Frequencies in the Binary  $X^- \cdot H_2O$  ( $X = Cl, Br, I$ ) Complexes via Argon Predissociation Spectroscopy. *J. Am. Chem. Soc.* 1998;120(47):12361-2.
170. Choi J-H, Kuwata KT, Cao Y-B, Okumura M. Vibrational Spectroscopy of the  $Cl^-(H_2O)_n$  Anionic Clusters,  $n = 1-5$ . *J. Phys. Chem. A.* 1998;102(3):503-7.
171. Ayotte P, Weddle GH, Kim J, Kelley J, Johnson MA. A Cluster Study of Anionic Hydration: Spectroscopic Characterization of the  $Cl^-(H_2O)_n$ ,  $1 \leq n \leq 3$ , Supramolecular Complexes at the Primary Steps of Solvation. *J. Phys. Chem. A.* 1999;103(4):443-7.
172. Feynman RP. *Progress in Low Temperature Physics* Amsterdam North-Holland; 1955.
173. Vinen W. The detection of single quanta of circulation in liquid helium II. *Proc. R. Soc. A Mathematical and Physical Sciences.* 1961;260(1301):218-36.
174. Donnelly RJ. *Quantized vortices in helium II*: Cambridge University Press; 1991.
175. Gordon EB, Karabulin AV, Matyushenko VI, Sizov VD, Khodos II. Structure of metallic nanowires and nanoclusters formed in superfluid helium. *J. Exp. Theor. Phys.* 2011;112(6):1061-70.
176. Loginov E, Gomez LF, Chiang N, Halder A, Guggemos N, Kresin VV, et al. Photoabsorption of AgN(N~6-6000) Nanoclusters Formed in Helium Droplets: Transition from Compact to Multicenter Aggregation. *Phys. Rev. Lett.* 2011;106(23):233401.
177. Dreher M, Pauly F, Heurich J, Cuevas JC, Scheer E, Nielaba P. Structure and conductance histogram of atomic-sized Au contacts. *Phys. Rev. B.* 2005;72(7):075435.
178. Fagas G, Greer JC. Ballistic Conductance in Oxidized Si Nanowires. *Nano Lett.* 2009;9(5):1856-60.
179. Pascual JI, Méndez J, Gómez-Herrero J, Baró AM, Garcia N, Landman U, et al. Properties of Metallic Nanowires: From Conductance Quantization to Localization. *Science.* 1995;267(5205):1793-5.
180. Teng X, Han W-Q, Ku W, Hücker M. Synthesis of Ultrathin Palladium and Platinum Nanowires and a Study of Their Magnetic Properties. *Angew. Chem. Int. Ed. Engl.* 2008;47(11):2055-8.

181. Arutyunov KY. Negative magnetoresistance of ultra-narrow superconducting nanowires in the resistive state. *Physica C: Superconductivity*. 2008;468(4):272-5.
182. Dresselhaus MS, Chen G, Tang MY, Yang RG, Lee H, Wang DZ, et al. New Directions for Low-Dimensional Thermoelectric Materials. *Adv. Mater.* 2007;19(8):1043-53.
183. Li H-H, Zhao S, Gong M, Cui C-H, He D, Liang H-W, et al. Ultrathin PtPdTe Nanowires as Superior Catalysts for Methanol Electrooxidation. *Angew. Chem. Int. Ed. Engl.* 2013;52(29):7472-6.
184. Zeng XQ, Latimer ML, Xiao ZL, Panuganti S, Welp U, Kwok WK, et al. Hydrogen Gas Sensing with Networks of Ultrasmall Palladium Nanowires Formed on Filtration Membranes. *Nano Lett.* 2010;11(1):262-8.
185. Jain A, Nair PR, Alam MA. Flexure-FET biosensor to break the fundamental sensitivity limits of nanobiosensors using nonlinear electromechanical coupling. *Proc. Natl. Acad. Sci.* 2012;109(24):9304-8.
186. Lieber CM. Nanoscale Science and Technology: Building a Big Future from Small Things. *MRS Bulletin*. 2003;28(07):486-91.
187. Kundu P, Chandni U, Ghosh A, Ravishankar N. Pristine, adherent ultrathin gold nanowires on substrates and between pre-defined contacts via a wet chemical route. *Nanoscale*. 2012;4(2):433-7.
188. Hong BH, Bae SC, Lee C-W, Jeong S, Kim KS. Ultrathin Single-Crystalline Silver Nanowire Arrays Formed in an Ambient Solution Phase. *Science*. 2001;294(5541):348-51.
189. Malisauskas M, Meskys R, Morozova-Roche LA. Ultrathin silver nanowires produced by amyloid biotemplating. *Biotechnol. Progr.* 2008;24(5):1166-70.
190. Liu Z, Xu D, Liang J, Shen J, Zhang S, Qian Y. Growth of Cu<sub>2</sub>S Ultrathin Nanowires in a Binary Surfactant Solvent. *J. Phys. Chem. B*. 2005;109(21):10699-704.
191. Yang S, Hong F, Wang L, Guo S, Song X, Ding B, et al. Ultrathin Pt-Based Alloy Nanowire Networks: Synthesized by CTAB Assisted Two-Phase Water-Chloroform Micelles. *J. Phys. Chem. C*. 2009;114(1):203-7.
192. Hong X, Wang D, Yu R, Yan H, Sun Y, He L, et al. Ultrathin Au-Ag bimetallic nanowires with Coulomb blockade effects. *Chem. Commun.* 2011;47(18):5160-2.
193. Koenigsmann C, Santulli AC, Gong K, Vukmirovic MB, Zhou W-p, Sutter E, et al. Enhanced Electrocatalytic Performance of Processed, Ultrathin, Supported Pd-Pt Core-Shell Nanowire Catalysts for the Oxygen Reduction Reaction. *J. Am. Chem. Soc.* 2011;133(25):9783-95.
194. Witten TA, Sander LM. Diffusion-Limited Aggregation, a Kinetic Critical Phenomenon. *Phys. Rev. Lett.* 1981;47(19):1400-3.
195. Liang CL, Zhong K, Liu M, Jiang L, Liu SK, Xing DD, et al. Synthesis of morphology-controlled silver nanostructures by electrodeposition. *Nano-Micro Lett.* 2010;2(1):6-10.

196. Billas IML, Châtelain A, de Heer WA. Magnetism from the Atom to the Bulk in Iron, Cobalt, and Nickel Clusters. *Science*. 1994;265(5179):1682-4.
197. Payne F, Jiang W, Bloomfield L. Magnetism and magnetic isomers in free chromium clusters. *Phys. Rev. Lett.* 2006;97(19):193401.
198. Baibich MN, Broto JM, Fert A, Van Dau FN, Petroff F, Etienne P, et al. Giant Magnetoresistance of (001)Fe/(001)Cr Magnetic Superlattices. *Phys. Rev. Lett.* 1988;61(21):2472-5.
199. Binasch G, Grünberg P, Saurenbach F, Zinn W. Enhanced magnetoresistance in layered magnetic structures with antiferromagnetic interlayer exchange. *Phys. Rev. B.* 1989;39(7):4828-30.
200. Edelstein RL, Tamanaha CR, Sheehan PE, Miller MM, Baselt DR, Whitman LJ, et al. The BARC biosensor applied to the detection of biological warfare agents. *Biosens. Bioelectron.* 2000;14(10–11):805-13.
201. Tsang C, Fontana RE, Lin T, Heim DE, Speriosu VS, Gurney BA, et al. Design, fabrication and testing of spin-valve read heads for high density recording. *Magnetics, IEEE Transactions on.* 1994;30(6):3801-6.
202. Daughton J. GMR applications. *J. Magn. Magn. Mater.* 1999;192(2):334-42.
203. Meiklejohn WH, Bean CP. New Magnetic Anisotropy. *Phys. Rev.* 1956;102(5):1413-4.
204. Finazzi M, Duò L, Ciccacci F. RETRACTED: Magnetic properties of interfaces and multilayers based on thin antiferromagnetic oxide films. *Surf. Sci. Rep.* 2007;62(9):337-71.
205. Nogués J, Sort J, Langlais V, Skumryev V, Suriñach S, Muñoz JS, et al. Exchange bias in nanostructures. *Phys. Rep.* 2005;422(3):65-117.
206. Dieny B, Speriosu VS, Parkin SSP, Gurney BA, Wilhoit DR, Mauri D. Giant magnetoresistive in soft ferromagnetic multilayers. *Phys. Rev. B.* 1991;43(1):1297-300.
207. Skumryev V, Stoyanov S, Zhang Y, Hadjipanayis G, Givord D, Nogués J. Beating the superparamagnetic limit with exchange bias. *Nature*. 2003;423(6942):850-3.
208. Aktas B, Mikailzade F. Nanostructured materials for magnetoelectronics: Springer; 2013.
209. Qureshi M, Baker S, Binns C, Roy M, Laureti S, Fiorani D, et al. Structure and magnetic properties of FE nanoparticles embedded in a CR matrix. *J. Magn. Magn. Mater.* 2014.
210. Binns C, Qureshi MT, Peddis D, Baker SH, Howes PB, Boatwright A, et al. Exchange Bias in Fe@Cr Core–Shell Nanoparticles. *Nano Lett.* 2013;13(7):3334-9.
211. Abdul-Razzaq W, Seehra MS. Observation of Oxidation and Mechanical Strain in Cr Nanoparticles Produced by Ball-Milling. *Phys. Status Solidi A.* 2002;193(1):94-102.
212. Fitzsimmons MR, Eastman JA, Robinson RA, Lawson AC, Thompson JD, Movshovich R, et al. Magnetic order in nanocrystalline Cr and suppression of antiferromagnetism in bcc Cr. *Phys. Rev. B.* 1993;48(11):8245-52.

213. Fitzsimmons MR, Eastman JA, Robinson RA, Lynn JW. The Néel temperature of nanocrystalline chromium. *J. Appl. Phys.* 1995;78(2):1364-6.
214. Tsunoda Y, Nakano H, Matsuo S. Antiferromagnetism of Cr fine particles. *J. Phys.: Condensed Matter.* 1993;5(3):L29.
215. Néel L. *Low Temperature Physics*: Gordon & Breach: New York; 1962.
216. Punnoose A, Magnone H, Seehra MS, Bonevich J. Bulk to nanoscale magnetism and exchange bias in CuO nanoparticles. *Phys. Rev. B.* 2001;64(17):174420.
217. Kodama RH, Makhlof SA, Berkowitz AE. Finite Size Effects in Antiferromagnetic NiO Nanoparticles. *Phys. Rev. Lett.* 1997;79(7):1393-6.
218. Makhlof SA, Parker FT, Spada FE, Berkowitz AE. Magnetic anomalies in NiO nanoparticles. *J. Appl. Phys.* 1997;81(8):5561-3.
219. Makhlof SA, Parker FT, Berkowitz AE. Magnetic hysteresis anomalies in ferritin. *Phys. Rev. B.* 1997;55(22):R14717-R20.
220. Gider S, Awschalom D, Douglas T, Mann S, Chaparala M. Classical and quantum magnetic phenomena in natural and artificial ferritin proteins. *Science.* 1995;268(5207):77-80.
221. Richardson JT, Yiagas DI, Turk B, Forster K, Twigg MV. Origin of superparamagnetism in nickel oxide. *J. Appl. Phys.* 1991;70(11):6977-82.
222. Li D, Han Z, Zheng J, Wang X, Geng D, Li J, et al. Spin canting and spin-flop transition in antiferromagnetic Cr<sub>2</sub>O<sub>3</sub> nanocrystals. *J. Appl. Phys.* 2009;106(5):053913--5.
223. Morales M, Serna C, Bødker F, Mørup S. Spin canting due to structural disorder in maghemite. *J. Phys.: Condensed Matter.* 1997;9(25):5461.
224. Sartiman SS, Djaja NF, Saleh R. Chromium-Doped ZnO Nanoparticles Synthesized by Co-Precipitation: Chromium Effects. *Mater. Sci. Appl.* 2013;4(09):528.
225. Mornet S, Vasseur S, Grasset F, Duguet E. Magnetic nanoparticle design for medical diagnosis and therapy. *J. Mater. Chem.* 2004;14(14):2161-75.
226. Tartaj P, Morales MdP, Veintemillas-Verdaguer S, González-Carreno T, Serna CJ. The preparation of magnetic nanoparticles for applications in biomedicine. *J. Phys. D: Applied Physics.* 2003;36(13):R182.
227. Pillai G, Ceballos-Coronel ML. Science and technology of the emerging nanomedicines in cancer therapy: A primer for physicians and pharmacists. *SAGE Open Med.* 2013;1:2050312113513759.
228. Kura H, Takahashi M, Ogawa T. Synthesis of Monodisperse Iron Nanoparticles with a High Saturation Magnetization Using an Fe (CO) x- Oleylamine Reacted Precursor. *J. Phys. Chem. C.* 2010;114(13):5835-8.
229. Park BJ, Song KH, Choi HJ. Magnetic carbonyl iron nanoparticle based magnetorheological suspension and its characteristics. *Mater. Lett.* 2009;63(15):1350-2.

230. Choi C-J, Dong X-L, Kim B-K. Microstructure and Magnetic Properties of Fe Nanoparticles Synthesized by Chemical Vapor Condensation. *Mater. Trans.* 2001;42(10):2046-9.
231. Choi BJ, Lee GH. Production and magnetic properties of in situ oligomer coated  $\alpha$ -Fe nanoparticles in the gas phase. *J. Appl. Phys.* 2007;102(10):104302.
232. Kelgenbaeva Z, Omurzak E, Takebe S, Sulaimankulova S, Abdullaeva Z, Iwamoto C, et al. Synthesis of pure iron nanoparticles at liquid–liquid interface using pulsed plasma. *J. Nanopart. Res.* 2014;16(9):1-11.
233. Chaubey GS, Kim J. Structure and Magnetic Characterization of Core-Shell Fe@ ZrO<sub>2</sub> Nanoparticles Synthesized by Sol-Gel Process. *Bulletin-Korean Chem. Soc.* 2007;28(12):2279.
234. Han YC, Heo JK, Kim YH, Kang YS. Heating temperature effect on the magnetic property of  $\alpha$ -Fe nanoparticle. *Mol. Cryst. Liq. Cryst.* 2007;472(1):69/[459]-75/[65].
235. Sun Q, Kandalam AK, Wang Q, Jena P, Kawazoe Y, Marquez M. Effect of Au coating on the magnetic and structural properties of Fe nanoclusters for use in biomedical applications: A density-functional theory study. *Phys. Rev. B.* 2006;73(13):134409.
236. Carpenter EE. Iron nanoparticles as potential magnetic carriers. *J. Magn. Magn. Mater.* 2001;225(1):17-20.
237. Chen M, Yamamuro S, Farrell D, Majetich SA. Gold-coated iron nanoparticles for biomedical applications. *J. Appl. Phys.* 2003;93(10):7551-3.
238. Lee C-C, Chen D-H. Large-scale synthesis of Ni–Ag core–shell nanoparticles with magnetic, optical and anti-oxidation properties. *Nanotechnology.* 2006;17(13):3094.
239. Cho S-J, Shahin AM, Long GJ, Davies JE, Liu K, Grandjean F, et al. Magnetic and Mössbauer Spectral Study of Core/Shell Structured Fe/Au Nanoparticles. *Chem. Mater.* 2006;18(4):960-7.
240. Cho S-J, Idrobo J-C, Olamit J, Liu K, Browning ND, Kauzlarich SM. Growth Mechanisms and Oxidation Resistance of Gold-Coated Iron Nanoparticles. *Chem. Mater.* 2005;17(12):3181-6.
241. Chen D, Li J, Shi C, Du X, Zhao N, Sheng J, et al. Properties of Core–Shell Ni–Au Nanoparticles Synthesized through a Redox-Transmetalation Method in Reverse Microemulsion. *Chem. Mater.* 2007;19(14):3399-405.
242. Wang L-S, Wu H, Cheng H. Photoelectron spectroscopy of small chromium clusters: Observation of even-odd alternations and theoretical interpretation. *Phys. Rev. B.* 1997;55(19):12884-7.
243. El-Hilo M, O'Grady K, Chantrell RW. Susceptibility phenomena in a fine particle system: I. Concentration dependence of the peak. *J. Magn. Magn. Mater.* 1992;114(3):295-306.
244. Söffge F, Schmidbauer E. AC susceptibility and static magnetic properties of AN Fe<sub>3</sub>O<sub>4</sub> ferrofluid. *J. Magn. Magn. Mater.* 1981;24(1):54-66.

245. Batlle X, Franco V, Labarta A, Grady K. Remanence breakdown in granular alloys at magnetic percolation. *J. Appl. Phys.* 2000;88(3):1576-82.
246. Batlle X, Franco V, Labarta A, Watson ML, O'Grady K. The effect of the microstructure on the magnetic interactions in CoFe–AgCu granular films: From demagnetizing to magnetizing interactions. *Appl. Phys. Lett.* 1997;70(1):132-4.
247. Zhu G-X, Wei X-W, Jiang S. A facile route to carbon-coated nickel-based metal nanoparticles. *J. Mater. Chem.* 2007;17(22):2301-6.
248. Johnston-Peck AC, Wang J, Tracy JB. Synthesis and Structural and Magnetic Characterization of Ni(Core)/NiO(Shell) Nanoparticles. *ACS Nano.* 2009;3(5):1077-84.
249. Apsel S, Emmert J, Deng J, Bloomfield L. Surface-enhanced magnetism in nickel clusters. *Phys. Rev. Lett.* 1996;76(9):1441.
250. Riegel D, Barth H, Büermann L, Haas H, Stenzel C. Fully localized 3 d-shell behavior of Fe ions in alkali-metal hosts. *Phys. Rev. Lett.* 1986;57(3):388.
251. Bansmann J, Kleibert A, Getzlaff M, Rodríguez AF, Nolting F, Boeglin C, et al. Magnetism of 3d transition metal nanoparticles on surfaces probed with synchrotron radiation—from ensembles towards individual objects. *Phys. Status Solidi B.* 2010;247(5):1152-60.
252. Sun S, Murray C, Weller D, Folks L, Moser A. Monodisperse FePt nanoparticles and ferromagnetic FePt nanocrystal superlattices. *Science.* 2000;287(5460):1989-92.
253. Rellinghaus B, Stappert S, Acet M, Wassermann EF. Magnetic properties of FePt nanoparticles. *J. Magn. Magn. Mater.* 2003;266(1):142-54.